New Solutions for Directive Antennas and Components for Millimeter Wave-Band Applications

by

Nafsika Memeletzoglou

A dissertation submitted by in partial fulfillment of the requirements for the degree of Doctor of Philosophy in

Multimedia and Communications

Universidad Carlos III de Madrid

Advisor and Tutor:

Eva Rajo Iglesias

May 2021

Acknowledgements

While this journey comes to an end, I couldn't be more grateful for all the people that supported me during these years. First of all, I would like to thank my advisor Eva, for always being there to help me when I needed her, for the knowledge she shared with me, and for always trying to make the best out of everything.

I would also like to thank Oskar Dalhberg and Qiao Chen from KTH Royal Institute of technology for the antenna measurements in the anechoic chamber.

Of course I would never be able to reach this point, if I didn't have the help of my parents and their support towards any decision I made. Special thanks to my brother Χάρης who made me laugh even in difficult times. I am grateful for my close friends who were always there for me. Last but not least, my greatest thanks to Ignacio for encouraging me and giving me strength. I could never do this without his 24/7 support during all these years.

Σας ευχαριστώ όλους και τον καθένα ξεχωριστά, χωρίς εσάς δεν θα είχα φτάσει ως εδώ.

Ναυσικά

Contents

Related Publications

Journal articles

"Holey Metasurface Prism for the Reduction of the Dispersion of Gap Waveguide Leaky-Wave Antennas", *in IEEE Antennas and Wireless Propagation Letters, vol. 18, no. 12, pp. 2582-2586, Dec. 2019*, **Nafsika Memeletzoglou**, Eva Rajo-Iglesias.

DOI: 10.1109/LAWP.2019.2943812

This publication is fully included in Chapter 7.

Whenever material from this source is included in this thesis, it is singled out with typographic means and an explicit reference.

"Array of stacked leaky-wave antennas in groove gap waveguide technology", *in Scientific Reports, 2021, 11.1: 1-10*, **Nafsika Memeletzoglou**, Eva Rajo-Iglesias.

DOI: 10.1038/s41598-021-81640-7

This publication is fully included in Chapter 6.

Whenever material from this source is included in this thesis, it is singled out with typographic means and an explicit reference.

"Analysis of Periodic Structures Made of Pins Inside a Parallel Plate Waveguide", *in Symmetry 11, no. 4: 582*, **Memeletzoglou, Nafsika**; Sanchez-Cabello, Carlos; Pizarro-Torres, Francisco; Rajo-Iglesias, Eva.

DOI: 10.3390/sym11040582

This publication is not included in this thesis.

"Design methodology of single layer dual-band metasurfaces for leaky-wave antennas", *in IEEE Transactions on Antennas & Propagation- Accepted, under major revisions*, **Nafsika Memeletzoglou**, Darwin Blanco.
This publication is fully included in Chapter 2.
The material from this source included in this thesis is not singled out with typographic means and references.

"Hybrid Analog-Digital SAR Instrument with Reflector antenna and Overlapped subarray feed for Earth Observation" *in IEEE Antennas and Wireless Propagation Letters- currently under review*, Javier del Castillo, Lara Orgaz, Quiterio Garcia, **Nafsika Memeletzoglou**, Carlos Biurrun-Quel, Carlos del-Río, Giovanni Toso, Ernesto Imbembo.
This publication is partially included in Chapter 4.
The material from this source included in this thesis is not singled out with typographic means and references.

Conference papers

"Cost-effective planar array of low profile horns in gap waveguide technology at 38 GHz", *XXXIV General Assembly and Scientific Symposium (GASS) of the International Union of Radio Science, 28 August-4 September, 2021, Sapienza Faculty of Engineering, Rome, Italy*, **Nafsika Memeletzoglou**, Eva Rajo-Iglesias.
This publication is included in Chapter 8.
The material from this source included in this thesis is not singled out with typographic means and references.

"Multi-Channel Feedarray Reflector Antenna Based Radar Concept for HRWS SAR Imaging", *2021 IEEE Radar Conference, May 10-14, Atlanda, GA, USA*, Javier del Castillo, Lara Orgaz, Quiterio Garcia, **Nafsika Memeletzoglou**, Carlos Biurrun-Quel, Carlos del-

Río, Giovanni Toso, Ernesto Imbembo.

This publication is partially included in Chapter 4.

The material from this source included in this thesis is not singled out with typographic means and references.

"Wideband metamaterial absorbing antenna ground planes for 21cm radio cosmology applications", *15th European Conference on Antennas and Propagation 2021, Virtual Conference*, **Nafsika Memeletzoglou**, Eloy de Lera Acedo, Eva Rajo-Iglesias.

DOI: 10.23919/EuCAP51087.2021.9411193

This publication is not included in this thesis.

This paper was awarded with the TICRA grant 2021 in the 15th European Conference on Antennas and Propagation.

"Planar leaky-wave dual-band antenna array, with a single layer metasurface", *Simposium Nacional de la Union Cientifica Internacional de Radio 2020, Malaga, Spain*, **Nafsika Memeletzoglou**, Eva Rajo-Iglesias.

This publication is included in Chapter 3.

The material from this source included in this thesis is not singled out with typographic means and references.

"Design of an array of stacked groove gap waveguide leaky-wave antennas in the Ka band", *14th European Conference on Antennas and Propagation 2020, Copenhagen, Denmark*, **Nafsika Memeletzoglou**, Eva Rajo-Iglesias.

DOI: 10.23919/EuCAP48036.2020.9135857

This publication is fully included in Chapter 6.

The material from this source included in this thesis is not singled out with typographic means and references.

"Design of a stacked array of leaky wave antennas in groove gap waveguide technology", *Simposium Nacional de la Union Cientifica Internacional de Radio 2019, Sevilla, Spain*,

Nafsika Memeletzoglou, Eva Rajo-Iglesias.
This publication is fully included in Chapter 6.
The material from this source included in this thesis is not singled out with typographic means and references.

"Array of stacked leaky wave antennas based on gap waveguide technology", *IEEE International Symposium on Antennas and Propagation (AP-S/URSI) 2019, Atlanta, Georgia, USA*, **Nafsika Memeletzoglou**, Eva Rajo-Iglesias.
DOI: 10.1109/APUSNCURSINRSM.2019.8888913
This publication is fully included in Chapter 6.
The material from this source included in this thesis is not singled out with typographic means and references.

"Design of a holey metasurface prism to reduce dispersion in groove gap waveguide leaky wave antennas", *13th European Conference on Antennas and Propagation 2019, Krakow, Poland*, **Nafsika Memeletzoglou**, Eva Rajo-Iglesias.
This publication is fully included in Chapter 7.
The material from this source included in this thesis is not singled out with typographic means and references.

"Design Methodology of Dual-Band Single-Layer Leaky Wave Antennas", *Simposium Nacional de la Union Cientifica Internacional de Radio 2018, Granada, Spain*, **Nafsika Memeletzoglou**, Darwin Blanco Montero, Eva Rajo-Iglesias.
This publication is fully included in Chapter 2.
The material from this source included in this thesis is not singled out with typographic means and references.

"Single-Layer Dual-Band Leaky Wave Antennas Design Methodology with Directivity Control", *2018 IEEE International Symposium on Antennas and Propagation (AP-S/URSI), Boston, USA*, **Nafsika Memeletzoglou**, Darwin Blanco Montero, Eva Rajo-Iglesias.

DOI: 10.1109/APUSNCURSINRSM.2018.8608717.

This publication is fully included in Chapter 2.

Whenever material from this source is included in this thesis, it is singled out with typographic means and an explicit reference.

"Design methodology for single layer dual band leaky wave antennas", *12th European Conference on Antennas and Propagation 2018, London, UK*, **Nafsika Memeletzoglou**, Darwin Blanco Montero, Eva Rajo-Iglesias.

This publication is fully included in Chapter 2.

The material from this source included in this thesis is not singled out with typographic means and references.

Resumen

En las últimas décadas se ha producido un avance tecnológico exponencial en el área de las telecomunicaciones. Cada pocos años surgen sistemas de comunicaciones de nueva generación, siendo el 5G el que, hoy en día, se va implementando y ofreciendo progresivamente a los usuarios de todo el mundo.

Los sistemas de comunicaciones 5G permiten tasas de datos mucho más altas, una velocidad ultrarrápida y un mayor ancho de banda que el 4G no soportaba debido a las bandas excesivamente utilizadas por debajo de los 6 GHz. Sin embargo, este aumento de la frecuencia introduce retos que no existen en frecuencias inferiores, como la absorción ambiental. Además, los obstáculos físicos que se interponen en el trayecto entre el emisor y el receptor también son un problema a estas frecuencias y las pérdidas inherentes a la propagación en el espacio libre son muy elevadas.

El objetivo de esta tesis ha sido desarrollar e introducir nuevos e innovadores diseños de antenas que puedan ser utilizados en las bandas de frecuencia de las comunicaciones 5G y superiores así como en otras aplicaciones de ondas milimétricas. Los diseños que se presentan tienen como principal objetivo conseguir una alta directividad, manteniendo bajas pérdidas. Estos diseños se pueden agrupar en dos categorías principales: antenas Fabry-Pérot, y antenas gap waveguide.

En la primera parte de esta tesis se han desarrollado tres diseños de antena Fabry-Pérot, incluyendo una metodología innovadora para el diseño de una metasuperficie que permite un funcionamiento en doble banda con control de directividad y que también puede ser utilizada también para implementar *arrays* de antenas en bandas de ondas milimétricas. Además, se muestra que este concepto de antenas Fabry-Pérot, implementado en un rango

de frecuencias mucho más bajas, puede utilizarse también en aplicaciones de sistemas radar. En la segunda parte, se han desarrollado e implementado diseños innovadores de antenas y arrays usando la tecnología *gap waveguide* en particular su versión *groove*. En ellos, se han diseñado novedosas redes de alimentación y sistemas de corrección de fase que proporcionan bajas pérdidas y alta eficiencia.

Introduction

Nowadays, wireless communications have a crucial role in the modern society. The first generation of wireless cellular communications (1G) was initially introduced in the 1980s, and supported analog audio transmissions. A few years later, the transmissions became digital and the second generation (2G) emerged. In the past decades, rapid and ground breaking technological progress has lead to the incorporation of wireless systems in the modern society as an integral part, from daily life to medical and science applications.

The increasing number of mobile users, and the need for internet access and wireless data communications have paved the way for new generations of communications that are developed every few years, with the current fifth generation (5G) [1], [2] being introduced to users worldwide since 2019. This new generation is expected to allow significantly higher data rates that were not possible with 4G, due to the heavily saturated frequencies below 6 GHz. The 5G communications networks will provide ultra-fast speed (up to 10 Gbit/s) and increased bandwidth, while the delays will be minimized, to cover the needs of a predicted 1.7 billion users by 2025. In addition, the 5G communication systems are expected to provide the means for new IoT (internet of things) "smart" applications and devices; a trending topic in technological progress in our days.

Unlike the over-used frequencies below 6 GHz, the millimeter wave (mm-wave) frequency bands (typically above 24 GHz and up to 300 GHz) are vastly unoccupied. Therefore, the interest of the researchers was drawn towards implementations of wireless communication systems operating in mm-wave bands. However, the increase of frequency, gives rise to undesired effects that are usually ignored in low frequencies. For instance, round 60 GHz, the resonance frequency of oxygen and water molecules, introduce losses, limiting these frequencies to indoor applications. Apart from the environmental absorption,

physical obstacles between the direct path from the transmitter to the receiver are also an issue at these frequencies and the inherent losses of free space propagation are very high. Nevertheless, high speed communications are allowed by these frequencies for over-crowded areas with a more efficient use of the spectrum compared to communication systems of previous generations.

In order to reach these new frequency bands, as the antenna is a key element in enabling the use of these frequencies, new antenna design technologies have been developed by the researchers in the past few years. One of the emerged technologies is known as gap waveguide, which is a contact-less technology that can be used to implement highly directive wideband antennas with low losses and easy integration. In addition, leaky-wave antennas are always a good option for medium to high directivity applications due to their simplicity and without requiring complicated and lossy feed networks. Among them, the Fabry-Pérot type antennas can be used in mm-wave bands, maintaining a low-profile and easy fabrication, while they achieve medium directivity enhancement.

In this direction lies the motivation of the present thesis. The aim has been to develop innovative antenna designs that can be used in 5G and beyond communication frequency bands and other millimeter wave applications. The antenna designs that will be presented aim to achieve high directivity, maintaining low losses and implementing novel design methodologies.

The antenna designs that were developed during this thesis, can be gathered in two main categories: Fabry-Pérot type antennas, and gap waveguide antennas. Three Fabry-Pérot antenna designs have been developed, including a novel methodology for the design of a metasurface that allows dual-band performance with a single layer and with directivity control and can be also used to implement antenna arrays in mm-wave bands. In addition, it will be shown that the Fabry-Pérot antenna concept was also implemented in much lower frequencies and can be used in applications of radar systems.

The second main category of the developed designs is the design of innovative antennas in gap waveguide technology. By using the groove version of this technology, because it is the one with less losses, antenna and array designs have been implemented during this work. Novel feeding and phase correction networks have been also designed providing

low losses and high efficiency designs.

Thesis organization

The current PhD dissertation is organized in two main parts, in order to present the obtained results with optimum consistency. In **Part I** the Fabry-Pérot type leaky-wave antennas are studied, more specifically as follows:

Chapter 1: The principles and the theory behind the Fabry-Pérot antennas are discussed in detail. After presenting the initial studies that introduced the first antennas using a resonant cavity, then the state of the art is presented, where we discuss the different applications found in literature that make use of Fabry-Pérot antennas. Afterwards the radiation mechanism in these antennas is explained, followed by the dispersion equation. Finally, the existence of an equivalence between a dielectric slab and a metasurface for the implementation of leaky-wave antennas is presented. The importance of this chapter is high, since it establishes the theoretical background for the designs carried out in the first part of this thesis.

Chapter 2: This chapter presents the design of a single layer dual-band Fabry-Pérot antenna, based on the equivalence of the resonant cavity made by a dielectric slab and a metasurface. This equivalence is the basis for a novel design methodology that was derived during the present thesis. Two examples of designs are presented for a dual band antenna. Their difference is found in the equivalence used at each of the two bands, that allows for directivity control.

Chapter 3: The design methodology for dual-band leaky-wave antennas using metasurfaces, is extended to a planar array configuration in this chapter. In addition to directivity control, this design achieves grating lobe suppression, and a planar thinned array is implemented fed by stacked patches.

Chapter 4: This chapter presents the design of a leaky-wave antenna using a metasurface

following the principles of Chapter 1, that was developed as a candidate for an overlapped feed of a large reflector used for Earth observation.

In **Part II** innovative antenna designs based on gap waveguide technology are presented, organized as described:

Chapter 5: The principles of gap waveguide technology are presented. In particular, the groove version of gap waveguide is reviewed, as it will be used in all the designs of this part of the thesis. Afterwards, the leaky-wave antenna made in groove gap waveguide is presented.

Chapter 6: Based on the leaky-wave antenna presented in the previous chapter, an array of stacked elements in groove gap waveguide technology is presented. For the implementation of the array, a novel feeding and phase shifters network is developed by using the same technology.

Chapter 7: In this chapter, the dispersive nature of gap waveguide leaky-wave antennas is addressed. The combination with a metamaterial prism is proposed, using holes as unit cells, to compensate the dispersion of leaky-wave antennas.

Chapter 8: This chapter presents the design of an array of low profile horn antennas entirely made in groove gap waveguide technology with high aperture efficiency and minimized losses.

The present thesis is then summarized in **Part III** where the conclusions of each chapter are gathered. In addition, guidelines for future work are discussed. Finally the related publications to this thesis are listed.

List of Figures

List of Tables

Acronyms

EBG Electromagnetic Band Gap.

EM Electro-Magnetic.

FSS Frequency Selective Surface.

ME Magneto-Electric.

mm-wave Millimeter Wave.

MTS Metasurface.

PEC Perfect Electric Conductor.

PMC Perfect Magnetic Conductor.

PRS Partially Reflective Surface.

SAR Synthetic-Aperture Radar.

TE Transverse Electric.

TEM Transverse Electromagnetic.

TM Transverse Magnetic.

Part I

Design of Fabry-Pérot leaky-wave antennas

Chapter 1

Leaky-wave antennas based on partially reflective surfaces

1.1 Introduction

The simplest form of a leaky-wave antenna consists of a radiating slot edged on a ground plane, and above it a surface that reflects back a part of the incident waves, while the rest "leaks" to free space. This concept was first introduced in 1956 by von Trentini [3], where multiple reflections in a parallel plate cavity were studied. The lower limit of the cavity was defined by a metallic ground plane, while the upper limit was a partially reflective surface (PRS) made by metallic patches, metallic grid or even wires. It was shown that the PRS obtained the increase of directivity of a simple radiation source that in this case was a slot on the ground plane, located centrally and fed by a waveguide. The importance of the height of the cavity was observed and simple formulas for its calculation were presented. It was reported that for specific values of height, high directivity radiation patterns are produced.

Some years later, this idea was explored again in [4] but this time with a dielectric material of high permittivity as a PRS and the cavity between the parallel plates was filled with another dielectric. A more complete study of the same design was presented in [5], where asymptotic formulas were derived for the leaky-wave propagation properties. This

configuration was then extended to multilayered dielectric PRS structures that further improved the directivity levels obtained [6]–[8]. Cascaded dielectrics were also used in [9]–[11] to create wideband performance.

In [12], [13] the authors addressed the similarities of the resonant cavity of [3] and the Fabry-Pérot interferometer [14] that consists of two reflective surfaces that create as well a resonant cavity. Therefore, in literature these antennas are often referred to as Fabry-Pérot antennas [15]–[17]. In other works, the term "electromagnetic band-gap (EBG) antennas" has been also used [18]–[20], referring to multilayered structures that form a band-gap and are used as a PRS.

The main advantage of this type of antennas is that they achieve directive beaming by using rather simple non-directive radiation sources. Many studies have been presented over the years, describing the case of a dielectric superlayer since it is the simplest solution for directivity enhancement [21]–[23]. Nevertheless, in some cases there are no commercially available materials with the required high permittivity and specific thickness. Furthermore, this is a solution with limited bandwidth performance, since the Fabry-Pérot cavity is designed for a single frequency, as it will be explained later. Lastly, there are applications in environments where the use of dielectric materials is not suitable due to the surrounding conditions. As a consequence, the use of periodic metamaterial structures gained popularity very quickly, and it is nowadays encountered in most research works on Fabry-Pérot leaky-wave antennas.

Metasurfaces (MTS) provide tailored electromagnetic performance. They have similar properties with frequency selective surfaces (FSS) that have been widely used to filter the incident EM waves, creating band-stop or band-pass performances [24]–[29]. Different approaches to the use of an MTS to design resonant cavity antennas have been presented. In its simplest implementation, an MTS can be made using metallic patches on a dielectric [13], [30]–[33] or they can have a grid-like form [34], [35]. In [36], [37] these configurations were studied and categorized in inductive and capacitive MTSs depending on their impedance characteristics. Based on this analysis, it is possible to design metasurfaces equivalent to dielectric slabs, as it will be discussed later, which allows for further flexibility in the design.

Regarding the bandwidth, the MTS based leaky-wave antennas, show advantageous properties. Wideband performance was reported in [38] by implementing cascaded MTS structures, in the same way that multilayered dielectric materials have been used, but enhanced with tunable characteristics. The same idea can be found as an array of printed unit cells on both sides of a dielectric [39]–[41]. In [42], [43] the wideband was achieved by extending the concept of the patch MTS in the combination with its complementary structure and this idea was used in other unit cells in [44]–[46]. Moreover, in [47]–[50] more complex wideband structures were designed. Multi-band designs [51], [52] and dual-band [53]–[55] designs have been also presented. Later in this thesis the design of dual-band Fabry-Pérot antennas and arrays will be presented.

In general, these leaky-wave antennas have the polarization of the source antenna [56]. Nevertheless, one more property of the metasurfaces, is the manipulation of polarization. In [57]–[60] a linear to circular polarization conversion MTS was included in the design of a Fabry-Pérot antenna. The authors of [61] reported that circular polarization was obtained by a planar array of patch antennas when the metasurface above each element of the array is rotated by 90^o. In [62] a fully metallic polarizing surface was added to the antenna design. By using a MTS to manipulate the polarization, bulky feeding networks are avoided; instead, simple linear polarization feed antennas can be used to excite the MTS that modifies the polarization.

This type of antennas provides a simple solution for directivity and therefore gain enhancement. Their low profile has gained them an increased popularity. In addition, when metasurfaces are used, the design gains degrees of freedom and flexibility, unlike the dielectric slab designs. From frequency band performance, to the manipulation of polarization, MTS based leaky-wave antennas provide tailored electromagnetic behavior following a simple principle [3], [5]. In the following chapters a novel design methodology for resonant cavity antennas using metasurfaces will be presented and validated through simulated and experimental results.

1.2 Radiation in PRS based leaky-wave antennas

The general case of a PRS leaky-wave antenna is shown in Fig. 1.1. A dielectric slab of ϵ_{r2} and thickness h_2 is located above the ground plane at a height h_1, forming a cavity. This cavity is excited by a source that can be modelled either as an electric dipole placed in the middle of the cavity, or as a magnetic dipole (e.g. a slot) on the ground plane level. The cavity can be filled with a dielectric material of ϵ_{r1}. Initially general formulas including $\epsilon_{r1} \neq 1$ will be presented, nevertheless later in this thesis, this region will be considered air-filled.

Inside the resonant cavity, the waves that emerge from the source, propagate with multiple reflections between the two limits of the cavity; however some of the incident EM waves get through the PRS and are leaking to free space, hence an antenna is created. Consequently, the shape of the produced radiation patterns depend mainly on the properties of the chosen PRS and to a less significant level, on the radiation source. As it will be discussed later, the pattern geometry of the PRS determines the beamwidth [63]. On the other hand, the type and location of the antenna that excites the cavity influences the levels of produced radiation.

In [23] the PRS leaky-wave antenna was modelled in parallel plate propagation terms. Let's consider Fig. 1.1 but with two parallel fully metallic plates. As it is well known, inside this waveguide TE_i and TM_i modes can propagate, and the vertical wavenumber of each mode is $k_z^{pp} = n\pi/h_1$. In addition, both modes have the same radial wavenumber with real value:

$$k_\rho^{pp} = \sqrt{k_1^2 - (\frac{\pi}{h_1})^2} \tag{1.1}$$

Now we suppose that the top plate is replaced by a surface that allows partial leakage of the energy outside the cavity; such as a dielectric slab. Fig. 1.1 illustrates the radially propagating leaky-modes in the parallel plate structure. In this case, TE_i and TM_i still propagate between the upper and lower plates. However, part of their energy is transferred to radiation and they are now called leaky-modes. Consequently, the vertical wavenumber along the propagation direction is complex : $k_\rho = \beta - j\alpha$. In other words, the complex

nature of the wavenumber expresses the amplitude decrease of the leaky-modes due to radiation [30]. Each mode has different wavenumbers: $k_\rho^{TE,TM} = \beta^{TE,TM} - j\alpha^{TE,TM}$. For the phase constants $\beta^{TE,TM}$ we can assume that they are approximately equal to k_ρ^{pp}, thus they are correlated with the radiation angle θ_0 as : $k_\rho^{pp} = k_0 sin\theta_0$, and by using this expression as well as Eq. 1.1 we find the height of the cavity h_1 as a function of the radiation angle θ_0 [23]:

$$h_1 = \frac{\pi}{k_0\sqrt{n_1^2 - sin^2\theta_0}} \tag{1.2}$$

where n_1 is the refractive index of the dielectric in region 1, and the numerator can be written as $n\pi$ if we wish to include higher order modes, which would lead to higher h_1. From the radiation angle:

$$\theta_0 = sin^{-1}(\frac{\beta}{k_0}) \tag{1.3}$$

it is apparent that there can be radiation either at broadside ($\theta_0 = 0$) or as a conical scanning beam ($\theta_0 > 0$). If in the above Eq. 1.2 we substitute $\theta_0 = 0$ for broadside direction, then we find that the height of the cavity should be $h_1 = \lambda_0/(2n_1)$, where $\lambda_0/(2n_1) = \lambda_{d1}$ is the wavelength in the dielectric of region 1. Therefore the height is directly connected with the radiation angle θ_0 and depending on its value, a pencil beam on broadside or a scanning conical beam can be produced.

In [23] a design restriction regarding the height is reported in order to ensure a single lobe in the case of conical beam. The height should be:

$$h_1 < \frac{\lambda_0}{\sqrt{\epsilon_{r1}\mu_{r1}}} \tag{1.4}$$

in order to avoid the $n = 2$ parallel plate modes propagating. In addition, in a case of a periodic metasurface used to replace the dielectric PRS, in order to have only the (0,0) Floquet mode, the period of the unit cells should be $per < \lambda_0/2$, otherwise higher Floquet modes would result in undesired lobes in the radiation pattern. This will be taken under consideration when designing the proposed MTS later in this thesis.

Regarding the thickness of the dielectric that forms the PRS, according to the resonant condition [7] it should be: $h_2 = \lambda_0/(4\sqrt{\epsilon_{r2}})$.

Furthermore, another consideration that must take place is regarding the illumination of the radiating aperture, which is determined by the attenuation constant α. In [64] it is stated that when the attenuation is low, the effective radiating aperture is large, and the radiation pattern has narrow beamwidth. Both the attenuation and the phase constants, depend on the chosen geometry of the MTS. A condition for maximum radiation at broadside was reported in [32]: when $\alpha = \beta$ then maximum power density is radiated at $\theta_0 = 0$, that is the broadside direction.

1.3 The dispersion equation

In a PRS-based leaky-wave antenna, it is critical to study the characterization of the dominant leaky-wave modes. In this direction, the leaky-wave poles should be determined in the spectral representation of Green's function. In [5], the authors presented approximate expressions for these poles, around a central frequency or in the case of high permittivity of the dielectric slab. A more wideband localization of the leaky-poles was presented in [22], including high or low permittivities.

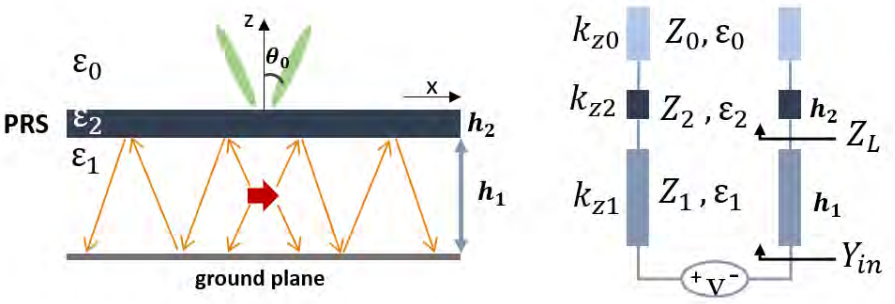

Fig. 1.1. The resonant cavity between a partially reflective surface (PRS) and a ground plane, of height h_1 (left). The same configuration can be represented as a transmission line (right).

In this section a multilayered configuration is considered and Fig. 1.1 shows the transmission line equivalent of this leaky-wave antenna made by a dielectric PRS of permittivity ϵ_{r2}. Initially we will suppose that the resonant cavity has a dielectric constant

ϵ_{r1} to create generalized expressions, but afterwards this region will be considered air-filled ($\epsilon_{r1} = 1$). Each region of the antenna is represented by the TE/TM characteristic impedance Z_i ($i = 0, 1, 2$), and has a vertical propagation constant $k_{zi} = k_0\sqrt{n_i^2 - sin^2\theta_0}$ [5], [63] with n_i being the refractive index of each region. The expression for the vertical propagation constant can be transformed into $k_{zi} = \sqrt{\epsilon_{ri}k_0^2 - k_\rho^2}$ [22], [36], by substituting the refractive index and also $k_\rho^{pp} = k_0 sin\theta_0$ [23] for the parallel plate waveguide analysis that was presented before.

Now we can calculate the input admittance by taking as a reference a point on the ground plane level [22]:

$$Y_{in}(k_p) = \frac{Z_1 + jZ_L tan(k_{z1}h_1)}{Z_1(Z_L + jZ_1 tan(k_{z1}h_1))} \tag{1.5}$$

where TE/TM impedance Z_L is at the interface of regions 1,2 and as it is well known from the transmission line theory it can be calculated as:

$$Z_L = Z_2\frac{Z_0 + jZ_2 tan(k_{z2}h_2)}{Z_2 + jZ_0 tan(k_{z2}h_2)} \tag{1.6}$$

Regarding the height h_i of each region, as explained previously, for a broadside beam and considering an air-filled region, it should be $h_1 = \lambda_0/2$ [23], while the thickness of the dielectric PRS is $h_2 = \lambda_0/(4\sqrt{\epsilon_{r2}})$, satisfying the resonant condition [5], with λ_0 the wavelength at the central frequency of the design.

By solving the denominator of Eq. 1.5 in order to find its poles, with the obvious solution $Z_1 = 0$, we can define the dispersion equation [22]:

$$D_{TE,TM}(k_p) = Z_l + jZ_1 tan(k_{z_1}h_1) = 0 \tag{1.7}$$

where Z_i is the TE/TM characteristic impedance with $Z_i^{TE} = \eta_0 k_0/k_{zi}$ and $Z_i^{TM} = \eta_0 k_{zi}/k_0$ corresponding to the TE and TM modes respectively in the case of region 1 being air-filled.

In order to solve the dispersion equation, the authors of [22] used an approximation of the function $tan(x)$ around its zeros in the region $x = \pm n\pi$ resulting to: $tan(x)_{|x\pm n\pi|\approx 0} = x \pm n\pi$. In addition, in the multilayered configuration that we are considering (Fig. 1.1), the

leaky-waves propagate along $x > 0$ and also $z > 0$, thus resembling a plane wave parallel to the z-axis. More specifically, in region 1, two waves with opposite directions emerge from the source and propagate with multiple reflections in between the limits of this region (between the ground plane and the PRS). Thus, in the above approximation, for the term $n = 1$ we can write:

$$tan(k_{z1}h_1) \approx k_{z1}h_1 - \pi \tag{1.8}$$

By replacing Eq. 1.8 in Eq. 1.7, the following approximate solution of the dispersion equation is derived:

$$k_{z1} = j\frac{Z_L}{Z_1 h_1} + \frac{\pi}{h_1} \tag{1.9}$$

Therefore, it is apparent that the propagation inside the resonant cavity, is directly affected by the load impedance Z_L which is located at the top of the cavity. In addition, when $Z_L = 0$, Eq. 1.9 corresponds to the modes propagating in a parallel plate waveguide [31] with $k_{z1} = n\pi/h_1$, that has a height h_1. Finally, for the load impedance in the case of a single dielectric slab, and for radiation at broadside ($\theta_0 = 0$), we can assume:

$$Z_L = \frac{\eta_0}{\epsilon_{r2}} \tag{1.10}$$

with the thickness of the dielectric slab being $h_2 = \lambda_0/(4\sqrt{\epsilon_{r2}})$. The above represents a case where the PRS consists of only one layer. Nevertheless, this analysis can be extended in a multiple cascaded PRSs configuration, with the load impedance being in the form of Eq. 1.6 instead of Eq. 1.10.

1.4 Equivalence between PRS and metasurfaces

In the previous section, the leaky-wave antenna made with a partially reflective surface was discussed and its radiation mechanism was analyzed. So far in the analysis, a dielectric of a single or multiple layers, has been used to partially leak the energy to free space, creating a resonant cavity whose characteristics have been presented.

Although the dielectric PRS is a simple and useful way to enhance the directivity of low profile radiation sources such as printed patch antennas, it does not allow a tailored performance. In addition, in some applications, it can be difficult to find commercial materials that fulfill high permittivity requirements. Lastly, there are environments where the use of dielectric materials is not preferable (e.g. to avoid dielectric break down).

However, it is possible to design a textured surface or metasurface (MTS) that has an equivalent performance to the dielectric slab. In [36] it was demonstrated that there are similarities in Green's functions of the two configurations shown in Fig. 1.2. More specifically, it was shown that a dielectric PRS above a slot edged on the ground plane, can be equivalent in propagation terms, to an MTS with inductive or capacitive characteristics [36], [37]. Said equivalence, can be shown by imposing the same solutions (Eq. 1.9) for the dispersion equation (Eq. 1.7).

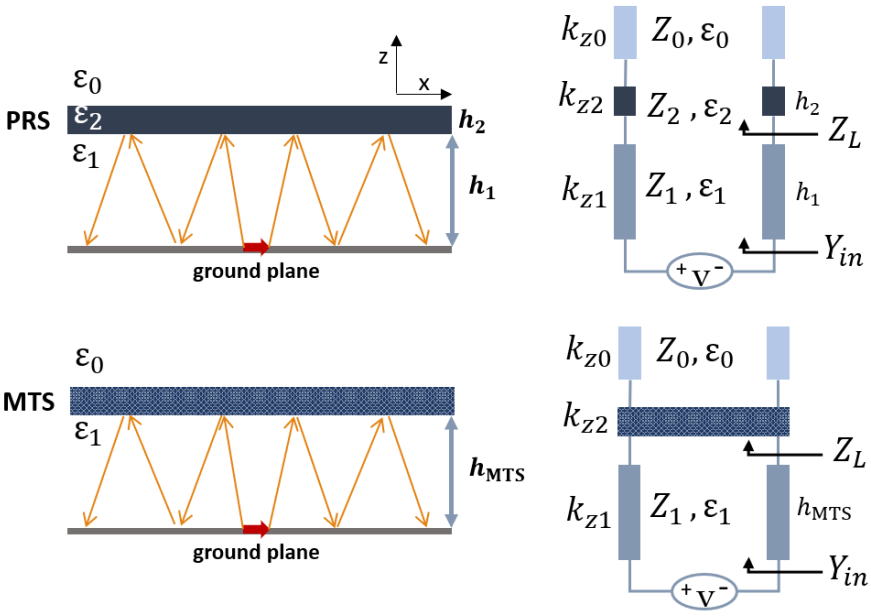

Fig. 1.2. Equivalent transmission line circuits for the two leaky-wave antennas that are being compared. On the top, the antenna is made using a dielectric slab as a PRS, and on the bottom, a metasurface is used to form the resonant cavity.

Let us consider the case of a dielectric PRS (Fig. 1.2(top)), with permittivity ϵ_{r2} and thickness $h_2 = \lambda_0/(4\sqrt{\epsilon_{r2}})$. Assuming normal incidence, the load impedance is $Z_L = \eta_0/\epsilon_{r2}$. In addition, for an air-filled region 1, the impedance is considered $Z_1 = \eta_0$ and the height

of the cavity is $h_1 = \lambda_0/2$. Under these conditions, the propagation constant along the z direction (Eq. 1.9), of the dominant leaky-wave TE/TM modes becomes:

$$k_{z1,diel} = j\frac{1}{\epsilon_{r2}h_1} + \frac{\pi}{h_1} \tag{1.11}$$

In the case of the metasurface (Fig. 1.2(bottom)), the load impedance around broadside is $Z_{L,MTS} = Z_{shunt}//Z_0$, meaning that it can be calculated as a shunt impedance parallel to free space. In [65] it was reported that the electromagnetic properties of an MTS with small periodicity, can be considered as an imaginary shunt impedance i.e. $Z_{shunt} = jX$. Consequently the load impedance is:

$$Z_{L,MTS} = \frac{j\eta_0 X}{\eta_0 + jX} \tag{1.12}$$

If we replace Eq. 1.12 in Eq. 1.9 we derive the following formula for the vertical propagation constant:

$$k_{z1,MTS} = \frac{\pi(\eta_0^2 + X^2) - X\eta_0}{h_{MTS}(\eta_0^2 + X^2)} - j\frac{X^2}{h_{MTS}(\eta_0^2 + X^2)} \tag{1.13}$$

Towards the equivalence of the PRS and the MTS case, we equalize the real and imaginary parts of (1.11) and Eq. 1.13. If we solve towards X in Eq. 1.13 in order to define Z_{MTS} and we suppose that $h_{MTS} = h_1$, we can derive the following expressions for the impedance and the height of the equivalent MTS configuration [36], [37]:

$$Z_{ind,cap}^{MTS} = j\eta_0\left(\frac{-1 \pm \sqrt{1 + 4\pi^2(\epsilon_r - 1)}}{2\pi(\epsilon_r - 1)}\right) \tag{1.14}$$

$$h_{ind,cap}^{MTS} = \frac{\lambda_0}{2}\frac{\epsilon_r|Z_{ind,cap}|^2}{\eta_0^2 + |Z_{ind,cap}|^2} \tag{1.15}$$

With these two formulas, it is possible to define an inductive ("+" sign), or capacitive ("-" sign) metasurface that will be placed on a certain height creating a resonant cavity where the propagation has same characteristics as in the case of the dielectric of ϵ_r PRS. The solutions of the TE_1 and TM_1 modes for the dielectric, the equivalent inductive and

capacitive surfaces, are presented in Fig. 1.3 for two examples of permittivity $\epsilon_{r1} = 6$ and $\epsilon_{r2} = 10$. It can be seen that the three equivalent surfaces have practically identical solutions of the dispersion equation.

One should note that the equivalent impedance $Z^{MTS}_{ind,cap}$ is frequency independent and is controlled only by the permittivity, and only the height of the MTS $h^{MTS}_{ind,cap}$ changes with frequency. In the following chapters it will be demonstrated how from the system of Eq. 1.14 & Eq. 1.15 it is possible to define a single MTS fulfilling two equivalences of ϵ_{r1} and ϵ_{r2} at two different frequencies.

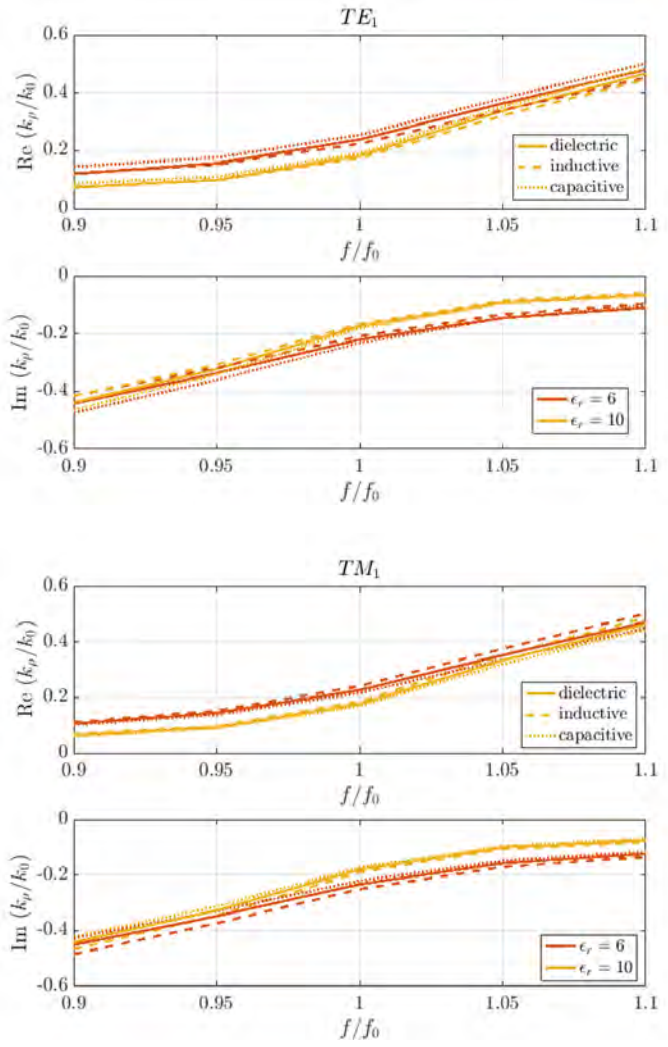

Fig. 1.3. Solutions of the dispersion equation for a dielectric slab of permittivity $\epsilon_r = 6, 10$ and the equivalent inductive and capacitive MTS.

Chapter 2

Design of dual-band single layer leaky-wave antenna

2.1 Introduction

Fabry-Pérot leaky-wave antennas have been gaining popularity over the years [12], [13], [15], [31], [34] since their first appearance [3]. By using a partially reflective surface (PRS) on top of a non directive source, they achieve narrow beams, thus being a good solution for directivity enhancement of a simple radiating element such as a slot on a ground plane fed by a waveguide [4], [5].

In the literature, many studies of leaky-wave antennas have been presented, and their operating principles have been studied in detail [22], [23], [32], [36], [63]. Although the use of the dielectric slab as a PRS is the simplest solution for directivity enhancement, it introduces limits on the performance in terms of bandwidth, since its height over the radiation source depends on the operating frequency. To overcome the single-band performance, many works have been presented using multiple cascaded dielectric slabs [9]–[11], [66]. Each slab forms a resonant cavity of different height, thus creating multiple resonances and wideband performance. Inhomogeneous implementations of the multilayered wideband dielectric PRS have been also presented [67].

An additional limitation in the use of dielectric slabs as a PRS, is found in the commer-

cially available thicknesses and permittivities which can be difficult to obtain. This has turned the interest of researchers to other solutions such as metasurfaces (MTS) that partially reflect the waves, and provide the required design flexibility. Following the concept of the cascaded dielectrics, wideband performance has been achieved with multilayered metasurfaces [38], [42], [44]. Dual-band performance has been also reported by following the same methodology of multiple layers [53], [54], [68]–[73], with some of the existing examples implementing complex geometries [49].

In this chapter, the design of a dual-band leaky-wave antenna is presented. The dual-band is obtained with a single layer metasurface. Other works have also used a single layer MTS [74]–[76], however they had printed elements on both sides of the MTS, on contrary to the presented MTS that has metallizations only on one side. Furthermore, the MTS is composed of an array of simple unit cells (interleaved slots and squares) while in other designs of metasurfaces, the dual band has been obtained with unit cells of high complexity for the design of filters [46], [50], [77]. A diode loaded MTS was presented in [78], where by changing the state of the diodes different reflection phase was obtained and so the resonance of the antenna can be tuned. Other examples using active (varactor diodes) and lumped elements (capacitive loads) were presented respectively in [79], [80]. In [81] the lower resonance of the dual-band was achieved with a single layered MTS, however for the higher frequency resonance, a ground plane made of an artificial magnetic conductor was required.

In this work we present a design methodology that has two important assets; it provides flexibility in the design process and it can be scaled to meet the requirements of the operation band of a potential application, maintaining the low profile of a Fabry-Pérot leaky-wave antenna. While in the majority of the examples in literature the multiple band performance was obtained through the reflection coefficient's phase analysis [53], [70], [74] or the characteristic modes' analysis [82], the basis of the proposed methodology is the analysis of the leaky modes with the transverse resonance method.

2.2 Single layer metasurface design methodology

In Chapter 1 the radiation mechanism of a leaky-wave antenna based on a resonant cavity h_1, was analyzed. More specifically, the propagation inside the cavity was discussed initially for the case of a dielectric PRS and afterwards the existence of an equivalent metasurface was demonstrated, following the works in [36], [37]. The equivalence between a dielectric slab of certain permittivity ϵ_r and a metasurface, was derived from the dispersion equation (Eq. 1.7) imposing the same solutions for the dielectric $k_{z1,diel}$ and the metasurface $k_{z1,MTS}$ for the TE_1/TM_1 modes, as seen in Fig. 1.3. In both cases, a source located at the bottom of the cavity (ground plane level), excites leaky-modes that are bouncing between the upper and lower limits of the cavity (multiple reflections) and part of their energy is transformed into radiation in free space. For an air-filled cavity ($\epsilon_{r1} = 1$), an expression for the impedance of the MTS (that can be either inductive or capacitive) $Z^{MTS}_{ind,cap}$ was derived in case of an equivalence with a dielectric ϵ_r (Eq. 1.14) as in [36]. While for the dielectric slab the height of the cavity is $h_1 = \lambda_0/2$ at a central frequency f_0, the approximated analytical solution of Eq. 1.7 results to the required cavity height $h^{MTS}_{ind,cap}$ where the equivalent MTS should be placed. It is worth noting that only the height (Eq. 1.15) depends on frequency, while the equivalent impedance (Eq. 1.14) is only a function of the permittivity.

From Eq. 1.15 it can be predicted that the inductive solution will give the same TE_1/TM_1 leaky-mode at a frequency f_1 lower than f_0 for a fixed cavity height. In the same way, there will be a frequency f_2 higher than f_0, where in a fixed cavity height the capacitive solution will result to the same TE_1/TM_1 leaky-modes. In other words, the cavity is reacting as inductive at $f_1 < f_0$ and as capacitive at $f_2 > f_0$. Consequently, if a metasurface is designed with impedance that ranges between inductive and capacitive passing through a central frequency f_0, then a single layer dual-band leaky-wave antenna can be created.

If Eq. 1.14 and Eq. 1.15 are solved as a system towards a common solution, for a certain cavity height h_0, the two frequencies that define the dual-band f_1, f_2 can be calculated as well as the impedance values required for each band. For instance, for a fixed cavity $h_0 = 5.79$ mm, the solutions for f_1 corresponding to the inductive case, and f_2 that is the capacitive case, are represented in Fig. 2.1, as a function of the dielectric permittivities

of the equivalent surface. With this methodology, it is possible to achieve permittivity equivalence of high values, that in commercially available materials could not be found. Higher permittivity will result in higher directivity.

This design methodology provides flexibility and it can be scaled by choosing a different height h_0. From Fig. 2.1 it is apparent that while ϵ_r increases, the distance between f_2 and f_1 decreases. This relative bandwidth can be seen in Fig. 2.2. Evidently, a compromise must take place between the separation of the two bands and the permittivity equivalence (and thus the directivity).

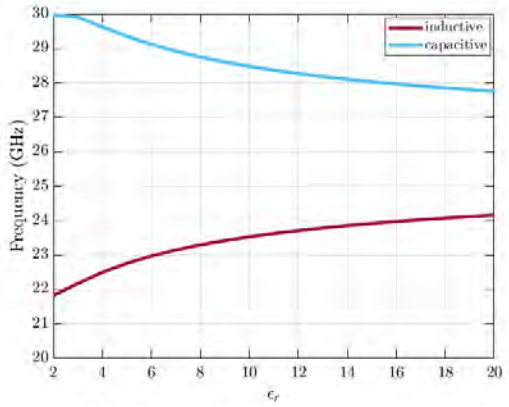

Fig. 2.1. Permittivity equivalence for the inductive (red) and the capacitive (blue) cases as a function of the frequency, for $h_0 = 5.79$ mm.

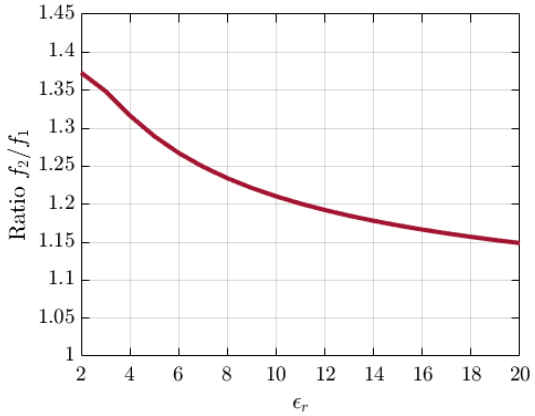

Fig. 2.2. Ratio of the two frequencies as a function of the permittivity.

Two implementations of the proposed methodology will be presented. In the first case of study, both frequency bands will correspond to the same equivalence of dielectric

permittivity. In the second case, a single metasurface will be designed, which will be equivalent to two different ϵ_{r1} and ϵ_{r2} for f_1 and f_2 respectively. In particular, at f_2 a higher permittivity $\epsilon_{r2} > \epsilon_{r1}$ will be chosen, thus increasing the directivity and the aperture efficiency at the higher frequency band.

2.2.1 First case of study: Metasurface equivalent to the same permittivity at f_1 and f_2

The first implementation of the presented theory, corresponds to a common permittivity equivalence at both bands. After solving the system of Eq. 1.14 and Eq. 1.15, from the results of Fig. 2.1 we have chosen $f_1 = 23$ GHz, $f_2 = 29$ GHz, for a common permittivity $\epsilon_r = 6$ and assuming $h_0 = 5.79$ mm. This solution will provide medium directivity levels at the Ka band with sufficient separation between the two bands. This solution is also depicted in Fig. 2.3, where the red line is the inductive equivalent at f_1, and the blue line is the capacitive equivalent at f_2. The two curves meet at $\epsilon_r = 6$, indicating that for these frequencies and permittivity a single cavity height is possible.

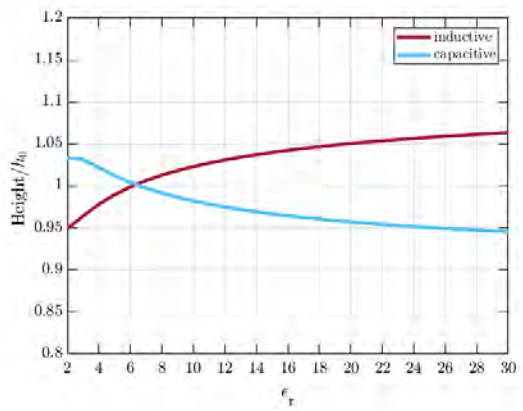

Fig. 2.3. For a common $\epsilon_r = 6$ equivalence, and a single cavity height, the resulting frequencies of the dual-band are $f_1 = 23$ GHz (inductive) and $f_2 = 29$ GHz (capacitive).

The next step in the designing process is the calculation of the impedance of the MTS. The unit cell that will be used to form the MTS, should have an impedance that varies with frequency. To this end and to maintain the low profile of the antenna, the unit cell that is seen in Fig. 2.4 has been chosen. From Eq. 1.14 and by substituting $\epsilon_r = 6$, the calculated

required impedance is: $Z_{ind}^{MTS} = 157j\ \Omega$ for the inductive and $Z_{cap}^{MTS} = -181j\ \Omega$ for the capacitive behavior. By changing the values of the parameters that control the geometry of the unit cell, it is possible to obtain the theoretically calculated values of impedance. Indeed, Fig. 2.5 shows that for $b_1 = 0.51$ mm, $b_2 = 2.77$ mm, $b_3 = 0.15$ mm, $per = 3.99$ mm, the impedance reaches the calculated values for each one of the two frequencies. The assumed material of the unit cell is a perfect conductor (PEC). As mentioned in Chapter 1, the period of the unit cell should be less than half wavelength at both frequencies, in order to avoid undesired grating lobes.

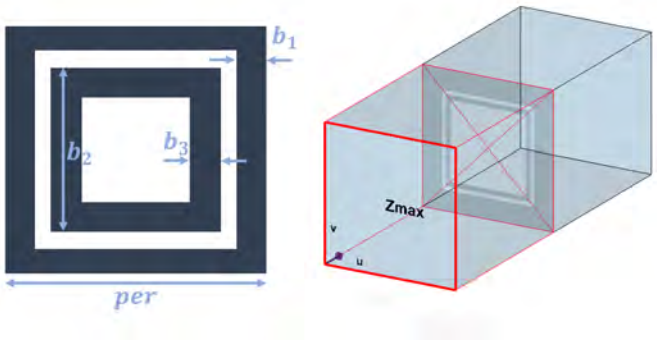

Fig. 2.4. The proposed MTS consists of a unit cell of square rings interleaved with slots (left). The unit cell and its excitation in the simulation environment can be seen on the right.

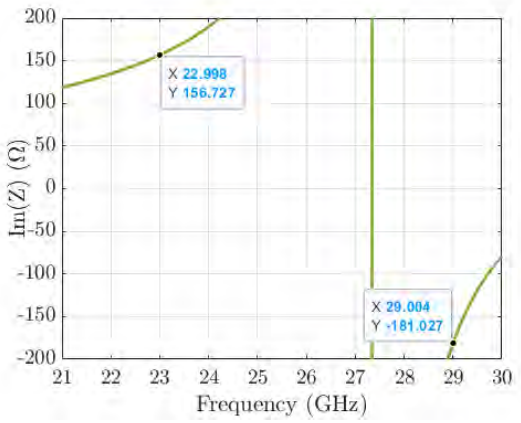

Fig. 2.5. Obtained impedance for the unit cell dimensions: $b_1 = 0.51$ mm, $b_2 = 2.77$ mm, $b_3 = 0.15$ mm, $per = 3.99$ mm. The theoretically calculated values are $Z_{ind} = 157j\ \Omega$ and $Z_{cap} = -181j\ \Omega$.

The synthesis of the unit cell's impedance, was performed in CST Microwave Studio, assuming periodic boundary conditions to simulate an infinite array. The unit cell is excited

by a port that is defined at the limits of z-direction as seen in Fig. 2.4. Since the unit cell is symmetric one Floquet mode is sufficient to calculate the value of impedance.

2.2.2 Second case of study: Metasurface equivalent to two different permittivities at f_1 and f_2

For the second case of study, the two frequencies of the dual-band are maintained $f_1 = 23$ GHz and $f_2 = 29$ GHz. The aim is to increase the directivity at f_2 by introducing a higher permittivity equivalence and thus improving the aperture efficiency at the higher frequency.

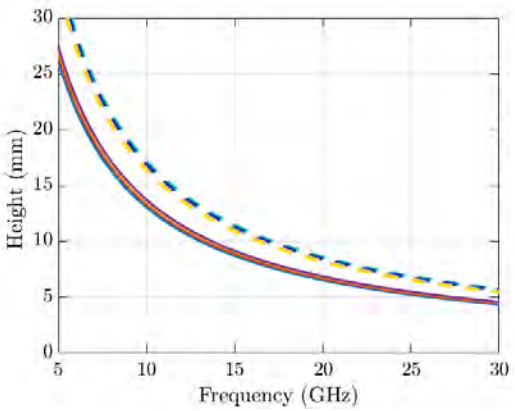

Fig. 2.6. Cavity height solutions as a function of frequency, for various values of $\epsilon_r = 4, 6, 10, 12$. The solid line represents the inductive equivalence and the dashed line is the capacitive equivalence.

Fig. 2.6 shows solutions for the cavity height, for the inductive h_{ind}^{MTS} (solid lines) and the capacitive h_{cap}^{MTS} case (dashed lines), as a function of frequency. Each coloured line corresponds to a different permittivity equivalence.

For the higher frequency $f_2 = 29$ GHz, we have chosen $\epsilon_{r2} = 10$, while maintaining $\epsilon_{r1} = 6$ at $f_1 = 23$ GHz. The resulting common height solution can be seen in Fig. 2.7, and is approximately 5.75 mm.

Since ϵ_{r1} remains the same, the theoretical value of impedance at this frequency does not change $Z_{ind}^{MTS} = 157\,j\ \Omega$. For $\epsilon_{r2} = 10$ at Eq. 1.14, the resulting impedance is $Z_{cap}^{MTS} = -132\,j\ \Omega$. The same type of unit cell as in the first case of study (Fig. 2.4) is used.

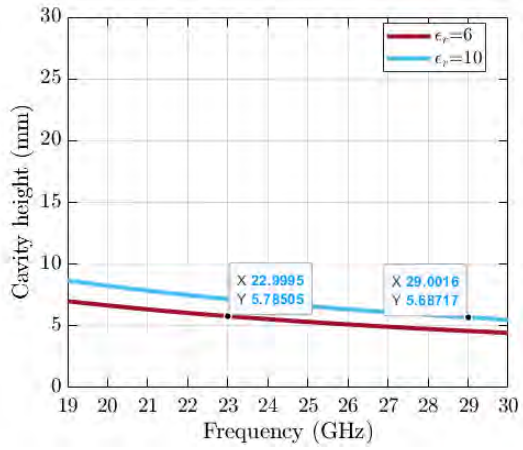

Fig. 2.7. At $f_1 = 23$ GHz and $f_2 = 29$ GHz, although the permittivity equivalence is for different ϵ_{r1}, ϵ_{r2}, an almost identical height can be found.

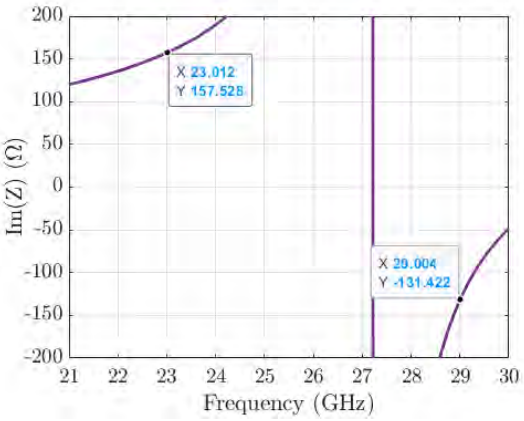

Fig. 2.8. For the second design, the obtained impedance of the unit cell with dimensions: $b_1 = 0.487$ mm, $b_2 = 2.75$ mm, $b_3 = 0.11$ mm, $per = 3.95$ mm. The theoretically calculated values are $Z_{ind} = 157\,j\,\Omega$ and $Z_{cap} = -132\,j\,\Omega$.

The theoretical values were practically reached in Fig. 2.8 for the following parameters of the unit cell: b_1 = 0.487 mm, b_2 = 2.75 mm, b_3 = 0.11 mm, per = 3.95 mm.

2.3 Antenna design

In this section the details of the antenna design will be presented, for both cases of study.

A 3D model of the antenna with the MTS is shown in Fig. 2.9. The radiation source that excites the resonant cavity, was chosen to be a double iris slot, edged on a metallic ground plane following the design presented in [37]. As discussed in [83], this feeding slot avoids the excitation of the TM_0 mode. The geometry of the double iris is shown in Fig. 2.10. The values of the parameters are: $\alpha = 127^o$, r_{out} = 3.75 mm, r_{in} = 0.55 mm. The slot is fed by a squared waveguide with side 9.4 mm. A transition to a standard rectangular waveguide WR34 was used and is depicted in Fig. 2.10.

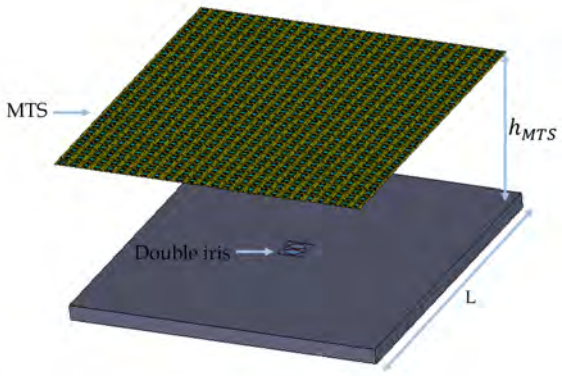

Fig. 2.9. 3D model of the antenna, where the double iris on the ground plane and the MTS can be seen.

The total size L of the ground plane and the MTS in both designs, is $9\lambda_1$ x $9\lambda_1$ at f_1 and $12\lambda_2$ x $12\lambda_2$. Since the aperture is bigger at the higher frequency, it is evident that by using a higher permittivity to achieve higher directivity, the aperture efficiency is improved. In addition, the size of the ground plane, must be $9\lambda_1$ at the lowest frequency so that the wave reaching the edges will be significantly attenuated to avoid diffraction.

For the design of the unit cell used in each design, the parametric study was done using

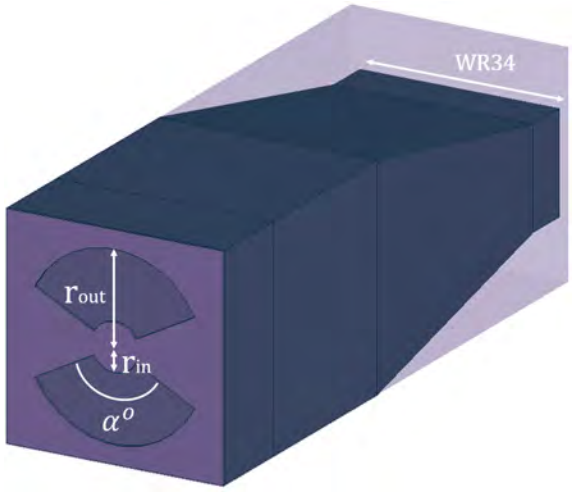

Fig. 2.10. The double iris slot on the ground plane was used to excite the resonant cavity. The parameters that define the iris slot are shown. Behind the slot, a WR-34 standard waveguide transition was used and can be seen here.

a perfect conductor (PEC). Since this is an ideal material used only in simulations, in order to approach a realistic case scenario, the unit cells were re-designed with copper on a very thin layer of kapton material (with $\epsilon = 3.6$ and thickness 0.025 mm). The new dimensions for the first design are: $b_1 = 0.83$ mm, $b_2 = 2.65$ mm, $b_3 = 0.51$ mm, $per = 4.56$ mm. Respectively for the second design: $b_1 = 0.73$ mm, $b_2 = 2.6$ mm, $b_3 = 0.4$ mm and $per = 4.2$ mm.

2.4 Results

2.4.1 Simulated antenna

The simulated results of the complete antenna model, were obtained using *CST Microwave Studio*. More specifically, the time domain solver was used for the complete antenna for both designs, whilst the frequency domain solver was used to synthesize the impedance of the unit cell.

First design

Initially, the reflection coefficient of the iris slot was calculated to ensure low return losses. Fig. 2.11 shows the resulting S_{11} of the antenna, reaching acceptable levels around -10 dB at 23 GHz and 29 GHz. The choice of the separation of the two bands, in combination with the feeding source, limits the levels obtained of the S_{11}. However, the iris slot is required to avoid the TM_0. Additionally, let us note that the matching of the iris does not only depend on its geometry, but also in this case, on the impedance seen from the ground plane, of the air-filled cavity parallel to the metasurface. Thus the height of the cavity should be re-adjusted to achieve optimum return loss results. To get an insight of the new height, one should observe the variation of the impedance of the MTS shown in Fig. 2.5. From inductive to capacitive, the impedance passes through a point of infinite value at 27.2 GHz approximately, indicating an open circuit behavior. Therefore, the new height will be close to half wavelength at this frequency. In this case the re-adjusted height is 5.6 mm.

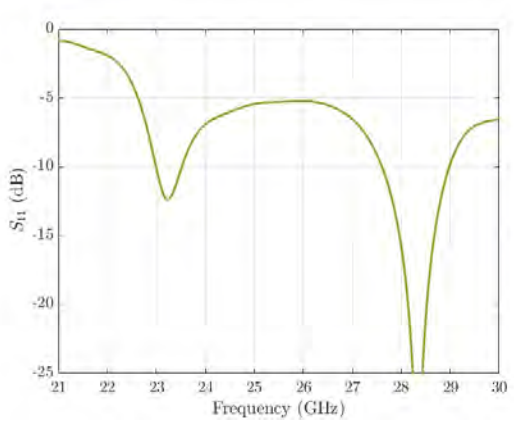

Fig. 2.11. S_{11} parameter of the first antenna design.

The normalized simulated radiation patterns at both planes are presented in Fig. 2.12 at $f_1 = 23$ GHz (left) and $f_2 = 29$ GHz (right). The directivity of the two bands is very close with 15.8 dBi at f_1 and 15 dBi at f_2. Regarding the realized gain, it is 15.1 dBi and 14.3 dBi at 23 GHz and 29 GHz respectively. The pencil beam is observed at the broadside direction ($\theta = 0$) at both frequencies, and the patterns are symmetrical at both E and H planes. The cross polarization is practically zero (-200 dB in CST).

Following the 3-dB gain definition, the frequency range between 22.5-23.8 GHz is the

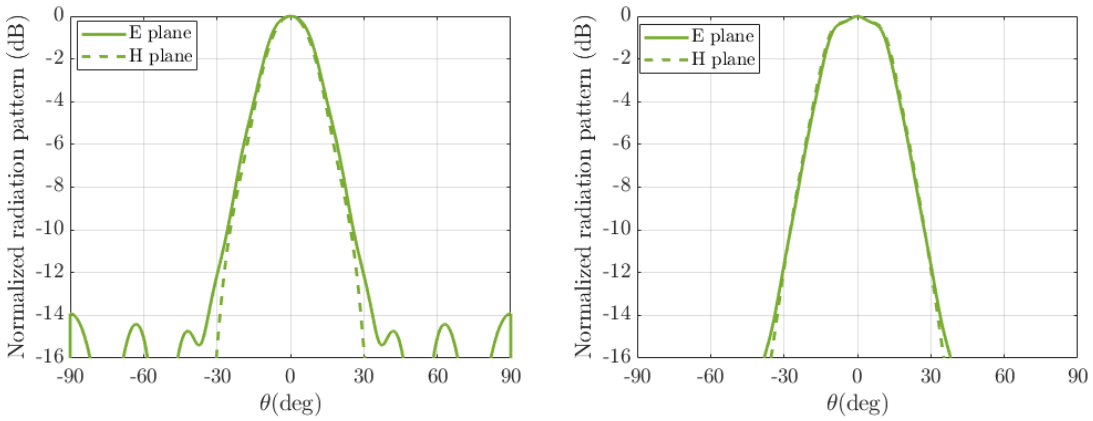

Fig. 2.12. Normalized radiation patterns at $f_1 = 23$ GHz (left) and $f_2 = 29$ GHz (right). At both frequencies the MTS is equivalent to $\epsilon_r = 6$

lower band, and the higher band covers the frequencies from 27.9 GHz to 29.6 GHz. The 3D radiation patterns are shown in Fig. 2.13 at f_1 (left) and f_2 (right). The deterioration of the radiation patterns for different frequencies than f_1,f_2 can be evidenced in Fig. 2.14.

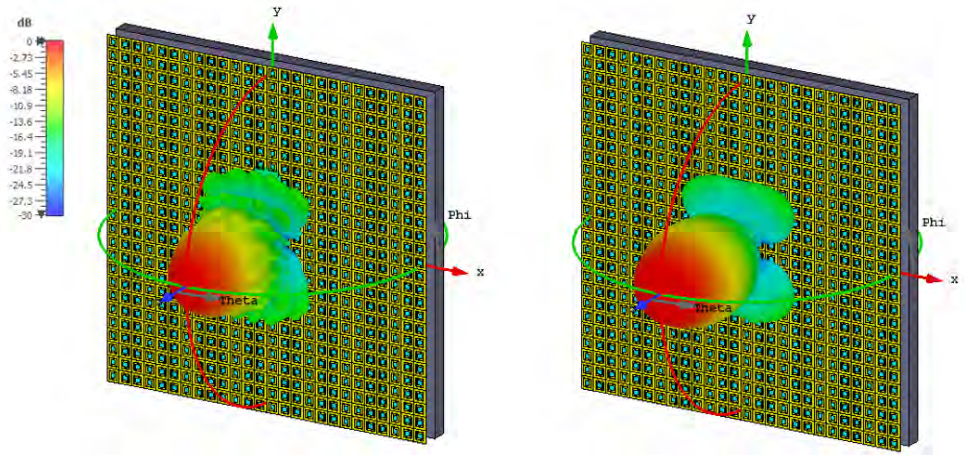

Fig. 2.13. 3D radiation patterns of the first design case for 23 GHz (left) and 29 GHz (right).

Second design

The simulated return loss of the second antenna is presented in Fig. 2.15, with acceptable S_{11} levels; -10.5 dB at 23 GHz and -8 dB at 29 GHz. As explained before, the higher the permittivity equivalence, the higher the directivity obtained, however this has an impact on the reached S_{11} levels as the matching of the antenna becomes more difficult. As for

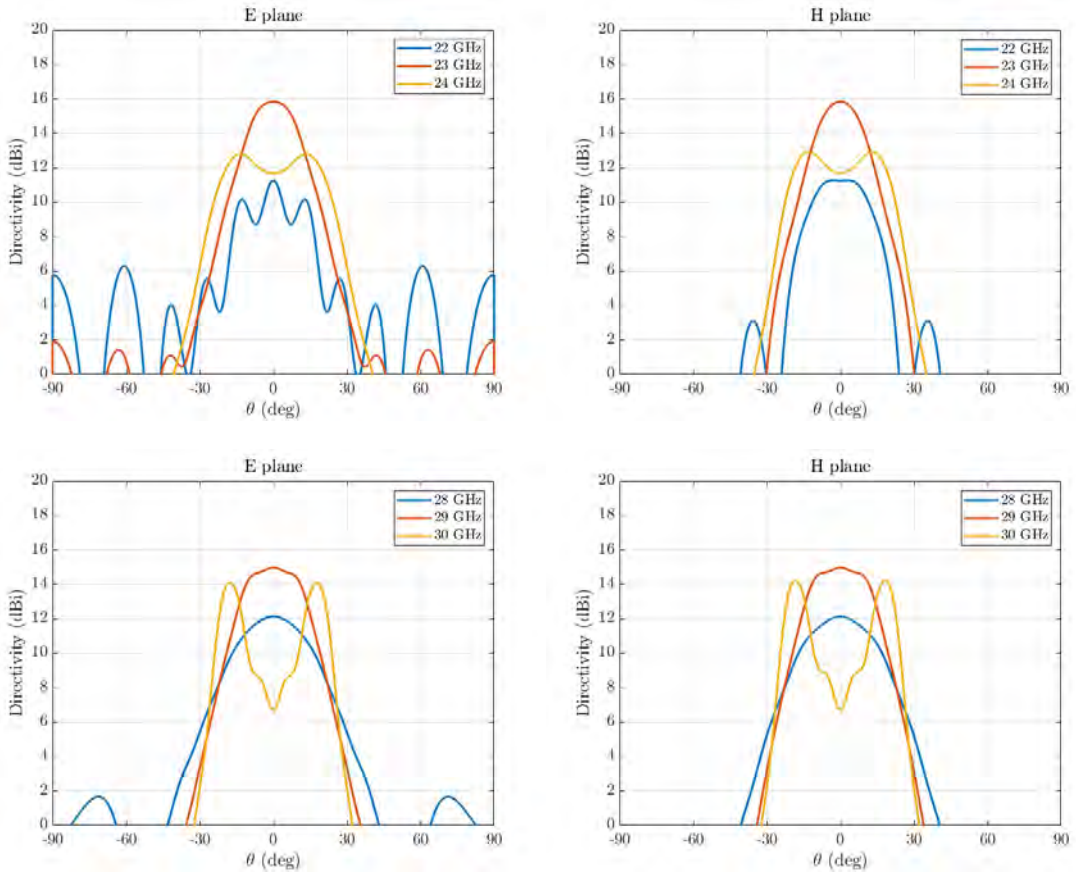

Fig. 2.14. Examples of radiation patterns of different frequencies compared to f_1 and f_2.

the cavity height, following the optimization as explained for the previous MTS design, the new value is 5.5 mm.

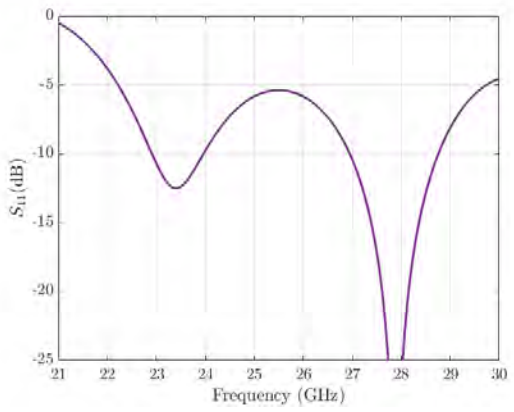

Fig. 2.15. S_{11} parameter of the second antenna design.

Pencil beams at broadside were observed at this case as well. Fig. 2.16 shows the normalized radiation pattern at 23 GHz and 29 GHz. The directivity corresponding to permittivity $\epsilon_{r1} = 6$ at 23 GHz is 15.3 dBi, and the realized gain 14.3 dBi. At 29 GHz for $\epsilon_{r2} = 10$ the directivity reaches 17.2 dBi and the realized gain 15.2 dBi. Therefore, the goal set by designing the second MTS to have higher directivity at f_2 is achieved. The lower band at this case is 22-24.6 GHz considering the 3-dB gain definition, and the frequency range 28.4-29.3 GHz corresponds to the higher band. The 3D radiation patterns of this design are shown in Fig. 2.17, where the narrower beam at 29 GHz indicates the higher directivity levels.

2.4.2 Experimental validation

To validate the proposed methodology, a prototype was manufactured and its experimental results are presented in this section.

The prototype corresponds to the first case of design as presented previously, with an equivalent permittivity of $\epsilon_r = 6$ at f_1 and f_2. The MTS was made of a very thin layer of copper on top of kapton, and it was placed on top of a foam layer, as seen in Fig. 2.18. A support was made in 3D printing to fix the MTS at the required height. The iris slot edged on the ground plane and the standard waveguide feeding are presented in Fig. 2.19.

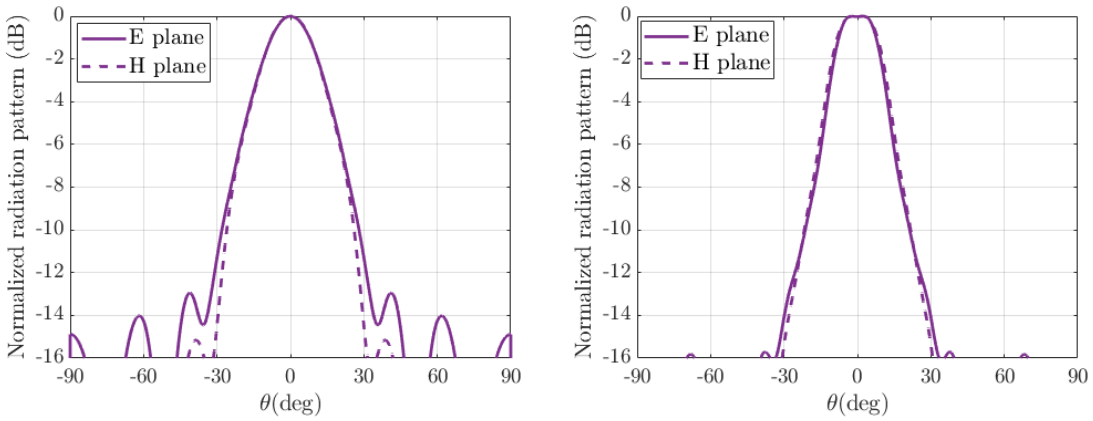

(a) (b)

Fig. 2.16. Normalized radiation patterns at (a) $f_1 = 23$ GHz for $\epsilon_{r1} = 6$, and (b) $f_2 = 29$ GHz $\epsilon_{r2} = 10$.

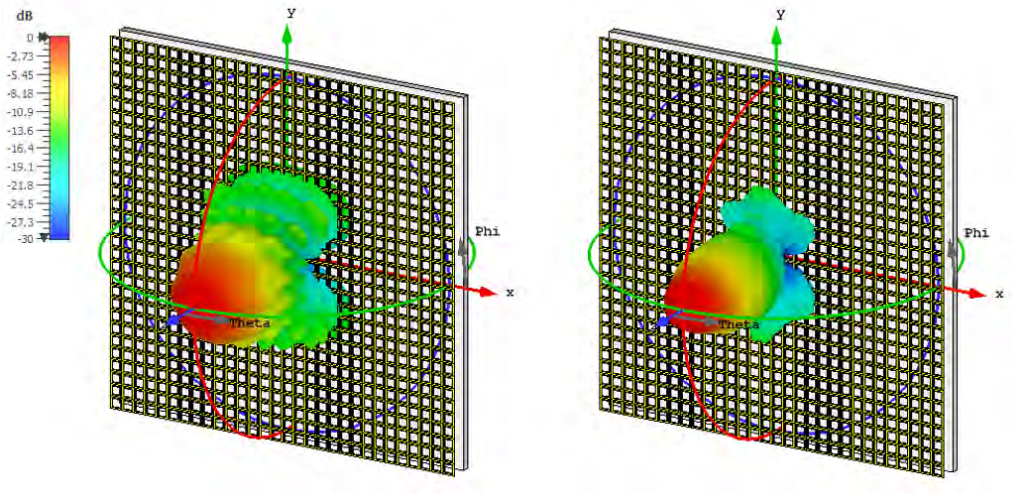

Fig. 2.17. 3D radiation patterns of the second design case for 23 GHz (left) and 29 GHz (right).

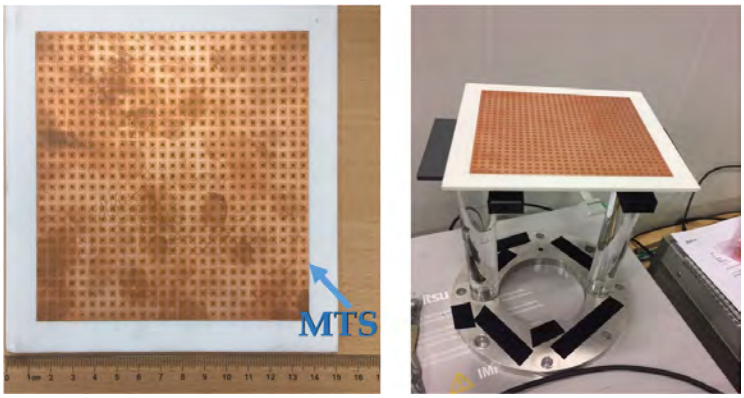

Fig. 2.18. Prototype of the designed metasurface on top of a foam layer (left), shown in the laboratory environment (right).

Fig. 2.19. A double iris slot was used as a radiation source (left). A standard waveguide transition was used to feed the iris slot (right).

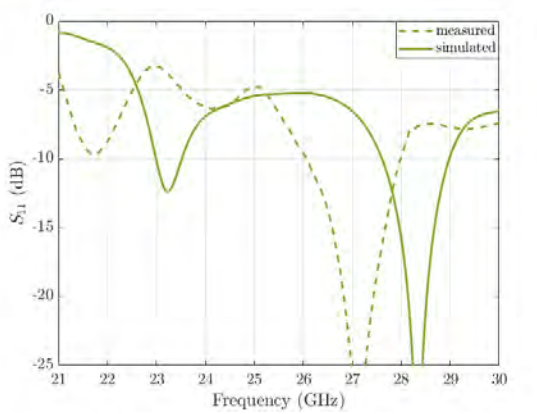

Fig. 2.20. Comparison between the simulated and the experimental S_{11} for the 1^{st} antenna design.

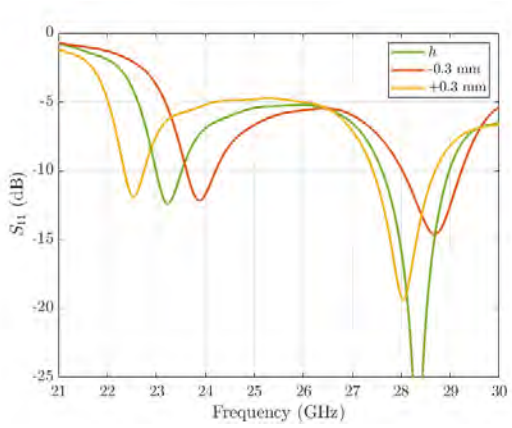

Fig. 2.21. Influence of height change $h_{MTS} \pm 0.3$ on the S_{11} of the antenna.

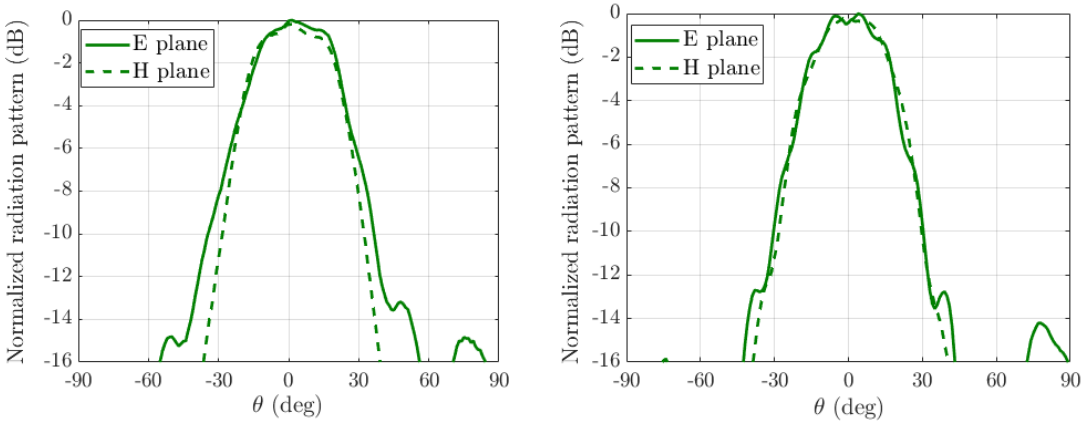

Fig. 2.22. Measured radiation patterns for: (a) 21.5 GHz and (b) 27.5 GHz.

Fig. 2.20 shows the measured S_{11} compared with the simulated result. A shift towards lower frequencies is apparent. This result of the S_{11} of the antenna, is due to a change in the cavity height, whose exact value is difficult to be implement with standard laboratory equipment. Small variations in the order of 10^{-1} mm can alter significantly the load impedance and thus the resonant frequency. The effect of this change of height on the S_{11} of the antenna is shown in Fig. 2.21. In addition, tolerances in fabrication also affect the matching of the antenna. Therefore, the new frequencies of the dual-band antenna are 21.5 GHz and 27.5 GHz as seen in Fig. 2.20.

The normalized measured radiation patterns are presented in Fig. 2.22 for both frequencies. At 21.5 GHz the measured realized gain is 13.4 dB while at 27.5 GHz it reaches 16.78 dB. The cross-polarization is below -20 dB for both frequencies. The difference in the realized gain at f_1 and f_2 is due to manufacturing tolerances and lack of sufficient characterization of the kapton material for the frequency band of this design, in addition to the variation of height with respect to the simulated 3D model. Nevertheless, the pencil beams with maximum at the broadside direction ($\theta = 0^o$), as well as the symmetrical E and H planes at both cases, are aligned with the expected performance of this type of antennas.

2.5 Conclusions

In this chapter a dual-band leaky-wave antenna has been presented. The proposed antenna, was designed using a novel methodology that allows dual-band performance with a single layer and single sided metasurface. In addition, it was shown that this methodology allows separate directivity control at each band.

The key aspect of the design methodology is that there can be an equivalence between a dielectric slab and an inductive or capacitive metasurface. For these two equivalent surfaces, there is a cavity height respectively lower and higher than the dielectric slab case. Therefore, by designing an MTS with impedance varying between inductive and capacitive behavior, a dual-band performance can be achieved. Equations for the impedance and the height have been presented for both equivalents. The unit cell can obtain these theoretical values by properly adjusting the parameters that define its geometry.

Furthermore, a metasurface designed to allow different permittivity equivalence at the two bands, has been presented. By choosing a higher permittivity at the higher band, the directivity is increased and the aperture efficiency is improved. The proposed methodology for the design of metasurface based leaky-wave antennas, allows flexibility in the design in terms of choice of the dual-band, and directivity achieved at each band. However, there is a limit for the separation between the two frequencies, which depends on the permittivity equivalence, and therefore a trade-off must take place between separation of bands and maximum directivity achieved.

A fabricated prototype of the case of same equivalent permittivities corresponding to both bands, has been also presented and the experimental results validated the simulations of the proposed design.

Chapter 3

Design of dual-band single layer leaky-wave antenna array

3.1 Introduction

In Chapter 1.4 the design methodology of single layer metasurfaces was presented. It was shown how the equivalence between a dielectric slab and an MTS [36], [37], can exist on a single metasurface for two different frequencies, thus creating a dual-band performance that can be tailored to the directivity requirements of the application under study.

In the literature there are many examples of leaky-wave antennas based on Fabry-Pérot resonant cavities [12], [13] as discussed in the previous Chapter. When it comes to operation frequencies, many dual-band and multi-band designs have been presented. Nevertheless, only a few examples can be found of arrays using Fabry-Pérot leaky-wave antennas. For instance, in [84] the authors designed an array where the basic element consisted of two waveguide apertures, that produced the dual-band, and above an MTS was placed, having metallic square patches on both sides.

The presented methodology for the design of dual-band single layer metasurfaces, can be extended to the case of arrays. In particular, the implementation of such MTS in thinned arrays, can have very interesting results. As discussed in [85] for the case of a thinned

array of radiating waveguide apertures, the use of dielectric partially reflective surfaces of a certain permittivity ϵ_r can reduce significantly the grating lobes. This technique made use of multiple dielectric layers, that were designed to have Chebyshev filters characteristics, reducing the grating lobes up to -20 dB. The same method was proposed in [86] to control the grating lobes. In [87] the multiple layer dielectrics configuration was used to suppress the grating lobes of a patch antenna array with inter-element spacing of $2.8\lambda_0$. Similarly, in [88] an array with large periodicity was presented, and more recently in [89], a thinned array of iris slots fed by waveguides, again using a dielectric slab as a PRS to control the grating lobes.

Although this concept has been explored, none of the above implementations presented a dual-band resonance. In the current Chapter, the design of a thinned array will be presented, with significant attenuation of the multiple maxima occurring in undesired directions, by the use of a dual-band metasurface with more sophisticated design than the previously reported works. To demonstrate the potential of the MTS-based Fabry-Pérot array, a 3x3 sub-array has been studied, in order to evaluate the embedded radiation pattern as well as the mutual coupling between the elements. The advantages of thinned arrays such as reduced cost and reduced complexity compared to large arrays, are combined with the simple solution for directivity enhancement that the MTS offers. In addition, this particular metasurface has the advantage of consisting of a single layer and also due to its design methodology, it allows directivity control which will be translated in control over the obtained attenuation of the grating lobes.

3.2 Planar thinned array

The proposed array consists of a 3x3 planar configuration of leaky-wave antennas, in this way we model a sub-array. The leaky-wave modes propagate in a resonant cavity of a certain height h, that is formed between the ground plane level and the metasurface placed above the array. In the following sections, the design of the metasurface will be presented, and also its usefulness in the suppression of grating lobes in thinned arrays. In addition, the stacked patch antenna that is used to excite the leaky-wave modes will be also presented.

3.2.1 Suppression of grating lobes

Thinned arrays make use of large periodicities. In this type of arrays, the distance between two contiguous elements is larger than a wavelength in the design frequency, $d > \lambda$. Thus, grating lobes appear in the radiation pattern. These unintended lobes, present equally strong radiation levels as the main lobe. The existence of grating lobes, is the main drawback of thinned arrays, as there is radiation in undesired directions which leads to important losses.

The formation of the grating lobes at an angle θ from the broadside direction ($\theta = 0$), can be predicted from the known equation derived from the array factor [90]:

$$2\pi = k_0 d \sin\theta_{gl} \tag{3.1}$$

where k_0 is the free space wavenumber and d is the inter-element distance expressed in λ. In Fig. 3.1, examples of two inter-element distances and the corresponding grating lobes, are presented for a planar patch antenna array. As expected from Eq. 3.1, the larger the inter-element distance, the closer the grating lobes will be to broadside direction. Indeed in Fig. 3.1, for $d = 4\lambda$, the grating lobes are located at $\theta_{gl} = 14.5^o$, while for $d = 3\lambda$ the grating lobe is at $\theta_{gl} = 19.5^o$.

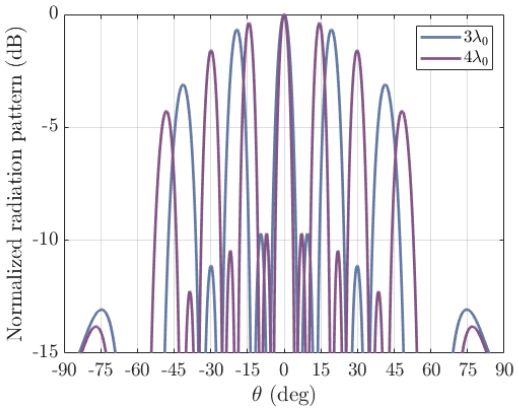

Fig. 3.1. Example of grating lobes in a planar 3x3 array, for two inter-element spacings.

Considering the above, we get an insight of the performance of the thinned dual-band array. If we suppose that the two frequencies of the dual-band are f_1 and f_2, with $f_1 < f_2$, then the electrical distance between the elements will be bigger for the higher frequency,

with $d_1 < d_2$.[1] As a result, the grating lobes will be closer to broadside at f_2.

A method for grating lobe suppression, is by placing a metasurface above the planar array [89], creating a leaky-wave antenna array. The metasurface, as discussed before, increases the directivity of the individual elements of the array, leading to significant attenuation of the grating lobes [88]. Previously, it was mentioned that θ_{gl} is closer to broadside for higher frequencies. In that case, to achieve severe attenuation of the grating lobes, higher directivity levels are required. This leads to the need of directivity control in the case of a dual-band array, aiming to achieve good grating lobes suppression levels at both bands of operation.

3.2.2 Single layer dual-band metasurface

As mentioned in the previous section, a good method for the suppression of the undesired grating lobes in a thinned planar array, is by achieving directivity enhancement with the use of a metasurface superstrate.

In Chapter 1.4 it was shown that there is an equivalence between a simple dielectric slab of a certain permittivity ϵ_r, and a metasurface [36], [37]. The equivalence is in terms of the propagation constant k_z which was derived from the dispersion equation (Eq. 1.7). Furthermore, it was shown that the impedance of the metasurface [37], [91] can be inductive and/or capacitive (Eq.1.14), leading to two height solutions of Eq. 1.15, which defines the resonant cavity. Afterwards it was demonstrated that a single cavity height can be defined, that has inductive characteristics for one frequency f_1 and capacitive for another frequency f_2, thus producing a dual-band performance.

The above, can be extended in the case of a dual-band array. In fact, a metasurface can be designed to exhibit an equivalence with two different dielectric permittivities at the two frequencies of the dual-band [91], as seen in Chapter 1.4. By implementing a solution that provides higher directivity at higher frequency, the grating lobe that will be closer to broadside, can be severely attenuated.

The first step for the design of the metasurface, is to define a single cavity for both

[1] d_i is the distance referring to the corresponding wavelength

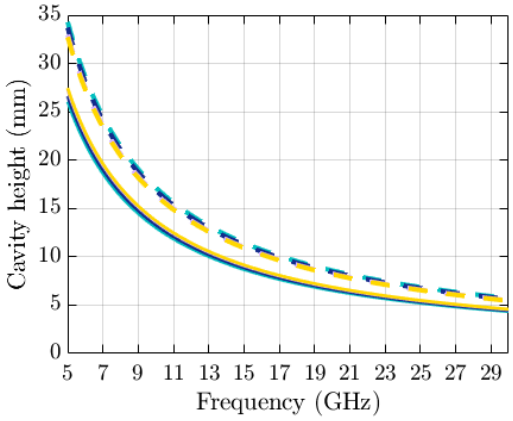

Fig. 3.2. Cavity height for the inductive (solid line) and the capacitive (dashed line) case for different values of $\epsilon_r = 4, 6, 10, 12$.

cases of equivalence of the different permittivities. In Fig. 3.2, different height solutions are presented, for several values of permittivity ($\epsilon_r = 4, 6, 10, 12$), for the inductive (solid line) and the capacitive (dashed line) case equivalence and for a selected frequency range. Defining a single cavity height for the inductive and capacitive case that each one corresponds to a different ϵ_r, means that a single metasurface can be designed. Fig. 3.3 shows a cavity solution for the two bands at 18 GHz and 22 GHz, with permittivities 6 and 10 respectively, and a common height 7.4 mm. By introducing these values of permittivity in Eq. 1.14, the impedance that the unit cell should achieve, can be calculated. Let us note here that the impedance is not a function of frequency, and depends only on the permittivity equivalence that was chosen.

Although the latter is a good solution, we have chosen to implement an array design in the X band. Fig. 3.4, shows that at $f_1 = 10.5$ GHz and $f_2 = 13$ GHz a common cavity can be defined having a height of 12.7 mm. The equivalent slab has a dielectric constant of $\epsilon_{r1} = 6$ and $\epsilon_{r2} = 10$ at f_1 and f_2 respectively. The choice of a higher permittivity for f_2 means that the metasurface will be more reflective, thus obtaining higher directivity which is critical for the attenuation of the grating lobes that are higher at f_2

From Eq. 1.14 the impedance was calculated to be $Z_{ind} = 157\,j\ \Omega$ and $Z_{cap} = -132\,j\ \Omega$. The unit cell that forms the metasurface is shown in Fig. 3.5, and is of the same shape as in Chapter 1.4. In order to obtain the required impedance, the parameters of the geometry of the unit cell should be adjusted. Indeed, the theoretical impedance values were achieved

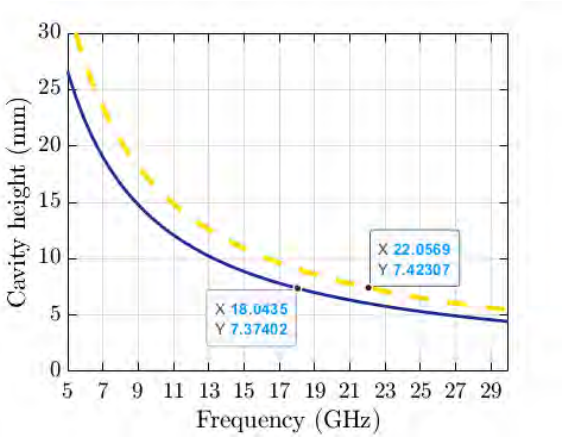

Fig. 3.3. A possible solution for a single cavity height is at the frequencies 18 GHz and 22 GHz, with permittivities 6 and 10 respectively. The cavity in this case has a height of 7.4 mm.

at the two frequencies as seen in Fig. 3.6, for the dimensions denoted in Table 3.1. One should note that between the inductive and capacitive regions, the impedance becomes infinite approximately at $f_{central} = 12.15$ GHz. This means that there is no radiation at this frequency, indicating the two bands of operation of the design. Moreover, the height of the cavity can be re-adjusted using the new value $\lambda_{central}/2$. Although the impedance has the same value in this case, and in the design implementation presented in Chapter 1.4 due to the same permittivity used, the dimensions of the unit cell are different since the frequency band has changed. The restriction of the periodicity of the unit cells that was discussed in Chapter 1.4 applies in this case as well; the period should be smaller than $\lambda_0/2$ at the lowest frequency, to avoid higher order Floquet modes that will lead to grating lobes in the radiation pattern of the single element [23].

b_1	b_2	b_3	per
1.47 mm	6.3 mm	0.37 mm	9.8 mm

Table 3.1. DIMENSIONS OF THE UNIT CELL

3.2.3 Stacked patch antenna design

As seen in Fig. 3.7, the basic element of the array consists of a radiation source that excites the leaky-modes, and a metasurface placed at a certain height, forming like this a

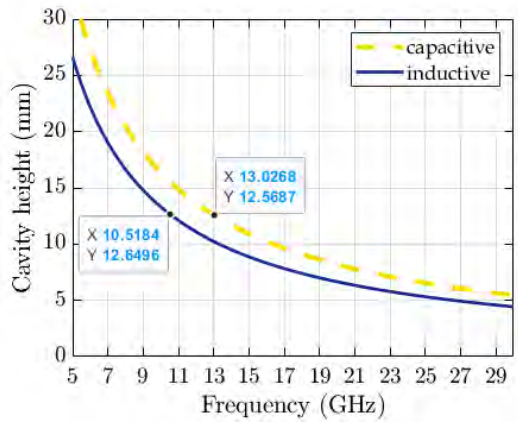

Fig. 3.4. A single cavity of 12.7 mm height is calculated at 10.5 GHz and 13 GHz, for the respective dielectric constants $\epsilon_{r1} = 6$ and $\epsilon_{r2} = 10$.

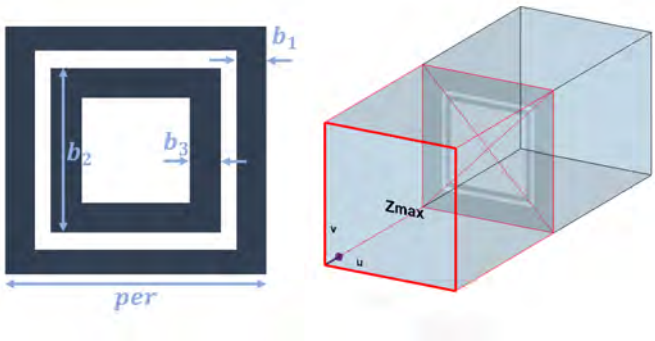

Fig. 3.5. Unit cell of the single layer dual-band metasurface, with its respective geometry parameters (left), and in the simulation environment (right with *Zmax* indicating the excitation port).

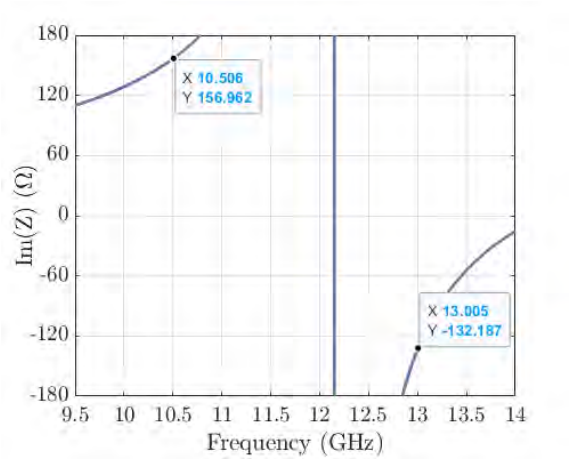

Fig. 3.6. Obtained impedance for the dimensions of the unit cell in Table 3.1. From inductive at 10.5 GHz, the impedance becomes capacitive at 13 GHz, passing through infinity, thus creating the dual-band.

resonant cavity. A stacked patch antenna was chosen in this case to excite the resonant cavity (see Fig. 3.7(right)). This antenna consists of two metallic patches each one lying on top of a dielectric substrate.

Each square patch antenna, should have the adequate dimensions to excite one of the two frequency bands. For this design, the bottom patch antenna, with dimensions 8.8 x 8.8 mm is responsible for the resonance at 10.5 GHz, whilst the top square patch resonates at 13 GHz with a size of 7.3 x 7.3 mm, thus creating the dual-band performance. Both antennas are fed by using a single coaxial probe. The dielectric used for each layer is *Rogers RT/Duroid 5880* with $\epsilon_r = 2.2$ and $tan\delta = 0.0009$, having a thickness of 0.5mm. Underneath the two antennas lies a metallic ground plane.

3.3 Results

3.3.1 Simulated antenna array

To simulate the proposed 3x3 array, CST Microwave studio was used. In particular for the whole array simulation, the time domain was used, while for the unit cell of the metasurface, we used the frequency domain solver. Additionally, the unit cell´s dimensions

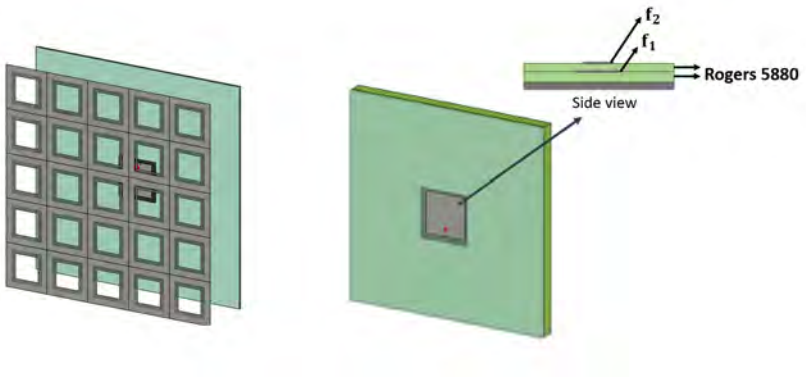

Fig. 3.7. The basic element of the array consists of a stacked patch antenna (right) and a metasurface with interleaved squares (left). The inset shows the side view of the stacked patch.

(Table 3.1) were slightly modified when the material was changed from PEC to copper and a layer of Rogers 5880 ($\epsilon_r = 2.2$) of thickness 0.25 mm was used instead of kapton as in the design of Chapter 2, to simulate the fabrication materials. The new dimensions are : $b_1 = 1.97$ mm, $b_2 = 5.8$ mm, $b_3 = 1.16$ mm and $per = 9.97$ mm. The obtained impedance is $Z_{ind} = 157.7\,j\ \Omega$ and $Z_{cap} = -132.7\,j\ \Omega$.

The total length of the metasurface and the ground plane, is 31 cm. This size corresponds to approximately $11\lambda_0$ at the lowest frequency 10.5 GHz, which is sufficient for the propagating waves to get attenuated before reaching the edges of the antenna.

The separation of elements affects the design of the array in two aspects. On one hand, the distance between the elements affects the location of the grating lobes. Therefore the metasurface should be designed in such way to attenuate sufficiently the grating lobes at both frequencies of the dual-band. On the other hand, the spacing of the elements affects directly the mutual coupling. This is a critical point for the resulting radiation patterns of the array [92]. To avoid the deformation of the radiation patterns, the mutual coupling should be below -25 dB according to [89], [93]. In these antennas, the coupling is mostly due to the leaky-waves propagating in the resonant cavity, apart from the coupling due to the surface waves on the dielectric layer where the array lies.

The chosen spacing between the elements of the array is $1.9\lambda_1$ at 10.5 GHz and $2.4\lambda_2$ at 13 GHz. To obtain the presented results, only the central element was excited, and the surrounding elements were considered to be connected to a matched load. The S-

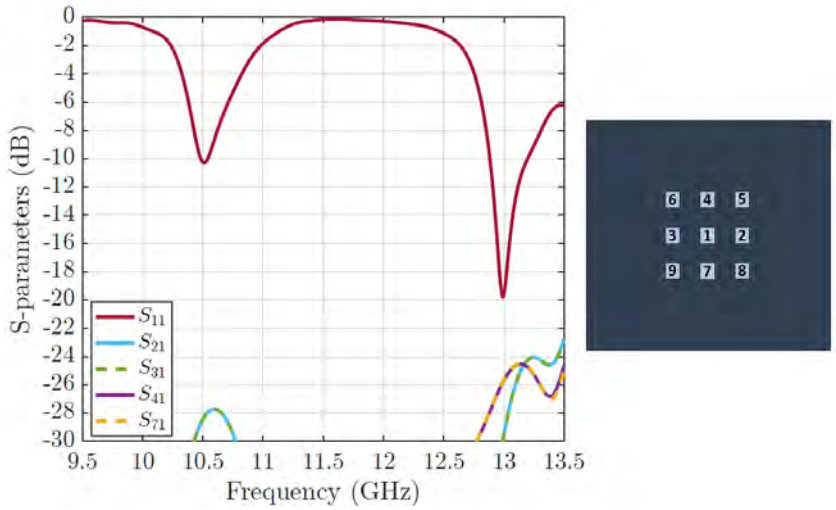

Fig. 3.8. S-parameters of the array. The elements are numbered as indicated on the right. The S_{41} and S_{71} correspond to the neighbouring elements on the E-plane, while S_{21} and S_{31} correspond to the H-plane.

parameters can be seen in Fig. 3.8. The S_{11} of the central element, reveals good matching levels with -10 dB at 10.5 GHz and -19 dB at 13 GHz. The mutual coupling is maintained below -25 dB at both frequencies.

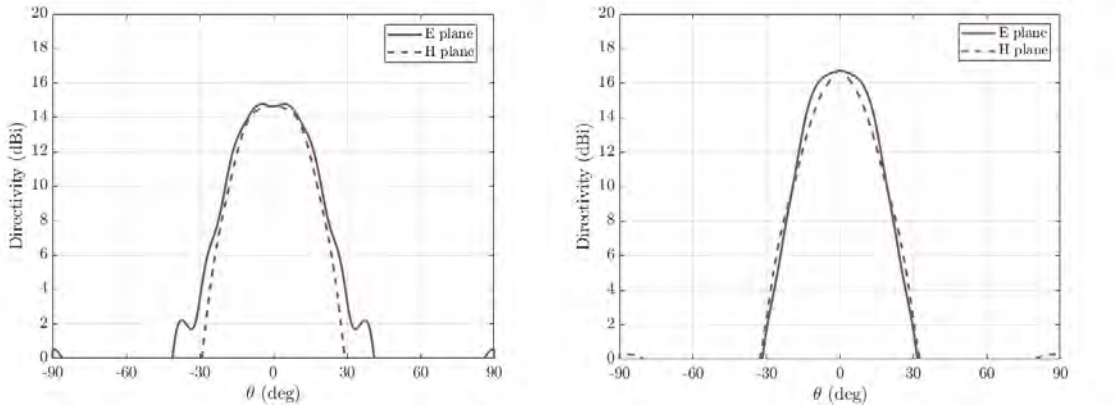

(a) (b)

Fig. 3.9. Directivity at (a) f_1 = 10.5 GHz and (b) f_2 = 13 GHz, the solid and dashed lines represent the E and H planes respectively.

The corresponding embedded radiation patterns of the lower frequency, are presented in Fig. 3.9(a). At 10.5 GHz, the directivity reaches 14.6 dBi. A small ripple can be noted in the E-plane of the radiation pattern, indicating either that there is some influence from

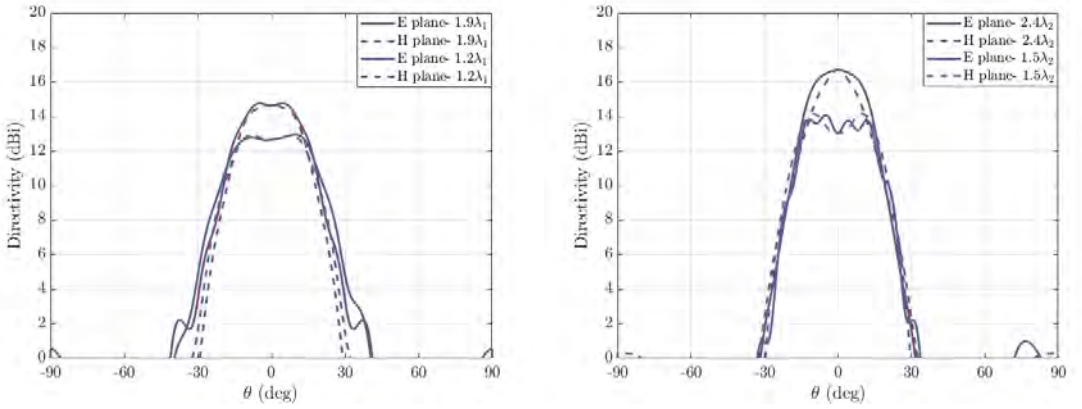

(a) (b)

Fig. 3.10. Comparison of the radiation patterns for two different inter-element distances.

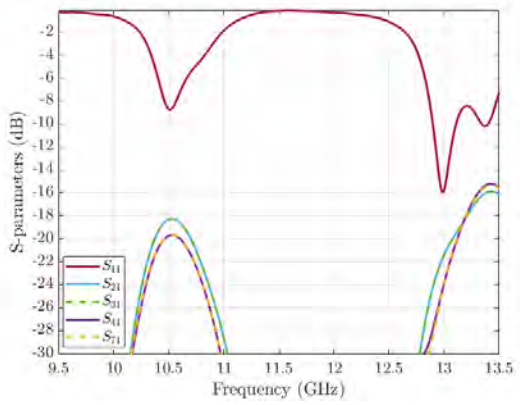

Fig. 3.11. S-parameters of the array for a smaller inter-element distance equal to $1.2\lambda_1$ and $1.5\lambda_2$. The configuration of the array is as shown in Fig. 3.8.

the surrounding array elements, or that the height of the metasurface should be slightly modified. Let us note here that the height of the cavity h was changed after the introduction of the real materials in the MTS (copper and Rogers 5880) in order to achieve the best result in the radiation patterns. Since this parameter also affects the resonance of the stacked patch antennas, the height should be optimized. For the presented case, the final value of the height is 11.5 mm.

Regarding the grating lobes at $f_1 = 10.5$ GHz where the inter-element distance is $1.9\lambda_1$, the radiation pattern without the metasurface, exhibits grating lobes at $\theta_{gl1} = 32^o$. At this angle θ_{gl1} we see in the embedded radiation pattern with the MTS, that the directivity is only 2 dBi, which indicates a decrease of 12.6 dBi.

At 13 GHz, 16.8 dBi of directivity is observed in Fig. 3.9(b). The approximately 2 dB of increase in the directivity of f_2 is a result of the equivalence of the metasurface, with a higher permittivity ($\epsilon_{r2} = 10$) with respect to f_1 ($\epsilon_{r1} = 6$). As for the grating lobes, from Eq. 3.1 they are calculated to be at $\theta = 25.7^o$ (for inter-element distance $2.4\lambda_2$), which is closer to the broadside direction than at f_1 as already discussed. In this case the attenuation is 10.6 dB as observed in Fig. 3.9(b).

To observe the effect of the mutual coupling on the radiation patterns, in Fig. 3.10 we present the results of inter-element distances $1.2\lambda_1$ and $1.5\lambda_2$ at $f_1 = 10.5$ GHz and $f_2 = 13$ GHz respectively. Evidently, the directivity decreases, and the radiation patterns are deformed. This gives us an intuition of the stronger coupling than in Fig. 3.8. Indeed, Fig. 3.11 the mutual coupling is around 20 dB at f_1 and f_2, indicating a significant increase compared to the coupling in Fig. 3.8.

3.3.2 Experimental validation

The manufactured prototype that was used to validate the presented array, is shown in Fig. 3.12. As mentioned previously, the MTS was fabricated using a very thin layer of copper on top of a dielectric, that in this case was Rogers 5880 of thickness 0.25 mm. The stacked patches were fabricated in two layers that afterwards were glued together. The experimental results are currently taking place.

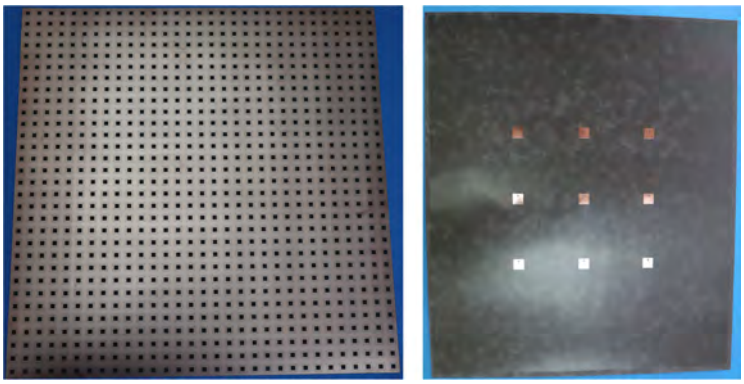

Fig. 3.12. The fabricated prototype: the MTS is seen on the left, while the top layer of the array is on the right.

3.4 Conclusions

The design of a dual-band planar thinned array with grating lobe suppression has been presented. The basic element of the 3x3 array, consists of a stacked patch and a metasurface that is located at a certain height h to create a resonant cavity.

The dual-band metasurface was designed following the methodology presented in Chapter 1.4. Since the MTS has the ability to enhance the directivity of a simple radiation source, in this case when it is combined with a thinned planar array, it attenuates the grating lobes that would occur due to large inter-element spacing. Furthermore, since the array has two bands of operation, the distance between the stacked patches is different at $f_1 < f_2$, with $d_1 < d_2$. Therefore, the grating lobes will be closer to the broadside direction ($\theta = 0$). This means that at f_2 higher directivity is required than at f_1.

In this direction, the metasurface was designed so that it exhibits an equivalence with different dielectric permittivities at the two frequencies of operation, which means that different directivities are obtained at each frequency. At $f_1 = 10.5$ GHz and $f_2 = 13$ GHz, the designed MTS is equivalent to a dielectric slab of $\epsilon_{r1} = 6$ and $\epsilon_{r2} = 10$ respectively. The simulated embedded pattern of the array showed that indeed the directivity at f_2 is enhanced by 2 dB reaching 16.8 dBi, whilst at f_1 14.6 dBi are obtained. The attenuation of the grating lobes is 12.6 dB at f_1 and 10.6 dB at f_2.

In conclusion, with the presented method for the design of a metasurface, a planar array using large inter-element spacing can be created, with good grating lobe suppression

levels at both operating frequencies of the design.

Chapter 4

Design of leaky-wave antenna as overlapped feed for a reflector

4.1 Introduction

In this chapter, a Fabry-Pérot array is presented, following the concept of leaky-wave antennas made with a metasurface as it was discussed in the previous Chapters 1-3. The array was developed as a part of the Airbus/ESA project for the *Overlapped Feed for a Reflector-"OLAF"*. The difference with the designs presented in the previous chapters, is the significantly lower targeting frequencies, from 1.215 GHz to 1.3 GHz.

The designed array was proposed as a candidate feed-array of a large reflector, part of an instrument of a L-band SAR system for Earth observation [94]–[96].

The array has to have 34x3 elements and should meet the following strict requirements: return loss below -20 dB, mutual coupling less than -30 dB, low cross-polarization (below -30 dB), taper at 27^o between -10 and -12 dB, isolation between H/V ports at -30 dB, insertion losses less than 1 dB, with a limitation of the inter-element distance having a maximum of $1.25\lambda_0$ at 1.25 GHz. This value of inter-element distance was chosen so that the overlapping between contiguous beams would not be less than a critical level defined by the application. However, as it will be demonstrated later, this limitation affects significantly the performance of the leaky-wave array, and despite the advantage of the

simple low-profile directivity enhancement, the otherwise narrow pencil beam array does not have the expected performance. In the following sections, the different approaches to the implementation of the leaky-wave array that were evaluated will be presented, as well as the results of the fabricated prototype.

4.2 Metasurface design

For the implementation of the leaky-wave array, two metasurfaces were evaluated. Aiming to increase the directivity of a non directive source antenna, the first MTS that was studied is a simple metallic grid, that was designed to behave as its equivalent dielectric slab [36], [37]. The second MTS was studied to increase the bandwidth, and consists of a double sided dielectric, with complementary geometrical patterns on each side [42]. The choice of MTS plays a significant role for the directivity reached, depending on the geometry of the metallic printed pattern, and therefore affects the taper at 27^o, for this specific application. In addition, the reflectivity of the MTS which is desirable to obtain narrow beamforming, affects negatively the performance of the array as it increases the coupling between the elements. Therefore and since the inter-element spacing has strict limitations, the design of each MTS must be evaluated and a trade-off between directivity and mutual coupling must take place. Furthermore, as it will be explained in the next stage of design, the impedance matching of the antenna is also affected by the MTS, which should be also taken into consideration.

4.2.1 Single layer inductive grid

As explained in Chapter 1.4, in a leaky-wave antenna the performance of a dielectric slab can find an equivalent in a metallic grid in terms of propagation inside the resonant cavity, following the studies presented in [36], [37]. Since the grid MTS shows an inductive character, the system of Eq. 1.14 & Eq. 1.15 leads to the inductive impedance Z and the height of the MTS h_{grid} for a given ϵ_r. The choice of the equivalent permittivity is subjective, and follows the directivity requirements of the application. For the presented design, and following the specifications for the taper (-10 dB to -12 dB at 27^o), the permittivity should

be such to produce directivity levels around 16 dBi. Therefore, we have chosen $\epsilon_r = 5$. This value results to a height $h_{MTS} = 105.5$ mm. The impedance was calculated to be $Z = 174\,j\,\Omega$, and the width of the grid can be found from the formula [37]:

$$w = \frac{2per}{\pi} + e^{-\frac{2\pi Z_0}{\eta_0 k_0 per}} \tag{4.1}$$

where $\eta_0 = 120\pi$ and k_0 are the impedance and propagation constant in free space respectively. The periodicity of the MTS should be less than half wavelength at the central frequency $f_0 = 1.25$ GHz to avoid grating lobes. For $per = \lambda_0/5$ and the aforementioned value of impedance, the width of the grid is $w = 3$ mm. Before the incorporation of the grid in the design of the leaky-wave element, the frequency solver of CST Microwave studio was used, to validate the calculated impedance for a unit cell with $per = \lambda_0/5$ and $w = 3$ mm, shown in Fig. 4.1. In the same figure, the reflectivity of the grid MTS is also presented as the S_{11} parameter of the unit cell. For these results, the thickness of the grid, was considered infinitesimally small. For an increased thickness, it was observed that the directivity is increasing. In the following sections, the grid in the full antenna simulations will be considered without thickness and placed on a FR4 layer of 0.5 mm.

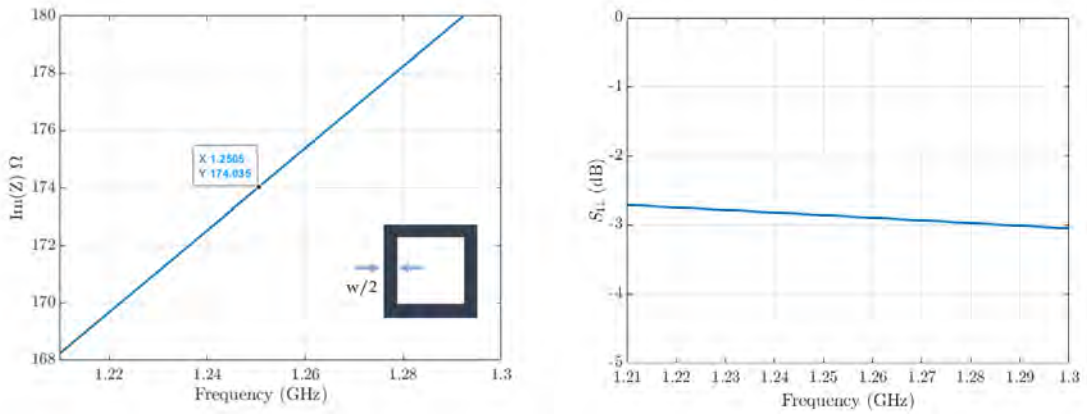

Fig. 4.1. Impedance of the simulated unit cell (inset) of the grid MTS (left). The S_{11} showing the reflectivity of the grid (right).

4.2.2 Complementary MTS

The second MTS that was designed, consists of a dielectric slab with metallic elements on both sides. More specifically, the 2D periodic printed arrays on the two sides are complementary with each other, following in particular the design presented in [42]. The top layer consists of an array of metallic patches, while the bottom array is made of square loops.

The performance of the MTS depends on the parameters of the complementary patterns. On the top layer, the gaps between the patches grant the surface a capacitance that is controlled by the size of the gap or in other words, the size of the metallic patches. On the bottom side of the MTS, the 2D array of square loops can be also considered as a grid, and shows an inductance that is controlled by the width of the grid.

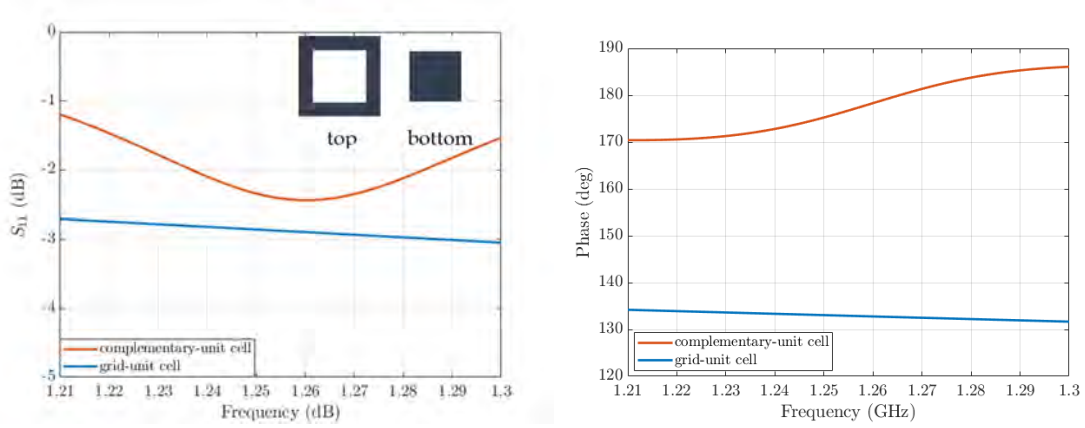

Fig. 4.2. Magnitude of S_{11} (left) and the corresponding phase (right) of the complementary unit cell compared to the grid unit cell.

In general, in the case of a dielectric PRS, the main disadvantage is the narrow band performance. In [42] it was reported that the complementary MTS can achieve a wideband performance when the reflection phase is increasing with frequency, thus having a positive phase gradient [20].

The unit cell can be seen in the inset of Fig. 4.2 along with its S_{11}. The dielectric layer between the complementary patterns is made of FR4 with thickness 2 mm. For the following parameters: $a = 40$ mm, $b = 27.5$ mm, $per = 52$ mm, this unit cell achieves higher reflectivity than the grid unit cell. These parameters where chosen after

an optimization process, taking into consideration the positive gradient of the reflection phase (reported in Fig. 4.2) as well as the reflectivity of the unit cell. As in the case of a simple dielectric slab, the theoretical value for the cavity height is $h_{comp} = \lambda/2$ at the central operating frequency.

4.3 Leaky-wave array

As mentioned before, the feed array will consist of 34x3 elements. However, for the initial stage of studies and performance evaluation, a 3x3 planar array has been designed and will be presented in the following sections. This corresponds to a subarray and studying the embedded radiation pattern will be representative of a larger array. Nevertheless, a 5x5 array was also evaluated; however the 3x3 array results were considered sufficient for this stage of the initial studies of the embedded radiation patterns.

In the following sections, the array will be evaluated with the two designs of MTS that were described in the previously. In addition, two dual-polarization radiation sources have been used to excite the resonant cavity between the ground plane and the MTS, the first being a differential patch antenna, and the second a magneto-electric dipole.

4.3.1 3x3 planar array

The basic element of the 3x3 array, consists of a leaky-wave antenna made of a differentially fed patch antenna [97]–[99] inside a resonant cavity that is defined by a metallic ground plane and a metasurface. This type of feeding antenna was chosen due to the low cross polarization levels required, that cannot be obtained with a conventional patch.

An illustration of the differential patch antenna is presented in Fig. 4.3. The radiating patch is fed by coupling from 4 patches placed underneath it. The coupling patches are directly fed with a phase difference of 180^o in pairs by an external microwave circuit. The radiating patch is placed on a post located centrally, that is not connected to any feeding.

Initially, a single patch antenna was combined with the grid and the complementary

MTS in order to obtain the resulting radiation patterns and good impedance matching levels. At this stage, the differential feeding was done by introducing a phase difference in the ports used in the simulated model with post-processing in CST Microwave Studio. For the values presented in Table 4.1 the S_{11d} of the antenna with the grid MTS is shown in Fig. 4.4. The differential S_{11d} is challenging to minimize, because it should be $S_{11} = S_{31}$. Fig. 4.5 shows the S_{11} and S_{31} parameters, and the result of their combination with the same amplitude but 180^o phase difference. The minimum happens when they have the same value. In this section, the combined return loss will be discussed; however the coupling presented here is not the combined one, which would be expected to be lower. Later in the final results, the microwave circuit that provides the phase difference will be simulated with the array and we will calculate the coupling among differential ports.

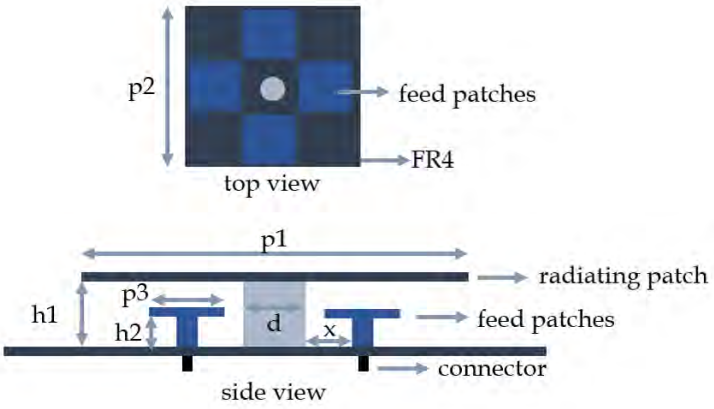

Fig. 4.3. Schematic representation of the differentially fed patch antenna. The side view shows the feeding patches beneath the top radiating patch.

Another parameter of the design that affects significantly the matching of the antenna, is the cavity height. In this case, for the grid MTS, the height was calculated to be $h_{grid} = 105.5$ mm using the analytical formula of Eq. 1.15. Since the cavity height directly affects the beamforming of the antenna, after optimization it was changed to $h_{grid} = 102$ mm. The change of height is due to the fact that h_{grid} was calculated for an ideal source like a slot on a ground plane, and the patch used is quite different to that.

However, this has an impact on the impedance perceived from the source antenna, and therefore limitations in the matching levels are introduced. The effect of the height on the combined S_{11} of the patch antenna can be observed in Fig. 4.4. Let us note here, that

despite the further optimization of the parameters of the antenna regarding the new height h_{grid}, the impedance matching levels were not improved. Nevertheless, it was observed that when the complementary MTS was used instead, better return loss levels were obtained. The optimized height in this case is h_{comp} = 117 mm.

p_1	p_2	p_3	h_1	h_2	d	x
87	54	15.5	13	19.5	17	12.16

Parameters of the patch antenna in mm.

Table 4.1. INDIVIDUAL ELEMENT

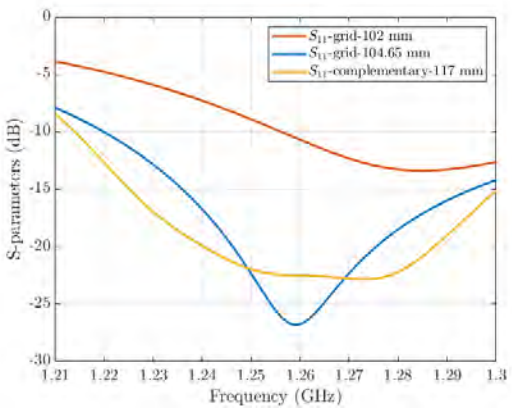

Fig. 4.4. S_{11} of the patch antenna with the grid MTS for two cavity heights, compared with the S_{11} obtained with the complementary MTS.

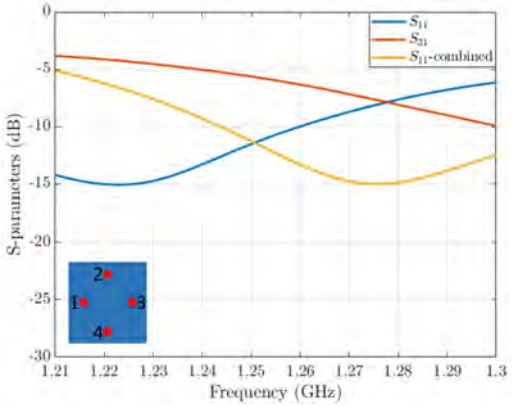

Fig. 4.5. S-parameters of the patch antenna before and after the post processing combination of ports 1,3 with phase difference 180^o.

For an MTS with total size of 7λ at f_0 the directivity of the individual element in the case of the grid is 15 dBi at f_1 = 1.21 GHz, 16 dBi at f_0 = 1.25 GHz and 16 dBi at f_2 = 1.3 GHz. The 3D radiation patterns can be seen in Fig. 4.6. For these values of directivity, the taper requirements are fulfilled with : -10 dB at f_1, -11 dB at f_0 and -11 dB f_2. For the same size of aperture, the complementary MTS enhances the directivity of the patch antenna reaching: 18 dBi at f_1, 16 dBi at f_0, 16.15 dBi at f_2, and it also fulfills the taper requirements. The corresponding 3D radiation patterns are shown in Fig. 4.7. This was expected according to the reflectivity seen in Fig. 4.2.

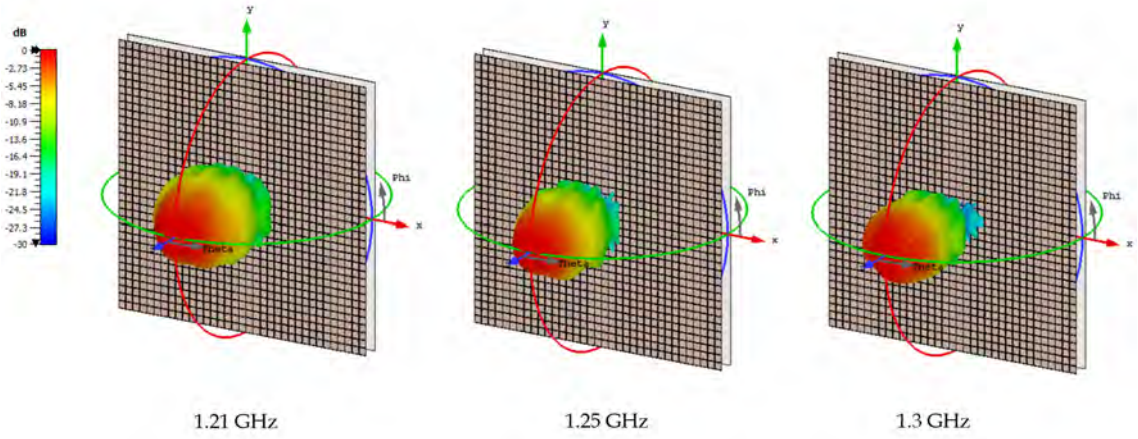

Fig. 4.6. 3D radiation patterns of the individual element with the grid MTS.

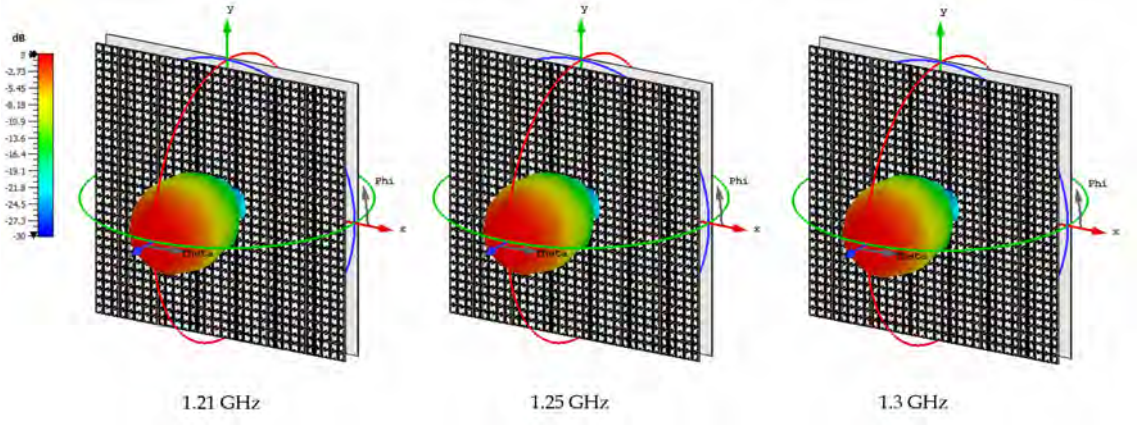

Fig. 4.7. 3D radiation patterns of the individual element with the complementary MTS.

For the evaluation of the planar array, the starting distance between the elements was 1λ at f_0. The total aperture of the MTS and the ground plane is 9λ. For the complementary MTS, and maintaining the height h_{comp} and the same parameters of the patch antenna, the

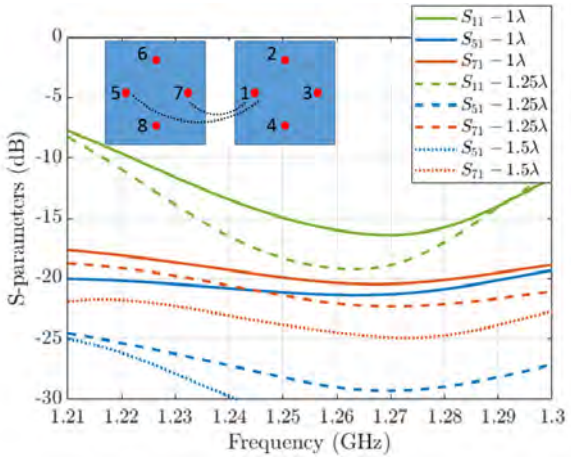

Fig. 4.8. S_{11} and coupling with the neighboring element for the same polarization.

S-parameters are shown in Fig. 4.8 (not combined). Due to the proximity of the elements, the coupling is high.[2] According to [93], the mutual coupling should be lower than -25 dB in order to avoid the deformation of the radiation patterns. Indeed the effect of strong mutual coupling is observed in the embedded radiation patterns of the central element shown in Fig. 4.9. Compared to the pencil beam obtained for the individual antenna seen in the same figure, the performance of the array is significantly degraded.

In order to reduce the mutual coupling, the elements were further separated reaching the maximum inter-element distance allowed by this specific application, that is $1.25\lambda_0$. The coupling between the central element and its closest neighbor, was reduced (Fig. 4.8) which is evidenced in the improvement of the radiation patterns in Fig. 4.9. Although the separation of elements cannot be larger, we have performed simulations to find the minimum distance between the elements where the coupling would not affect the radiation of the array. In particular, it was observed that with $1.5\lambda_0$ between the patch antennas, the coupling (Fig. 4.8) does not affect the radiation (i.e. the embedded pattern is almost identical to the individual pattern in Fig. 4.9). For all the above cases, the simulated cross polarization is practically zero.

An additional disadvantage of the array with the complementary MTS, is the level of dielectric losses that is higher than the specifications of the application (1 dB), due to the thickness of the dielectric layer (2mm-FR4) between the top and bottom metallic

[2]The final coupling between differential ports must be evaluated by calculating these parameters.

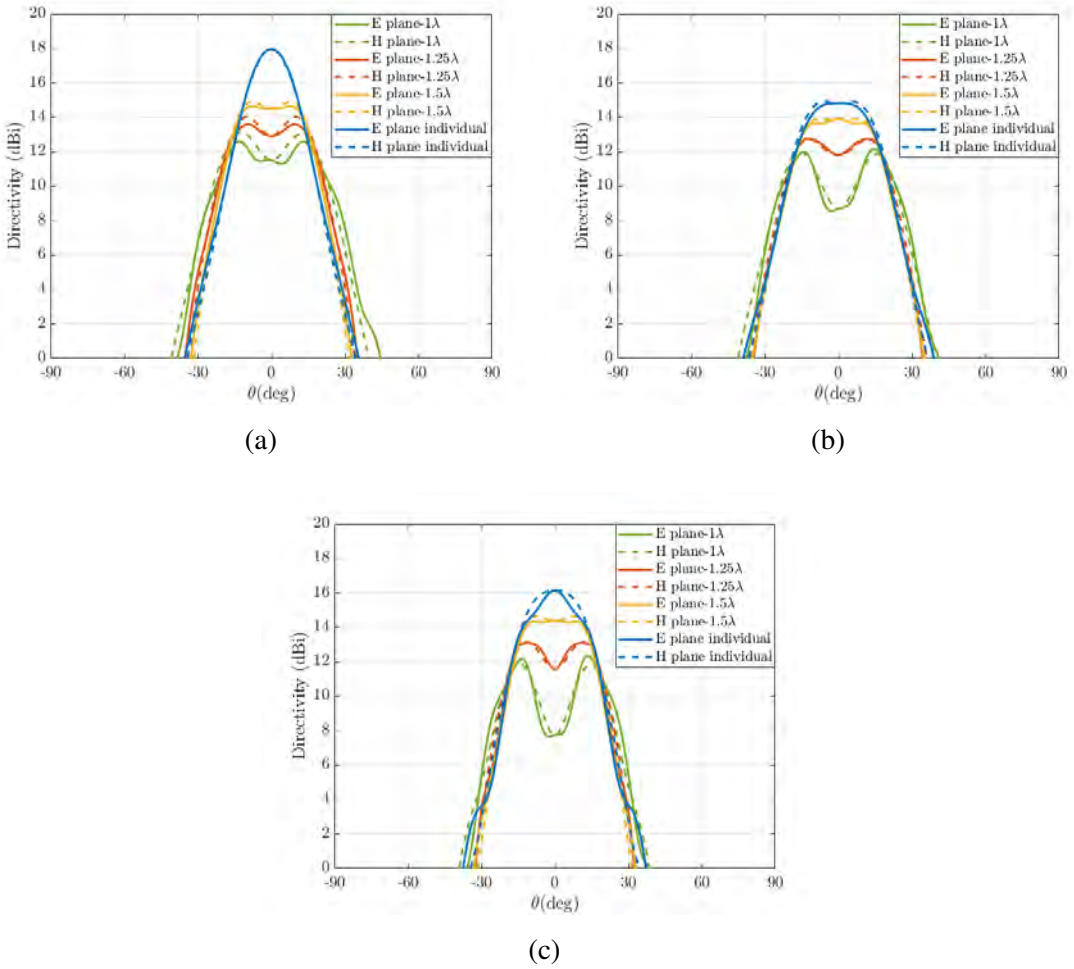

Fig. 4.9. Radiation pattern of the embedded element (in a 3x3 array) with the complementary MTS for three different inter-element distances, compared to the individual element at: (a) 1.21 GHz, (b) 1.25 GHz, (c) 1.3 GHz.

patterns. The grid MTS does not require a thick dielectric layer, hence it exhibits lower dielectric losses, consisting a preferable solution for the realization of the leaky-wave array prototype. The results of the design with the grid MTS will be thoroughly presented in the following sections.

4.3.2 Magneto-electric dipole antenna

Aiming to fulfill the requirement of impedance matching below -20 dB, with low mutual coupling at the same time, one more antenna design was studied and evaluated as an individual element as well as in a planar array configuration. Said antenna is the MTS fed by a magneto-electric (ME) dipole that belongs to the category of complementary antennas.

This type of antennas was introduced in 1954 by Clavin [100]. The initial design consisted of an electric dipole and a coaxial line left with an open end, with the TE_{11} mode propagating, which performed like a magnetic dipole. It demonstrated that when two complementary sources are excited simultaneously with equal amplitude and proper phase, then unidirectional radiation patterns can be obtained, with identical E-H planes and reduced back radiation. In Fig. 4.10 the combination of an electric and a magnetic source is illustrated. Following this concept, other works based on the monopole/dipole and slot combination were presented in [101], [102]. A few years later, in 1974 [103], Clavin presented an improved version of the same idea; the complementary antenna consisted of a slot on a ground plane and two inverted L-shaped parasitic wires on its sides. The slot was used to perform like a magnetic dipole, whereas the L-wires had the role of a electric dipoles.

Based on the same concept, the magneto-electric dipole antenna was presented in [104]. The authors reported wideband performance, low cross-polarization and low back radiation, as well as symmetrical E-H planes radiation patterns. The antenna consisted of a $\lambda_0/2$ electrical planar dipole, and a $\lambda_0/4$ shorted patch vertically oriented and performing as a magnetic dipole. This design has attracted the interest of researchers with many designs found in literature [105]–[108]. Furthermore, these antennas have been reported to have

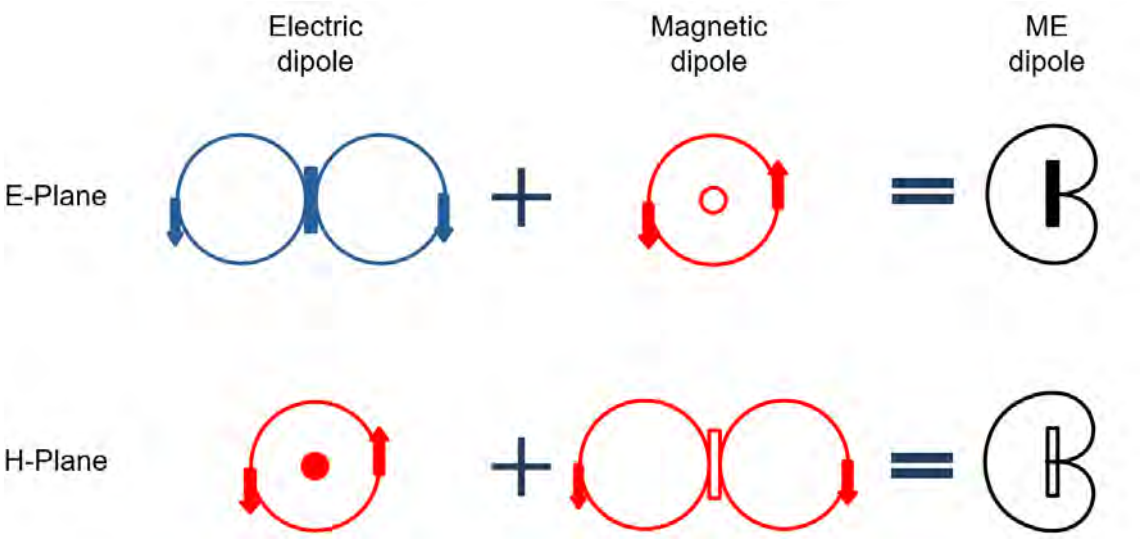

Fig. 4.10. Radiation in the two planes of a magneto-electric dipole.

reduced mutual coupling when placed in an array [103].

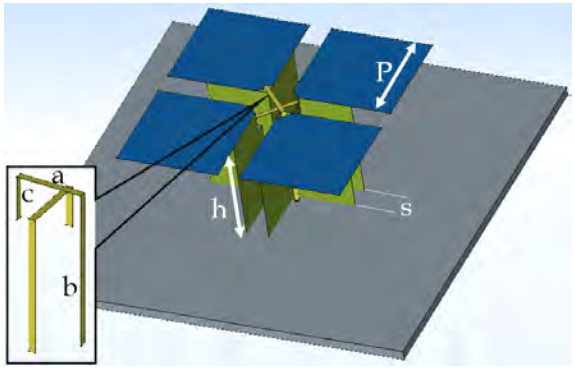

Fig. 4.11. The magneto-electric dipole antenna. The inset shows the feeding lines.

The chosen topology of the ME dipole is shown in Fig. 4.11 and follows the dual-polarized design presented in [109]. The upper part of the antenna consists of two square-shaped electric dipoles of side approximately $P = 0.25\lambda_0$. The vertical walls are the magnetic dipoles of height $h = 0.25\lambda_0$. The separation between the vertical walls should be $s = 0.05\lambda_0$ [109]. Two Γ-shaped probes are used to feed the antenna. They are made of a folded metallic strip line of width w, that consists of three parts, as seen in the inset of Fig. 4.11. With "a" is denoted the upper horizontal part of the probe, that is responsible to couple the energy to the shorted patch and planar dipole. The connection to the SMA-coaxial feed is denoted with "b". The third part "c" is an open ended transmission line and enters the ME dipole vertical wall. This part presents a capacitive reactance, and is used to

compensate the horizontal "a" part that is inductive [104]. The feeding lines have different height to increase the isolation between the two ports [109].

The performance of the ME dipole when used to feed the leaky-wave antenna, was evaluated as an individual element as well as in a 3x3 array, for the two MTS cases: with the inductive grid, and the complementary MTS. When using the ME dipole as a feed antenna, there is no need for a differential feeding like in the case of the patch antenna that was presented. Therefore, the absence of the differential microwave circuit simplifies the design.

Initially, the dipole was combined with the grid MTS to form a leaky-wave antenna. After a parametric procedure, satisfying return loss levels were obtained. As seen in Fig. 4.12 the result for both ports is below -15 dB at the central frequency 1.25 GHz, for the following parameters: P = 51.2 mm, h = 51.2 mm, s = 8 mm, a = 24 mm, b_1 = 62.2 mm, b_2 = 50.2 mm, c_1 = 22.4 mm, c_2 = 42.2 mm and w = 1.9 mm, when the resonant cavity has a height of 103.5 mm. The corresponding 3D radiation patterns are presented in Fig. 4.13. The symmetrical shape of the beam in both planes is evident. The directivity reaches 15.1 dBi at f_1 = 1.21 GHz, 16.3 dBi at f_0 = 1.25 GHz, and 15.3 dBi at f_2 = 1.3 GHz. Since the performance of the ME dipole is symmetrical for both ports, only the results of port 1 are represented in Fig. 4.13.

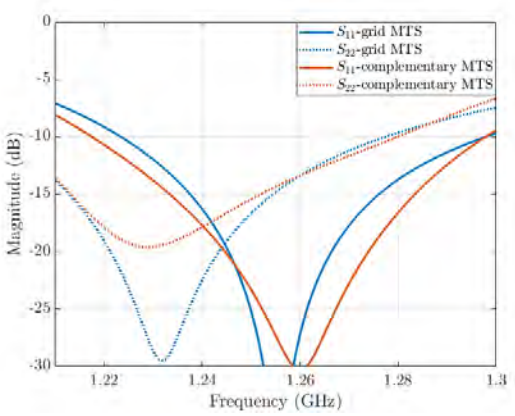

Fig. 4.12. Impedance matching of the ME dipole in a leaky-wave antenna made of: an inductive grid MTS (blue lines), a complementary MTS (red lines).

If the grid is replaced by the complementary MTS, the radiation characteristics of the antenna should be the same. In Fig. 4.12 good impedance matching is obtained for both

ports, showing that this radiation source has potential when it comes to low return loss. Since the impedance of the two MTSs is different, the parameters of the ME dipole should be re-adjusted to center its response. For the presented results, the parameters that change with respect to the ones reported for the grid case, are the following: P = 53.2 mm and c_2 = 49.2 mm. The 3D radiation patterns can be seen in Fig. 4.15. The directivity is 18 dBi at f_1 = 1.21 GHz, 16.1 dBi at f_0 = 1.25 GHz and 16.6 dBi at f_2 = 1.3 GHz. Both ports have symmetrical radiation patterns as expected (Fig. 4.14).

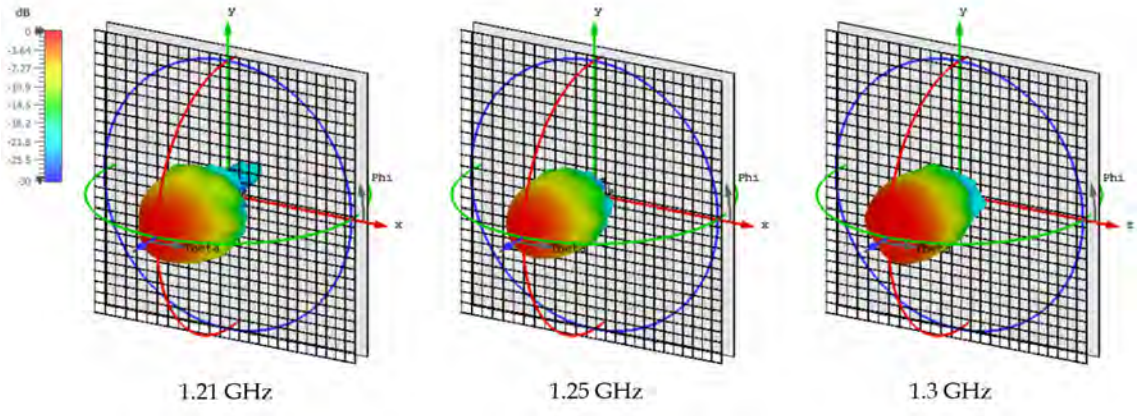

Fig. 4.13. 3D radiation patterns at three frequencies for the ME dipole with the inductive grid MTS.

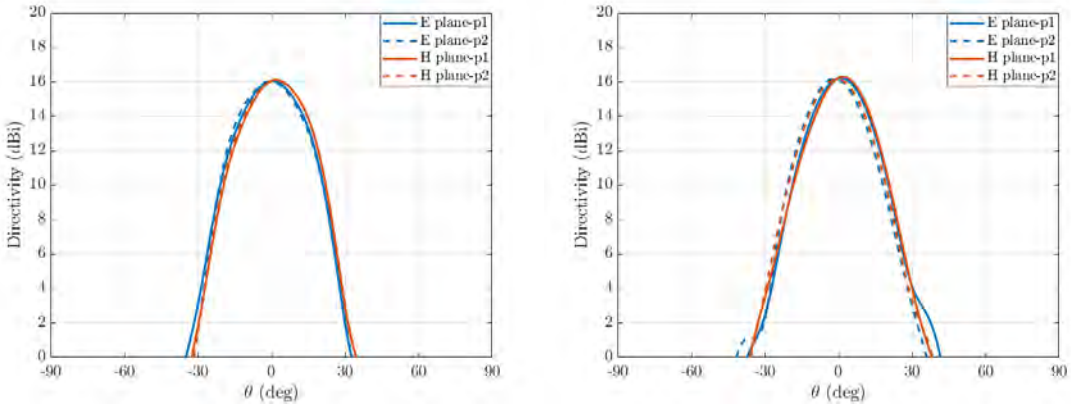

(a) (b)

Fig. 4.14. At the central frequency, the individual element has symmetrical radiation patterns at both planes and for both ports, here presented in the case of (a) the complementary MTS, and (b) the grid MTS.

After studying the performance of the leaky-wave individual element with the ME dipole as a radiation source and for the two cases of the MTS, the next step is the incorporation of the design in a 3x3 planar array to calculate the embedded radiation pattern.

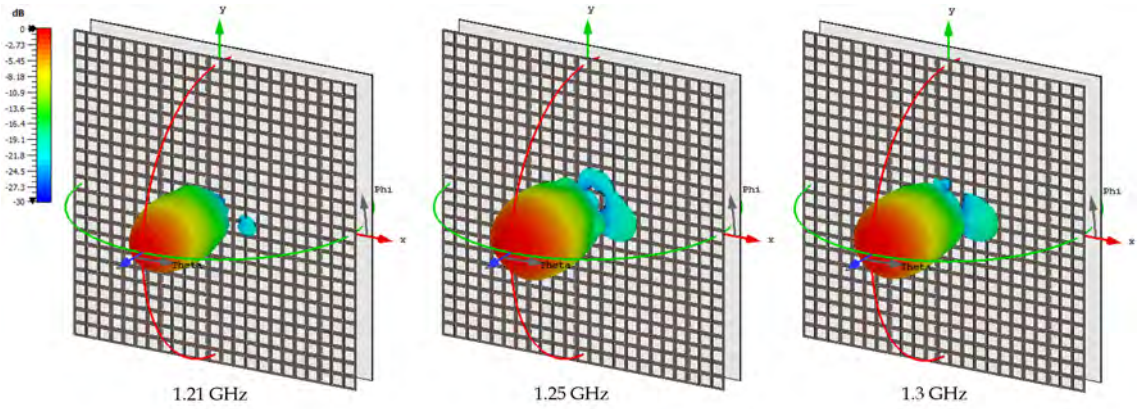

Fig. 4.15. 3D radiation patterns at three frequencies for the ME dipole with the complementary MTS.

Let us consider the complementary MTS and a 3x3 ME dipole array, with inter-element distance $1\lambda_0$ at $f_0 = 1.25$ GHz. For the aforementioned parameters of the ME dipole, the S_{11}, S_{22} of the central element are presented in Fig. 4.16(a). In the same figure, the mutual coupling with the near neighboring elements of the same polarization can be seen. Since the inter-element distance is small, the coupling is high enough to deteriorate the performance of the array, reaching a maximum of -18 dB, when according to [93] it should be less than -25 dB. As a consequence, an undesired ripple is apparent in the embedded radiation patterns in Fig. 4.17, indicating the strong mutual coupling.

Consequently, the next step was to further increase the inter-element distance, reaching the limit set by the requirements of the application $1.25\lambda_0$. The S-parameters are presented in Fig. 4.16(b). The mutual coupling in this case has decreased and reaches a maximum of -20 dB. The corresponding radiation patterns can be seen in Fig. 4.17. Due to the reduced coupling, the ripple at broadside has decreased. Nevertheless, even a small defect in the radiation pattern in the feed array can lead to significant deterioration of the reflector performance. Therefore, this array of leaky-wave elements composed of a planar array of ME dipoles and the complementary MTS, does not qualify as a candidate for the application under study.

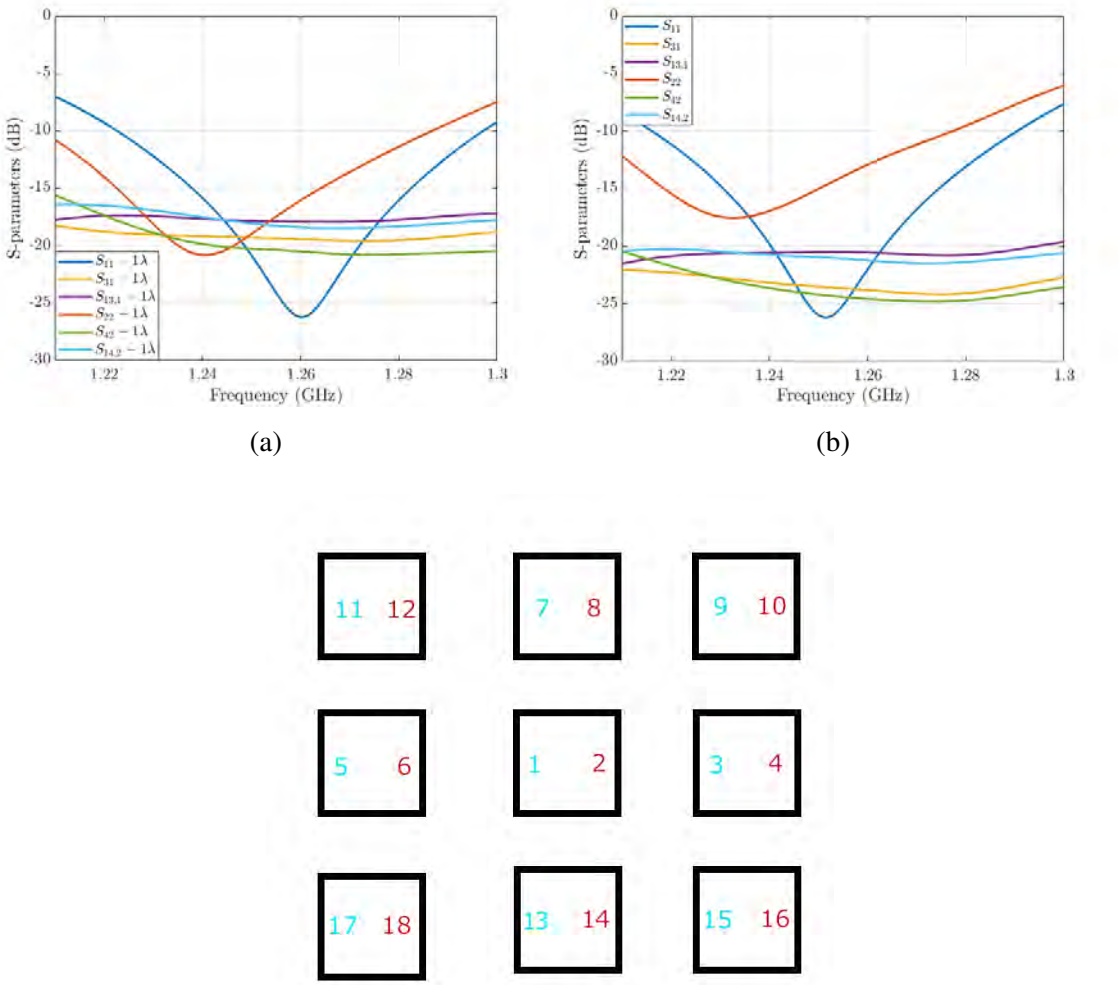

(a) (b)

Fig. 4.16. S-parameters of the central element of the 3x3 array and examples of the coupling with its near neighbors for distance: (a) $1\lambda_0$ and (b) $1.25\lambda_0$. The configuration of the array is also presented.

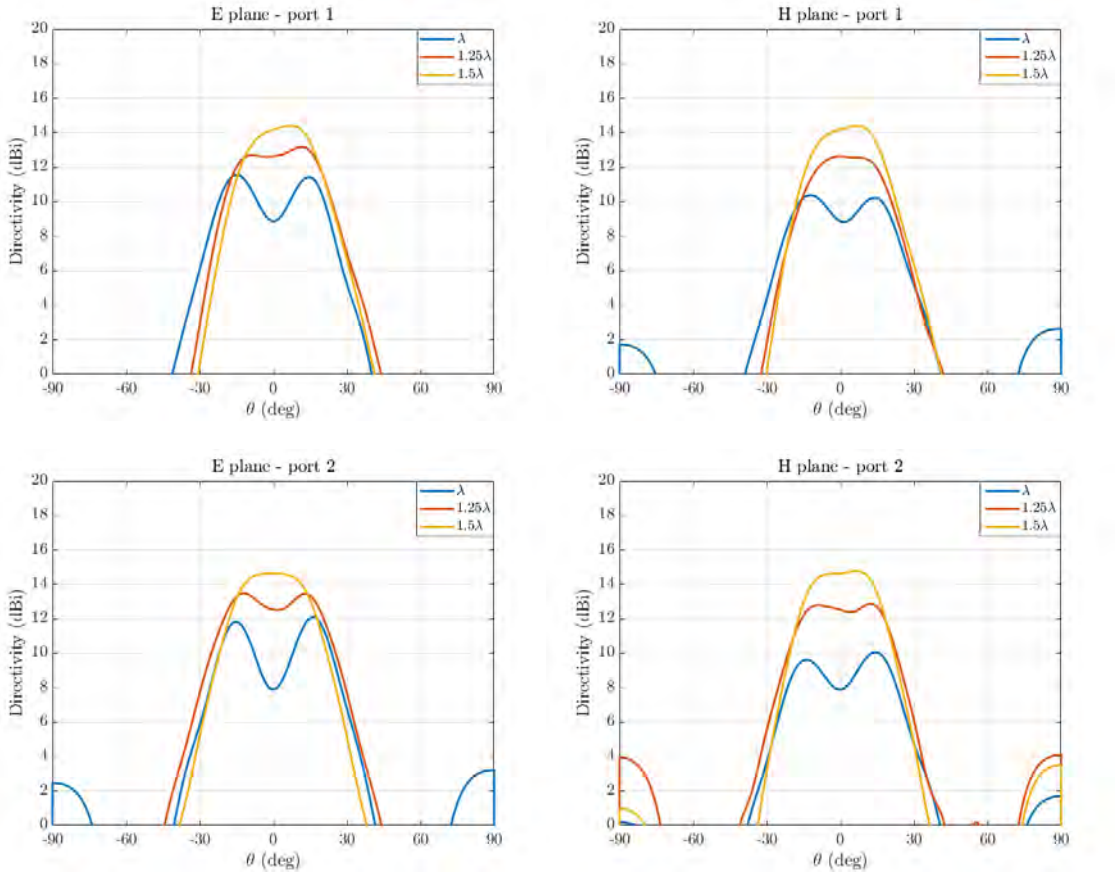

Fig. 4.17. Embedded radiation patterns of the 3x3 ME dipole-based leaky-wave array made with the complementary MTS, for three different inter-element spacings and at the central frequency 1.25 GHz.

However, as a proof of concept, the results of the array with inter-element spacing $1.5\lambda_0$ are also reported for comparison. For this spacing, the mutual coupling is below the required -25 dB and thus the radiation patterns are not affected as shown in Fig. 4.17.

While both MTSs have been used to implement the array, we present only a brief comparison with the grid MTS, for a spacing of $1.25\lambda_0$ in Fig. 4.18. Given the proximity of the elements, the results of mutual coupling and radiation patterns are similar with the ones of the complementary MTS.

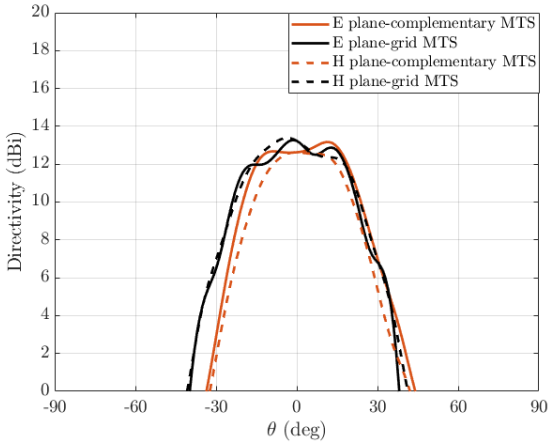

Fig. 4.18. Comparison of the embedded pattern at 1.25 GHz, for the grid MTS and the complementary MTS fed by the ME dipole.

In conclusion, the ME dipole shows promising results for the achievement of good impedance matching, even at the order of -20 dB. In addition, although the ME dipole antenna has a more complicated design than the patch antenna shown before, it achieves low cross polarization levels without requiring a differential feeding network. However due to the limitations of the inter-element spacing enforcing a maximum of $1.25\lambda_0$, the strong mutual coupling affects significantly the radiation patterns of the array, independently of the MTS used to create the leaky-waves. Therefore, this solution is unsuitable for the specific application it would be designed for.

4.4 Results

4.4.1 Simulations of the fabricated prototype

In this section, the final results of the simulated array are presented. All the simulations were executed with CST Microwave Studio.

The design that was chosen to be implemented is composed of a 3x3 array of differential patch antennas, and the inductive grid MTS. The spacing between the elements is $d = 1.25\lambda_0$, and after simulations the final ground plane size was chosen to be $L = 9\lambda_0$. However, due to the low frequency of operation ($f_0 = 1.25$ GHz), a ground plane of $9\lambda_0$ would result to a very large prototype (almost $2m\ x\ 2m$), and was not considered feasible for the stage of experimental validation. Therefore, the prototype was scaled to the double central frequency $f_{sc} = 2.5$ GHz, and therefore the new band is 2.4 GHz to 2.6 GHz. The MTS was scaled uniformly without a change of performance, resulting to a total physical aperture of approximately $1m^2$.

Initially, a single differential patch antenna was simulated with the grid MTS on top. While to feed the antenna with a phase difference of 180^o between its two ports initially a post processing was used for the simulated results, instead in this stage a microwave circuit was simulated with the array. For the parameters shown in Table 4.2, the S-parameters of the antenna are presented in Fig. 4.19. The return loss is at sufficiently low levels for both ports although it doesn't reach the -20 dB required, and the coupling between the feeding patches of the antenna (isolation level), is practically zero.

p_1	p_2	p_3	h_1	h_2	d	x
48.5	11.5	46	6.5	10.25	9	12

Parameters of the patch antenna in mm for the scaled array.

Table 4.2. INDIVIDUAL ELEMENT

The starting height of the scaled MTS is 52.75 mm, being the height calculated from Eq. 1.2 as explained before. Since the height affects the impedance it also affects the response of the antenna's return loss. On the other hand, the change of height has an

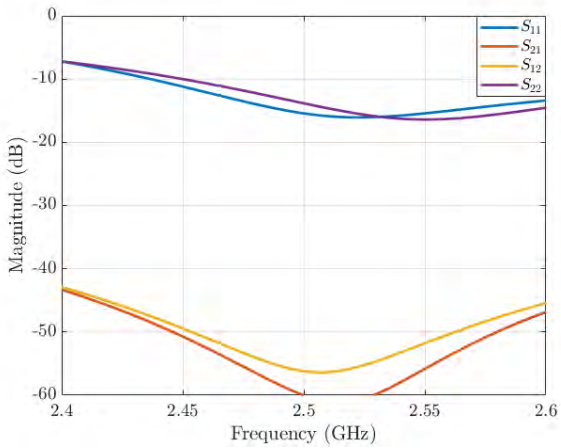

Fig. 4.19. S-parameters of the individual antenna.

impact on the radiation patterns of the antenna. Thus, the optimization of the height should take place considering the effect on the radiation pattern. Once the height is fixed, then the parameters of the source antenna are re-adjusted to achieve impedance matching. The resulting height of the inductive grid MTS is $h_{sc} = 51$ mm.

Fig. 4.20 shows the radiation patterns of the individual element, at the three frequencies of interest. Pencil beams are observed, almost symmetrical for the two planes as expected for this type of leaky-wave antennas. The maximum directivity is 15.8 dBi at $f_{sc} = 2.5$ GHz and the realized gain at the same frequency is 14.6 dB. The values of both the directivity and gain at the three frequencies are presented in Table 4.3.

	Port 1			Port 2		
Frequency (GHz)	2.4	2.5	2.6	2.4	2.5	2.6
Directivity (dBi)	15	15.8	14	15	15.8	14
Realized Gain (dBi)	12.5	14.6	12.7	12.4	14.4	12.7

Directivity and realized gain of the two ports of the individual element with the inductive grid MTS.

Table 4.3. INDIVIDUAL ELEMENT

Afterwards, the array was simulated, using the same MTS and placed at the same height above the ground plane, as in the case of the individual element. For the central element, the S-parameters are presented in Fig. 4.21. We have chosen to excite only the central

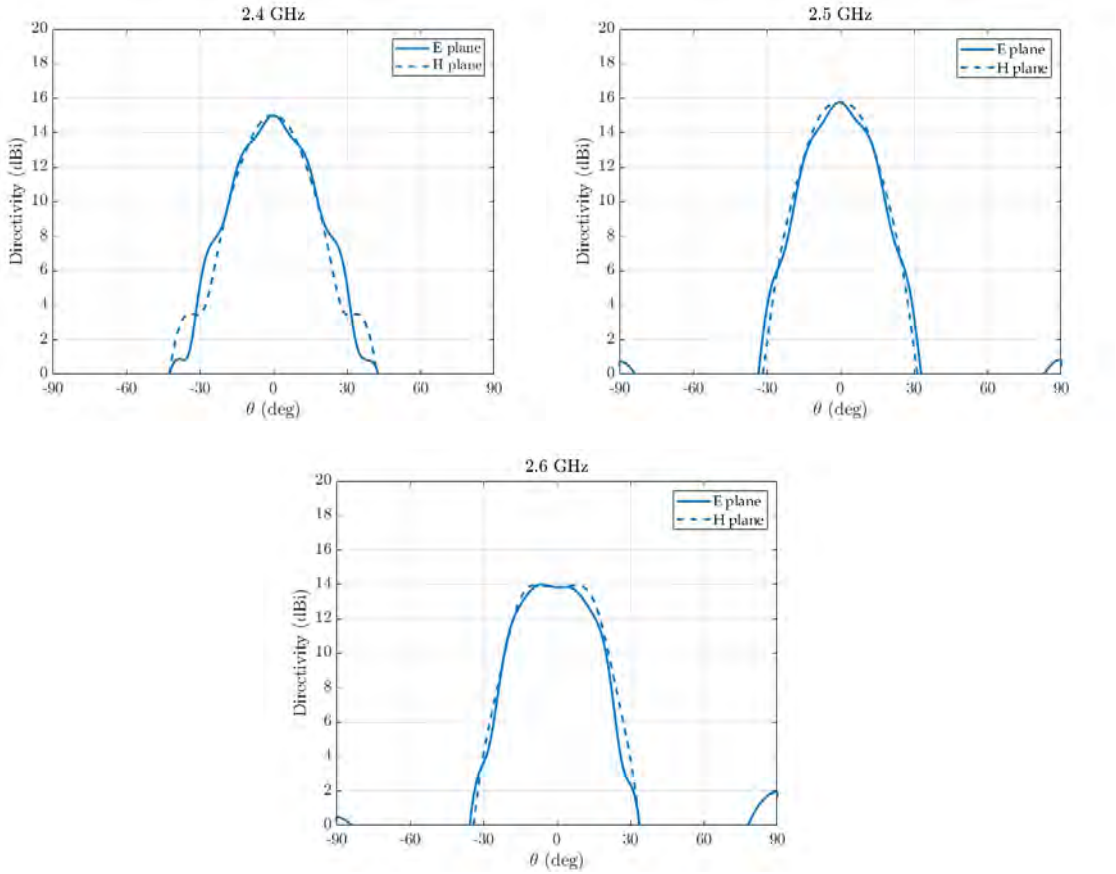

Fig. 4.20. Radiation patterns of a single patch antenna with the inductive grid MTS at the three frequencies of interest.

element of the array, while the others are considered connected to matched loads. The coupling between the neighboring elements and the central one, is presented in Fig. 4.22. This coupling corresponds to the excitation with the differential circuits in the simulation of the array. For both ports, the coupling is maintained below -20 dB. However this is not sufficient to ensure good radiation patterns. Indeed, in Fig. 4.23 the effect of coupling on the embedded radiation patterns is apparent. For instance, the beam formed at 2.5 GHz, where the coupling is close to -20 dB, presents a ripple that can lead to significantly reduced performance when combined with a reflector.

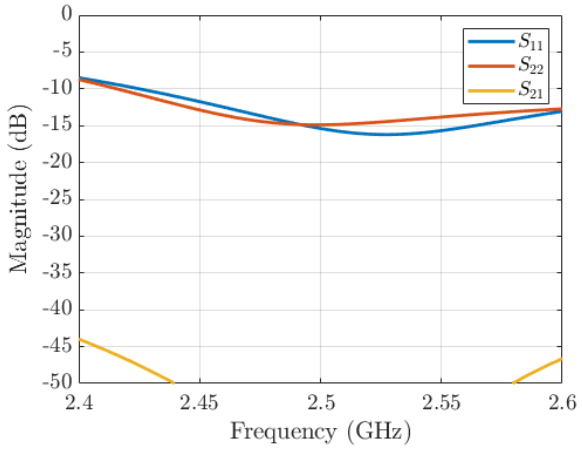

Fig. 4.21. S-parameters of the central element of the 3x3 array.

The directivity reached at 2.5 GHz is 11.8 dBi for the broadside direction ($\theta = 0^o$), while the maximum is 13 dBi, indicating a ripple of 1.2 dB. At the same frequency, the realized gain is 10.5 dBi. Detailed values of directivity and realized gain at each frequency are presented in Table 4.4. In the same Table, the taper at 27^o is also denoted. Since the directivity does not reach 16 dBi, the array does not meet the -12 dB taper requirements of the application. The 3D radiation patterns can be seen in Fig. 4.24. Let us comment here that with a higher permittivity equivalence for the MTS, higher directivity would be achieved in the individual element. Nevertheless, in the array this would result to higher coupling between the elements, and would therefore deteriorate more the performance of the array. Consequently, the permittivity equivalence was maintained as $\epsilon_r = 5$.

However, if the application would allow for larger separation between the array elements such as $1.5\lambda_0$, the coupling would be lower thus leading to improved performance.

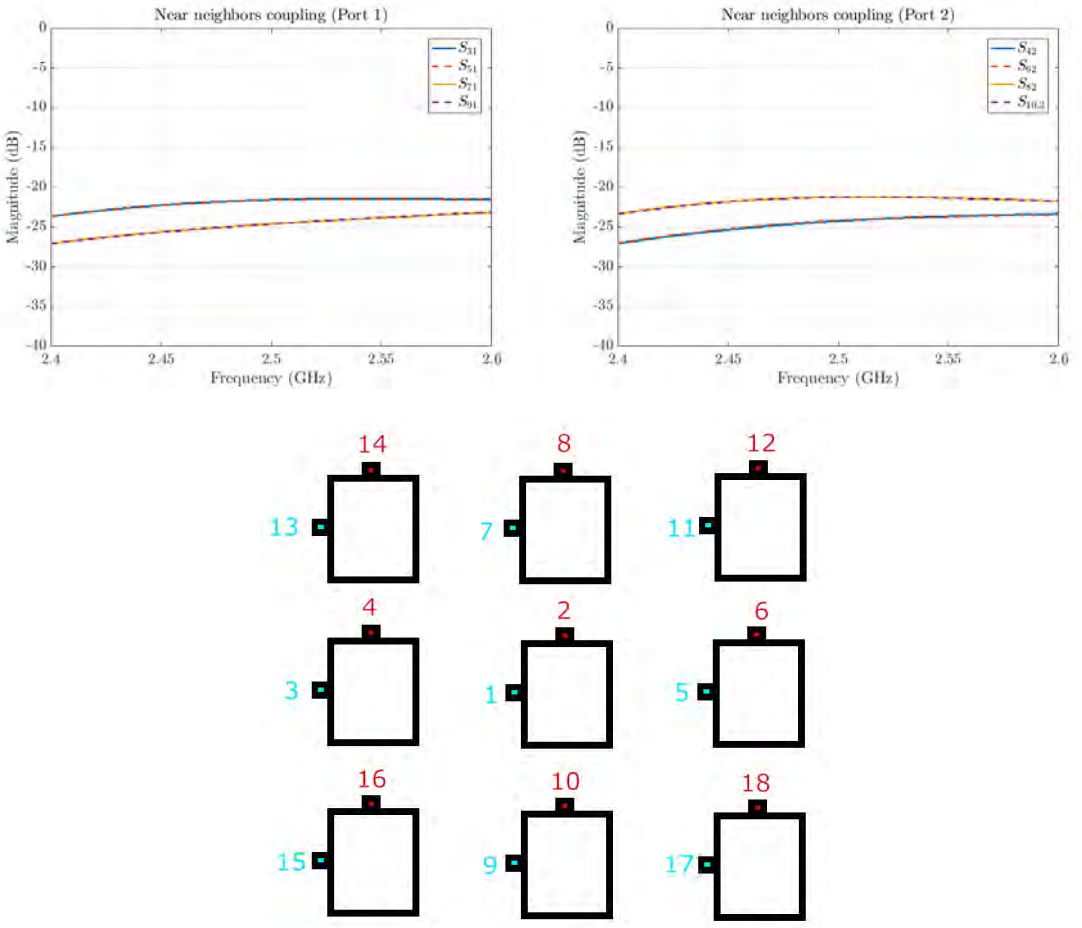

Fig. 4.22. Coupling between the central element and its neighbors for both excitation ports. The configuration of the elements in the array is also shown.

For this case, the results of the directivity at the central frequency are presented in Fig. 4.25.

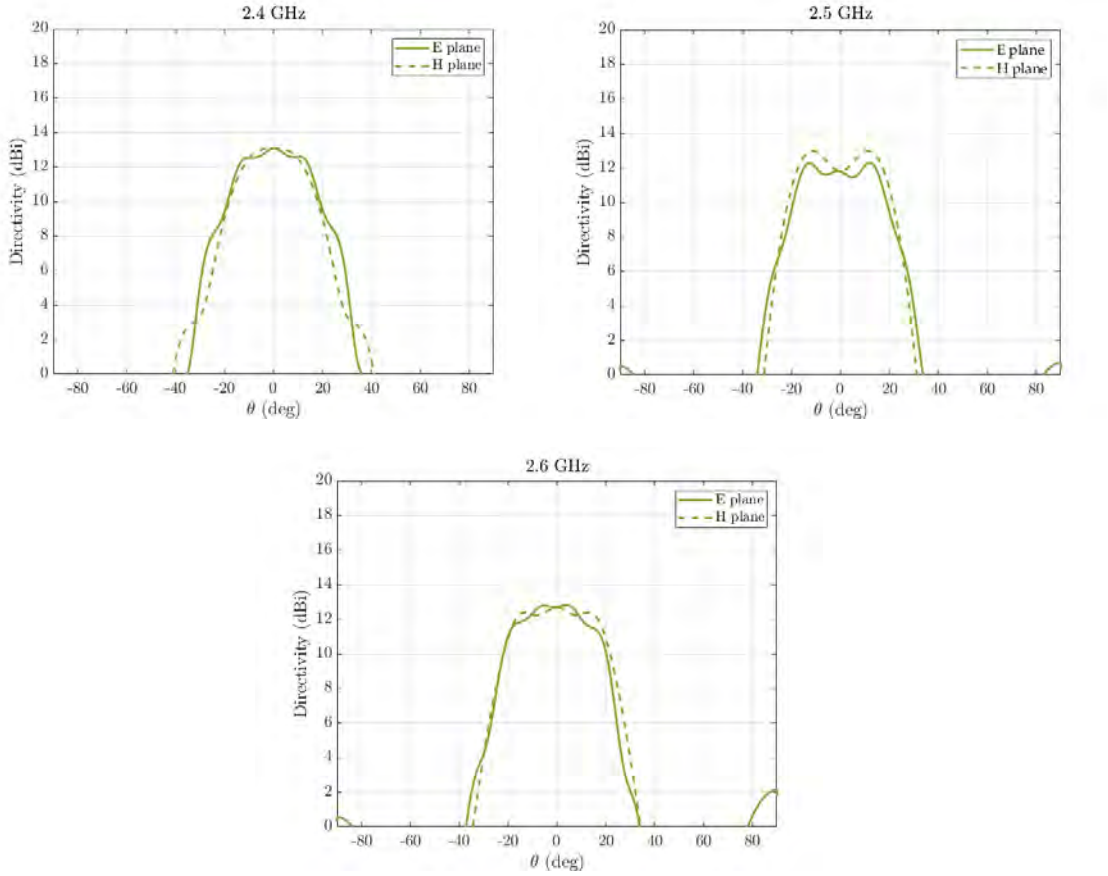

Fig. 4.23. Embedded radiation patterns of the array at the three frequencies of interest.

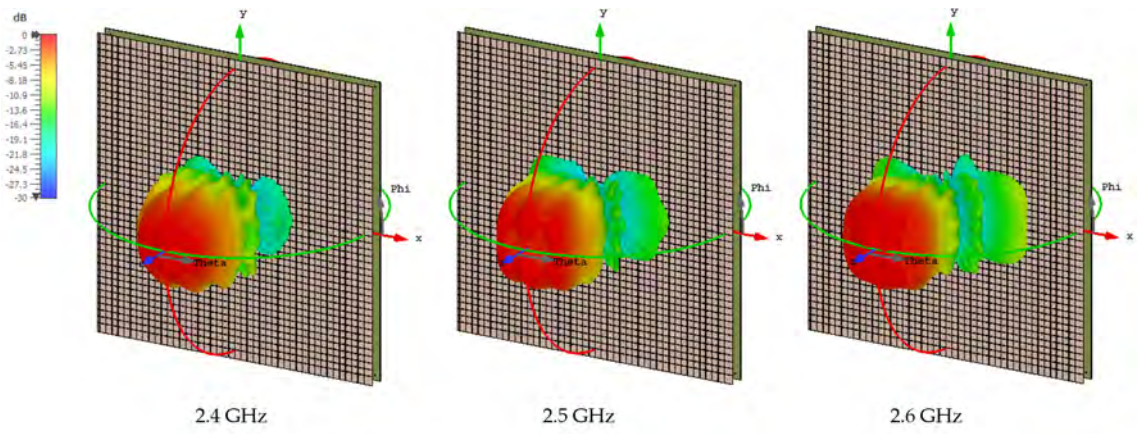

Fig. 4.24. 3D radiation pattern of the array at 2.4 GHz, 2.5 GHz and 2.6 GHz.

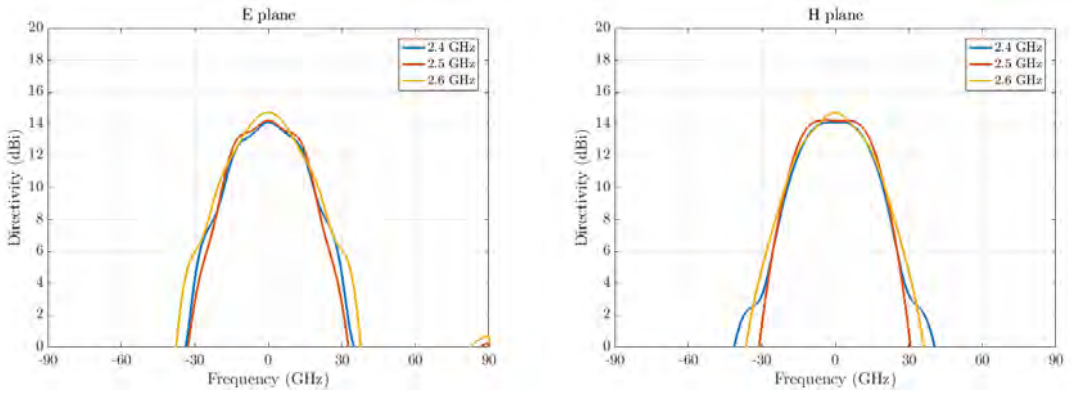

(a) (b)

Fig. 4.25. Radiation patterns for inter-element distance $1.5\lambda_0$ for (a) the E plane and (b) the H plane.

4.4.2 Experimental validation

In order to validate the simulated performance of the array, a prototype was manufactured and the experimental results are presented in the current section.

Due to its large size, the MTS was fabricated in two pieces, that were then soldered together. The metallic grid was printed on top of an FR4 layer of thickness 0.765 mm. The effect of the thickness of the FR4 on the embedded radiation patterns and the matching of the central antenna was studied before choosing this value, since it affects the impedance of the MTS. A smaller thickness would be preferable, however since the MTS is very large, the chosen value was considered sufficient to create a robust prototype. The same material was used to fabricate the patch antennas, in this case, with thickness 0.4 mm for both the upper patch and the feeding patches.

Fig. 4.26 shows the back side of the prototype, where the feeding circuits are connected, having a spacing between them of 2.67 cm that is enough to connect the cables of the network analyzer. Each circuit was measured separately to ensure that their performance validates the simulations. The differential patch antenna is presented in the same figure. The top patch that is responsible for the radiation is removed and the four feeding patches are revealed printed on FR4. In addition, the positions of the other elements can be also seen.

Fig. 4.26. On the left: the back side of the ground plane of the array, where the microwave circuits are located. On the right: the central element is shown with the top patch removed (shown at its side) for the feeding patches to be revealed. The locations where the other elements of the array will be placed, are also visible, with the central metallic ring.

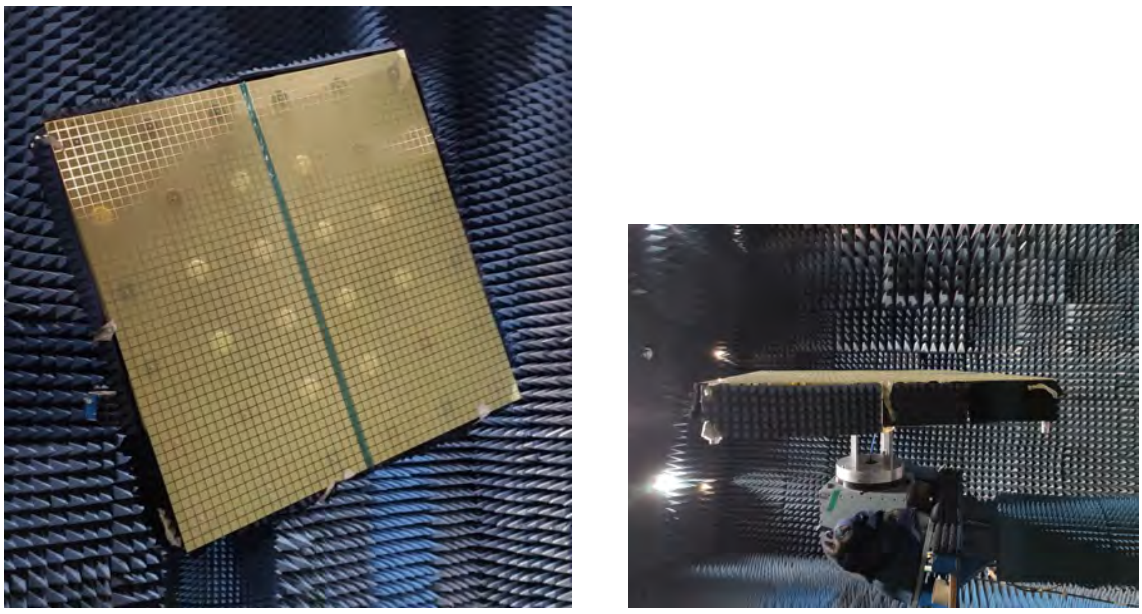

Fig. 4.27. The $1m^2$ fabricated prototype in the Airbus anechoic chamber. The absorbers placed around the prototype can also be seen (right).

The array was measured in the anechoic chamber of Airbus (Fig. 4.27). An additional metallic piece was fabricated to mount the prototype on the positioner in the anechoic chamber. The 1x1 m^2 MTS was held above the ground plane at the calculated height, with 36 posts made with 3D printing that can be seen in Fig. 4.27(left). Furthermore, an absorber was placed around the antenna. After simulations, it was evident that improved results were obtained with an absorbing material around the antenna (conditions "*open*" in CST), compared to the case without an absorber (conditions "*add space*" in CST).

The measured S-parameters of the central element are shown in Fig. 4.28. The return loss is maintained below -10 dB from 2.4 GHz to 2.6 GHz, with the lowest being around the central frequency. However, the requirement of -20 dB for the whole frequency band, is not fulfilled. The measurements are in good agreement with the simulated results presented in the previous section. Moreover, the isolation between the two ports is very high (S_{21}<-35 dB).

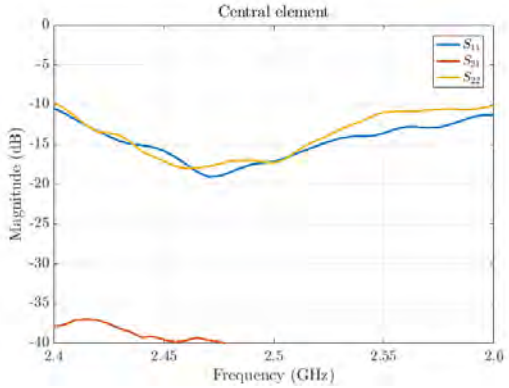

Fig. 4.28. Measured S-parameters of the central element.

Regarding the coupling, the results for the near neighboring elements are presented in Fig. 4.29. As expected from the simulations, the coupling is not lower than 25 dB, thus the radiation patterns will be affected. The coupling with the farther elements is very low, as well as the coupling between the closest neighbors of different polarizations (Fig. 4.30), satisfying the requirement of -30 dB isolation.

In Fig. 4.31 the measured radiation patterns are compared with the simulated results. The simulated individual element is also plotted for comparison. In the same figures the cross-polarization is shown and compared with the simulations. The requirement for cross-

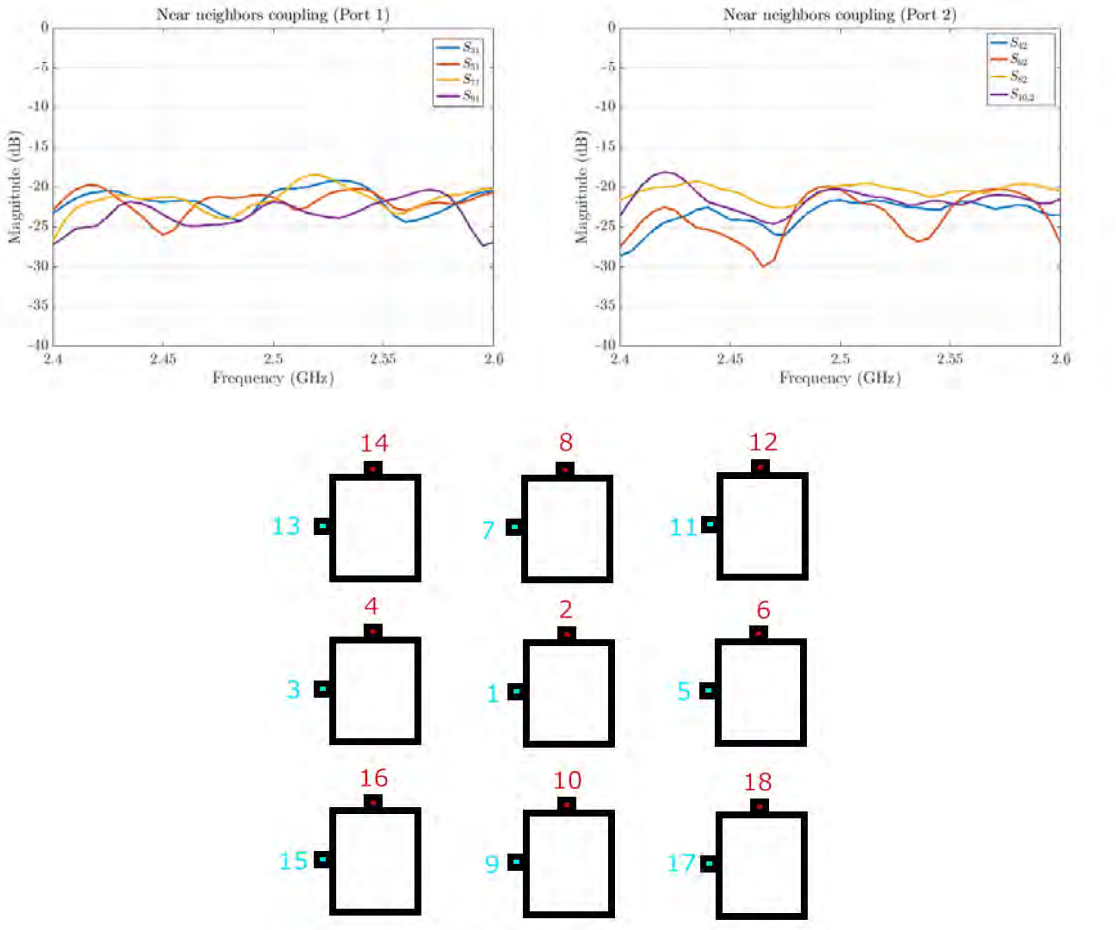

Fig. 4.29. Measured coupling of the near elements to the central antenna.

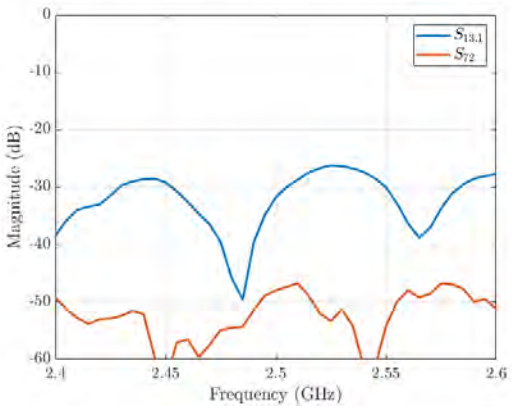

Fig. 4.30. Example of coupling between the central element and its far neighbors ($S_{13,1}$), and coupling between the two polarizations.

polarization below -30 dB is fulfilled. However, the ripple in the radiation patterns follows the simulations. The resulting radiation patterns of both feeding ports are symmetrical, thereby only the results for one port are presented here. Table 4.4 shows in detail the maximum directivity and realized gain for both feeding ports.

	Port 1			**Port 2**		
Frequency (GHz)	**2.4**	**2.5**	**2.6**	**2.4**	**2.5**	**2.6**
Simulated results						
Directivity (dBi)	13.1	13	12.8	13	13	13
Realized Gain (dBi)	11	11.6	11	10.8	11.6	11.2
Taper-E (dB)	-5.5	-6	-9.2	-8.2	-7.9	-6.7
Taper-H (dB)	-8.5	-7.7	-6.2	-5.4	-6.4	-7.7
Experimental results						
Directivity (dBi)	13.6	13.4	13.9			
Realized Gain (dBi)	11.1	11.5	11.9			
Taper-E (dB)	-6	-6.6	-10	-6.3	-6.8	-6.2
Taper-H (dB)	-8.1	-8.6	-6.5	-9.3	-9	-7.3

Table 4.4. ARRAY SIMULATED AND MEASURED RESULTS

4.5 Conclusions

In this chapter, the concept of Fabry-Pérot leaky wave antennas made by metasurfaces, has been used to implement a planar array. The array was developed as a candidate for the feed array of a large reflector used for a SAR system for Earth observation in the L-band.

Following the strict specifications of the application such as low return loss, low cross polarization with limitation in the spacing between the elements, several approaches to the design of the feed array have been presented. For the excitation of the leaky-waves in the resonant cavity, two antennas were proposed: a differentially fed patch antenna [97]–[99], and a magneto-electric dipole antenna [109], both being dual-polarization antennas. The

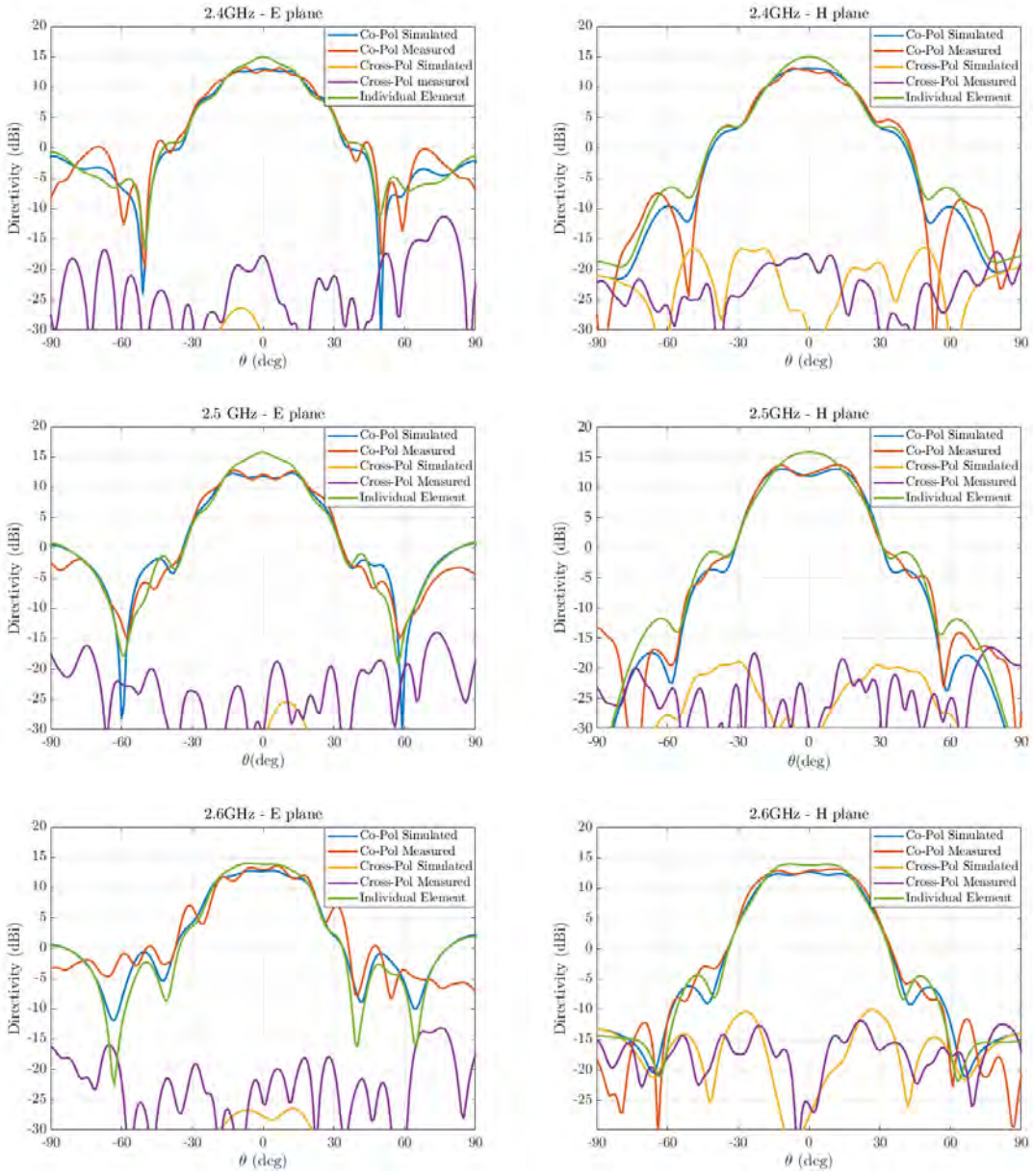

Fig. 4.31. Radiation patterns of the presented array: simulations and measurements of co-pol. and cross-pol., compared with the simulated individual element.

first consists on four patches that are directly fed by a microwave circuit that provides 180^o phase difference to the couplers by pairs. Then the energy is coupled to the patch that radiates inside the resonant cavity. For the second antenna, its upper part consists of two square-shaped electric dipoles, while the vertical walls act like magnetic dipoles. This antenna does not need a feed circuit and has a high isolation between ports and low cross-polarization. Both antennas were designed to cover the band 1.215 GHz to 1.3 GHz.

The two excitation antennas were then combined with two types of metasurfaces. The first MTS was a metallic grid printed on top of a very thin FR4 layer. This MTS was designed following the equivalence with a dielectric slab [36], [37] as in previous chapters, that in this case was chosen to have permittivity $\epsilon_r = 5$. This value was chosen according to the required directivity that would result to the specified taper level at 27^o. Therefore, the dimensions and periodicity of the grid were designed to fulfill said equivalence. The second MTS, consisted of a complementary pattern printed on both sides of an FR4 layer. The design of the complementary MTS was done by studying the reflection coefficient of the unit cell to control the directivity achieved, and at the same time by taking under consideration the positive phase gradient required to avoid single frequency resonance [42]. This second MTS provides more bandwidth.

Both MTS were simulated and evaluated with the two excitation antennas as individual elements, and then in a 3x3 planar array configuration to study the embedded radiation patterns. The maximum inter-element distance allowed by the application is 1.25λ. This limitation leads to deformed radiation patterns due to strong coupling between the elements. Additionally, the MTS should be reflective enough to achieve directivity around 16 dBi, in order to fulfill the taper specification (-10 to -12 dB) of the application. However, the more reflective the MTS is, the stronger the coupling becomes and the radiation patterns are more affected. To reduce the coupling we should reduce the reflectivity of the MTS, but then the requirement for the taper would not be fulfilled.

The fabricated prototype consisting on the grid MTS and the differentially fed patch antenna, validated the performance observed in the simulated array model. The inter-element spacing is not enough to achieve the pencil beam radiation patterns otherwise obtained in this type of antennas. The S_{11} was measured to be low, however it did not

reach the value of -20 dB as specified. Nonetheless, the cross polarization was maintained in the required levels. The grid MTS was chosen to be fabricated due to the low losses it exhibits, since the complementary MTS not only presented higher losses, but it did not fulfill the specifications of the application either.

Part II

Design of groove gap waveguide innovative antennas

Chapter 5

Gap waveguide technology

Gap waveguide technology was initially developed based on the principles of soft & hard surfaces [110]. These surfaces have the ability to manipulate the propagation of electromagnetic waves. For instance, in the case of corrugated horn antennas [111], [112], the transversely located corrugations represent a soft surface (i.e. soft horn antenna) [113], depending on their height. When longitudinal corrugations are created and filled with a dielectric material, a hard electromagnetic surface can be made [114]. On one hand, soft surfaces have the ability to prohibit the propagation of waves independently of their polarization [110]. On the other hand, a hard surface has the ability to enhance the propagation of waves [115], again without dependence on the polarization of the EM waves. The research on these electromagnetic materials, eventually resulted to the gap waveguide technology [116].

The basic concept behind the gap waveguide, is the manipulation of the propagation in the desired directions by generating a stop band for parallel plate modes. The aim is to create boundary conditions by using periodic textured structures in order to guide the propagation in the desired directions.

Let us consider two parallel fully metallic plates (perfect conductors-PEC). Between the two plates, there will be always modes propagating, despite the distance between them, due to the fact that Maxwell's equation always have a solution for these boundary conditions. Now if one of the two plates is replaced by a perfect magnetic conductor

(PMC), and the distance is no greater than $\lambda/4$ on the operating frequency [117], no electromagnetic wave can propagate between the two plates [118]. However, if a region of PEC is introduced interrupting the PMC plate (see Fig. 5.1) maintaining the restriction for the height, the electromagnetic waves will propagate along the PEC area, and will be strictly confined there. In addition, as the propagation is mainly in the air, low losses are ensured.

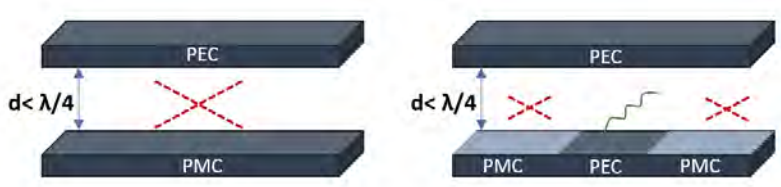

Fig. 5.1. The fundamental concept of gap waveguide technology. No modes can propagate between a PEC and a PMC for $d < \lambda/4$ (left). When the we introduce a PEC zone in the PMC, propagation is supported (right).

Perfect magnetic conductors do not exist in nature. However, high impedance periodic textured surfaces can be used to replicate the equivalent boundary conditions [65], [119]. In the literature, the most common implementation of a high impedance PMC surface, is with a bed of nails [120] made of periodic metallic pins that in a way resemble 2D corrugations, or in other words the cross section of a corrugated surface. The pins can be circular or rectangular without an effect on the stopband that they create, as demonstrated in [121]. Other configurations use mushroom-like patches [65], pin-vias structures [122], springs [123], printed zigzag wires [124], conical pins [125], [126], while most recently, holes on both plates have been demonstrated to be as well a possible candidate for a high impedance surface [127]–[129]. All these alternatives to the bed of nails, create the required parallel-plate stopband that confines the propagating waves in a certain region of the structure.

To guide the electromagnetic waves in the desired direction in the aforementioned configuration (Fig. 5.1), different structures can be used, defining the different versions of gap waveguide. Initially, the ridge gap waveguide [116], [130], [131] was designed, as a result of the research on hard electromagnetic surfaces. Other implementations of gap waveguide are the groove (with a vertical and horizontal polarization version) [132], [133],

the microstrip-ridge [134]–[136] and the inverted microstrip [137]. By using these guiding structures, surrounded with a high impedance surface, the necessary boundary conditions are created in order to have propagation only along the guiding structure, without leakage to other directions. Consequently, with this configuration, a waveguide with virtual lateral walls can be created.

It should be mentioned that studies have been conducted to extend the bed of nails using dielectric materials [138] in order to lead the way to the incorporation of active components in gap waveguide technology. Nonetheless, the dielectric pins would introduce undesired losses and cannot be used for higher frequency bands.

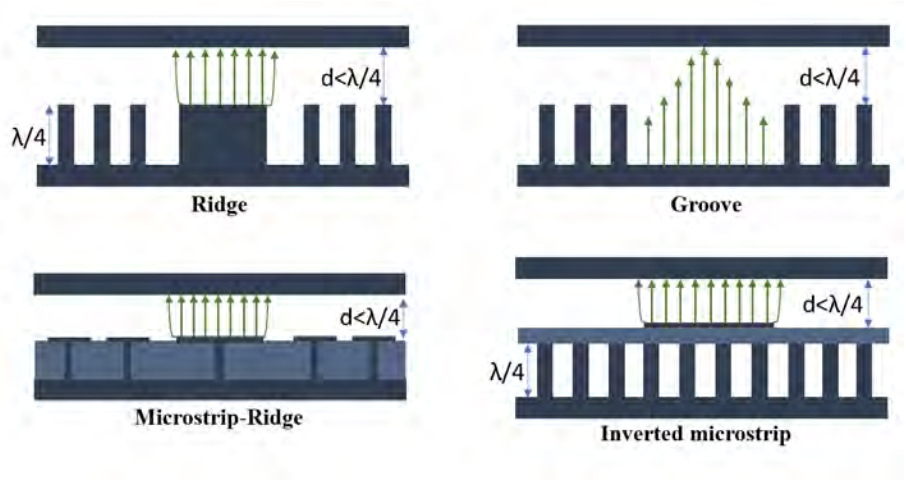

Fig. 5.2. Different versions of gap waveguide technology.

Regarding the operating modes that propagate in each version of gap waveguide, there are some differences [118]. In the case of the ridge and microstrip geometries, a quasi-TEM mode is supported (Fig. 5.2). As mentioned previously, the high impedance surface can be considered as virtual lateral walls. Consequently, in the case of the groove gap waveguide, the geometry resembles a rectangular waveguide, thus TE/TM modes are supported that depend on the cross section dimensions of the groove surrounded by the textured surface. In most cases, the TE_{10} mode is preferred (Fig. 5.2). This mode has a dispersive nature, which can be used to implement leaky-wave antennas for beam-scanning applications. In the following chapters, the dispersive behavior of antennas made in this technology will be discussed.

The advantages of this technology, are a consequence of the boundary conditions that

are created by the described geometry. There are several characteristics that make gap waveguide technology a strong candidate for applications in millimeter-wave bands [139], that continuously attract the researchers nowadays. Compared to the standard rectangular waveguide, in gap waveguide there is no need for direct metal contact between the upper and lower plates and so it can be fabricated in two parts. Nevertheless, leakage of energy is avoided by the high impedance surface boundary conditions. Therefore, the manufacturing is made easier and is cost-effective as well as less time consuming. Furthermore, gap waveguide provides a certain flexibility during the design process and it also allows the design of different fully metallic parts with the same technology, e.g. phase shifters and coupling networks [140]. This technology can be used to avoid dielectric losses and coupling between components in high frequency bands.

In [141] a study of the losses of each type of gap waveguide was conducted. The authors after an experimental procedure reported that the groove version, has losses of the same magnitude level as the standard rectangular waveguide. More specifically, the groove version was reported to have losses practically the same as the rectangular waveguide (0.03-0.04 dB/cm) [141]. In the case of the ridge, its width is smaller than the width of the rectangular waveguide, leading to higher conductor losses due to higher current density on the ridge. As for the other two versions of microstrip gap waveguide, they show more losses, however they perform better in this aspect than regular microstrip lines in high frequencies (e.g. 60 GHz). On one hand, the guiding strips in gap waveguide can have a larger width thus reducing the conductor losses. On the other hand, compared to the regular microstrip, the propagation happens mostly in the air, and so the dielectric losses are significantly reduced.

Each version presents advantages and disadvantages, depending on the application. In the following chapters, the groove gap waveguide will be used for the proposed designs. Initially presented in [132], this type of gap waveguide shows many similarities to the rectangular waveguide, in terms of propagating modes as already discussed. In Fig. 5.3 the electric field distribution is shown, for a TE_{10} propagating mode. The design procedure of the groove gap waveguide, starts with the design of the bed of nails. Although an infinite array of periodic unit cells is considered to study the band-gap, it has been shown that

three rows of pins are enough to avoid the propagation in other directions. Later on this thesis, it will be shown that even two rows are sufficient [142].

In [143] the authors studied the propagation inside the groove and they highlighted the differences with the rectangular waveguide. In the same paper it was demonstrated that they two waveguides have different cut-off frequency. In particular it was shown that the gap waveguide has higher cut-off frequency for a wider groove, which can be translated as effectively smaller propagating aperture than the rectangular waveguide. Moreover, as the width of the groove decreases, the cut-off frequency becomes lower than the rectangular waveguide, meaning that the effective aperture of the groove is larger than the standard waveguide. Lastly, the groove waveguide shows a more dispersive character, which will be discussed later in this thesis.

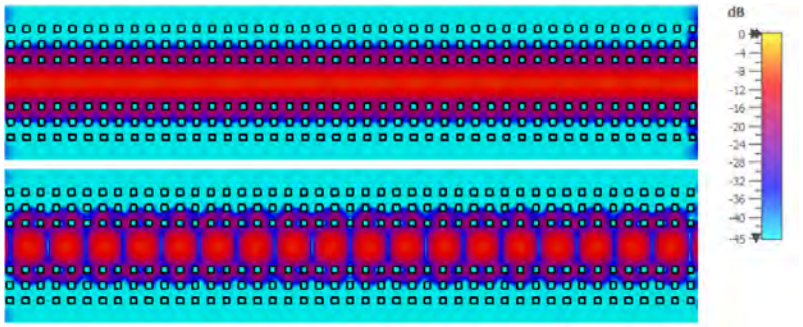

Fig. 5.3. Electric field distribution in the groove gap waveguide (snapshot at the bottom, magnitude at the top) at 10 GHz. Three rows of pins are used to prohibit the propagation outside the groove. It can be seen that the effective width of the groove is larger than the physical width.

With the increasing interest in millimeter-wave frequency bands applications, this technology has caught the attention of many researchers, and many examples of designs can be found in literature. From filters [144]–[147] to feeding networks [148]–[154] and couplers [155]–[157], the different versions of gap waveguide have found many implementations. Antennas have also been developed using the ridge [158], [159], microstrip [160], [161], and groove gap waveguide [162].

In the following chapters, the groove version of the gap waveguide technology, will be used to implement antennas. We have chosen this version of gap waveguide technology because it presents minimum losses, which is an important asset when it comes to

millimeter-wave frequency bands.

The high impedance surface that will be designed to confine the propagation in one region (in the groove), will be made of pins or holes on a metallic plate. The dispersion and characteristics of these pin and holes lattice will be discussed, as well as the band-gap that they create as a function of their parameters. In addition, the groove gap waveguide will be compared to the rectangular waveguide and their similar electromagnetic performance will be demonstrated [163]. This will be done through initial studies based on the rectangular waveguide which then will be replaced by the design of the groove gap waveguide.

5.1 Leaky-wave antenna in groove gap waveguide technology

Leaky-wave antennas are travelling wave antennas, and more specifically fast-travelling wave antennas. According to the *IEEE* definition a leaky-wave antenna is an antenna that couples per unit length energy by small amounts continuously or discretely, from a travelling wave structure to free-space.[3]

The concept of leaky-waves was initially introduced by Marcuvitz in [164], and Hansen [165] was the first to propose the use of leaky-wave structures, such as a slotted waveguide, as antennas circa 1940. After its appearance, the analysis of the leaky-wave antenna has been presented by many researchers employing different methods[166]–[172]. For instance, referred to as *travelling wave slot antennas*, the fields in the slot of a leaky-wave waveguide, were studied in [166], [167] as a two dimensional problem in the same way that a standard rectangular waveguide is also a two dimensional problem. In 1958 Oliner and Goldstone [173] employed a microwave network approach to describe leaky-wave antennas in great detail.

Let us assume a continuous longitudinal slot in a lossless metallic waveguide (Fig. 5.4). As the electromagnetic waves travel in the guiding structure, along the slot, the strength of

[3] "IEEE Standard for Definitions of Terms for Antennas," in IEEE Std 145-2013 (Revision of IEEE Std 145-1993) , vol., no., pp.1-50, 6 March 2014, doi: 10.1109/IEEESTD.2014.6758443.

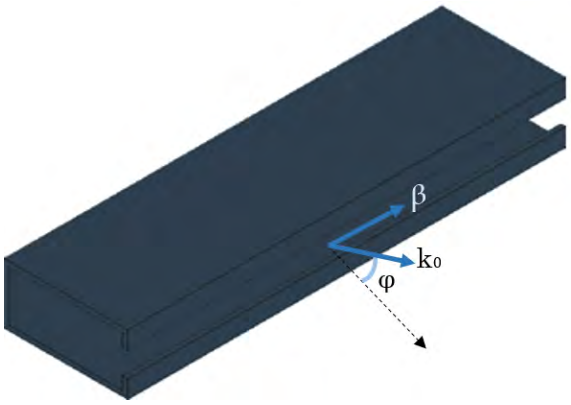

Fig. 5.4. Slotted waveguide. The direction of the propagation constant is shown inside and outside of the waveguide. The direction of the main lobe is represented by the angle ϕ with respect to the broadside direction.

the waves is gradually attenuated due to radiation. The leaky-wave has a phase velocity v_{ph} that is greater than the speed of light c, thus indicating the fast-wave characteristic. It has a complex propagation constant $\gamma = \alpha + j\beta$, where the real part α describes the attenuation of energy due to the slot, and the imaginary part β controls the angle of maximum radiation [173]. Following the relation of the wavenumbers in a rectangular waveguide, the wave can be described as:

$$k_o^2 = k_x^2 + k_y^2 + k_z^2 \tag{5.1}$$

where k_o is the wavenumber of free space. The wavenumbers k_x,k_y depend on the waveguide dimensions, and if we consider the propagation along the z axis, then [174]:

$$k_z = -j\gamma_z = \beta_z - j\alpha_z \tag{5.2}$$

If we consider that the antenna radiates in the x direction, and more specifically for x>0, the following expression describes the variation of the leaky-waves in this direction:

$$e^{(\alpha_x - j\beta_x)x} \tag{5.3}$$

with the wavenumber along the transverse direction being $k_x = \beta_x + j\alpha_x$, while $k_y > 0$ is

real. The angle of radiation for each frequency can be calculated as [162], [173]:

$$\phi_{rad} = arcsin(\frac{\lambda}{\lambda_g}) = arcsin(\frac{\beta_z}{k_o}) \tag{5.4}$$

when ϕ_{rad} is considered with reference to the broadside direction of the antenna. From (5.4), the dependency of the angle of radiation on frequency is apparent, thus providing this antenna with scanning properties.

The above analysis can be extended in the case of a waveguide made in groove gap waveguide technology. In the case of the conventional waveguide, a longitudinal slot was the responsible for the leakage of energy. In a gap waveguide, the boundary conditions of the lateral walls are created by a high impedance surface, which for the presented analysis will be metallic pins. As seen in Fig. 5.3, three rows of electromagnetic band-gap pins (EBG pins), are enough to ensure that the field is mainly located in the groove. Now if on one side, the three rows of EBG pins, are replaced by one row of pins (i.e. leaky-pins) the waves will no longer be confined in the groove. Thus the leaky-wave antenna in groove gap waveguide technology is created (Fig. 5.5), as initially presented in [162] in 2016. In order to further enhance the leakage of energy, the leaky-pins should have a smaller height than the EBG pins, in order to support a TM mode that propagates at the lowest frequencies of the antenna. The detailed dimensions of the pins and the antenna will be discussed in the following chapters.

The propagation inside the groove can be described by the propagation constant γ, in the same way as for the conventional waveguide. The direction of the main lobe with respect to the broadside, is ϕ_{rad} calculated from Eq. 5.4. In Fig. 5.5 the direction of the radiated leaky-waves can be observed.

Following the classical formula for the guided wavelength inside the rectangular waveguide, and introducing the term w_{eff} which represents the effective width of the groove, then the distance between two equiphase planes is:

$$\lambda_g = \frac{\lambda_0}{\sqrt{1 - (\frac{\lambda_0}{2w_{eff}})^2}} \tag{5.5}$$

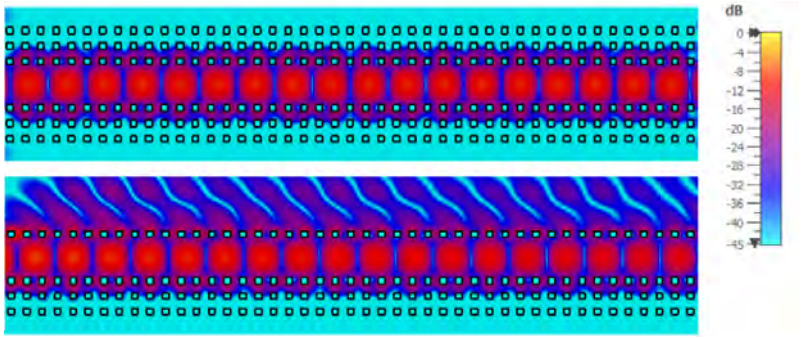

Fig. 5.5. Comparison of the groove gap waveguide (top), and the leaky-wave antenna (bottom) made with the same technology, here at 10 GHz.

Consequently, the phase constant can be expressed as:

$$\beta = k_0 \sqrt{1 - (\frac{\lambda_0}{2w_{eff}})^2} \tag{5.6}$$

The effective width of the groove depends on frequency. A detailed study of the propagation inside the groove was conducted by the authors of [143], where it was proposed that the groove has a width $w_{eff} = w + x_o$, with w being the physical width of the groove, and x_o the difference between the effective and physical width (see Fig. 5.3). In the same work it was suggested that the difference term x_o is expressed as:

$$x_o = -\frac{1}{\beta_{pp}} tan^{-1}(jZ_{in}) \tag{5.7}$$

where β_{pp} is the parallel plate propagation phase constant, and Z_{in} is the input impedance that the rows of pins create in the transverse direction. The above relation for x_o shows the reason why the effective width of the groove w_{eff} varies with frequency. In addition, depending on the sign of x_o, the width w_{eff} can be larger or smaller than the actual physical width of the waveguide w. By looking at the electric field distribution in the gap waveguide (Fig. 5.3), we get a physical visualization of the effective width of the groove, which in this case seems to be larger than the physical width as the energy expands to almost the second row of pins.

The amount of energy lost to radiation, is represented by the attenuation constant α. The leakage of energy happens between the pins and in the air gap between the upper plate and the top of the leaky-pins. The value of α must be cautiously chosen in order to achieve

high radiation and aperture efficiency. If the attenuation is very strong, and the energy leaks to free space very quickly, the effective aperture efficiency will be reduced, and poor directivity levels will be obtained. However, if the attenuation is small, the radiated power will not reach the desired 90% [162] and reflections will be produced at the end of the waveguide. Consequently, the value of α must be such to achieve good radiation properties. Many formulas have been reported in literature [143], [162], [167], [173], [175], [176] to describe the attenuation due to radiation leakage. In the original paper of the groove gap leaky-wave antenna [162], the authors reported that the normalized S_{21} parameter ($|S_{21}|/(1-|S_{11}|^2)$) can be approximated by $\alpha \approx (\lambda_0/(\sqrt{1-(\frac{\lambda_0}{2w_{eff}})^2}))^4$.

The width of the groove, is directly related with the attenuation of the propagating waves, as well as the distance (periodicity) between the pins. Since the value of w_{eff} depends on frequency, the attenuation will be subjected to changes with the frequency variation. In addition, the waves get attenuated by radiation that occurs in the gap between the pins, and due to the fact that the projection of this gap is smaller with frequency (ϕ_{rad} is closer to broadside for higher frequencies), then the attenuation is decreasing for higher frequencies. In order to tailor the attenuation along the length of the antenna, the authors of [162], suggested the gradual change of the groove´s width, taking under consideration the frequency behavior of the groove gap waveguide. In Fig. 5.6, the field distribution is compared for two variations of the groove´s width. Fig. 5.7 shows how the attenuation is frequency dependent. For the same groove width, the propagating wave is severely attenuated at 9.5 GHz, whereas at 11.5 GHz there is much lower attenuation. The difference in the angle of radiation ϕ_{rad} is also visible. As discussed previously, for higher frequencies, the direction of radiation is closer to broadside.

The detailed design of leaky-wave antennas in groove gap waveguide technology, will be analysed in the following chapters. The electromagnetic band-gap will be obtained with square metallic pins in Chapter 6, and holes in Chapter 7. The hole unit cell will be again used in 8 to design an array of horn antennas.

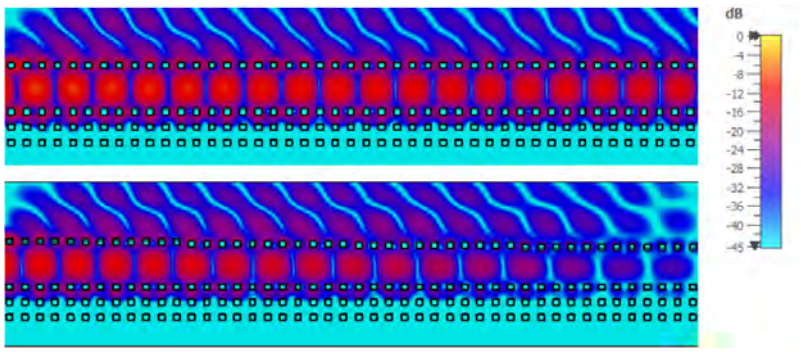

Fig. 5.6. Electric field distribution at 10 GHz, of a leaky-wave antenna in gap waveguide technology. The width of the groove waveguide controls the attenuation. The distribution at the top, corresponds to a case where the width remains constant for all the length of the antenna. At the bottom, the width is gradually changed. The colour bar applies for both distributions.

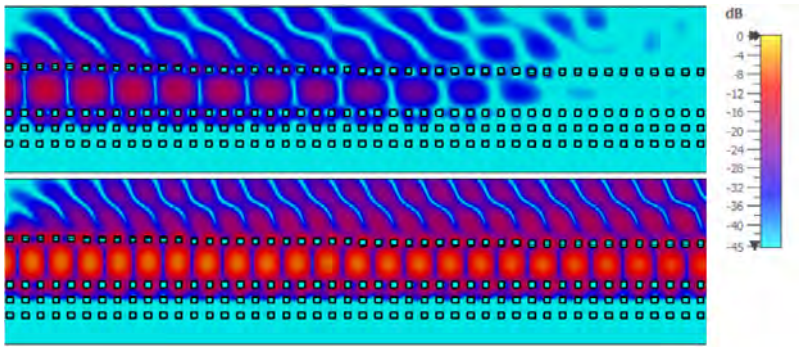

Fig. 5.7. Attenuation of the e-field at 9.5 GHz (top) and 11.5 GHz (bottom), for the same groove width.

Chapter 6

Array of stacked leaky-wave antennas in groove gap waveguide technology

6.1 Introduction

Gap waveguide technology offers a lot of potential when it comes to millimeter-wave bands that has become a rather popular field of research over the past few years. On one hand, in implementations using this technology, there is no demand for direct electrical contact between the different metallic parts of the waveguide structures. Because of the band-gap created by the use of high impedance surfaces, losses due to multiple connections are avoided, and the fabrication requirements are relaxed. In fact, the manufacturing can be made by plates that are then assembled together simply with screws, thus proving the reduced complexity that this technology offers in terms of the fabricated prototypes. In addition, low dielectric losses are ensured [141], which is an important advantage for applications in high frequencies (above 30 GHz).

As mentioned, the first leaky-wave antenna in groove gap waveguide technology was presented by the authors of [162] in 2016. The antenna was formed when one lateral side of the groove was made with one row of pins that allowed and enhanced the radiation leakage, while the other side of the groove was defined by three rows of EBG pins. Various examples of leaky-wave antennas using the groove gap waveguide can be found in literature [160],

[162], [176]–[179]. All these antennas focus the radiation mainly in the H-plane, producing fan-beam radiation patterns, thus obtaining moderate directivity levels. Consequently, to enhance the directivity of this type of antennas, a pencil beam radiation pattern must be formed.

In this chapter, the leaky-wave antenna of [162] is revisited and extended in a stacked vertical array, aiming to obtain high directivity levels by producing a narrow beam in both planes. A vertical array of leaky-wave antennas in groove gap waveguide, was proposed in [180], [181]. The latter, was composed of four antennas and included a Butler matrix all in the same technology. However, the feeding of the four elements of the array, was done directly at each one of the four levels, by waveguide port transitions. This increases the complexity in terms of fabrication and feeding in a real case scenario, and it may also introduce increased losses due to flaws in the connections of the waveguide transitions.

The proposed leaky-wave array, is composed of four vertically stacked elements. Contrary to the aforementioned examples of vertical arrays, a novel feeding network is used made by rectangular slot apertures. The direct feeding with a waveguide transition is done only at the bottom element, and then the energy is uniformly coupled to all the stacked elements. In addition, the phase is corrected separately at each level, by phase shifters made in gap waveguide technology. Hence, all the elements radiate in-phase, and maximum directivity levels are achieved. This novel feeding and phase correction network, has reduced complexity compared to [180], [181]. The distance between the elements, as well as the number of antennas to be stacked were studied as well, in order to achieve maximum directivity avoiding grating lobes for the targeting frequency of 28 GHz.

6.2 Array design

The proposed array was designed following a four-step procedure. As mentioned before, the basic element of the array is the leaky-wave antenna in groove gap waveguide technology, as it was presented in [162]. Hence, the first step was to re-design said antenna and study the crucial parameters that affect its response, in order to adapt its design to the implementation of a stacked array.

The next step, was to place n of the antennas designed in the first step, on top of each other, and study the directivity levels achieved as a function of the number of radiating elements, and of the inter-element distance.

After deciding the number of antennas that would form the array, it became apparent that a feeding network was required, which would provide uniform amplitude and phase to all the radiating elements. As a result, a vertical coupler was developed, followed by phase shifters all made in gap waveguide technology. The aim was to couple the energy that was fed to the array by a single waveguide port at the bottom element, and afterwards correct the phase at each element in order to achieve maximum directivity levels.

6.2.1 Design of a leaky-wave antenna in groove gap waveguide

The leaky-wave antenna in groove gap waveguide technology, was first presented in [162]. The two side limits of the groove are defined by rows of square metallic pins. On one side, three rows of electromagnetic band-gap (EBG) pins ensure that the propagation is well confined in the groove waveguide (Fig. 6.1). On the other lateral side, a single row of lower pins leaks the energy into the free space and thus the leaky-wave antenna is created. A metallic plate is placed on top of the groove waveguide, at a distance smaller than $\lambda/4$ above the EBG pins, where λ corresponds to the central frequency of the design. On both top and bottom metallic plates, and on the radiating side of the groove, corrugations are placed.

To create the electromagnetic band-gap in the frequencies of interest, the dimensions of the EBG pin unit cell (inset of Fig. 6.2) must be studied. The parameters that should be taken under consideration are : the height of the pin h_{pin}, the air gap between the metallic plate and the pin h_{gap} that should be smaller than $\lambda/4$, the width of the pin w, and the period of the unit cell $period$. These parameters control the electromagnetic behavior of the pins, and must be modified according to the frequency requirements of the design. For instance, if the pin is higher (h_{pin} bigger), the band-gap is located lower in frequency, but for a narrower pin (smaller w) the band gap moves up in frequency. In Fig. 6.2 and for the following dimensions: height h_{pin}= 2.8 mm, width w= 1.31 mm, periodicity $period$=

3.19 mm and air gap h_{gap}= 0.94 mm, the obtained EBG is marked by the gap between the first and the second mode, and expands from 21 GHz to 36 GHz, covering the central frequency of 28 GHz.

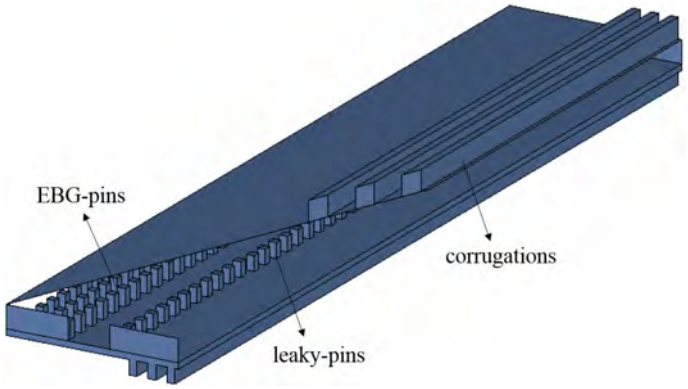

Fig. 6.1. 3D model of the groove gap waveguide leaky-wave antenna used as the basic element of the array. The model follows the antenna design proposed in [162].

Once the dimensions of the pins on the non radiating side of the groove have been chosen and the band-gap that they provide ensures that the energy is well confined, the dimensions of the pins on the other side must be defined in order to allow the radiation from that side. With a single row of the EBG pins (same dimensions and periodicity), some leakage would be achieved through the gaps between the pins. However, for an enhanced leakage of electromagnetic energy, the height of the $leaky-pins$ should be lower than the EBG pins. The reduction of the height of the pins leads to higher radiation levels due to the proximity of the first mode of propagation. Therefore, the height of the leaky-pins is h_{leaky} = 2.44 mm and so the air gap between the pin and the metallic plate is larger $h_{gap,leaky}$ = 1.3 mm, whereas on the other side the EBG pins are higher and the air gap is h_{gap}= 0.94 mm. Fig. 6.2 shows that there is one propagating mode in frequencies where on the other side of the groove the EBG pins do not allow propagation.

As shown in [162], the width of the groove controls the attenuation coefficient α. The value of α is critical for the leaky-wave antenna since it describes the amounts of energy that leaks to free space, and must be carefully chosen to ensure maximum efficiency of the antenna. The aim is to obtain radiation of 90% of the incoming power. If the attenuation coefficient is too large, the energy will be radiated quickly, and the effective aperture of the

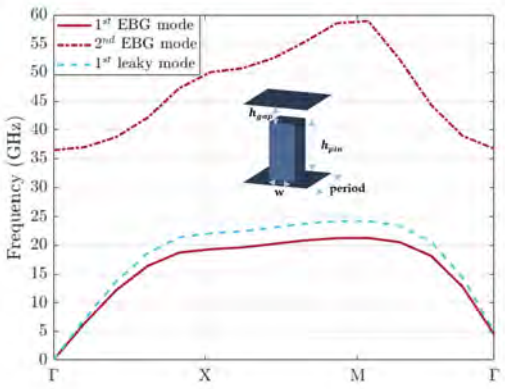

Fig. 6.2. Dispersion diagram of the pin unit cell (shown in the inset) with the following dimensions: h_{pin} = 2.81 mm, h_{gap} = 0.94 mm, w = 1.31 mm and $period$ = 3.19 mm for the band-gap (EBG) pins. The leaky-pins have the same dimensions except for their height that is h_{leaky} = 2.44 mm and the air gap $h_{gap,leaky}$ = 1.3 mm. An electromagnetic band-gap is located between the first and the second mode from 21 GHz to 36 GHz.

antenna will be significantly smaller than its actual physical size, thus the directivity levels will not be optimum. On the other hand, a significantly decreased attenuation coefficient α, will result to less than 90% of the incoming energy radiated, and reflections at the end of the waveguide.

In [162] it was reported that for an antenna with physical length of 39 cm and a central frequency of 10 GHz, the ideal attenuation coefficient is 26 dB/m. For the implementation of the presented design, the same electrical length, approximately 13λ, as in [162] was chosen. In order to control the radiation via the attenuation coefficient, the width of the groove is gradually changed throughout the length of the antenna. The entrance of the groove has similar width to a standard WR34 waveguide, 8.2 mm. Then the width is progressively changed and the ending of the antenna has a groove 6.6 mm wide. This change of width results to 28 dB/m attenuation.

The energy leakage is shown in Fig. 6.3, where the electric field distribution is presented when the groove of the leaky-wave antenna is gradually changed. The phase front shows that the energy is leaking from the antenna to free space under a certain angle ϕ_{rad} (see Eq. 5.4) which is the direction of the main beam in the radiation pattern. Furthermore, it is

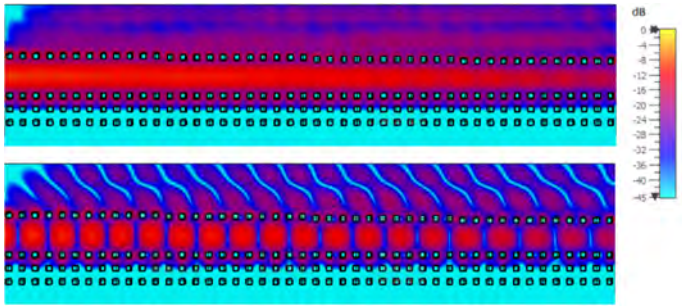

Fig. 6.3. Electric field distribution of the leaky-wave antenna at 28 GHz, magnitude (top) and snapshot (bottom). The colour bar applies for both distributions.

evident that the value of α is sufficient for the radiation of the majority of the incoming power, and at the same time the energy is radiated slowly enough to ensure that the effective aperture is not significantly small. The S_{21} parameter of the antenna (Fig. 6.4), shows that 90% of the incoming power is radiated at the central frequency. The S_{11} indicates that the antenna is well matched for the frequency range of interest 27.4-28.6 GHz.

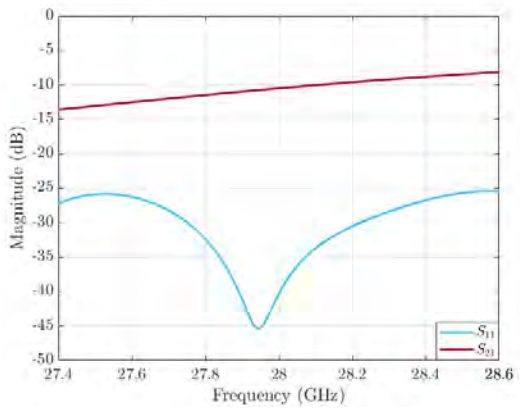

Fig. 6.4. Simulated S-parameter of the leaky-wave antenna in groove gap waveguide technology.

The directivity for the leaky-wave antenna varies between 19.3 dBi and 19.6 dBi, from 27.4 GHz to 28.6 GHz, and the radiation pattern is shown in Fig. 6.5 for the two principal planes. The direction of the main beam is $\phi_{rad} = 44^o$ from broadside. The dispersive nature of the radiation pattern of this type of leaky-wave antennas, makes it a good candidate in applications where beam-scanning is required.

At the top and bottom plates of the antenna, and more specifically on the radiating

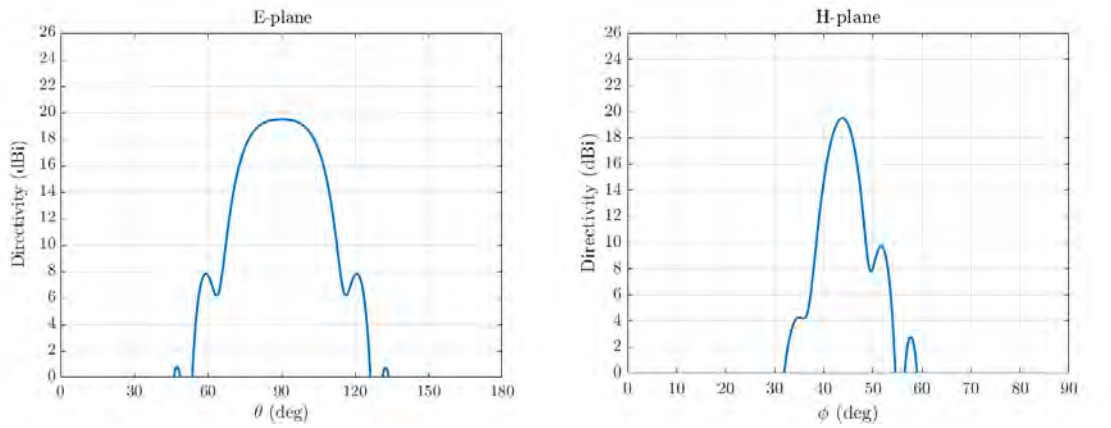

Fig. 6.5. Directivity of the leaky-wave antenna at 28 GHz (a)E-plane (b)H-plane.

side, rectangular corrugations were placed. These corrugations were used to prevent the diffraction of the field on the edges of the metallic plates. Furthermore, they prevent the radiation on the non radiating side of the antenna (back radiation). Their dimensions are 1.3 mm width, 4.5 mm periodicity, length 13λ at 28 GHz, and height 3.4 mm.

6.2.2 Stacked elements

The next step in the design process of the array, was to place vertically-or stack, n of the leaky-wave antennas presented in section 6.2.1. For a single leaky-wave antenna, it was shown that the directivity varies from 19.3 dBi to 19.6 dBi from 27.4 GHz to 28.6 GHz. Now let us suppose that we place two identical leaky-wave antennas on top of each other, and we directly feed each one with same amplitude and phase, by standard WR34 waveguide port transitions, while they are all terminated with a matched load. The directivity increases up to 22-22.2 dBi for the same frequency range (Fig. 6.7). For a total of four stacked radiating elements, the directivity reaches 25.14 dBi. More elements could be stacked to implement the array, however, we have decided to use four antennas, in order not to complicate the fabrication, as this work is a proof of concept.

An important parameter in the design of an array of antennas, is the inter-element distance. In the proposed design, the inter-element distance is defined as indicated in the inset of Fig. 6.6 as the sum of the thickness of the broad wall that separates the antennas, and the height of the waveguide itself. However the height of the waveguide that is defined

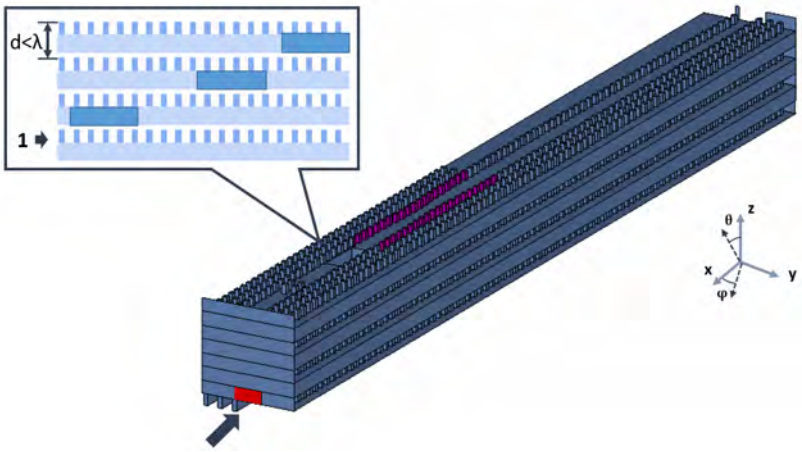

Fig. 6.6. 3D model of the array in perspective view. The inset shows the rectangular apertures that form the coupling network, placed in a progressive manner. The feeding port is indicated as number 1. With purple are the pins that are used to modify the width of the groove and so to correct the phase of each element before the radiating part of the presented array.

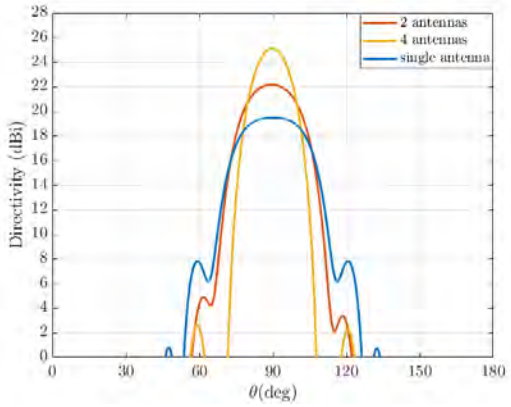

Fig. 6.7. Comparison of the directivity achieved with a single leaky-wave antenna, and an array of two or four stacked antennas, all fed directly by waveguide ports.

as the height of the pin and the air gap, is fixed and cannot change, the distance between the elements of the array is exclusively controlled by the thickness of the broad wall that separates the antennas. In order to avoid grating lobes, this distance should be smaller than λ_0 at the central frequency. The aforementioned directivity levels for two or four stacked antennas, correspond to an inter-element spacing of $0.7\lambda_0$ at 28 GHz (7.9 mm). In Fig. 6.8, the directivity in the case of two stacked antennas is presented, as a function of the inter-element distance. Note that for larger spacing d between the elements, the directivity increases, with d always less than λ_0. Nevertheless, as it will be discussed later, the thickness of the broad wall that separates the antennas, affects the coupling between the different elements of the array, as Oliner initially states in [182], and so a trade-off must take place in order to achieve the best possible performance.

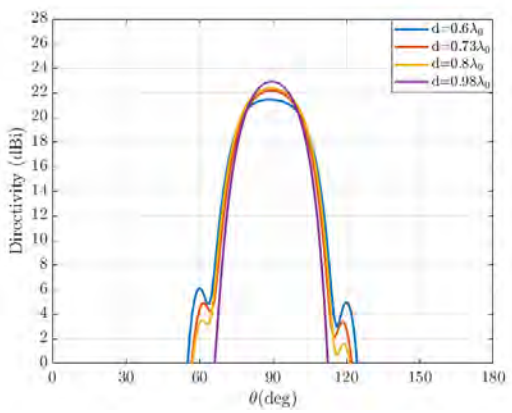

Fig. 6.8. Comparison of directivity of two stacked elements, as a function of the inter-element distance.

6.2.3 Coupling and phase correction network

In the previous two sections, the leaky-wave antenna that is the basic element of the array was presented and its design was discussed, and then n of these antennas were stacked in order to study the directivity levels achieved as a function of the number of elements used, and the inter-element distance. We concluded that for the purposes of this thesis, four stacked elements would be used to implement the array, with an inter-element spacing of $0.7\lambda_0$ at 28 GHz. To obtain these results, all the stacked elements were fed directly with

waveguide ports, in order to have uniform amplitude and phase, achieving this way the maximum directivity levels possible. However, in a true-case scenario, this would not be possible. Thus, the need of a coupling network was apparent, that would ensure uniform amplitude and phase.

The study of the coupling among the stacked elements, was initially done with four standard hollow waveguides, each one with a rectangular slot in the broad wall between them. As a first approach, the rectangular slots were identical in terms of dimensions, and were aligned with each other. The initial dimensions used were: length λ_g, width $\lambda_g/2$, and distance from the beginning of the waveguide $\lambda_g/4$, with λ_g being the guided wavelength at 28 GHz (13.66 mm). Then the slots were placed in a progressive manner as seen in the inset of Fig. 6.6, so as to achieve a progressive coupling between the elements. A parametric study of the dimensions of the slots, resulted in the values shown in Table 6.1. The coupling that was obtained with this vertical coupling configuration, is presented in Fig. 6.9. At the central frequency, the incoming power at the bottom antenna (as indicated in Fig. 6.9) is divided in an approximately uniform way.

Coupling of antennas	Distance from the edge	Width	Length
1^{st} and 2^{nd}	5.1 mm	8.3 mm	15.3 mm
2^{nd} and 3^{rd}	32.9 mm	8.3 mm	15.3 mm
3^{rd} and 4^{th}	49 mm	8.3 mm	14.2 mm

Dimensions of the rectangular slots that form the feeding network. The distance of each slot to the beginning of the waveguide, is referred to as distance from the edge.

Table 6.1. DIMENSIONS OF THE COUPLING SLOTS

Once we ensured the equal division of the incoming power to the four stacked elements, the phase in the output of the vertical coupler configuration must be studied. If the incoming wave in the radiating part of the antenna results in out of phase radiation at each element, then the radiation efficiency will be decreased. Hence, it is important that the phase is corrected after the coupler, but before the radiating part. In Fig. 6.10(a), the phase after the coupler in the four waveguides is presented. It is evident that a phase shifter is required to achieve in-phase radiation.

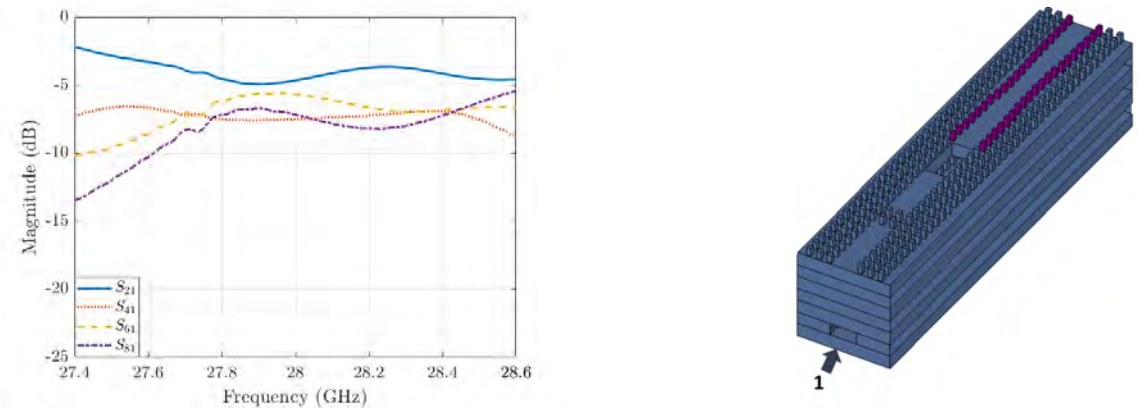

Fig. 6.9. On the left: coupling achieved with the designed feeding network, expressed in S-parameters. Waveguide ports were placed at the end of the phase shifters at each of the 4 elements of the array for the simulation. The S_{21} parameter corresponds to the coupling of the 1^{st} (bottom) element, and respectively the S_{41}, S_{61}, S_{81} show the coupled energy for the 2^{nd} , 3^{rd} and 4^{th} element. The configuration of the feeding network and the phase shifters (purple pins) is presented on the right.

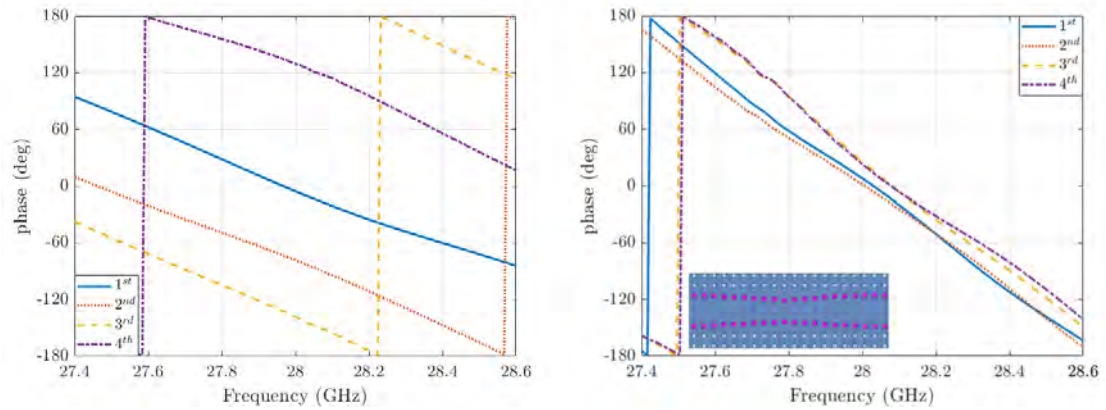

(a) (b)

Fig. 6.10. (a) Phase at the exit of the coupling network, before placing the phase shifters. (b) Corrected phase with the phase shifters placed right after the coupling network. The inset shows an example of a phase shifter in gap waveguide technology.

In gap waveguide technology, a phase shift in the wave propagating in the groove, can be achieved by slightly changing the width of the waveguide by moving the pins on both sides of the groove. A different width change, means different phase shift. Thus, first we calculated the required phase shift Δ_ϕ at each element, having as reference the phase of the second from the bottom element. Then we started changing the width of each element, until the phase was corrected. The values of the phase shift and the corresponding width change, can be seen in Table 6.2. In Fig. 6.10(b) the result of the corrected phase is presented. The phase is practically equal in all the four elements. In the inset, the phase shifter configuration in gap waveguide technology is shown. The inset of Fig. 6.9 shows the configuration of the vertical coupler and the phase shifters. In this part of the array, three rows of EBG pins are used on both lateral sides of the groove, and thus they ensure that the energy is well confined in the gap waveguide.

To demonstrate how the change of the groove waveguide can manipulate the propagating wave, the electric field distribution is presented in Fig. 6.11. The difference between the normal groove waveguide and the phase shift arrangement, is evident. However, the change of width, when drastic, can result to high reflections. Fig. 6.12 shows an example of a phase shifter where the groove is changing drastically producing strong reflections that are apparent. This was taken under consideration when designing each phase shifter, by ensuring transmission coefficients close to unity.

Antennas	$\Delta\phi$	Width
1^{st}	137.17^o	5.8 mm
2^{nd}	0	8.3 mm
3^{rd}	-56.56^o	6.8 mm
4^{th}	31^o	6.4 mm

Required phase shift for each antenna, and corresponding changed width of the groove. The phase difference is calculated having as reference the phase of the 2^{nd} antenna. The length of the phase shifter is 5.5 mm in all cases.

Table 6.2. PHASE SHIFTERS

To verify the overall effectiveness and importance of the phase correction at each

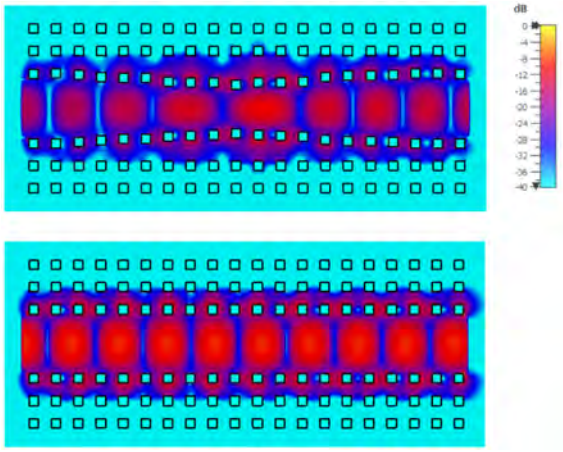

Fig. 6.11. Electric field distribution for: a phase shifter in gap waveguide technology (top), and a conventional groove gap waveguide with constant width (bottom). The colour bar applies for both E-fields.

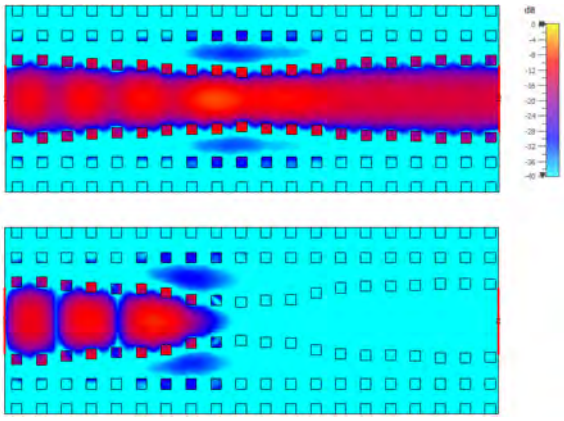

Fig. 6.12. Comparison between a gradual change (top) of groove and a drastic change (bottom) in a phase shifter.

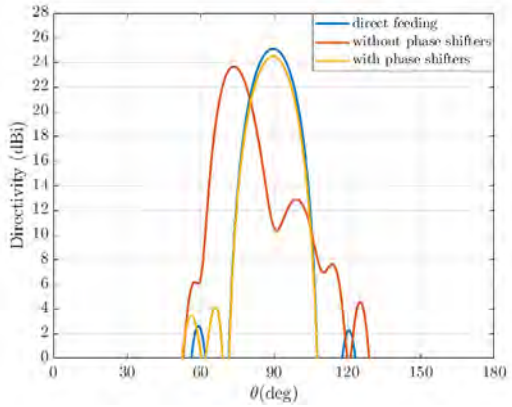

Fig. 6.13. Directivity of a 4-element array when direct feed is applied (blue), the feeding network is used to couple the energy and direct feed is only at the bottom antenna (red), and the feeding network is used but with phase shifters placed before the radiating part of each one of the 4 elements.

element separately, we compare in Fig. 6.13 the radiation pattern and the directivity achieved with the four stacked elements, when : a) there is direct feed at each element, b) with the vertical coupling network but without the phase shifters, and c) with the coupling network and the phase shifters. The maximum directivity is achieved for uniform amplitude and phase provided by ideal direct feed with waveguide ports, 25.14 dBi. Now when the vertical coupler is used to feed each antenna in the array, the directivity is 23.5 dBi, the radiation pattern is deformed and the maximum is not located at $\theta = 90^o$ which is the broadside direction. However, when the phase shifters are placed right after the coupler, the directivity increases up to 24.3 dBi. The pencil beam radiation pattern is now pointing at the broadside direction, validating that all the elements radiate in-phase with each other. Consequently, the use of a phase correction is necessary for optimal performance of the array.

While the total length of the array is 27.7 cm, each element has a radiating part that occupies 14.6 cm, the feeding network occupies 7.4 cm and the phase shifters are 5.5 cm long.

6.3 Results

6.3.1 Simulated antenna array

The 3D model and the full-wave simulations, were done using CST Microwave Studio. Once all the separate parts of the proposed design were designed and assembled, the array was simulated as seen in Fig. 6.6. A standard waveguide port transition was used at the bottom antenna, and its reflection coefficient is shown in Fig. 6.14. Very good matching of the array was obtained in the frequencies of interest, and more specifically at 28 GHz the S_{11} parameter is around -16 dB.

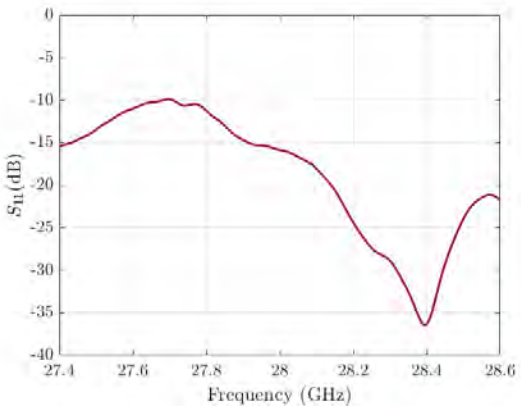

Fig. 6.14. S_{11} parameter of the simulated leaky-wave array.

In previous sections the performance of the leaky-wave antenna that is used to form the array, was presented. The directivity levels it achieved vary between 19 and 19.6 dBi. When four of these antennas are stacked vertically, and the coupler and phase shifters are placed, the directivity reaches a maximum of 24.5 dBi at 28 GHz (see Fig. 6.15), indicating an increase of +5 dBi. The simulated realized gain is 24.4 dBi at the central frequency. The directivity levels of the single leaky-wave antenna and the array in the H-plane, are compared in the inset of Fig. 6.15. Note how despite the increase of directivity, the dispersive nature of this kind of antennas is evident by the change of angle in the direction of radiation ϕ. The maximum occurs at $\phi = 46^o$.

This array achieves to focus the energy in both the E and H planes by creating a pencil beam radiation pattern. In Fig. 6.16 the E-plane of the array is compared to the single

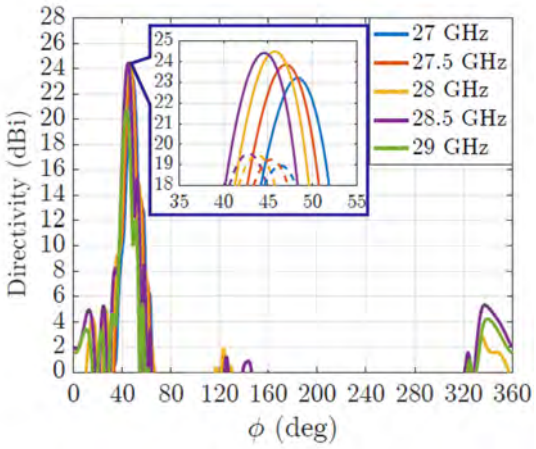

Fig. 6.15. Simulated directivity for a range of frequencies, the H-plane of the array (solid line), compared in the inset with a single antenna of this type (dashed line).

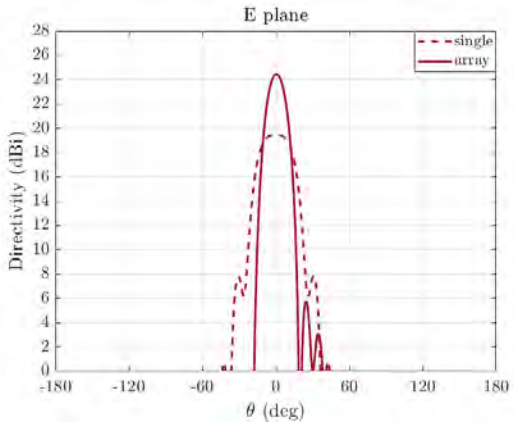

Fig. 6.16. The E-plane of the array at the central frequency 28 GHz (solid line) and the single leaky-wave antenna (dashed line).

leaky-wave antenna. The maximum is located at the broadside direction, indicating that all the elements radiate in-phase. The focalized energy in both planes is evident in the 3D radiation patterns shown in Fig. 6.17, where we can see how the fan beam of the single leaky-wave antenna, is transformed into a pencil beam in the case of the array.

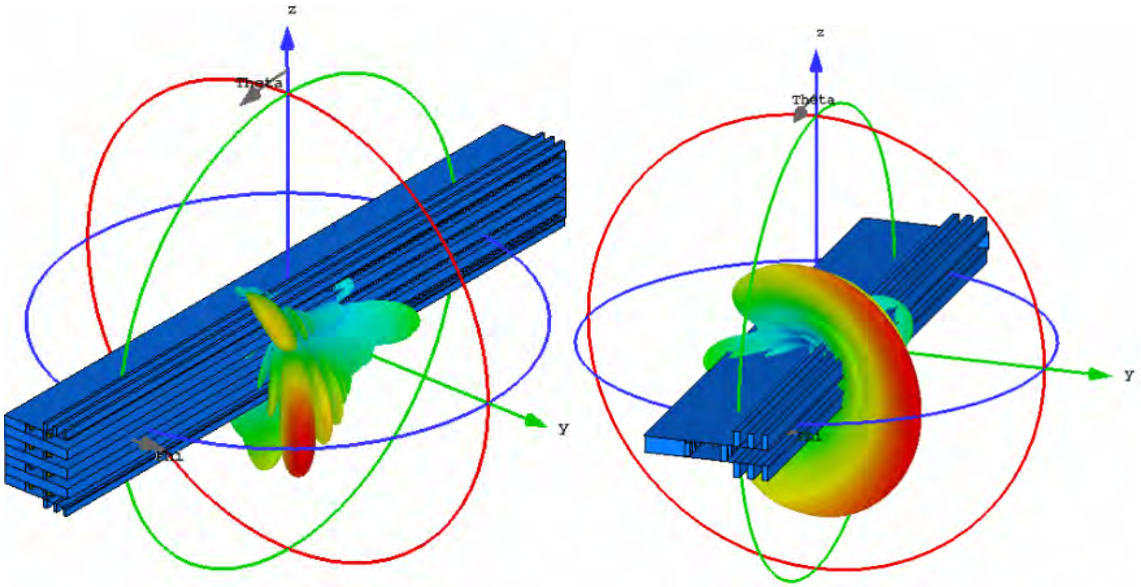

(a) (b)

Fig. 6.17. 3D radiation patterns of (a) the designed array, (b) the single leaky-wave antenna, both at the central frequency 28 GHz.

The distribution of the amplitude of the electric field is shown in Fig. 6.18. The different numbers indicate the individual elements that are stacked vertically. Note how the phase shifting arrangement of the pins manipulates the wave at each element. At the second element (denoted as *2*) there is no phase shift, as this was the reference element for the calculation of the phase difference. At the bottom element (denoted as *1*), where the phase difference was the highest (see Table 6.2), the manipulation of the electromagnetic wave is clearly evidenced.

As mentioned before, for the whole length of the coupler and phase shifters, three rows of EBG pins confine the energy inside the groove waveguide. Then, one side of the groove is reduced to one row of pins, with lower height, and the energy leaks from the antenna to the free space. In Fig. 6.18, the attenuation of the wave reaching the end of the radiating part is also observed. Approximately -20 dB reach the end of each element, in terms of

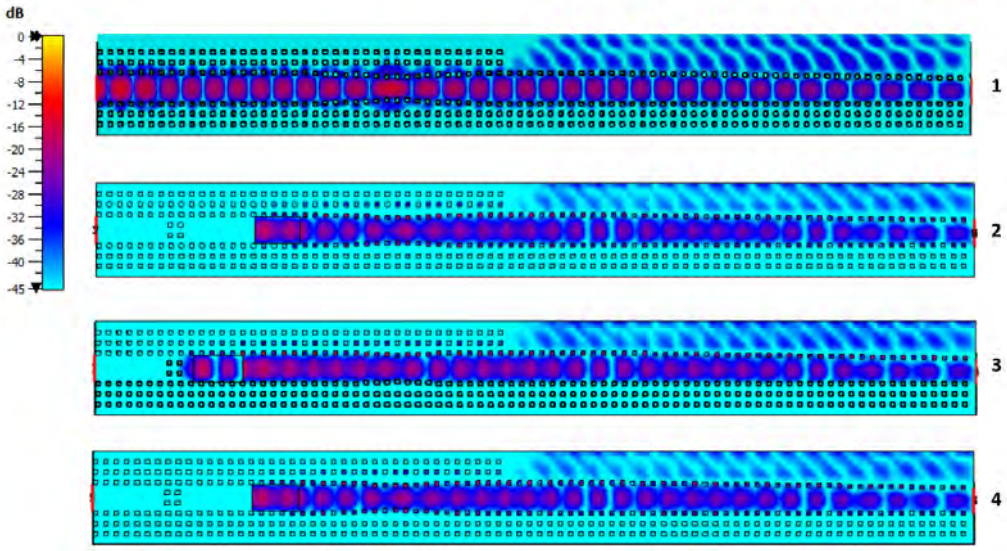

Fig. 6.18. Distribution of the amplitude of the E-field at each one of the stacked radiating elements of the array. The bottom element is referred to as "1" and the top element is "4".

their transmission coefficients.

6.3.2 Experimental results

To validate the proposed design and the simulations´results, a prototype was manufactured and measured. In this section the experimental results will be presented, and some manufacturing issues will be addressed.

In Fig. 6.19(a) the four radiating elements of the array are presented. The top and bottom metallic plates have the necessary corrugations, that as explained before, prevent back radiation and diffraction from the edges of the plates. The three rectangular slots can be also seen, located at the broad walls between the elements and in a progressive manner with respect to one another. With a closer look, the phase shifters are also evident. The total length of each element is 27.7 cm, with a feeding network of 7.4 cm, phase shifters 5.5 cm, while the radiating part of each element, occupies 14.6 cm of the total length.

To ensure the alignment of the four elements, only four screws were located at the front, back and middle of the array. The required air gap is established with thick borders at both ends of the individual elements. For the same purpose, pillars were used in the middle of each element on the non radiating side. The bottom element, was fed using a

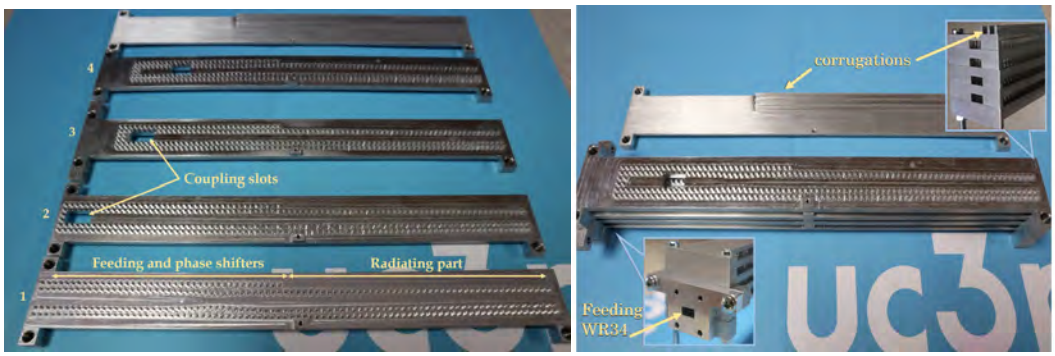

(a) (b)

Fig. 6.19. The manufactured prototype. In (a) each level of the array is presented, and in (b) all the elements are assembled together. The two inset show the front and ending (open) of the array.

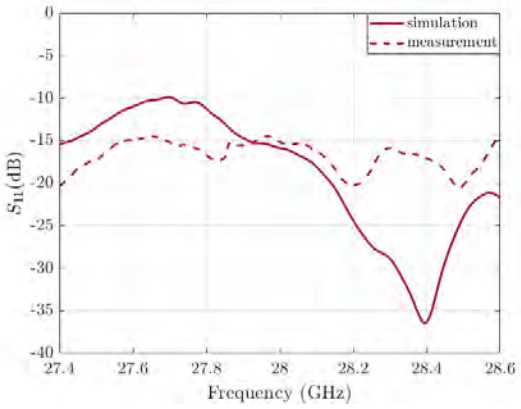

Fig. 6.20. Comparison of the S_{11} parameter of the simulated and the measured leaky-wave array.

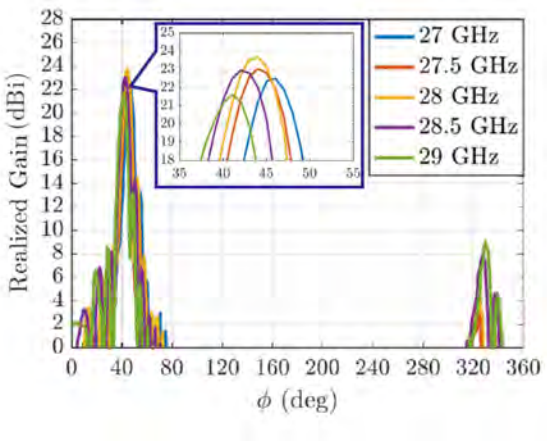

(a)

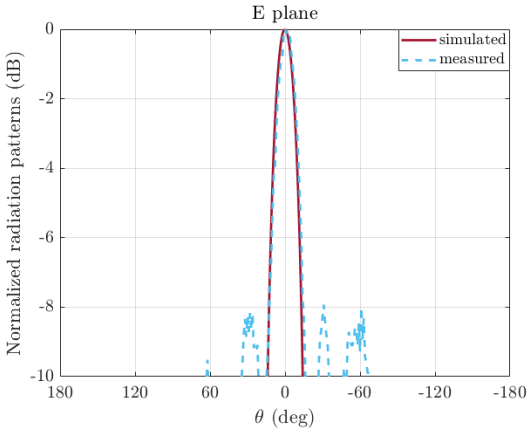

(b)

Fig. 6.21. (a) Measured realized gain of the fabricated prototype for a range of frequencies. The realized gain reaches 23.7 dBi of magnitude at 28 GHz. (b) Normalized measured radiation pattern (dashed line) and simulated (solid line) representing the E-plane at 28 GHz. The maximum is at $\theta = 90^o$, showing that all the elements radiate in-phase.

flange to connect a standard WR34 transition. In Fig. 6.19(b) all the different parts of the array are assembled together. The front and back of the array are shown in the insets.

At this point we would like to address two important fabrication issues that had to be taken under consideration. The first is that to simplify the manufacturing process, the EBG rows of pins were reduced to two instead of three. After simulations, we concluded that two rows are enough to confine the energy and ensure that no leakage takes place. The other critical issue, is the termination of each radiating element. During the initial simulations of the array, waveguide ports were used and the energy that reaches the end of each element is absorbed. In a real case scenario, this would mean that all the elements would be connected to matched loads at the end of the groove waveguide, which is not practical. In this direction, we decided to terminate in open all the groove waveguides, and the antenna was redesigned slightly for further attenuation of the wave that is not radiated, by changing gradually the width of the groove to force radiation. As seen in Fig. 6.18 after the phase shifters, starts the radiating part of each element, where part of the waves escape to free space under an angle, and the rest is attenuated before the end of each element. Consequently, only -44 dB reach the ending of a single element, and thus the reflection from the open end are avoided.

Fig. 6.20 shows the measured S_{11} parameter of the prototype, compared to the simulated result. Good matching is obtained for the prototype at the frequencies of interest, as the S_{11} remains below -15 dB. The measured realized gain can be seen in Fig. 6.21(a). At the central frequency the realized gain is 23.7 dBi, which indicates a reduction of only 0.7 dB compared to the simulated gain. The variation of the realized gain is between 21.6 dBi and 23.68 dBi for the frequencies of interest. The directivity at 28 GHz is 26.1 dBi, calculated from the half power beam width [90]. In Fig. 6.21(b) the normalized radiation pattern at 28 GHz is presented for the E-plane (dashed line) in comparison to the simulated normalized pattern (solid line). For both the simulated and the measured results, the maximum is located at broadside ($\theta = 90^o$), verifying the in-phase radiation of the elements of the array. A couple of low side lobes appear in the measured radiation pattern, nevertheless the agreement of the measured and the simulated results are in very good agreement overall. In terms of radiation efficiency, the prototype reaches 93.2% at the central frequency of 28

GHz compared to 96.7% that is the simulated efficiency.

6.4 Conclusions

The design of a leaky-wave antenna array in gap waveguide technology has been presented. The basic element of the array is the groove gap waveguide leaky-wave antenna [162]. By placing vertically four of these antennas one on top of the other, there is an enhancement of +5 dB in the directivity. Compared to the single leaky-wave antenna element as well as other gap waveguide based leaky-wave antennas [176]–[179], [183], the advantage of directivity enhancement is combined with a pencil beam radiation pattern that is a novel aspect in the antennas designed with this technology.

The total physical aperture of each of the stacked elements, is divided in three parts. First, a feeding network is responsible for the equal coupling of energy to all the antennas. The direct feeding is done only at the bottom (first) antenna, and then the energy is coupled through rectangular shaped apertures. These apertures where placed on the common wall separating the elements, in a progressive way.

The second part of each element, is the phase shifter. After coupling the energy to all the antennas, the phase is corrected separately at each element. Maintaining the full-metallic character of the design, the phase shifters were implemented by changing the width of the groove waveguide with the pins. In this manner, a tailored correction of phase can be achieved. Consequently, the radiation of all the elements is in-phase, and maximum directivity is obtained.

The third part of each element, is the radiating part. While for all the length of the coupling and phase correction network, three lines of pins ensure that the radiation is confined in the waveguide, in the last part, one row of pins allows partial leakage of the energy to free space. Let us mention here that due to manufacturing simplification, the three rows of EBG pins were substituted by two rows, without introducing radiation leakage.

The designed antenna array has been examined experimentally with a fabricated

prototype. The experimental results confirmed the simulations. At the central frequency of 28 GHz, the measured realized gain is 23.68 dBi. As mentioned previously, the presented array focuses the radiation at both the E and H planes, thus creating a pencil beam. In addition, the measured radiation patterns of the E plane, showed that the maximum radiation occurs at the broadside direction ($\theta = 0$), proving that the phase shifters have the desired performance correcting the phase at each element.

Due to the use of gap waveguide technology, the fabrication cost is reduced and the mechanical requirements are more relaxed, since no direct electrical contact is required between the different layers of the 3D structure. Each of the array elements was fabricated in a single piece. The viability of a fully metallic structure that has low losses, and also it achieves directivity enhancement simply by stacking the radiating elements, has been demonstrated. This design can be directly scaled in a subjectively frequency band without deterioration of the array performance. Furthermore, the number of radiating elements can be increased following the proposed methodology, which can be also used to implement arrays of other leaky-wave antenna designs such as [176].

Chapter 7

Non-dispersive groove gap waveguide prism antenna

7.1 Introduction

As discussed in Chapters 5&6, the leaky-wave antenna made in gap waveguide technology [162] is dispersive. This means that the direction of the main lobe changes with frequency (see radiation patterns of Fig. 6.21). Referred to as *beam squinting effect* in literature, this property can be an advantage or disadvantage depending on the application. For instance, in the case of beam scanning applications, these antennas can be promising candidates [180], [181], [183], [184]. However, in cases where a single direction is considered, the beam squinting results to gain losses, which is an important disadvantage in applications where high gain in a constant direction is needed for a certain frequency range, such as point to point satellite or wireless communications.

In literature, several solutions have been proposed to combat the dispersion. For instance, in [185]–[189] metamaterials were used to correct the direction of radiation. In [178] a new approach was presented, where the leaky-wave antenna in groove gap waveguide was combined with a metamaterial prism. The prism was made of squared metallic pins that created a dispersion complementary to the one of the leaky-wave antenna, thus producing a constant angle of radiation. The same idea was also reported in [179],

[190], [191], and in [192] it was implemented in substrate integrated waveguide technology.

In this chapter, the concept of the metamaterial prism [178], [179], [190]–[192] is re-investigated but with a different configuration of the prism and the leaky-wave antenna. Unlike [178], the metamaterial prism is designed by using the hole unit-cell [127]–[129] instead of pins. The main advantages of the holes, are their easier fabrication (drilling holes is simple) and their robustness in high frequencies where the pin-made structures result in fragile components. High precision can be achieved with this unit cell without excessive manufacturing cost. The leaky-wave antenna, is as well designed in gap waveguide technology with the electromagnetic band-gap created by glide symmetric holes covering the frequency range of interest 25-30 GHz. By using the groove [132] version of gap waveguide [118], low losses are ensured [141].

7.2 Prism effect

In his book *Opticks*, Sir Isaac Newton first studied optical prisms in great detail. In 1666 he conducted the first experiment bending light with the use of a prism. After a series of experiments, he proved that prisms possess the ability to separate light into its constituent colours due to their frequency dependent refractive indices which cause their dispersive behavior. He also proved that prisms work in a reversed manner as well, meaning that they can also focus different frequencies (or colours in the visible spectrum) in a single direction (Fig. 7.1).

The dispersive nature of prism-like structures, applies within all the electromagnetic spectrum. The concept of the frequency dependent refractive index, creates interesting possibilities for the manipulation of the direction of radiation, even in millimeter wave applications. By gaining control over the refractive index of the materials used, or by designing metamaterials that allow tailoring of the refractive index, it is possible to modify as desired the dispersive nature of antennas, and more specifically for the purposes of this thesis, leaky-wave antennas.

When a longitudinal slot is placed on the narrow wall of a standard rectangular waveguide, the electromagnetic waves will escape from inside the waveguide and energy "leak-

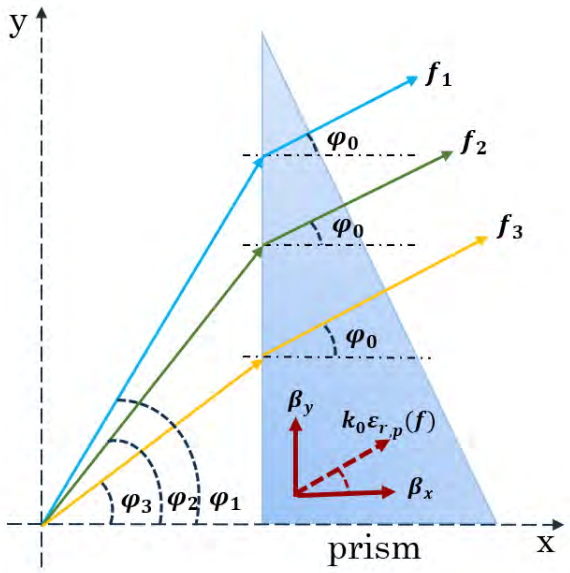

Fig. 7.1. An optic prism can focus different frequencies in a single direction.

age" is produced [173]. Thus a leaky-wave antenna is created.

As seen in the previous chapter, if the longitudinal slot leaks the radiation in the y axis, then the direction of radiation can be calculated as:

$$\phi_L(f) = sin^{-1}(\frac{\beta_y}{k_0}) \tag{7.1}$$

From Eq. 7.1 it is evident that for different frequencies, the radiation will point in different directions, or different angles ϕ_L, as both the propagation constants β_y in the waveguide and k_0 in free space are frequency dependent.

Now let's consider that the leaky-wave antenna has an equivalent refractive index n_L. A metamaterial prism, has as well an equivalent refractive index n_P. Therefore, when the aforementioned leaky-wave antenna is radiating in free space through a prism, the resulting angle of radiation will depend on the interaction of the two structures in terms of their refractive indices:

$$\phi_0(f) = sin^{-1}(\frac{n_L(f)}{n_P(f)}) \tag{7.2}$$

Consequently, if the refractive index of the prism n_P produces a dispersion that compensates the dispersion of the leaky-wave antenna, a constant radiation angle ϕ_0 can be obtained in a given frequency range. For this to occur, the two refractive indices must have complementary behavior with respect to the frequency, as it will be demonstrated later in this chapter.

7.2.1 The unit cell

The textured surface of the prism is made of drilled holes placed in a periodic way in a parallel plate structure. It is critical for the design to study the dispersion characteristics of the hole unit cell. This first step will allow us to design the prism with the required dispersive behavior that will compensate the dispersion of the leaky-wave antenna.

The resulting equivalent refractive index of the prism, can be calculated from the dispersion of the unit cell (Fig. 7.2). The behavior of the unit cell depends on its geometry. Consequently, the parameters that affect the refractive index of the unit cell (seen in the inset of Fig. 7.2), are its radius r, the height or depth of the hole h, the air gap between the two metallic plates h_{gap}, and the periodicity under which the holes are placed in the prism per. Therefore, in order to gain control over the produced dispersion, the effect of these parameters on the refractive index was initially studied.

Considering the first propagating mode k_1 and the free space propagation constant k_0, the refractive index of the holes is expressed as:

$$n_P(f) = \frac{k_1}{k_0} \tag{7.3}$$

Another consideration for the calculation of the refractive index, must be the direction towards which we calculate the dispersion. As seen in Fig. 7.2, if we consider the zone Γ-X in the Brillouin diagram of the hole, the resulting dispersion is different from the case where the M-Γ direction is considered. In Fig. 7.3 the difference in the refractive index is presented when it is calculated considering (a) Γ-X and (b) M-Γ directions. For the purposes of the present design, the direction Γ-X was initially used.

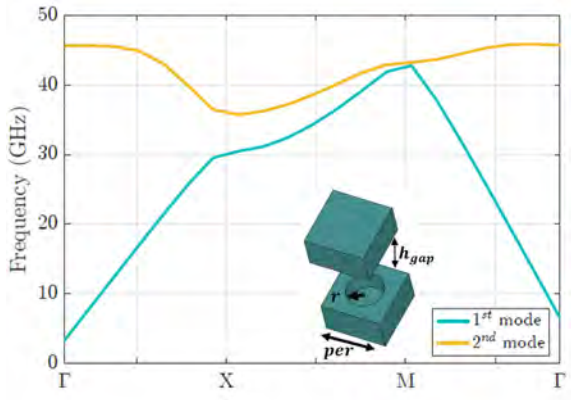

Fig. 7.2. The dispersion diagram of the unit cell, as it is calculated in CST. The inset shows the unit cell-hole.

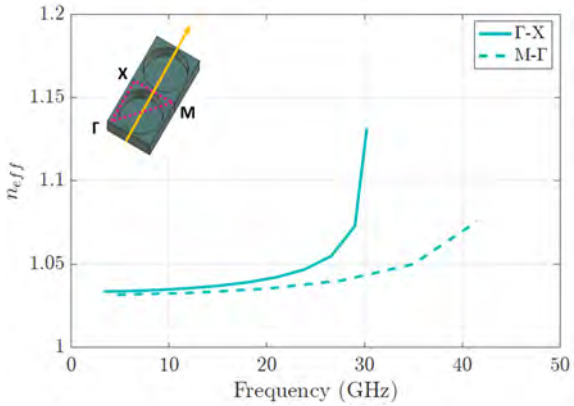

Fig. 7.3. The direction where we consider the propagation, affects the result of the equivalent refractive index n_{eff}. For the presented design, the Γ-X direction was considered.

A selection of the results of the parametric study can be seen in Fig. 7.4. The periodicity *per* of the holes defines the frequency range where the dispersion occurs. In addition, the air gap h_{gap} as well as the radius r, also affect the refractive index. However, the height of the hole h has a minimum value after which it has no further influence on the refractive index.

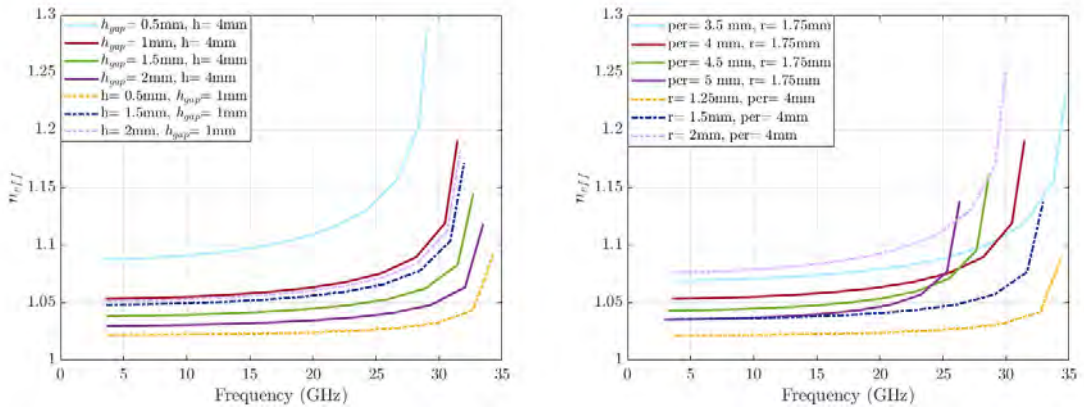

(a) (b)

Fig. 7.4. Parametric study of the equivalent refractive index of the holes. The initial values of the parameters are : $h = 4mm, h_{gap} = 1mm, per = 4mm, r = 1.75mm$.

7.2.2 Combination with a leaky-wave antenna

The next step in the design process is to calculate the dispersion of the radiating element that will be combined with the metamaterial prism. As mentioned the prism will be used to compensate for the dispersion of leaky-wave antennas. Fig. 7.5 shows the two structures that will be combined to create a low dispersive antenna.

When gap-waveguide technology is used to implement a leaky-wave antenna (Chapter 6), the non radiating side of the rectangular waveguide, is replaced by a high impedance structure that avoids radiation. In the present design, glide symmetric holes are used instead of pins [127]–[129], [193], [194]. Simple holes could not be used since they do not guarantee the stop band in all the directions. The glide symmetry configuration [195] creates an electromagnetic band-gap [118], [196], therefore the energy only escapes through the longitudinal slot.

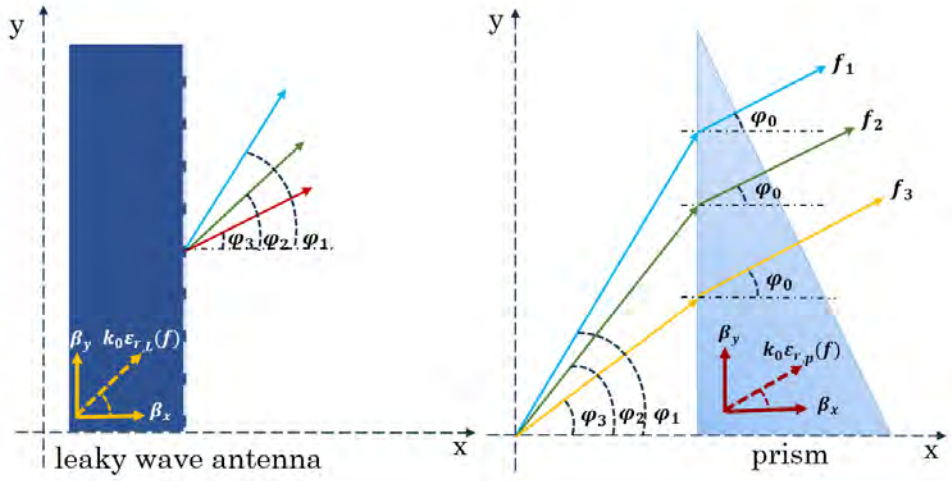

Fig. 7.5. Dispersion of the leaky-wave antenna (left) and the prism effect (right). While the radiation of each frequency occurs under a different angle in the case of the leaky-wave antenna, the prism obtains a constant angle of radiation independent of frequency.

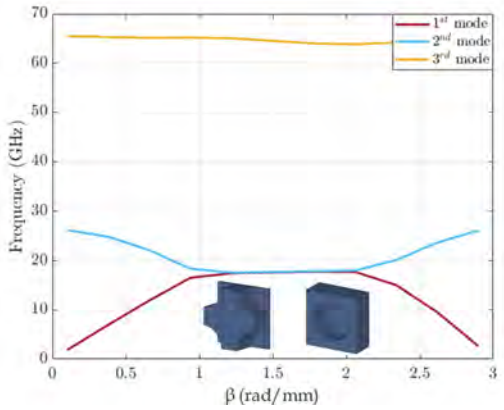

Fig. 7.6. The electromagnetic band-gap created by the hole unit cell in glide symmetry. No mode is propagating between 25-63 GHz. The inset shows the unit cell with glide symmetry.

To implement the non-radiating side with glide symmetry, the corresponding unit cell (inset of Fig. 7.6) was designed in order to achieve the band-gap that will prohibit the propagation of electromagnetic waves [197]. The band-gap is shown in Fig. 7.6, where no mode is propagating from 25 to 63 GHz. The dimensions of the glide symmetric holes control the band-gap and in this case are: period per_{glide} = 5 mm, radius r_{glide} = 1.75 mm, air gap $h_{gap,glide}$ = 0.01 mm, depth h_{glide} = 2 mm. The cross-section of the gap waveguide with glide symmetric holes of the above dimensions, is shown in Fig. 7.7. It can be seen that the waves mainly propagate in the groove waveguide, and the smalls amounts of energy leaking through the gap between the lateral upper and lower plates, are severely attenuated before reaching the outer (third) row of holes.

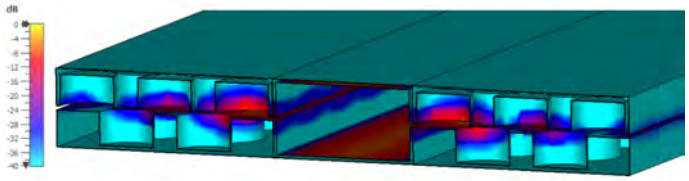

Fig. 7.7. Cross section of the groove gap waveguide with glide symmetric holes. The E-field is mainly confined in the groove, and there is insignificant amounts of energy leaking from the gap between the plates, at 28 GHz.

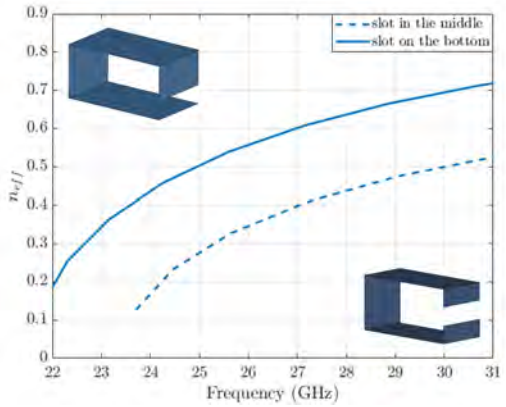

Fig. 7.8. Equivalent refractive index of a slotted standard WR34 rectangular waveguide for the middle and bottom location of the slot. The insets show the two different cases.

Since the energy escapes only through the longitudinal slot, the dispersion of the antenna depends on the geometry of the slot. While periodic slots on the lateral or top wall [173], [198], [199], or a continuous slot on the top broad wall of the waveguide [200],

[201], would also create a leaky-wave antenna, for this design the longitudinal lateral wall slot was selected to illuminate the prism aperture. In addition, the location, middle or bottom, of the slot with respect to the lateral wall of the waveguide, affects the dispersion and consequently the radiation angle (see Eq. 7.2). In Fig. 7.8, the equivalent refractive index of the slotted standard rectangular waveguide is compared for the middle located slot case, and the bottom one (as seen in the inset), for a common size (1 mm). For the present design the slot will be located in the bottom of the lateral wall. After the initial study of the location of the slot, the rectangular waveguide is replaced its gap waveguide version with glide symmetrical holes. This step should take place before studying the dispersion and equivalent refractive index of the radiating element. As reported in [143] the gap waveguide implement with pins, tends to a more dispersive behavior compared to the standard waveguide. The authors of [143] proved that the gap waveguide in dispersion terms would be equal to a standard waveguide whose width is increasing as a function of frequency.

The size of the longitudinal slot controls the equivalent refractive index of the antenna. In this design, the size or width of the radiating slot, is identical to the air gap h_{gap} between the top and bottom metallic plates of the prism structure. As a consequence, this parameter affects both the response of the prism as well as the dispersion of the leaky-wave antenna (see Fig. 7.9). To calculate the equivalent refractive index of the antenna n_L we can either use the propagation constant inside the gap waveguide β_y that can be calculated by simulations, or we can use approximate analytical expressions [173].

7.2.3 Angle of radiation

In the previous sections the dispersion of both the leaky-wave antenna and the metamaterial prism was studied, and the equivalent refractive index in each case, was calculated. Furthermore, it was also shown that the two structures have complementary dispersion characteristics, as seen in Fig. 7.9. This result gives us itself an intuition of the compensation of the change in the final radiation angle.

By using Eq. 7.2 we can calculate the final angle ϕ_0 where the radiation will be

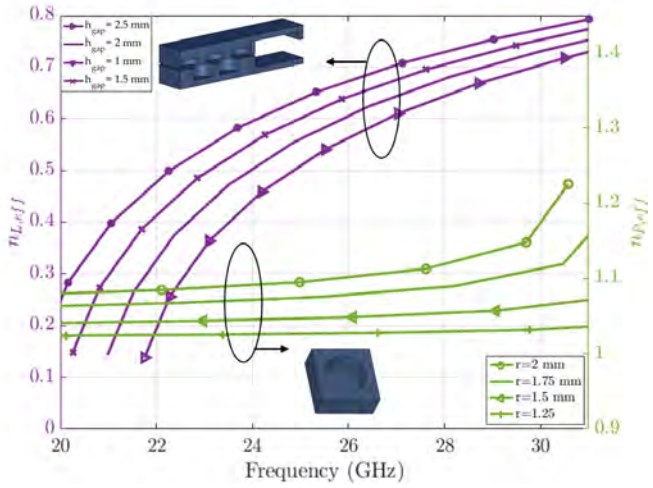

Fig. 7.9. The equivalent refractive indices of the unit cell $n_{p,eff}$ and of the leaky-wave antenna $n_{L,eff}$, represented as a function of the radius r of the hole unit cell, and the size of the slot of the leaky-wave antenna, which is equal to the air gap in the unit cell h_{gap}.

directed. Since ϕ_0 depends on the refractive indices of the two combined structures, their geometrical characteristics will control the final radiation direction. In Fig. 7.10, the direction of radiation is presented as the parameters of the unit cell and the size of the slot change. The aim is to have the same radiation angle for each frequency in the band of interest, thus avoiding the beam squinting effect.

7.3 Antenna design

The gap waveguide that was used to implement the leaky-wave antenna, has a height of 4.318 mm, and width of 8.636 mm, following the dimensions of the standard rectangular WR34 waveguide. The slot that leaks the energy to the prism, has a size of $h_{gap} = 2.35$ mm. This is a crucial parameter for the design. On one hand we have already seen in Sections 7.2.2 & 7.2.3, how it affects the equivalent refractive index and the final radiation angle. On the other hand, since the slot is responsible for the leakage of energy, it also controls the attenuation coefficient α of the groove gap waveguide.

The attenuation should be such, in order to radiate the majority of the energy before reaching the end of the waveguide [162]. As discussed in Chapter 6, for large values

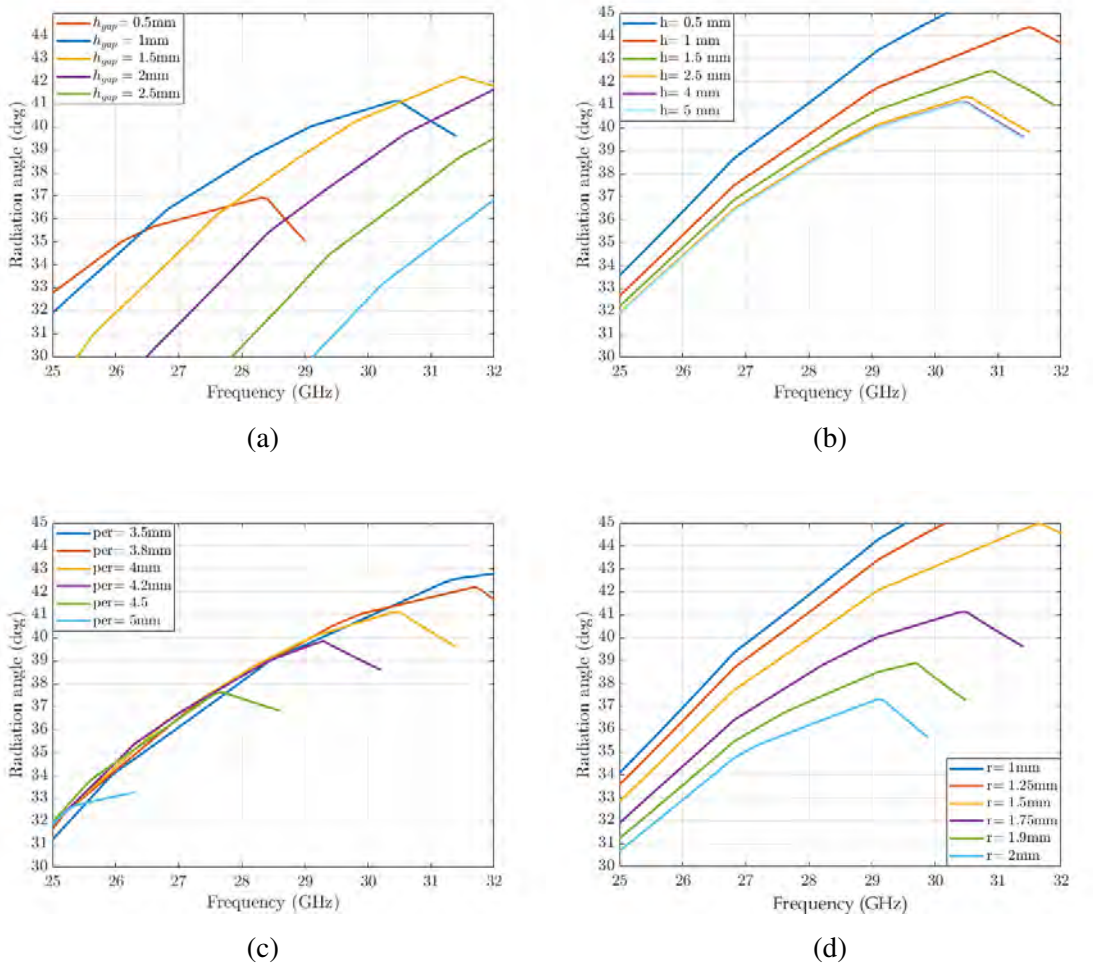

Fig. 7.10. The resulting angle of radiation as a function of the parameters of the hole unit cell for: (a) changing air gap, (b) changing height of hole, (c) changing the period, and (d) changing the radius of the hole. For these variations, the initial values of the unit cell were: h = 4 mm, per = 4 mm, r = 1.75 mm, h_{gap} = 1 mm, w = 1 mm.

of α the radiation happens very fast and the effective aperture of the antenna is small in comparison to its actual physical size. To obtain a high gain antenna, the attenuation coefficient must be tailored for the requirements of the design.

Furthermore, as mentioned before, the size of the slot is identical to the air gap between the two metallic plates in the prism and its unit cell. Since this parameter h_{gap} is chosen based on the performance of the leaky-wave antenna (attenuation and dispersion), the rest of the parameters of the unit cell of the prism, should be selected based on the final angle of radiation. After a parametric study, the final dimensions of the unit cell are: period per = 4.38 mm, radius r = 2 mm, and depth h = 4 mm. The aforementioned values, result to a final radiation angle $\phi_0 = 50.5^o$. After careful observation of the calculated results we decided to allow ±1 degree of change in the direction of maximum radiation.

The total length of the antenna is $L = 10\lambda$, with λ at 30 GHz (100 mm). The phase front should be parallel to the radiating side of the prism. Consequently, the prism was cut under an angle of 50.5 degrees. The radiating side of the prism has a length equal to $Lsin\phi$.

The other lateral side of the gap waveguide, is made of glide symmetric holes placed on two parallel metallic plates, with dimensions as mentioned in Section 7.2.2.

A flare transition was placed on the radiating side, in order to have a smooth impedance transition from the prism to free space to avoid strong reflections that would influence the radiation patterns. To design the flare, its S_{11} parameter was studied, by placing a waveguide port at the point where the prism would radiate into the flare, and where the distance between the top and bottom parts of the flare is equal to h_{gap} the air gap of the prism (see inset Fig. 7.11). The final reflection coefficient of the designed transition can be seen in Fig. 7.11.

Another consideration we had to make, was the alignment of the holes with respect to the three sides of the prism. There are three possible alignments, that are shown in Fig. 7.12. In the first one, the holes are placed in such way to be aligned with the radiation angle ϕ and also the phase front (i.e.the radiating side of the prism). The second possible configuration, is with the holes aligned with the radiation angle but this time also with the waveguide. The third possible alignment is with the radiating side of the prism and the waveguide but not with the radiation angle. Based on the fundamental hypothesis of

this design, that the holes should compensate for the dispersion of the antenna, and also by calculating the angle of radiation, it is apparent that the last alignment of the holes is not profitable as it does not correct the angle of radiation. After the comparison of the results of the other two alignments (A,B in Fig. 7.12), the first one was selected due to the angle stability it exhibits. This is due to the fact that the refractive index of the holes, was calculated considering the first region of the Brillouin diagram that corresponds to a specific direction (see Fig. 7.2 & 7.3); while for other directions the result would be different.

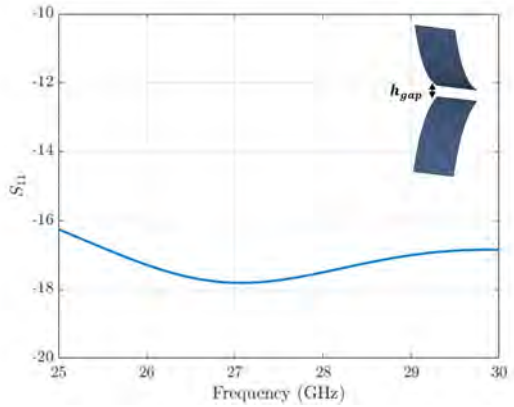

Fig. 7.11. The S_{11} of the flare (shown in the inset), which was designed to avoid reflections in the transition from the prism to free space.

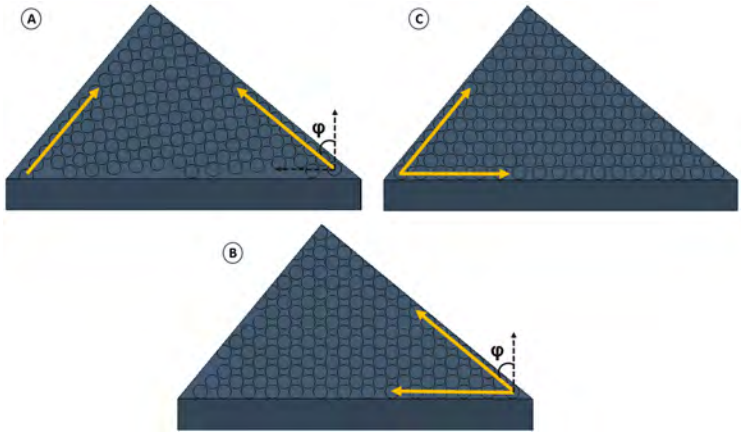

Fig. 7.12. Representation of the three cases of alignment of the holes with respect to the geometry of the prism antenna: A) the holes are aligned with the radiation angle ϕ and the radiating side of the prism, B) holes aligned with the radiation angle and the waveguide, and C) alignment with the radiating side of the prism and with the waveguide.

7.4 Results

7.4.1 Simulated antenna

In this section the results of the full-wave simulations will be presented and discussed. To obtain the simulated results, CST Microwave studio was used for both the full structure and the unit cells.

In Fig. 7.13, the S-parameters of the two ports of the gap waveguide are presented and correspond to the design A as seen in Fig. 7.12. Good levels of return loss are observed for the band of interest. The low S_{21} shows that the energy is radiated before reaching the end of the antenna. Thus this waveguide port can be replaced by an open end later on the fabricated model. Prior to this step, the S_{11} parameter of the antenna was simulated with an open ended gap waveguide, and no difference was observed in the return loss.

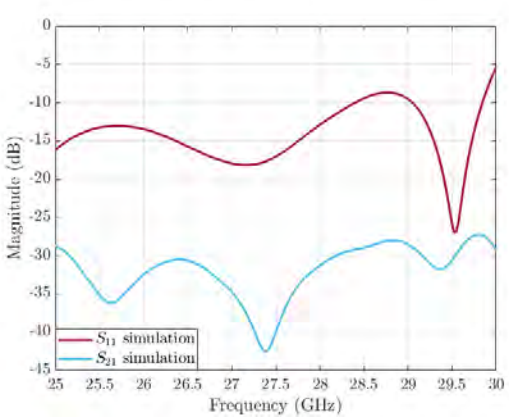

Fig. 7.13. S_{11} and S_{21} parameters of the prism antenna.

The resulting radiation patterns are shown in Fig. 7.14. The realized gain as seen in Table 7.1, varies between 14 dBi and 15.5 dBi. The maximum directivity is 15.4 dBi at 28 GHz.

The radiation angles for different frequencies as seen in Fig. 7.14 are presented in detail in Table 7.1. The same leaky-wave antenna without the prism, has an overall angle variation of ±4.65 degrees, while the maximum variation reaches 9.3^o. When the antenna is combined with the proposed prism, there is an overall variation of $\pm 1.1^o$, and the maximum variation is only 2.2^o. As for the side lobes that are present in the radiation pattern of all

the frequencies, this type of antennas tends to higher side lobes when the radiation happens far from the broadside direction. Moreover, a comparison of the radiation direction of each of the three cases of alignment (Fig. 7.12) is shown in Table 7.2. For the case where the holes are aligned with the radiation angle (design B) the maximum angle variation is similar to that of the antenna without the prism.

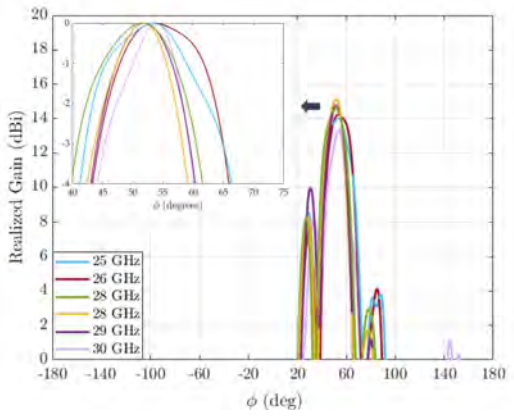

Fig. 7.14. The H-plane realized gain of the simulated antenna. In the inset the normalized patterns show the angular stability of the direction of radiation.

The electric field distribution on the proposed antenna is presented in Fig. 7.15 at four different frequencies. It is evident that the energy is radiated from the slot of the leaky-wave antenna, and approximately no energy reaches the end of the gap waveguide. In addition, from the E-field distribution, we can observe how the phase front progresses through the prism, and that the radiation occurs only on the radiating side of the prism. Furthermore, no strong reflections are observed, thus making the use of the flare transition successful.

In terms of radiation efficiency for the simulated antenna, it is over 95% from 25 GHz to 29 GHz. In similar works [178] the reported efficiency was 98%, while in [179] it reached 90%.

7.4.2 Experimental results

To validate the simulated results, a prototype was manufactured, and is shown in Fig. 7.18. Due to the use of gap waveguide technology, the main body of the antenna

Radiation Angle ϕ (deg)								
Freq (GHz)	25	26	27	28	29	30	Max variation	Overall variation
Without prism	41.5	42.8	44.7	46.4	48.3	50.8	9.3^o	46.15 ± 4.65
With prism-simulations	53.4	53.5	51.6	51.8	51.9	54	2.2^o	52.89 ± 1.1
With prism- measurements	54	54	54	55	55	57	3^o	55.5 ± 1.5
Realized Gain (dBi)								
Without prism	12	13.1	14.2	14.2	13.6	14.4		
With prism-simulations	14	14.23	14.6	15.5	15	14		
With prism- measurements	15	16.9	16	17.8	16.6	12		

Table 7.1. VARIATION OF RADIATION ANGLE AND REALIZED GAIN

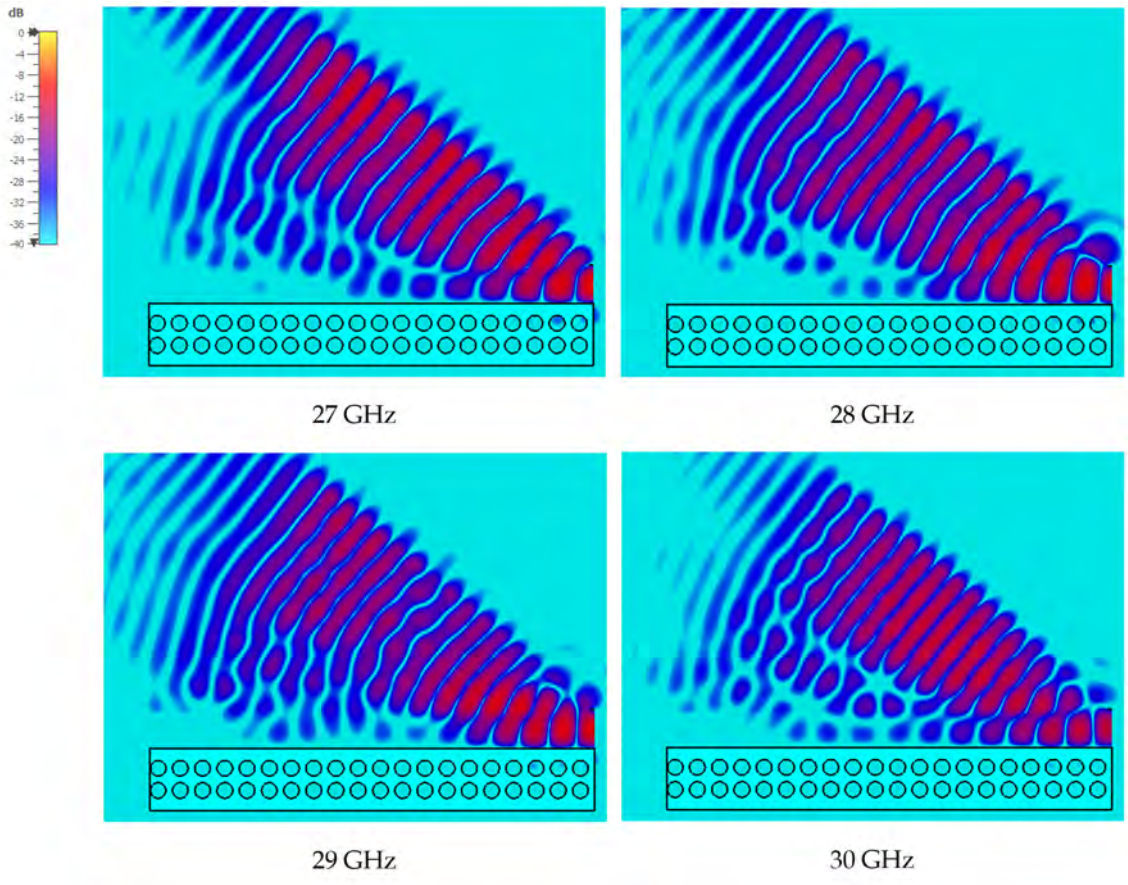

Fig. 7.15. E-field distribution at four different frequencies. The constant angle of radiation is evident. The colour bar applies in all cases.

Radiation Angle ϕ (deg)								
Freq (GHz)	25	26	27	28	29	30	Max variation	Overall variation
Design A	53.4	53.5	51.6	51.8	51.9	54	2.2^o	52.89 ± 1.1
Design B	54.8	54.6	46.2	49.6	50.9	56	9.8^o	51.1 ± 4.9
Design C	52.5	51.5	53.1	51.4	58.8	53.8	3^o	52.3 ± 1.5

Table 7.2. RADIATION ANGLE FOR THE DIFFERENT ALIGNMENTS OF THE HOLES IN THE PRISM.

(prism and leaky-wave waveguide), was fabricated in two pieces. Then these two top and bottom metallic plates were assembled together by two flanges that were used to connect the standard WR34 waveguide transition.

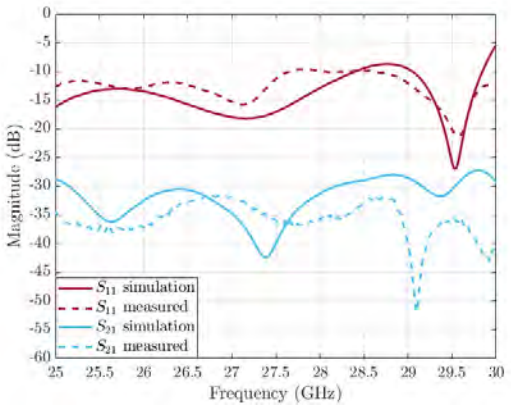

Fig. 7.16. S_{11} and S_{21} parameters of the prism antenna.

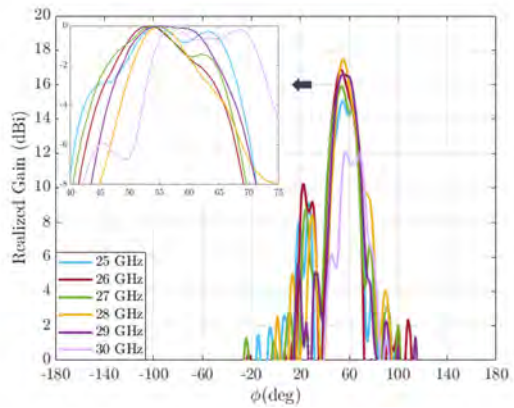

Fig. 7.17. The realized gain of the fabricated prototype. In the inset the normalized patterns show the angular stability of the direction of radiation.

The measured S_{11} of the antenna shows matching levels below -10 dB from 25 GHz

to 30 GHz, and is very similar to the simulated result (Fig. 7.16). The S_{21} showed that significantly low amounts of energy reach the ending of the gap waveguide, as expected from the simulations.

The measured radiation patterns are presented in Fig. 7.17, and the exact values of the realized gain are described in Table 7.1. The normalized patterns (inset Fig. 7.17), demonstrate the small variation in the direction of radiation. However, irregularities in the shape of the radiation patterns in some frequencies appear. This can be due to reflections in the waveguide flange; note that it is located closely to the radiating side of the prism (see Fig.7.18). Also, at 30 GHz, we observe that the realized gain is significantly reduced. This may be a consequence of manufacturing inaccuracies in the air gap h_{gap} between the two plates, that results to a stop band in the holey structure for this frequency. Nevertheless, the maximum radiation in all the frequencies points at the same direction, since the overall variation is $\pm 1.5^o$, compared to the $\pm 1.1^o$ of the simulated antenna. Excluding the result at 30 GHz, the realized gain varies between 15 dBi and 17.8 dBi. As for the side lobe levels, they could be reduced in future applications by using the tapering aperture illumination method as it was described in [179], but adapted to the hole unit cell presented here.

7.5 Conclusions

In this chapter, the design of a non dispersive leaky-wave antenna in groove gap waveguide technology, was presented. Two structures are combined in the presented design: a leaky-wave antenna and a metasurface prism. Both are implemented in groove gap waveguide technology with the use of the simple hole unit-cell. Similar works have been reported [178], [190], however they used the pin unit-cell whose main drawback is found in high frequencies where the pins are very fragile and expensive.

The presented design covers the band 25-30 GHz. The antenna is formed when on one lateral side the wall of the standard rectangular WR34 waveguide is replaced by two metallic plates with glide symmetric holes on both. This higher symmetry structure, prohibits the leakage of radiation between the plates in any direction, due to the electromagnetic band gap created by the glide symmetric unit cell. Hence, no direct contact is required

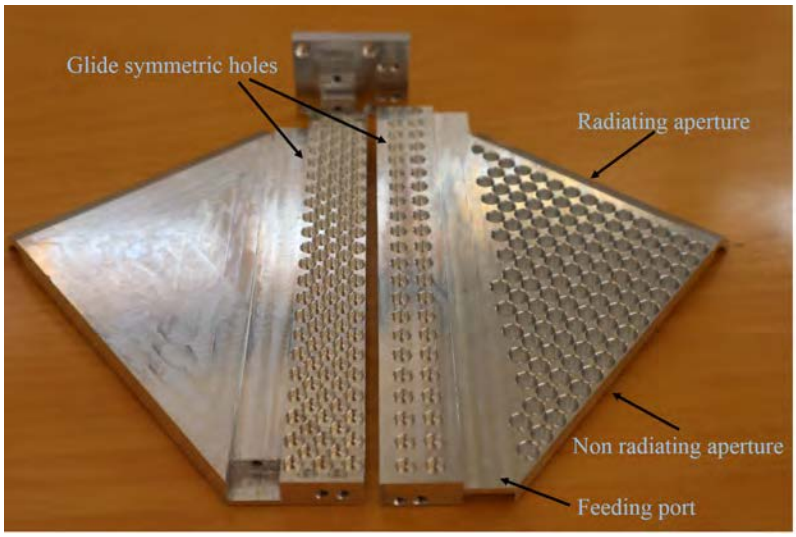

(a)

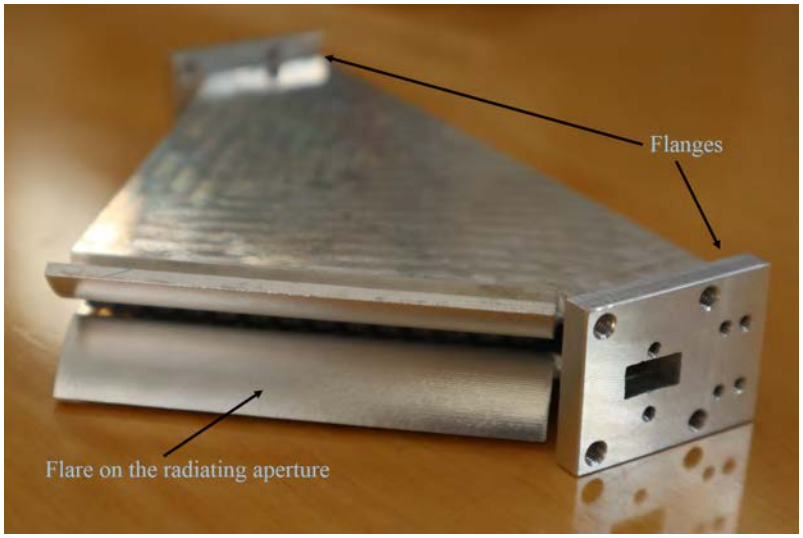

(b)

Fig. 7.18. (a)The two plates of the leaky-wave antenna with the prism. The glide symmetric holes that prevent the radiation can be seen, as well as the dispersive holes of the prism. (b) All the pieces of the proposed antenna assembled together. A flare transition was designed for the radiating side of the prism, to avoid reflections.

and the manufacturing can be simply made in two pieces. The other lateral side, has a longitudinal slot that allows the leakage of radiation from the waveguide [173], thus the leaky-wave antenna element is created. As a consequence, the size of the slot controls the radiation.

The nature of the leaky-wave antenna is dispersive, meaning that the direction of maximum radiation is changing depending on the frequency that propagates in the gap waveguide. In order to manipulate the radiation direction to create a non-dispersive antenna, a metasurface prism was added to the design. The prism is made of holes with a refractive index that also changes with frequency in a complementary way to the leaky-wave antenna. The resulting radiation angle of the simulated model showed only $\pm 1.1^o$ of variation around a central angle, in comparison to $\pm 4.65^o$ of the antenna without the prism.

To validate the simulated results, a prototype was fabricated. Without the need of physical contact due to the gap waveguide, the fabrication of the whole structure was made in two plates (top and bottom), which is one of the advantages of this design. All the components are metallic, making this type of antenna a good candidate for high frequencies, where dielectric parts would have severe losses. In addition the hole unit-cell apart from having easier and less expensive fabrication than the pins, shows robustness even in high frequency bands.

The experimental results, are in very good agreement with the simulated antenna. The measured radiation patterns, showed very small change in the direction of maximum radiation, achieving an overall $\pm 1.5^o$ of variation which is only 0.4^o away from the simulated results. Moreover, low cross polarization levels were measured.

For future applications revisiting the proposed design, the side lobes level could be decreased if the radiation direction is closer to broadside. In addition, improved illumination of the prism aperture could be achieved by controlling the attenuation constant along the slotted gap waveguide. However, the presented antenna is a proof of concept of the viability of the holey metasurfaces for the implementation of a dispersion controlled antenna.

Chapter 8

Array of low profile horn antennas in groove gap waveguide technology

8.1 Introduction

In this chapter we present the design and implementation of a cost-effective array of low profile horn antennas made exclusively in gap waveguide technology [116], [117], [121], [130], [131], [135] and more specifically its groove version [132], [133], [141], [143], as already discussed in previous chapters.

The idea of this design is based on a low profile horn antenna array that was presented in [202]. In said design, the feeding was done in inverted microstrip gap waveguide. In order to minimize the losses, we have decided to implement the feeding network in groove gap waveguide. Additionally, since we are aiming to a cost-effective design, the classical bed of nails [120], is replaced by holes in glide symmetry [127]–[129] that create the electromagnetic band gap (EBG) that avoids the radiation to free space. As seen in the low dispersive leaky-wave antenna (Chapter 7), due to the use of the holey EBG structure, the manufacturing cost can be significantly reduced. Nevertheless, there are some limitations introduced to the design, since the holes are too large and make impossible the use of a classical corporate feeding network [151]–[154], [203], [204]. Thus, the feeding of the horn antennas is done through a network of groove waveguides with resonant slots. The

number of the radiating elements of the array can be arbitrarily selected. In the presented design, we chose to implement a 6x6 array, however the methodology of the design can be used for larger or smaller arrays.

The central frequency of the design that will be presented, is 38 GHz. Due to the fact that the array is entirely made of aluminium, and has neither dielectric nor very small parts, it can be easily scaled to any frequency, maintaining its performance.

This chapter is organized as follows: first the design of the low profile horn antenna that is the basic and key element of the array, will be presented and discussed. Then a linear array of horn antennas fed by a slotted waveguide will be designed, and afterwards the linear array will be extended to a planar 6x6 array.

8.2 Low profile horn antenna design

The proposed design consists on a feeding network that divides uniformly the incoming energy to a planar array of low profile horn antennas. This type of aperture antenna was chosen as a simple solution to achieve increased directivity levels of a slotted waveguide.

A standard pyramidal horn antenna [90] consists on four flaring sides that end in a larger aperture. This geometry can be seen in Fig. 8.1 (b). Typically the flaring is done in both E and H planes of the horn. The flare of a horn antenna is important as it acts as a gradual transition in order to achieve impedance matching from the feeding aperture (usually fed by waveguide) to free space.

The length and angle of the flare are critical to define the performance of a horn antenna. The electromagnetic waves travel within the horn in the form of spherical wavefronts, with the phase center being in the apex of the structure. Due to the different distance of the center and the edges to the apex of the horn, the phase increases from the edges of the antenna aperture to the center, thus a phase difference is produced. This phase error can reduce significantly the performance of the antenna. If the flare angle is too large, and the horn "opens" too fast (i.e., small length of flare), the phase error will be higher, and the beamwidth will increase. For a narrower beamwidth, a larger length of the flare

must be used to keep the phase error constant. Consequently, the flare length should not be too small, and the flare angle should not be very large, as observed for instance in commercially available horns.

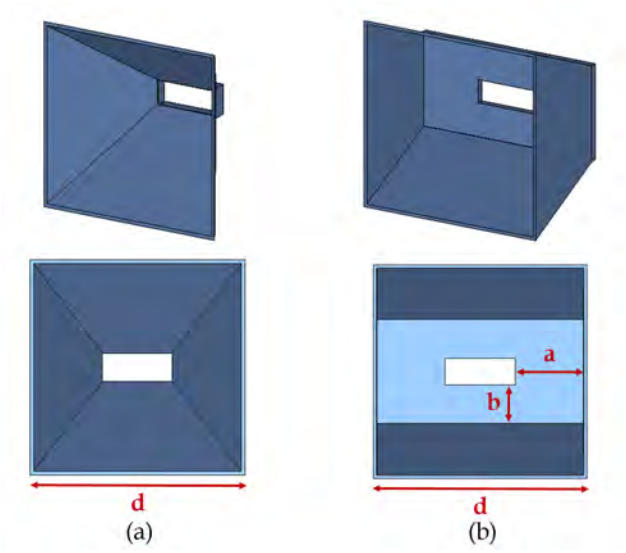

Fig. 8.1. 3D representation of the two horn antennas studied for this array design: (a) shows the standard pyramidal horn antenna that was taken as reference for comparison, (b) shows the dual-mode horn antenna and its geometry parameters.

Aiming to design a planar array of low profile horns as in [202], the dual-mode horn antenna was studied. The geometry of the dual-mode horn is shown in Fig. 8.1 (a). This antenna achieves the excitation of two modes, the TE_{30} and the dominant TE_{10} mode. The excitation of the two modes is done by creating a step in the H plane of the horn antenna, and only the E plane sides are flared. This step is defined by the distance from the feeding slot of the horn to the side, denoted as "a" in Fig. 8.1, and it controls the excitation of the second mode in the horn.

The dual-mode excitation results to significant difference in the efficiency of the two horn antennas when compared. In Fig. 8.2, the amplitude distribution of the field in the aperture of the two horns is shown. The uniformity of the distribution in the case of the dual-mode horn can be evidenced, in comparison to the distribution of the standard horn antenna. The uniform distribution, is due to the simultaneous combination of the TE_{10} and TE_{30} modes that have opposite phase. Fig. 8.3 shows the phase in the aperture of the two

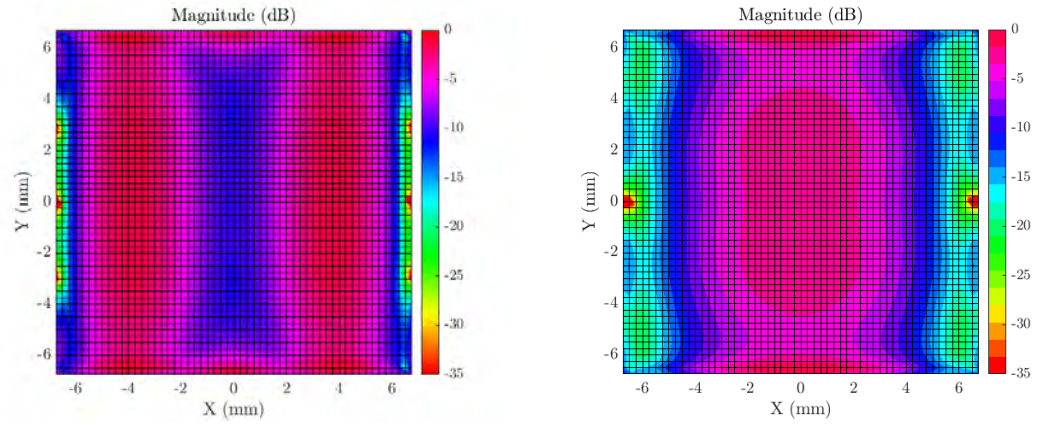

Fig. 8.2. Amplitude distribution of the field in the aperture of the dual-mode horn (left) and the standard horn (right).

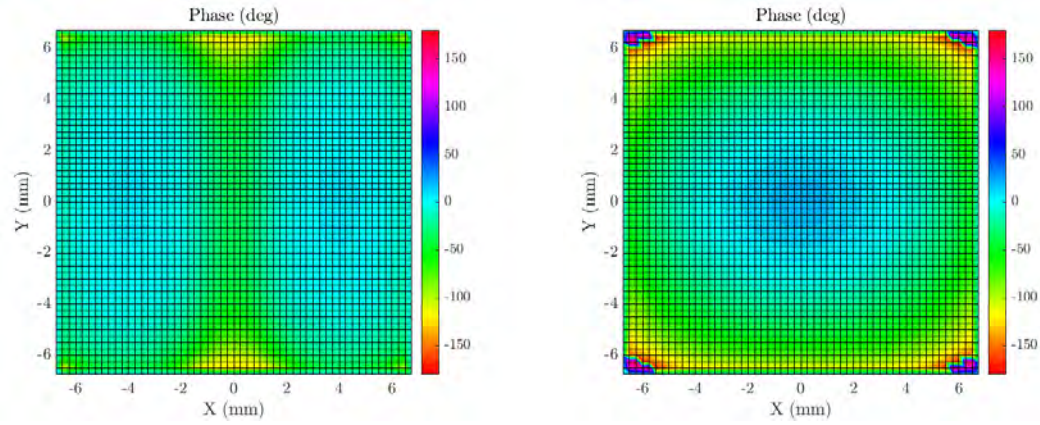

Fig. 8.3. Phase distribution of the field in the dual-mode horn (left) and the pyramidal horn (right).

horn antennas. As mentioned before, in the case of the standard horn antenna, the phase is increasing from the edge to the center of the horn, and a phase difference is produced that reduces the efficiency of the antenna. However, the phase of the fields in the aperture of the dual-mode horn, shows more uniform distribution, and thus the phase error is reduced.

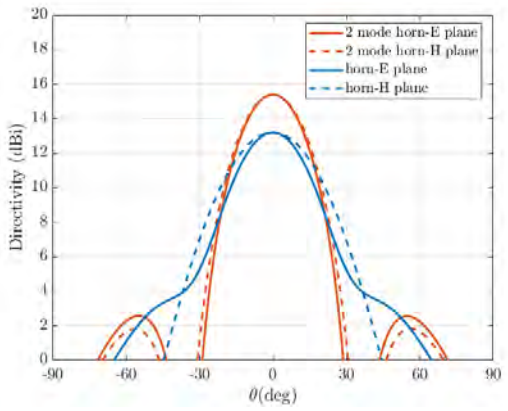

Fig. 8.4. Directivity achieved with the dual-mode horn antenna (purple line) and the reference standard pyramidal horn (blue line) for both E and H planes.

The above, lead to differences in the radiation patterns of the two antennas, seen in Fig. 8.4. The dual-mode horn achieves 15.4 dBi of directivity, while the pyramidal horn antenna reaches only 13.2 dBi. The aperture efficiency is 93% for the designed dual-horn antenna, and only 56% for the standard pyramidal horn. Thus the presented dual-mode horn is a better candidate for the implementation of the array under research.

The aforementioned results, correspond to the following optimized antenna dimensions for the dual-horn antenna: $a = 4.3$ mm, $b = 1.9$ mm, and $d = 13.57$ mm, with length of the horn $h_1 = 7.79$ mm which is approximately λ_0 at 38 GHz. For the pyramidal antenna, the size d is the same as in the dual-mode horn, and the length as well. The size d of the designed dual-mode horn antenna, is related with the inter-element distance of the array. In fact, the dimensions of the low profile horns, are defined by the transverse slots that directly feed the horns, and that must be separated λ_g. Therefore this is the inter-element distance, and the horn antennas are designed to have an aperture $d = \lambda_g$.

8.3 Linear array of low profile horn antennas

Aiming to use the low-profile horn antenna that was designed in the previous section, in a planar array, the first step is to study the case of a linear array of horn antennas [205]. This first step in the implementation of the planar array is critical, since we are aiming to achieve uniform amplitude and phase in all the radiating elements, and the linear array is a convenient structure for the studying of the feed system.

The linear array used in this step of the design process, consists of 6 dual-mode antennas, that are fed by a standard waveguide with transverse slots etched on its upper broad wall [182], [206]. The transverse slots are typically thin ($< 0.1\lambda$) with a starting length of $\lambda/2$, and they must interrupt the surface currents in order to radiate.

Let us note here a key point in the design. The spacing between the transverse slots used to directly feed the horns, is one guided wavelength which was intentionally chosen to be equal to $1.7\lambda_0$, and that is also the size of the aperture of the horn antennas. In order to force that value of guided wavelength, the transverse dimension or width of the standard WR-28 that was taken as reference, was modified to 4.88 mm. Nevertheless, the height of the WR-28 waveguide was maintained 3.56 mm.

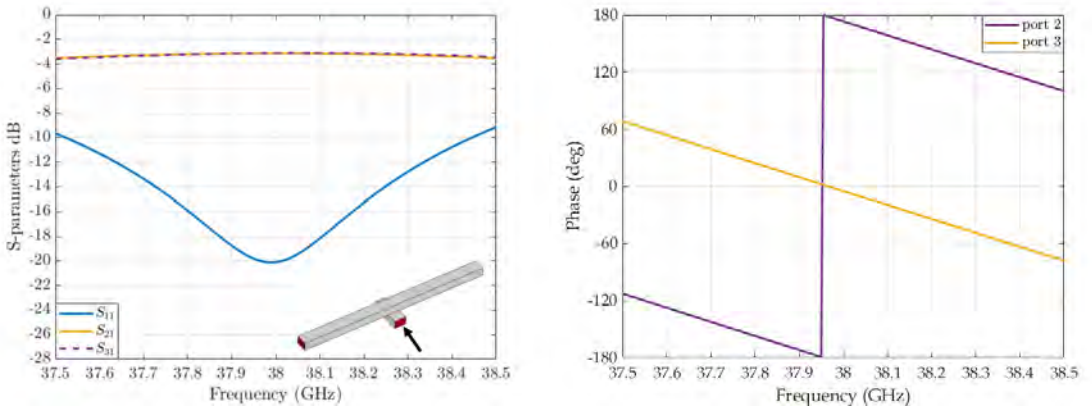

(a) (b)

Fig. 8.5. Coupling achieved with a single inclined slot, in form of S-parameters(a). The inset shows the simulated structure, and the arrow indicates the port of direct feeding (port 1).The phase of the ports on the upper waveguide in (b) shows that there is a difference of 180 degrees between the two ports.

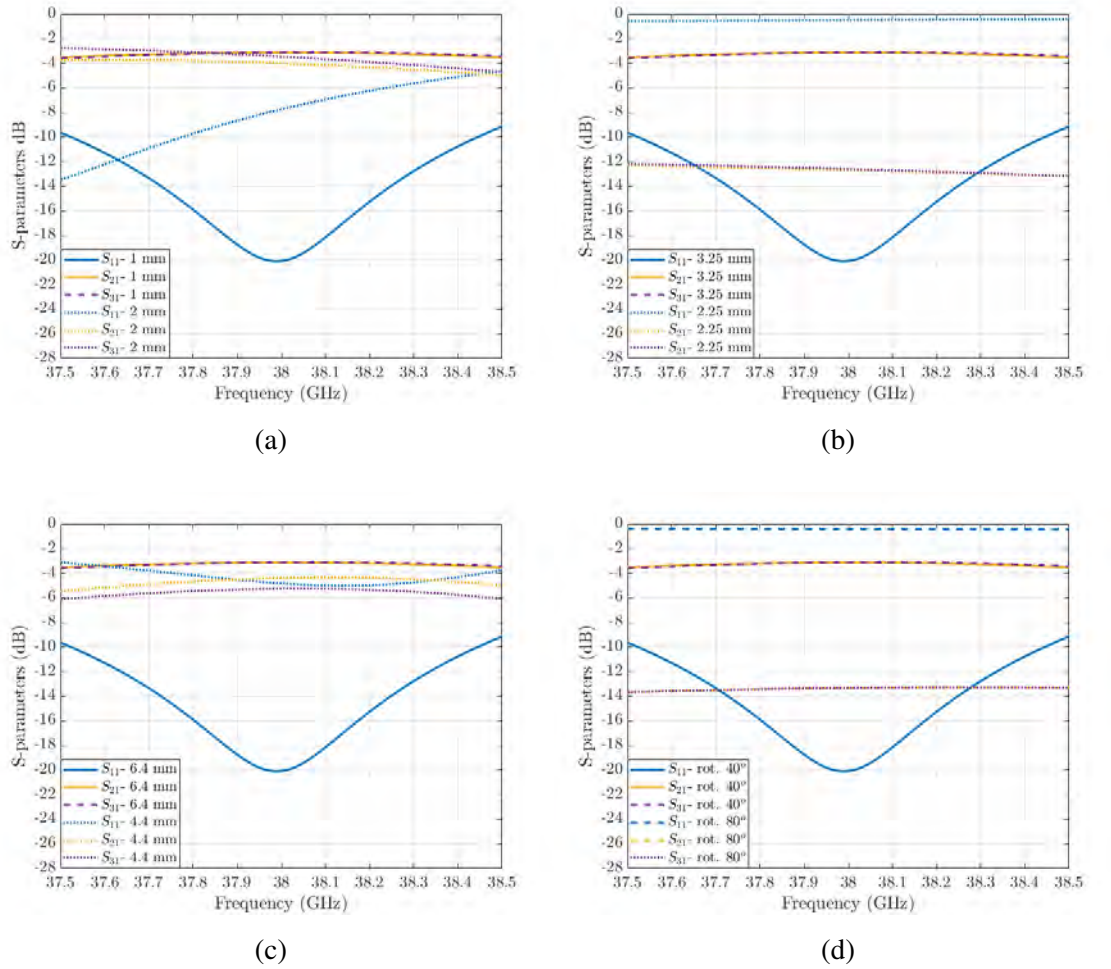

Fig. 8.6. S-parameters of the configuration shown in Fig. 8.5(a), for different values of the inclined slot for: (a) the width, (b) the length, (c) the distance from the beginning of the waveguide and (d) the rotation of the slot.

To feed the waveguide that radiates through the transverse slots into the horn antennas, we used a waveguide with inclined longitudinal slot [207]–[209] etched on its upper broad-wall. This waveguide is directly fed by a waveguide port in the simulation environment. To observe how the inclined slot couples the energy to the radiating waveguide, first we used a structure without radiating slots, and with waveguide ports at both ends of the radiating waveguide, as seen in the inset of Fig. 8.5(a), with the arrow indicating the feeding point. In the same figure, the S-parameters of the structure show how the energy is divided in two equal parts. The phase shown in Fig. 8.5(b) of the two ports in the radiating waveguide, was observed with 180 degrees of difference. This is due to the direction of inclination of the slot [206]. For reversed direction of inclination, the polarity of the induced E-field in the coupling slot changes, and as a result the phase of the two ports in Fig. 8.5(b) would be inter-changed.

The above results correspond to the following parameters of the inclined coupling slot: width 1 mm, length 3.25 mm, distance from the beginning of the waveguide 6.4 mm, and inclination 40^o. The inclination and the dimensions of the coupling slot are critical for its electromagnetic behavior, and will be discussed in Section 8.4.2. The results for different values of the slot are presented in Fig. 8.6.

Once the coupling through the inclined slot was verified, the next step was the implementation of a linear array. This array consisted on a waveguide with direct feed by a waveguide port, with an inclined slot on its upper broad wall. Through this slot the energy is coupled to another waveguide as shown in the inset of Fig. 8.5(a), that has transverse slots etched on the upper broad wall, with distance λ_g as already mentioned. A total of 6 transverse slots were placed to feed 6 dual-mode horn antennas.

The 3D radiation pattern of this configuration is shown in Fig. 8.7 with directivity reaching 22.6 dBi. The S_{11} parameter of the array can be seen in Fig. 8.8. By using field probes in the slots that feed the horn antennas, we verified the uniform amplitude and phase distribution in all the elements, as seen in Fig. 8.9. To obtain these results, the width of the inclined slot at the bottom waveguide was slightly modified to 0.95 mm, keeping the same length and degrees of inclination. Furthermore, the dimensions of the transverse slots that feed the horn antennas are: width 1.7 mm, length 4.5 mm.

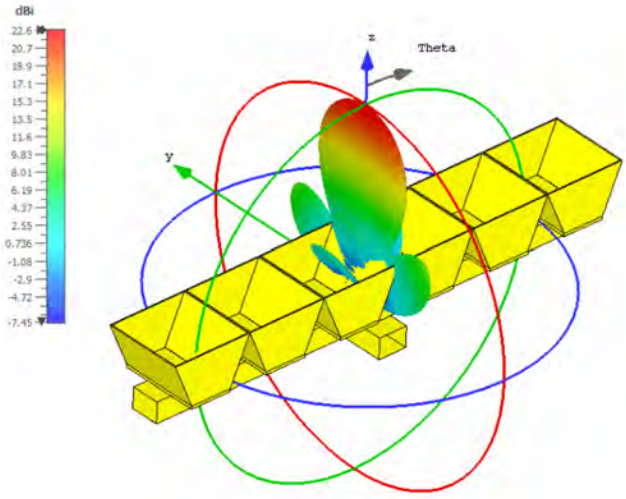

Fig. 8.7. 3D radiation pattern of the linear array of horn antennas.

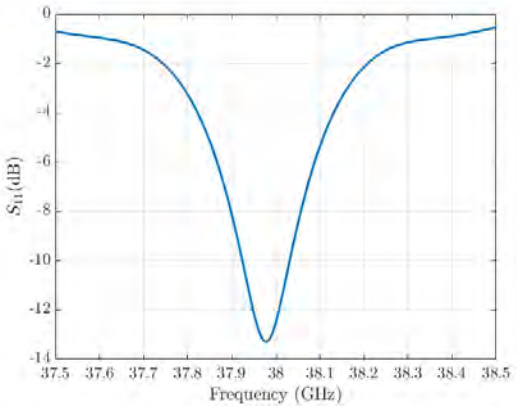

Fig. 8.8. S_{11} of the linear array of horn antennas.

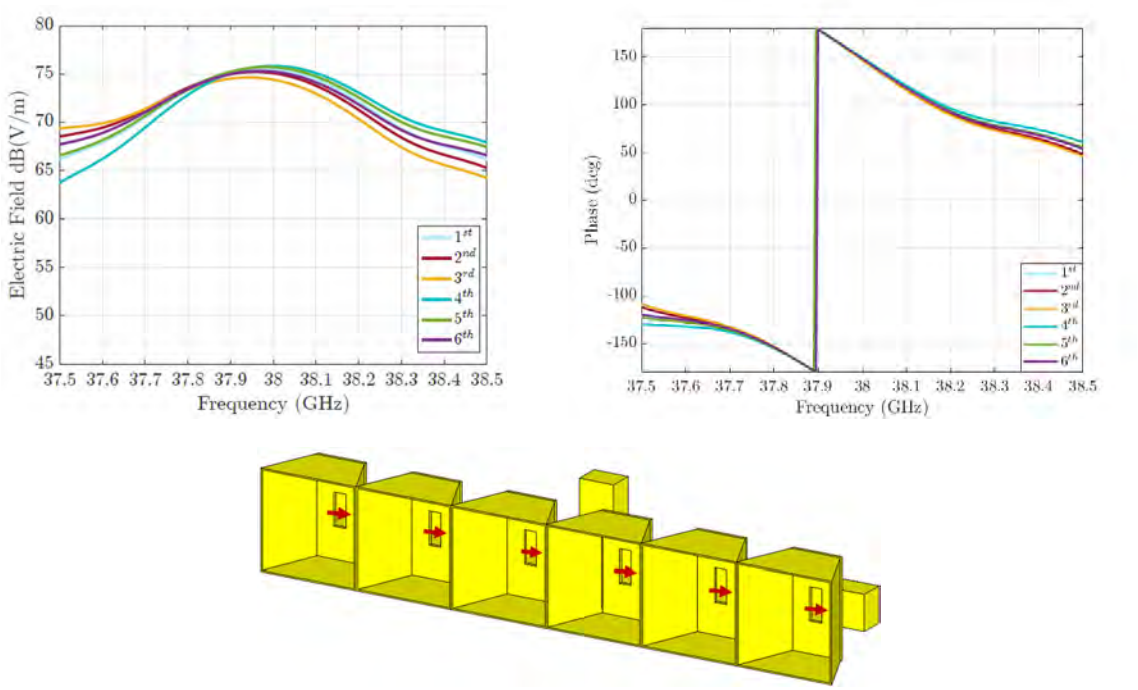

Fig. 8.9. Amplitude and phase of the radiating slots that feed the horn antennas. To get this value, field probes were used during the simulation (red arrows), at the corresponding slots.

8.4 Planar array

In the previous steps of the design, we have studied the dual-mode horn antenna, and then we expanded it in a linear array using the standard WR-28 with transverse slots and width modified in order to achieve a guided wavelength of $1.7\lambda_0$.

In the next step we develop a directive planar antenna array in gap waveguide technology, which simplifies the fabrication process since no metal contact is required. In addition, with this technology, very low losses can be obtained.

8.4.1 Groove gap waveguide technology version

As mentioned before, for this array the groove waveguide will be implemented with glide symmetrical holes [127]–[129] instead of the classical bed of nails [120]. As in Chapter 7, the holes are located at the top and bottom of a two parallel plate structure. The holey version of the groove waveguide, is more cost-effective and has easier manufacturing

process. However, as it will be shown, the holes need to have large radius in order to create the required electromagnetic band-gap, thus prohibiting the use of corporate feeding networks as in [149], [210].

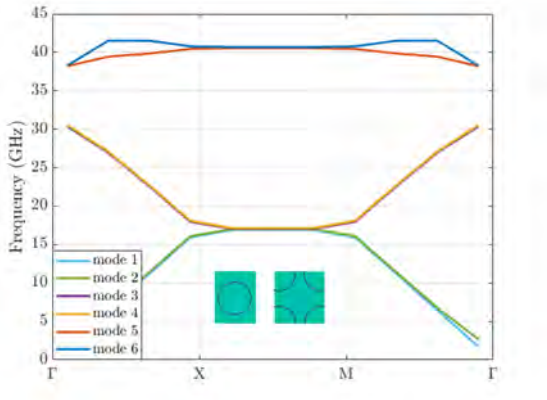

Fig. 8.10. Dispersion diagram of the glide symmetric hole unit cell, with dimensions: radius $r = 2.7$ mm, periodicity $p = 8.5$ mm, depth $d = 3$ mm. The band gap covers the central frequency of the design 38 GHz.

For the implementation in groove gap waveguide technology, first the study of the unit cell takes place. The radius r, the periodicity p, and the depth d of the hole are the critical parameters that define the electromagnetic behavior of the unit cell. The air gap between the two metallic plates which is also important, was set to $h_{gap} = 0.01$ mm for this design[4].

For the following dimensions, an electromagnetic band-gap that covers 38 GHz, is created: $r = 2.7$ mm, $p = 8.5$ mm, $d = 3$ mm (Fig. 8.10). Let us note here that the hole unit cell was simulated in an infinite array, using glide symmetry in both x and y directions.

8.4.2 The feeding network

The planar array is composed of n linear sub-arrays as the one shown in Section 8.3. For the purpose of this design, we implemented a 6x6 planar array. Nevertheless, this design offers the possibility for a subjectively chosen number of elements in both E and H planes. The feeding of the each T-branch or linear sub-array, is done with waveguides implemented

[4]In practise there will be no gap; however this value represents possible gap between the parts of the prototype due to fabrication errors

in groove gap waveguide technology as seen in Fig. 8.11 (denoted as *radiating waveguides*). A feeding waveguide is placed in the middle of the structure (see Fig. 8.11), and couples the energy to the radiating waveguides, through inclined slots [211]. This resonant structure of feeding is based on the standing waves inside the waveguide, and was initially used to implement the linear array of horns, as explained in Section 8.3. However, at this step the standard waveguide is abandoned and both the feeding and the radiating waveguides, are surrounded by holes in glide symmetry, to obtain the required electromagnetic band-gap as described in Section 8.4.1.

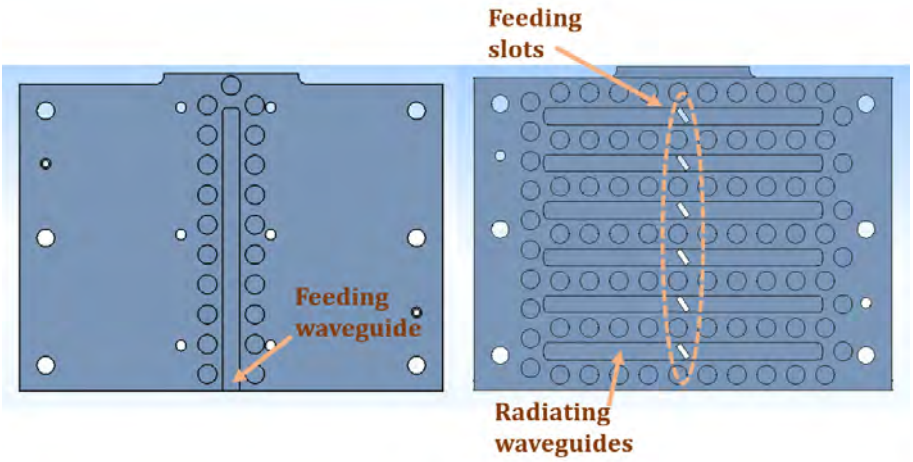

Fig. 8.11. 2D representation of the groove gap waveguide that is directly fed by a waveguide transition (right), and the inclined coupled slots that feed each of the radiating waveguides (left).

Aiming to achieve uniform amplitude and phase in all the coupling slots, first we studied the case of two waveguides fed centrally with two inclined coupling slots (as seen in Fig. 8.13). For practical reasons, we used ports at the ending of the two waveguides, in order to see the energy coupled through the feeding slot.

For the conducting walls of a waveguide, we know that the linear conduction current density on the surface is expressed as: $\mathbf{J}_s$=**n** x **H**, with **n** being the normal to the surface unit vector, and **H** is the magnetic field for the particular mode that is propagating. When a discontinuity is created on the conducting surface, and interrupts $\mathbf{J}_s$, radiation can occur if the structure is open [206]. In [182], Oliner presented a study of the different geometries of the radiating slots, in terms of their electromagnetic characteristics. Transverse slots,

longitudinal inclined or with an offset, or even side wall slots have been studied in literature, however for the presented design inclined longitudinal slots will be used.

In general, for a longitudinal slot that is centrally placed, no radiation can be produced, since it does not interrupt significantly the conduction current (shown in Fig. 8.12). However, when the longitudinal slot has some degrees of inclination [182], [207], then it interrupts the longitudinal conduction current $\mathbf{J}_{sy}$ in this case, and thus radiation is produced. Consequently, the inclination of the slots strongly affects the coupled energy [208], [209]. From a circuit equivalent point of view, the impedance of the slot depends on the inclination angle [212]–[214]. Additionally, the direction of inclination changes the polarity of the electric field induced in the slot.

With the case of a single waveguide fed centrally by an inclined slot, already reported in Fig. 8.5, this T-branch is extended to two fed waveguides as seen in Fig. 8.13. In the same figure, the amplitude in form of S-parameters is presented along with the return loss of the feeding waveguide port. Note how the amplitude is practically identical for all the ports. The phase of this configuration can be seen in Fig. 8.13 as well as the structure in the inset. At the central frequency, phase difference of approximately 180^o was observed between the two ports of each waveguide, which is due to the opposite direction of propagation. As mentioned, the direction of inclination has an effect on the polarity of the electric field. This can be evidenced by changing the inclination direction of one of the two coupling slots. Fig. 8.14 shows a comparison of the phase of the waves as they reach the end of each respective waveguide. Indeed a difference of 90^o in the inclination of the two coupling slots, results to a change in the phase of the coupled wave, as perceived by the waveguide ports. However, the amplitude of the coupled energy does not change, and for both cases is as shown in Fig. 8.13. For the purposes of this design, all the coupled slots were chosen to have the same direction of inclination.

Other parameters that affect the electromagnetic behavior of the slots, are the length, the width, the distance from the beginning (or ending) of the waveguide, as well as the thickness of the broad wall where the slot is etched. In order to radiate, the slots should reach a resonant length [206], [208]. The width of the slot, plays an important role in the bandwidth obtained, as for wider slots, the bandwidth is increased [215]. Furthermore,

the thickness of the broad wall, and consequently the thickness or vertical width of the slot, influences the coupled energy, and it also limits the bandwidth [216], [217]. The position of the slots, that can be easily defined by their distance from the beginning of the waveguide, is important as it should be following the standing-wave peaks, as a resonant type feed system based on standing waves will be used. This distance should be initially set to $\lambda_{g1}/2$, where $\lambda_{g1} = 1.7\lambda_0$ in this case, and then it should be optimized.

For the results presented so far in Fig. 8.13 but also in Fig. 8.14, the coupling slot is 1.3 mm wide, and 3.25 mm long, and is placed with an angle of 40^o with respect to the longitudinal axis of the feeding waveguide. The distance of the slot to the feeding point of the waveguide is 5.4 mm.

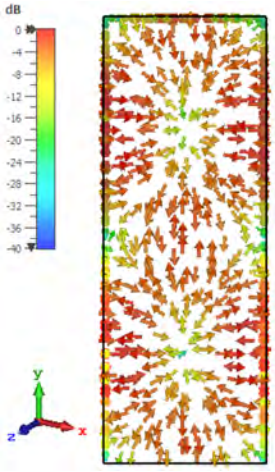

Fig. 8.12. Representation of the surface currents $\mathbf{J}_s$ in a closed end waveguide.

This design is flexible in terms of the size of the planar array wished to be designed. The feeding structure that has just been described, can be extended to any subjective number of radiating waveguides (and corresponding coupling slots). Let us mention here, that as the number of coupling slots increases and more radiating waveguides are placed, the parameters of the coupling slots must be slightly modified in order to maximize the performance of the feeding network. The number of coupling slots, also affects the bandwidth of the array [215]–[217].

For the proposed array, six coupling slots were required to feed the six radiating waveguides. In Fig. 8.15, the phase and amplitude of the coupled energy with the inclined

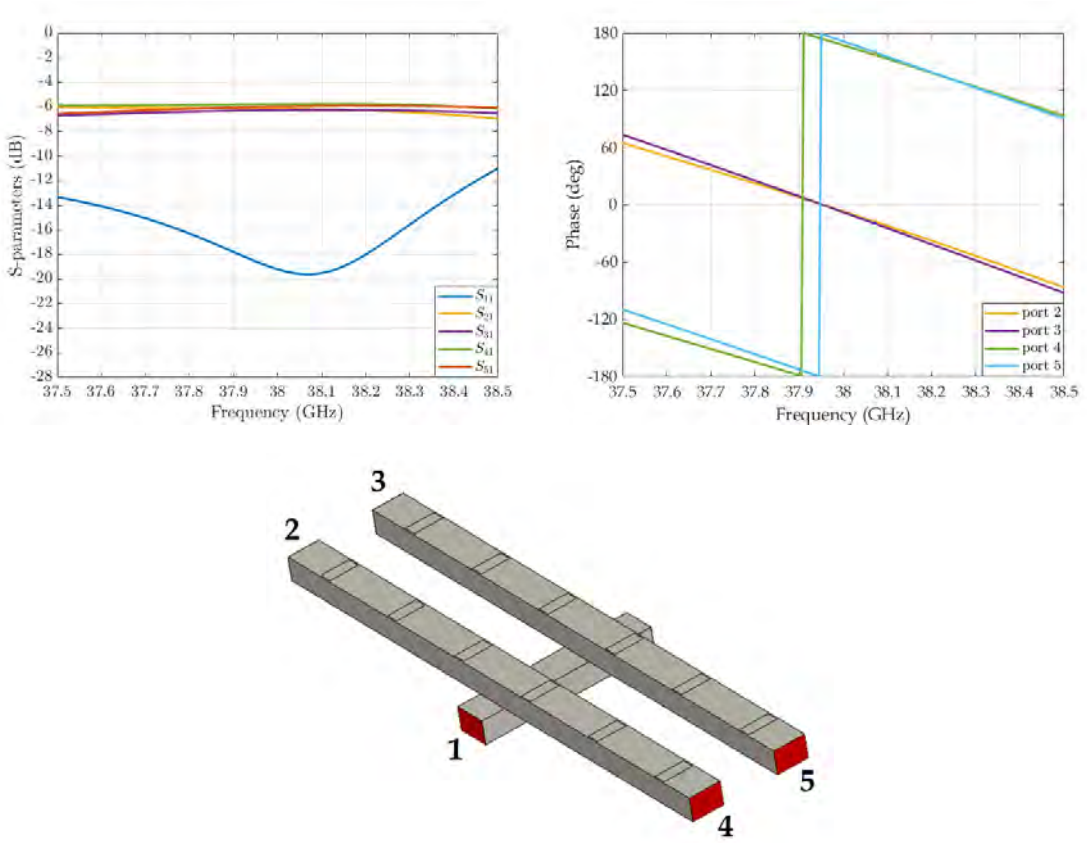

Fig. 8.13. S-parameters of the two waveguides fed by two inclined slots. Low return loss is observed as well as uniform coupling in both waveguides. The phase of the ports revealed a difference of 180 degrees in the corresponding ports of the same waveguide. Ports 2,4 correspond to one waveguide, and ports 3,5 are placed on the second waveguide. Port 1 is the feeding point of the structure.

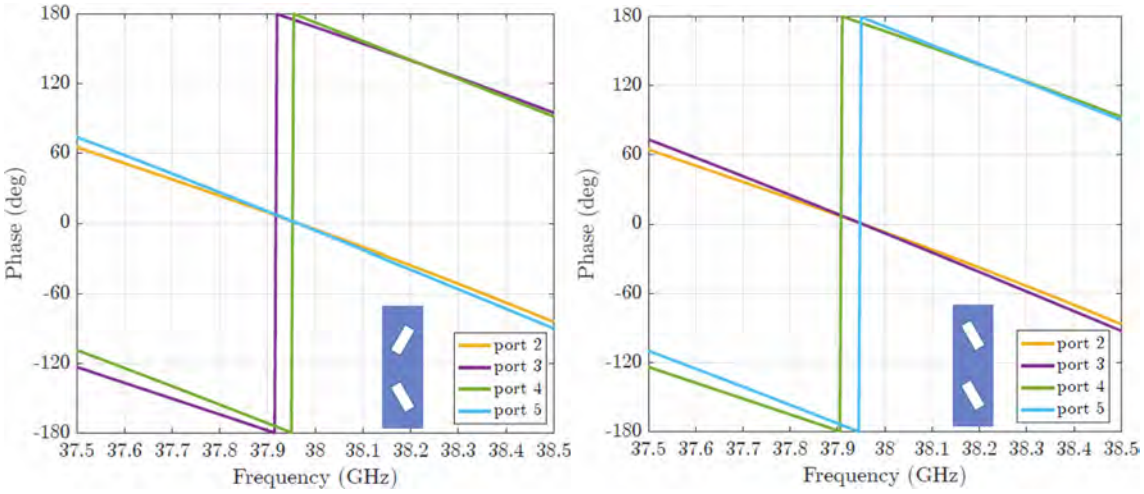

(a) (b)

Fig. 8.14. The phase of the coupled energy for: slots with opposite direction of inclination (a), and with the same direction of inclination (b). The phase was calculated with ports at the ends of each waveguide. Port 2,3 correspond to the first waveguide, and ports 4,5 correspond to the second one.

slots, is shown. It can be observed that at the central frequency, all the slots couple the same amplitude of electric field, and with the same phase for all the six slots. These results were obtained for slots with width 1.55 mm and length 4.7 mm, and 35^o inclination. The distance between the first coupling slot and the beginning of the feeding waveguide is 7.9 mm. As for their periodicity, it is the same as for the radiating waveguides, and is equal to $1.7\lambda_0$. Later in the design, to optimize the performance of the feeding network, the periodicity was modified by +0.15 mm. Thus, the coupling slots, the radiating waveguides, and the horn antennas have a final periodicity of 13.57 mm. The aperture of the horn antennas is also modified according to this value. The amplitude and phase with which the horns are fed can be seen in Fig. 8.16 for the radiating slots with dimensions: width 1.8 mm, length 4.5 mm, and periodicity 13.57 mm.

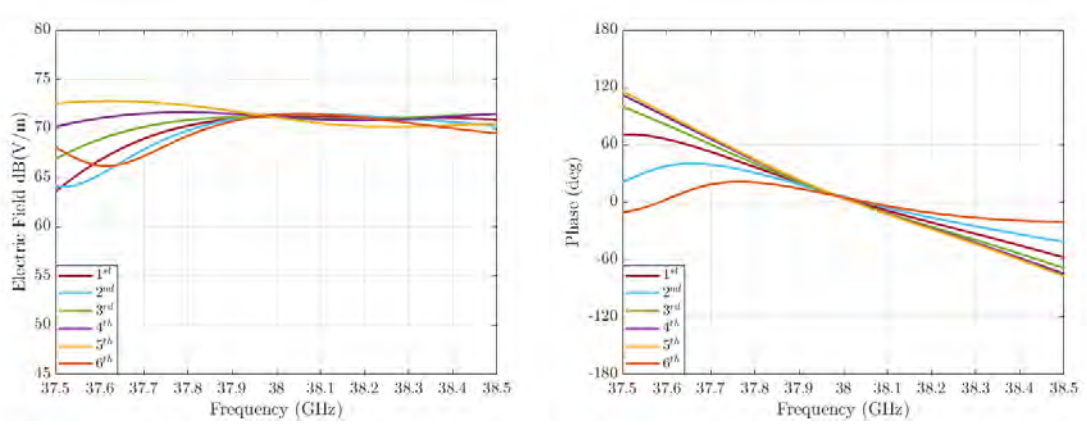

(a) (b)

Fig. 8.15. Amplitude (a) and phase (b) of the coupling inclined slots that are used to feed each of the six radiating waveguides. At 38 GHz, the energy is distributed with equal amplitude and phase through all the inclined coupling slots.

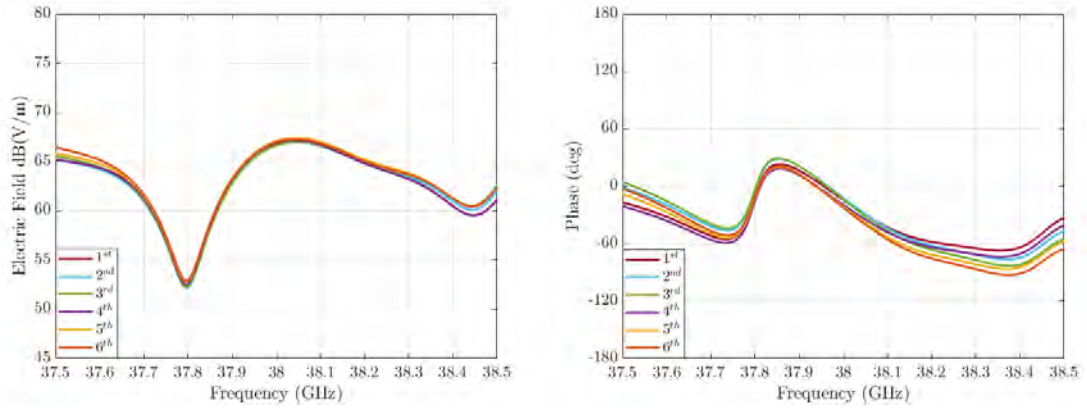

(a) (b)

Fig. 8.16. Amplitude (a) and phase (b) of the radiating slots that feed the horn antennas. At 38 GHz, both the amplitude and the phase of the six elements are equal.

8.5 Results

8.5.1 Simulated array

The proposed array was modeled and simulated using CST Microwave Studio. The different parts that constitute the array are presented in Fig. 8.20.

In Fig. 8.17, the matching of the array is presented as the S_{11} parameter of the feeding waveguide where the waveguide transition is connected. Satisfying levels of matching are observed at the central frequency, together with the narrow band behavior.

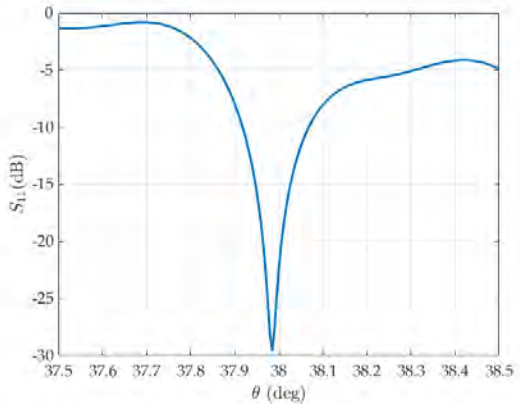

Fig. 8.17. S_{11} parameter of the proposed array.

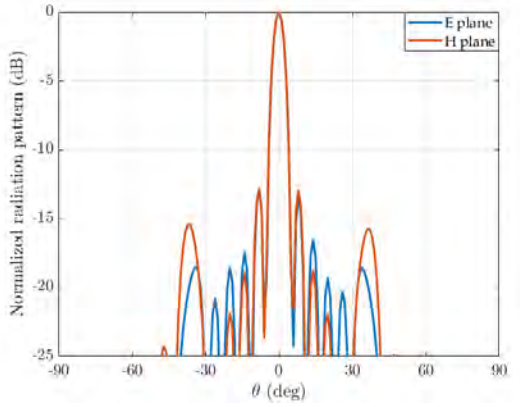

Fig. 8.18. Simulated radiation pattern of the proposed simulated array, for both E and H planes.

The simulated radiation pattern is shown in Fig. 8.18 for the E and H planes. The maximum is located at the broadside direction ($\theta = 0$), hence all the 6x6 elements radiate

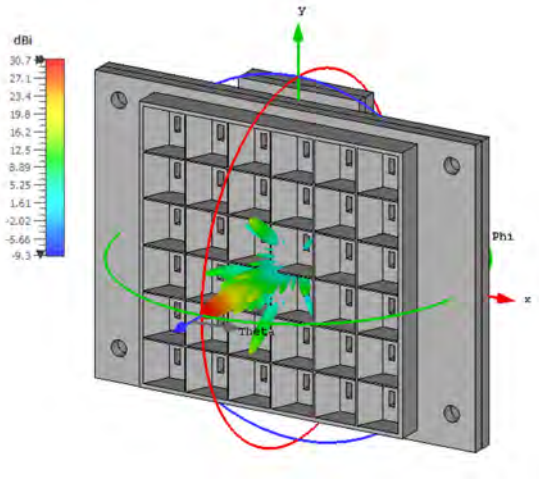

Fig. 8.19. 3D radiation pattern of the simulated array.

in-phase. The array reaches 30.7 dBi of directivity at the central frequency 38 GHz which indicates that the aperture efficiency is 89%. The 3D radiation pattern is shown in Fig. 8.19, together with the antenna. The cross polarization is approximately -38 dB.

8.5.2 Experimental results

To validate the simulated results and show the effectiveness of the proposed array, a prototype was manufactured and is shown in Fig. 8.21. The total size of the prototype is 12 cm x 8.9 cm, and it was fabricated exclusively in aluminium by milling. The fabrication as well as the assembling of the prototype was rather simplified, as it was fabricated in three pieces fully metallic that can be seen in Fig. 8.22.

The three parts were assembled together using four screws at the four corners of the structure, while two more screws were added for the mounting in the anechoic chamber. Two pins of alignment were used, one on each side (Fig. 8.22).

As mentioned, the width of the WR-28 was modified to achieve the guided wavelength $1.7\lambda_0$. However, the feeding would be done with the standard WR-28 waveguide transition, thus a flange was designed with tapered width in order to achieve good impedance matching and avoid reflections. The flange transition has an initial width of 7.11 mm and ending width 4.8 mm, while the height of the waveguide is constant, 3.56 mm. The obtained S_{11}

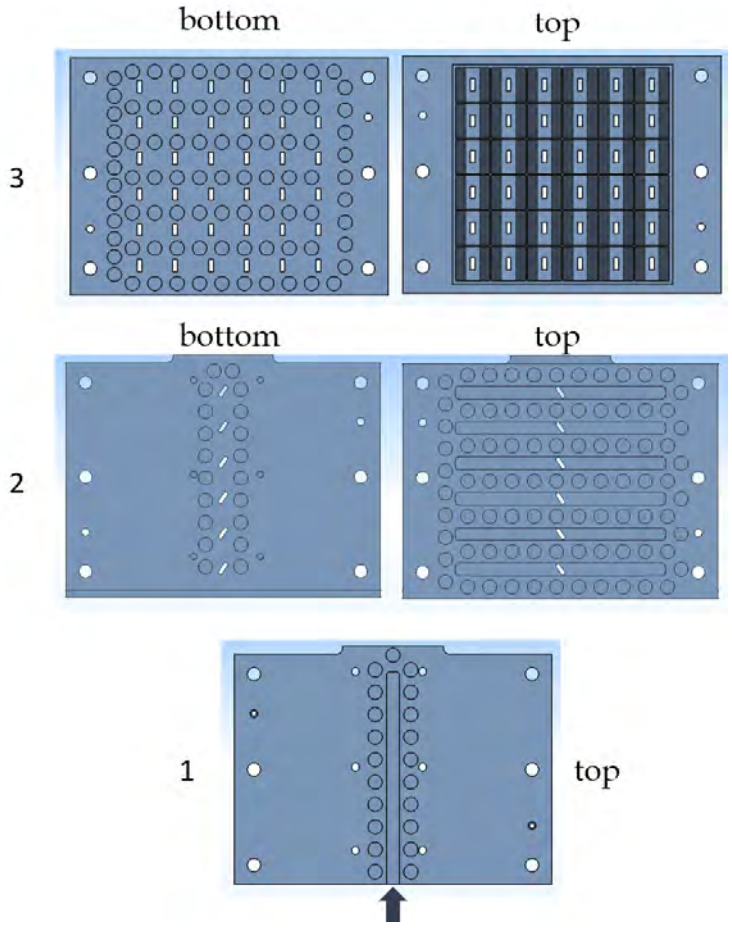

Fig. 8.20. The 3D model of the fabricated array, as it appears in CST. The parts of the array are enumerated, and the top and bottom view are shown. The direct feeding is done where the arrow indicates. Image number 3-top is the array of horn antennas, which is the top layer of the structure.

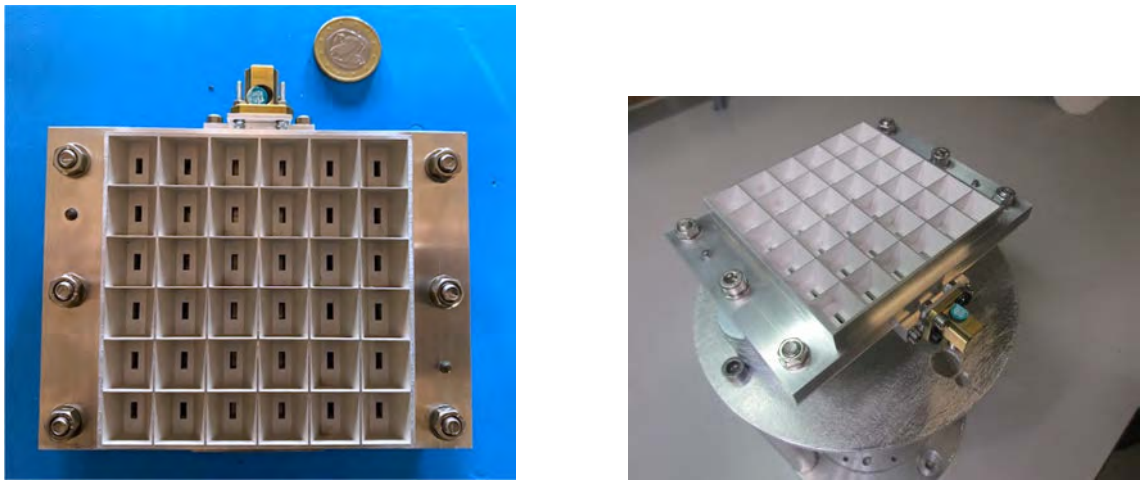

(a) (b)

Fig. 8.21. (a) Top view of the fabricated prototype, with a coin for size comparison. (b) The fabricated prototype in the laboratory, mounted on a plate for measurements in the anechoic chamber.

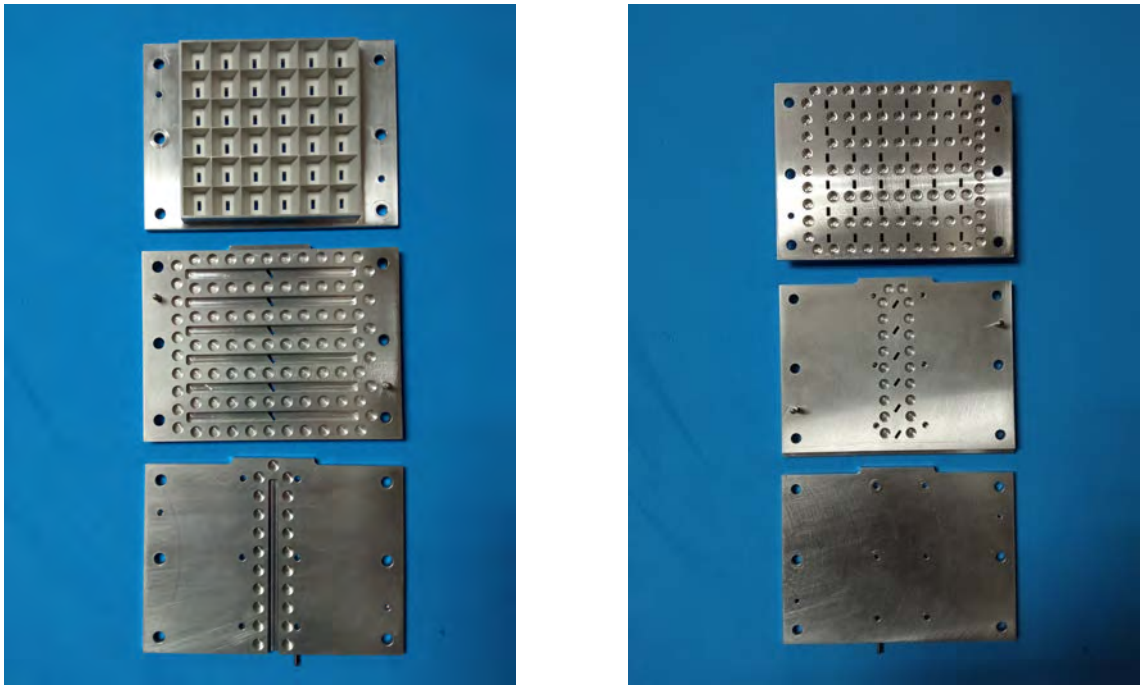

(a) (b)

Fig. 8.22. The fabricated prototype disassembled into its constituent layers. (a) Top view, (b) bottom view of each layer.

of the flange can be seen in Fig. 8.23.

The S_{11} of the fabricated prototype is shown in Fig. 8.24 and reaches -18 dB at the central frequency. The measured radiation patterns are shown in Fig. 8.25 normalized. For both E and H planes, there is an excellent agreement between the simulated and measured radiation patterns, indicating that the directivity obtained by the prototype, is in the same levels as the simulation. The array achieves a pencil beam not only in the E and H planes, but in the diagonal as well (Fig. 8.26). The measured realized gain is 29.3 dBi, which is below the simulated one (30.4 dBi). This could be due to the presence of Ohmic losses that were not included in the simulated model, or even due to insufficient contact between the WR-28 feed and the waveguide transition.

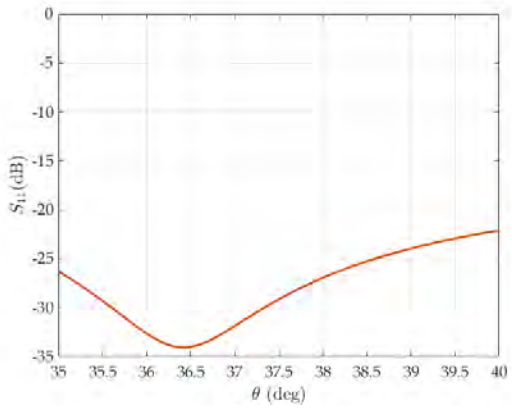

Fig. 8.23. Reflection coefficient of the flange transition.

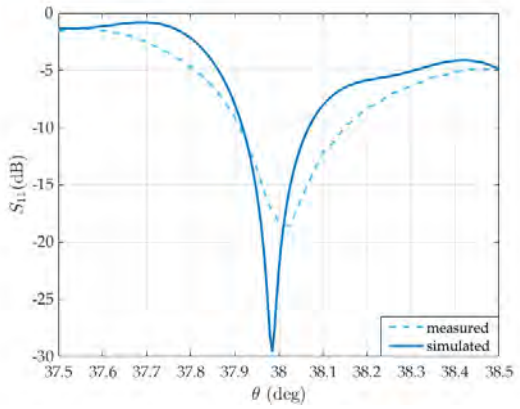

Fig. 8.24. Comparison between the simulated and measured S_{11} parameter of the array.

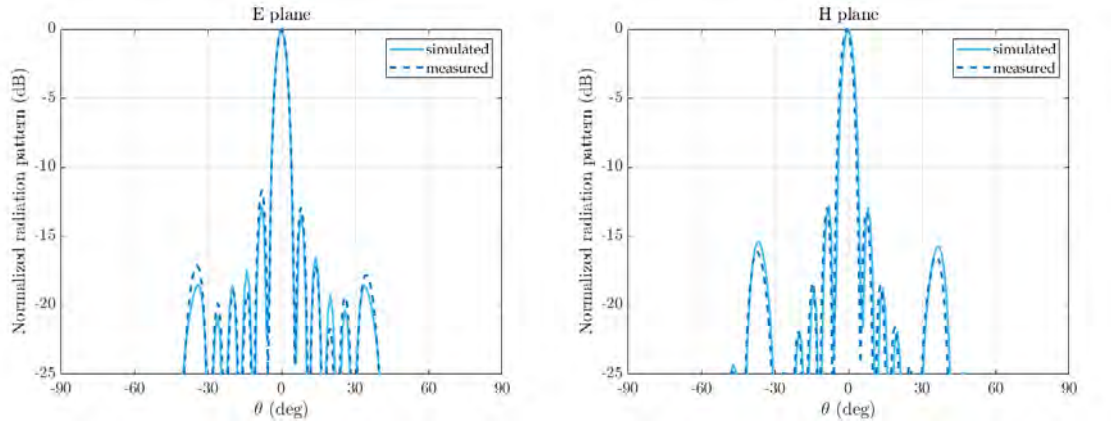

Fig. 8.25. Comparison of the normalized radiation pattern of the fabricated array and the simulated one, for E and H plane.

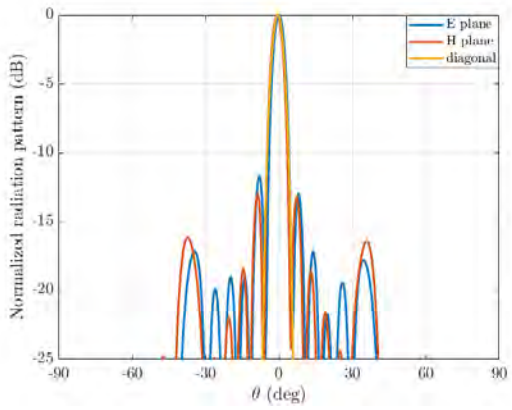

Fig. 8.26. Normalized radiation pattern of the fabricated prototype for the E, H and diagonal planes.

8.6 Conclusions

The design of an array of low profile horn antennas in groove gap waveguide technology has been presented. The array consists of a 6x6 configuration of dual-mode horn antennas. These horn antennas, achieve a uniform field distribution compared to the standard pyramidal horn antennas, thus exhibiting higher aperture efficiency. This is due to the simultaneous excitation of the TE_{10} and TE_{30} modes.

The feeding network is entirely made in groove gap waveguide technology, where the band-gap was achieved using glide symmetrical holes. Because of the size of the holes, the use of a corporate feeding network is not possible in this case. The horns are fed by transverse slots in a waveguide, forming linear arrays of an arbitrary number of elements. This constitutes one row of the array. Then each row is fed centrally with inclined longitudinal slots. The coupling through the inclined slots has been studied, and equal division of the incoming energy has been achieved.

The simulated results showed 30.7 dBi of maximum directivity and 30.4 dBi realized gain at 38 GHz, having 89% aperture efficiency. To validate the simulated results, a prototype was manufactured. The experimental results showed excellent agreement with the simulated ones. The measured realized gain reaches 29.3 dBi at 38 GHz. The difference of 1.4 dBi in the realized gain, can be attributed to Ohmic loses that were not included in the simulations, or even not tightly enough connection of the feeding transition.

The example design was a 6x6 array; however the number of elements of each row and also the number of rows can easily change in order to design an array of NxM elements.

The idea behind this design was to implement an array where the losses are minimized as much as possible. This array with a feed network implemented in groove gap waveguide technology, fulfills the low losses requirement, as this version of gap waveguide has the lowest losses.

Part III

Conclusions and Future Work

Conclusions

Design of Fabry-Pérot leaky-wave antennas

The first part of this thesis was focused on the design of Fabry-Pérot leaky-wave antennas. More specifically, in the first chapter a dual-band leaky-wave antenna has been presented. The proposed antenna, was designed using a novel methodology that allows dual-band performance with a single layer and single sided metasurface. In addition, it was shown that this methodology allows separate directivity control at each band.

The key aspect of the design methodology is that there can be an equivalence between a dielectric slab and an inductive or capacitive metasurface. For these two equivalent surfaces, there is a cavity height respectively lower and higher than the dielectric slab case. Therefore, by designing an MTS with impedance varying between inductive and capacitive behavior, a dual-band performance can be achieved. Equations for the impedance and the height have been presented for both equivalents. The unit cell can obtain these theoretical values by properly adjusting the parameters that define its geometry.

Furthermore, a metasurface designed to allow different permittivity equivalence at the two bands, has been presented. By choosing a higher permittivity at the higher band, the directivity is increased and the aperture efficiency is improved. The proposed methodology for the design of metasurface based leaky-wave antennas, allows flexibility in the design in terms of choice of the dual-band, and directivity achieved at each band. However, there is a limit for the separation between the two frequencies, which depends on the permittivity equivalence, and therefore a trade-off must take place between separation of bands and maximum directivity achieved.

A fabricated prototype of the case of same equivalent permittivities corresponding to both bands, has been also presented and the experimental results validated the simulations of the proposed design.

The same design methodology was used in the second chapter, where a dual-band planar thinned array with grating lobe suppression has been presented. The basic element of the 3x3 array, consists of a stacked patch and a metasurface that is located at a certain height h to create a resonant cavity.

The dual-band metasurface was designed following the methodology presented in Chapter 1.4. Since the MTS has the ability to enhance the directivity of a simple radiation source, in this case when it is combined with a thinned planar array, it attenuates the grating lobes that would occur due to large spacing. Furthermore, since the array has two bands of operation, the electrical distance between the stacked patches is different at $f_1 < f_2$, with $d_1 < d_2$. Therefore, the grating lobes will be closer to the broadside direction ($\theta = 0$). This means that at f_2 higher directivity is required than at f_1.

In this direction, the metasurface was designed so that it exhibits an equivalence with different dielectric permittivities at the two frequencies of operation, which means that different directivities are obtained at each frequency. At $f_1 = 10.5$ GHz and $f_2 = 13$ GHz, the designed MTS is equivalent to a dielectric slab of $\epsilon_{r1} = 6$ and $\epsilon_{r2} = 10$ respectively. The simulated embedded pattern of the array showed that indeed the directivity at f_2 is enhanced by 2 dB reaching 16.8 dBi, whilst at f_1 14.6 dBi are obtained. The attenuation of the grating lobes is 12.6 dB at f_1 and 10.6 dB at f_2.

The concept of the MTS-based leaky-wave antennas, was again explored in the third chapter; however unlike the previous two designs that were presented, in this design the targeting frequencies were significantly lower being in the L-band. More specifically, an array was developed as a candidate for the feed array of a large reflector used for a SAR system for Earth observation in the L-band.

Following the strict specifications of the application such as low return loss, low cross polarization with limitation in the spacing between the elements, several approaches to the design of the feed array have been presented. For the excitation of the leaky-waves in the resonant cavity, two antennas were proposed: a differentially fed patch antenna [97]–[99],

and a magneto-electric dipole antenna [109], both being dual-polarization antennas. The first consists of a patch antenna fed by four small coupling patches that are directly fed by an external microwave circuit that provides 180^o phase difference to the couplers by pairs. Then the energy is coupled to the patch that radiates inside the resonant cavity. For the second antenna, its upper part consists of two square-shaped electric dipoles, while the vertical walls act like magnetic dipoles. This antenna does not need an external feed circuit to provide low cross-polarization. Both antennas were designed to cover the band 1.215 GHz to 1.3 GHz.

The two excitation antennas were then combined with two types of metasurfaces. The first MTS was a metallic grid printed on top of a very thin FR4 layer. This MTS was designed following the equivalence with a dielectric slab [36], [37] as in previous chapters, that in this case was chosen to have permittivity $\epsilon_r = 5$. This value was chosen according to the required directivity that would result to the specified taper level at 27^o. Therefore, the dimensions and periodicity of the grid were designed to fulfill said equivalence. The second MTS, consisted of a complementary pattern printed on both sides of an FR4 layer. The design of the complementary MTS was done by studying the reflection coefficient of the unit cell to control the directivity achieved, and at the same time by taking under consideration the positive phase gradient required to avoid single frequency resonance [42]. This second MTS provides more bandwidth.

Both MTSs were simulated and evaluated with the two excitation antennas as individual elements, and then in a 3x3 planar array configuration to study the embedded radiation patterns. The maximum inter-element distance allowed by the application is 1.25λ. This limitation leads to deformed radiation patterns due to strong coupling between the elements. Additionally, the MTS should be reflective enough to achieve directivity around 16 dBi, in order to fulfill the taper specification (-10 to -12 dB) of the application. However, the more reflective the MTS is, the stronger the coupling becomes and the radiation patterns are more affected. To reduce the coupling we should reduce the reflectivity of the MTS, but then the requirement for the taper would not be fulfilled.

The fabricated prototype consisting on the grid MTS and the differentially fed patch antenna, validated the performance observed in the simulated array model. The inter-

element spacing is not enough to achieve the pencil beam radiation patterns otherwise obtained in this type of antennas. The S_{11} was measured to be low, however it did not reach the value of -20 dB as specified. Nonetheless, the cross polarization was maintained in the required levels. The grid MTS was chosen to be fabricated due to the low losses it exhibits, since the complementary MTS not only presented higher insertion losses, but it did not fulfill the specifications of the application neither.

Design of groove gap waveguide innovative antennas

The second part of this thesis was focused on the design of antennas in groove gap waveguide technology, that is a very good candidate for mm-wave band applications.

The first design with this technology was that of a vertical leaky-wave antenna array. The basic element of the array is the groove gap waveguide leaky-wave antenna [162]. By placing vertically four of these antennas one on top of the other, there is an enhancement of +5 dB in the directivity. Compared to the single leaky-wave antenna element as well as other gap waveguide based leaky-wave antennas [176]–[179], [183], the advantage of directivity enhancement is combined with a pencil beam radiation pattern that is a novel aspect in the leaky-wave antennas designed with this technology.

The total physical aperture of each of the stacked elements, is divided in three parts. First, a feeding network is responsible for the equal coupling of energy to all the antennas. The direct feeding is done only at the bottom (first) antenna, and then the energy is coupled through rectangular shaped apertures. These apertures were placed on the common wall separating the elements, in a progressive way.

The second part of each element, is the phase shifter. After coupling the energy to all the antennas, the phase is corrected separately at each element. Maintaining the full-metallic character of the design, the phase shifters were implemented by changing the width of the groove waveguide with the pins. In this manner, a tailored correction of phase can be achieved. Consequently, the radiation of all the elements is in-phase, and maximum directivity is obtained.

The third part of each element, is the radiating part. While for all the length of the coupling and phase correction network, three lines of pins ensure that the radiation is confined in the waveguide, in the last part, one row of pins allows partial leakage of the energy to free space. Let us mention here that due to manufacturing simplification, the three rows of EBG pins were substituted by two rows, without introducing radiation leakage.

The designed antenna array has been examined experimentally with a fabricated prototype. The experimental results confirmed the simulations. At the central frequency of 28 GHz, the measured realized gain is 23.68 dBi. As mentioned previously, the presented array focuses the radiation at both the E and H planes, thus creating a pencil beam. In addition, the measured radiation patterns of the E plane, showed that the maximum radiation occurs at the broadside direction ($\theta = 0$), proving that the phase shifters have the desired performance correcting the phase at each element.

Due to the use of gap waveguide technology, the fabrication cost is reduced and the mechanical requirements are more relaxed, since no direct electrical contact is required between the different layers of the 3D structure. Each of the array elements was fabricated in a single piece. The viability of a fully metallic structure that has low losses, and also it achieves directivity enhancement simply by stacking the radiating elements, has been demonstrated.

In the second chapter of this part, the design of a non dispersive leaky-wave antenna in groove gap waveguide technology, was presented. Two structures are combined in the presented design: a leaky-wave antenna and a metasurface prism. Both are implemented in gap waveguide technology with the use of the hole unit-cell. Similar works have been reported [178], [190], however they used the pin unit-cell whose main drawback is found in high frequencies where the pins are very fragile and expensive.

The presented design covers the 25-30 GHz band. The antenna is formed when on one lateral side the wall of the standard rectangular WR34 waveguide is replaced by two metallic plates with glide symmetric holes on both. This higher symmetry structure, prohibits the leakage of radiation between the plates in any direction, due to the electromagnetic band gap created by the glide symmetric unit cell. Hence, no direct contact is required

and the manufacturing can be simply made in two pieces. The other lateral side, has a longitudinal slot that allows the leakage of radiation from the waveguide [173], thus the leaky-wave antenna element is created. As a consequence, the size of the slot controls the radiation.

The nature of the leaky-wave antenna is dispersive, meaning that the direction of maximum radiation is changing depending on the frequency that propagates in the gap waveguide. In order to manipulate the radiation direction to create a non-dispersive antenna, a metasurface prism was added to the design. The prism is made of holes with a refractive index that also changes with frequency in a complementary way to the leaky-wave antenna. The resulting radiation angle of the simulated model showed only $\pm 1.1^o$ of variation around a central angle, in comparison to $\pm 4.65^o$ of the antenna without the prism.

To validate the simulated results, a prototype was fabricated. Without the need of physical contact due to the gap waveguide, the fabrication of the whole structure was made in two plates (top and bottom), which is one of the advantages of this design. All the components are metallic, making this type of antenna a good candidate for high frequencies, where dielectric parts would have severe losses. In addition, the hole unit-cell apart from having easier and less expensive fabrication than the pins, shows robustness even in high frequency bands.

The experimental results, were in very good agreement with the simulated antenna. The measured radiation patterns, showed very small change in the direction of maximum radiation, achieving an overall $\pm 1.5^o$ of variation which is only 0.4^o away from the simulated results. Moreover, low cross polarization levels were measured.

The version of the holey-EBG groove gap waveguide, was again used in the third chapter of this part, to implement an array of low profile horn antennas. The array consists of a 6x6 configuration of dual-mode horn antennas. These horn antennas, achieve a uniform field distribution compared to the standard pyramidal horn antennas, thus exhibiting higher aperture efficiency. This is due to the simultaneous excitation of the TE_{10} and TE_{30} modes.

The feeding network is entirely made in groove gap waveguide technology, where the band-gap was achieved using glide symmetrical holes. Because of the size of the holes, the use of a corporate feeding network is not possible in this case. The horns are

fed by transverse slots in a waveguide, forming linear arrays of an arbitrary number of elements. This constitutes one row of the array. Then each row is fed centrally with inclined longitudinal slots. The coupling through the inclined slots has been studied, and equal division of the incoming energy has been achieved.

The simulated results showed 30.7 dBi of maximum directivity and 30.4 dBi realized gain at 38 GHz, having 89% aperture efficiency. To validate the simulated results, a prototype was manufactured. The experimental results showed excellent agreement with the simulated ones. The measured realized gain reaches 29.3 dBi at 38 GHz. The difference of 1.4 dBi in the realized gain, can be attributed to ohmic loses that were not included in the simulations, or even not tightly enough connection of the feeding transition.

The example design was a 6x6 array; however the number of elements of each row and also the number of rows can be easily changed in order to design an array of NxM elements.

The idea behind this design was to implement an array where the losses are minimized as much as possible. This array with a feed network implemented in groove gap waveguide technology, fulfills the low losses requirement, as this version of gap waveguide has the lowest losses.

Future Work

This section presents future work guidelines regarding the designs and design methodologies that have been developed during this thesis.

With respect to the Fabry-Pérot leaky-wave antennas that were presented, the methodology that was developed could be implemented using other geometries of the MTS unit cell instead of the double square ring. Moreover, the leaky-wave thinned array could be measured experimentally and also it could be studied in order to use it for beam scanning applications. It could be also interesting to use the same methodology to design MTSs for circular polarization. Regarding the L-band MTS-based leaky-wave array that was presented, it could be used in applications that allow for larger inter-element distance.

With respect to the groove gap waveguide designs that were presented, all these antennas could be directly scaled in frequency, since they only consist on metallic parts. Furthermore, in the case of the stacked leaky-wave array, more elements could be used. The same concept of stacked array could be implemented with the non dispersive antennas in the same technology as the one presented in this thesis. For this particular antenna, future work could consists on better control over the tapering of the aperture to reduce the side lobes. Lastly, when revisiting the low profile horn antennas array that was presented, the bandwidth could be improved, since the design that was presented has very narrow band. This was due to the fact that it is a resonant structure, and more specifically the kind of the feeding slots was the responsible for the narrow band. Therefore, in future re-investigations of this design, using feed networks based on slotted waveguides with travelling waves could be studied. In addition, a polarizer could be also added in this design.

Bibliography

[1] Y. Niu, Y. Li, D. Jin, L. Su, and A. V. Vasilakos, "A survey of millimeter wave communications (mmwave) for 5G: Opportunities and challenges," *Wireless networks*, vol. 21, no. 8, pp. 2657–2676, 2015.

[2] W. Roh *et al.*, "Millimeter-wave beamforming as an enabling technology for 5G cellular communications: Theoretical feasibility and prototype results," *IEEE Communications Magazine*, vol. 52, no. 2, pp. 106–113, 2014. DOI: 10.1109/MCOM.2014.6736750.

[3] G. V. Trentini, "Partially reflecting sheet arrays," *IRE Transactions on Antennas and Propagation*, vol. 4, no. 4, pp. 666–671, 1956. DOI: 10.1109/TAP.1956.1144455.

[4] D. Jackson and N. Alexopoulos, "Gain enhancement methods for printed circuit antennas," *IEEE Transactions on Antennas and Propagation*, vol. 33, no. 9, pp. 976–987, 1985. DOI: 10.1109/TAP.1985.1143709.

[5] D. R. Jackson and A. A. Oliner, "A leaky-wave analysis of the high-gain printed antenna configuration," *IEEE Transactions on Antennas and Propagation*, vol. 36, no. 7, pp. 905–910, 1988. DOI: 10.1109/8.7194.

[6] H. Yang and N. Alexopoulos, "Gain enhancement methods for printed circuit antennas through multiple superstrates," *IEEE Transactions on Antennas and Propagation*, vol. 35, no. 7, pp. 860–863, 1987. DOI: 10.1109/TAP.1987.1144186.

[7] D. R. Jackson, A. A. Oliner, and A. Ip, "Leaky-wave propagation and radiation for a narrow-beam multiple-layer dielectric structure," *IEEE Transactions on Antennas and Propagation*, vol. 41, no. 3, pp. 344–348, 1993. DOI: 10.1109/8.233128.

[8] A. R. Weily, K. P. Esselle, B. C. Sanders, and T. S. Bird, "High-gain 1D EBG resonator antenna," *Microwave and Optical Technology Letters*, vol. 47, no. 2, pp. 107–114, 2005.

[9] R. M. Hashmi, B. A. Zeb, and K. P. Esselle, "Wideband high-gain EBG resonator antennas with small footprints and all-dielectric superstructures," *IEEE Transactions on Antennas and Propagation*, vol. 62, no. 6, pp. 2970–2977, 2014. DOI: 10.1109/TAP.2014.2314534.

[10] R. M. Hashmi and K. P. Esselle, "A class of extremely wideband resonant cavity antennas with large directivity-bandwidth products," *IEEE Transactions on Antennas and Propagation*, vol. 64, no. 2, pp. 830–835, 2016. DOI: 10.1109/TAP.2015.2511801.

[11] N. Wang *et al.*, "Wideband Fabry-Pérot resonator antenna with two layers of dielectric superstrates," *IEEE Antennas and Wireless Propagation Letters*, vol. 14, pp. 229–232, 2015. DOI: 10.1109/LAWP.2014.2360703.

[12] J. Vardaxoglou, "High gain planar antenna using optimised partially reflective surfaces," English, *IEE Proceedings - Microwaves, Antennas and Propagation*, vol. 148, 345–350(5), 6 Dec. 2001. [Online]. Available: https://digital-library.theiet.org/content/journals/10.1049/ip-map%5C_20010828.

[13] A. P. Feresidis, G. Goussetis, Shenhong Wang, and J. C. Vardaxoglou, "Artificial magnetic conductor surfaces and their application to low-profile high-gain planar antennas," *IEEE Transactions on Antennas and Propagation*, vol. 53, no. 1, pp. 209–215, 2005. DOI: 10.1109/TAP.2004.840528.

[14] M. Vaughan, *The Fabry-Pérot interferometer: history, theory, practice and applications*. Routledge, 2017.

[15] N. Guerin *et al.*, "A metallic Fabry-Pérot directive antenna," *IEEE Transactions on Antennas and Propagation*, vol. 54, no. 1, pp. 220–224, 2006. DOI: 10.1109/TAP.2005.861578.

[16] T. Akalin, J. Danglot, O. Vanbesien, and D. Lippens, "A highly directive dipole antenna embedded in a Fabry-Pérot type cavity," *IEEE Microwave and Wireless Components Letters*, vol. 12, no. 2, pp. 48–50, 2002. DOI: 10.1109/7260.982873.

[17] Z.-g. Liu, "Fabry-Pérot resonator antenna," *Journal of Infrared, Millimeter, and Terahertz Waves*, vol. 31, no. 4, pp. 391–403, 2010.

[18] M. Thevenot, C. Cheype, A. Reineix, and B. Jecko, "Directive photonic-bandgap antennas," *IEEE Transactions on Microwave Theory and Techniques*, vol. 47, no. 11, pp. 2115–2122, 1999. DOI: 10.1109/22.798007.

[19] Young Ju Lee, Junho Yeo, R. Mittra, and Wee Sang Park, "Application of electromagnetic bandgap (EBG) superstrates with controllable defects for a class of patch antennas as spatial angular filters," *IEEE Transactions on Antennas and Propagation*, vol. 53, no. 1, pp. 224–235, 2005. DOI: 10.1109/TAP.2004.840521.

[20] Y. Ge, K. P. Esselle, and T. S. Bird, "The use of simple thin partially reflective surfaces with positive reflection phase gradients to design wideband, low-profile EBG resonator antennas," *IEEE Transactions on Antennas and Propagation*, vol. 60, no. 2, pp. 743–750, 2012. DOI: 10.1109/TAP.2011.2173113.

[21] H. Ostner, J. Detlerfsen, and D. R. Jackson, "Radiation from one-dimensional dielectric leaky-wave antennas," *IEEE Transactions on Antennas and Propagation*, vol. 43, no. 4, pp. 331–339, 1995. DOI: 10.1109/8.376029.

[22] A. Neto and N. Llombart, "Wideband localization of the dominant leaky wave poles in dielectric covered antennas," *IEEE Antennas and Wireless Propagation Letters*, vol. 5, pp. 549–551, 2006. DOI: 10.1109/LAWP.2006.889558.

[23] D. R. Jackson *et al.*, "The fundamental physics of directive beaming at microwave and optical frequencies and the role of leaky waves," *Proceedings of the IEEE*, vol. 99, no. 10, pp. 1780–1805, 2011. DOI: 10.1109/JPROC.2010.2103530.

[24] B. A. Munk, *Frequency selective surfaces: theory and design*. John Wiley & Sons, 2005.

[25] J. Vardaxoglou, *Frequency Selective Surfaces: Analysis and Design*. Research Studies Press, UK, 1997.

[26] T.-K. Wu, "Frequency selective surfaces," *Encyclopedia of RF and Microwave Engineering*, 2005.

[27] D. Lockyer, J. Vardaxoglou, and R. Simpkin, "Complementary frequency selective surfaces," *IEE Proceedings-Microwaves, Antennas and Propagation*, vol. 147, no. 6, pp. 501–507, 2000.

[28] F. Costa, C. Amabile, A. Monorchio, and E. Prati, "Waveguide dielectric permittivity measurement technique based on resonant FSS filters," *IEEE Microwave and Wireless Components Letters*, vol. 21, pp. 273–275, 2011.

[29] F. Costa, A. Monorchio, and G. Manara, "Efficient analysis of frequency-selective surfaces by a simple equivalent-circuit model," *IEEE Antennas and Propagation Magazine*, vol. 54, no. 4, pp. 35–48, 2012. DOI: 10.1109/MAP.2012.6309153.

[30] C. Mateo-Segura, M. Garcia-Vigueras, G. Goussetis, A. P. Feresidis, and J. L. Gomez-Tornero, "A simple technique for the dispersion analysis of Fabry-Pérot cavity leaky-wave antennas," *IEEE Transactions on Antennas and Propagation*, vol. 60, no. 2, pp. 803–810, 2012. DOI: 10.1109/TAP.2011.2167900.

[31] Tianxia Zhao, D. R. Jackson, J. T. Williams, H. .-. D. Yang, and A. A. Oliner, "2-D periodic leaky-wave antennas-part I: Metal patch design," *IEEE Transactions on Antennas and Propagation*, vol. 53, no. 11, pp. 3505–3514, 2005. DOI: 10.1109/TAP.2005.858579.

[32] G. Lovat, P. Burghignoli, and D. R. Jackson, "Fundamental properties and optimization of broadside radiation from uniform leaky-wave antennas," *IEEE Transactions on Antennas and Propagation*, vol. 54, no. 5, pp. 1442–1452, 2006. DOI: 10.1109/TAP.2006.874350.

[33] A. Foroozesh and L. Shafai, "Investigation into the effects of the patch-type FSS superstrate on the high-gain cavity resonance antenna design," *IEEE Transactions on Antennas and Propagation*, vol. 58, no. 2, pp. 258–270, 2010. DOI: 10.1109/TAP.2009.2037702.

[34] Tianxia Zhao, D. R. Jackson, and J. T. Williams, "2-D periodic leaky-wave antennas-part II: Slot design," *IEEE Transactions on Antennas and Propagation*, vol. 53, no. 11, pp. 3515–3524, 2005. DOI: 10.1109/TAP.2005.858580.

[35] M. Pasian, M. Bozzi, and L. Perregrini, "Design of a large bandwidth planar antenna using inductive frequency selective surfaces," in *The Second European Conference on Antennas and Propagation, EuCAP 2007*, 2007, pp. 1–5. DOI: 10.1049/ic.2007.0863.

[36] M. Ettore, *Analysis and design of efficient planar leaky-wave antennas*. Siena: Universita Degli Studi di Siena, 2008.

[37] D. Blanco, E. Rajo-Iglesias, S. Maci, and N. Llombart, "Directivity enhancement and spurious radiation suppression in leaky-wave antennas using inductive grid metasurfaces," *IEEE Transactions on Antennas and Propagation*, vol. 63, no. 3, pp. 891–900, Mar. 2015. DOI: 10.1109/TAP.2014.2387422.

[38] K. Konstantinidis, A. P. Feresidis, and P. S. Hall, "Multilayer partially reflective surfaces for broadband Fabry-Pérot cavity antennas," *IEEE Transactions on Antennas and Propagation*, vol. 62, no. 7, pp. 3474–3481, 2014. DOI: 10.1109/TAP.2014.2320755.

[39] Y. Lv, X. Ding, and B. Wang, "Dual-wideband high-gain Fabry-Pérot cavity antenna," *IEEE Access*, vol. 8, pp. 4754–4760, 2020. DOI: 10.1109/ACCESS.2019.2962078.

[40] M. Asaadi, I. Afifi, and A. Sebak, "High gain and wideband high dense dielectric patch antenna using FSS superstrate for millimeter-wave applications," *IEEE Access*, vol. 6, pp. 38 243–38 250, 2018. DOI: 10.1109/ACCESS.2018.2854225.

[41] A. Lalbakhsh, M. U. Afzal, K. P. Esselle, S. L. Smith, and B. A. Zeb, "Single-dielectric wideband partially reflecting surface with variable reflection components for realization of a compact high-gain resonant cavity antenna," *IEEE Transactions on Antennas and Propagation*, vol. 67, no. 3, pp. 1916–1921, 2019. DOI: 10.1109/TAP.2019.2891232.

[42] N. Wang *et al.*, "Wideband Fabry-Pérot resonator antenna with two complementary FSS layers," *IEEE Transactions on Antennas and Propagation*, vol. 62, no. 5, pp. 2463–2471, 2014. DOI: 10.1109/TAP.2014.2308533.

[43] P. Qin, L. Ji, S. Chen, and Y. J. Guo, "Dual-polarized wideband Fabry-Pérot antenna with quad-layer partially reflective surface," *IEEE Antennas and Wireless Propagation Letters*, vol. 17, no. 4, pp. 551–554, 2018. DOI: 10.1109/LAWP.2018.2802439.

[44] H. Attia, M. L. Abdelghani, and T. A. Denidni, "Wideband and high-gain millimeter-wave antenna based on FSS Fabry-Pérot cavity," *IEEE Transactions on Antennas and Propagation*, vol. 65, no. 10, pp. 5589–5594, 2017. DOI: 10.1109/TAP.2017.2742550.

[45] M. A. Meriche, H. Attia, A. Messai, S. S. I. Mitu, and T. A. Denidni, "Directive wideband cavity antenna with single-layer meta-superstrate," *IEEE Antennas and Wireless Propagation Letters*, vol. 18, no. 9, pp. 1771–1774, 2019. DOI: 10.1109/LAWP.2019.2929579.

[46] X. Hu, X. Zhou, L. Wu, L. Zhou, and W. Yin, "A miniaturized dual-band frequency selective surface (FSS) with closed loop and its complementary pattern," *IEEE Antennas and Wireless Propagation Letters*, vol. 8, pp. 1374–1377, 2009. DOI: 10.1109/LAWP.2009.2039110.

[47] N. O. Parchin, M. Shen, and G. F. Pedersen, "Wideband Fabry-Pérot resonator for 28 GHz applications," in *2016 IEEE International Conference on Ubiquitous Wireless Broadband (ICUWB)*, 2016, pp. 1–4. DOI: 10.1109/ICUWB.2016.7790537.

[48] J. Romeu and Y. Rahmat-Samii, "Fractal FSS: A novel dual-band frequency selective surface," *IEEE Transactions on Antennas and Propagation*, vol. 48, no. 7, pp. 1097–1105, 2000. DOI: 10.1109/8.876329.

[49] W. Yin, H. Zhang, T. Zhong, and X. Min, "A novel compact dual-band frequency selective surface for GSM shielding by utilizing a 2.5-dimensional structure," *IEEE Transactions on Electromagnetic Compatibility*, vol. 60, no. 6, pp. 2057–2060, 2018. DOI: 10.1109/TEMC.2018.2790584.

[50] B. Zhang, C. Jin, X. Ye, and R. Mittra, "Dual-band dual-polarized quasi-elliptic frequency selective surfaces," *IEEE Antennas and Wireless Propagation Letters*, vol. 18, no. 2, pp. 298–302, 2019. DOI: 10.1109/LAWP.2018.2889505.

[51] A. Pirhadi, H. Bahrami, and J. Nasri, "Wideband high directive aperture coupled microstrip antenna design by using a FSS superstrate layer," *IEEE Transactions on Antennas and Propagation*, vol. 60, no. 4, pp. 2101–2106, 2012. DOI: 10.1109/TAP.2012.2186230.

[52] F. Qin *et al.*, "A triband low-profile high-gain planar antenna using Fabry-Pérot cavity," *IEEE Transactions on Antennas and Propagation*, vol. 65, no. 5, pp. 2683–2688, 2017. DOI: 10.1109/TAP.2017.2670564.

[53] A. Krauss, H. Bayer, R. Stephan, and M. A. Hein, "Dual-band leaky-wave antenna based on a dual-layer frequency selective surface for bi-directional satcom-on-the-move in Ka-band," in *2016 International Workshop on Antenna Technology (iWAT)*, 2016, pp. 25–28. DOI: 10.1109/IWAT.2016.7434791.

[54] Z. Yu *et al.*, "Dual-band three-dimensional FSS with high selectivity and small band ratio," *Electronics Letters*, vol. 55, no. 14, pp. 798–799, 2019. DOI: 10.1049/el.2019.1283. eprint: https://ietresearch.onlinelibrary.wiley.com/doi/pdf/10.1049/el.2019.1283.

[55] T. Hong, M. Wang, K. Peng, and S. Gong, "Ultrathin and miniaturized frequency selective surface with closely located dual resonance," *IEEE Antennas and Wireless Propagation Letters*, vol. 18, no. 6, pp. 1288–1292, 2019. DOI: 10.1109/LAWP.2019.2915396.

[56] A. Polemi and S. Maci, "On the polarization properties of a dielectric leaky wave antenna," *IEEE Antennas and Wireless Propagation Letters*, vol. 5, pp. 306–310, 2006. DOI: 10.1109/LAWP.2006.878889.

[57] Z. Liu, Z. Cao, and L. Wu, "Compact low-profile circularly polarized Fabry-Pérot resonator antenna fed by linearly polarized microstrip patch," *IEEE Antennas and Wireless Propagation Letters*, vol. 15, pp. 524–527, 2016. DOI: 10.1109/LAWP.2015.2456886.

[58] P. Xie, G. Wang, H. Li, J. Liang, and X. Gao, "Circularly polarized Fabry-Pérot antenna employing a receiver–transmitter polarization conversion metasurface," *IEEE Transactions on Antennas and Propagation*, vol. 68, no. 4, pp. 3213–3218, 2020. DOI: 10.1109/TAP.2019.2950811.

[59] Z. Wu, L. Li, Y. Li, and X. Chen, "Metasurface superstrate antenna with wideband circular polarization for satellite communication application," *IEEE Antennas and Wireless Propagation Letters*, vol. 15, pp. 374–377, 2016. DOI: 10.1109/LAWP.2015.2446505.

[60] J. Ren, W. Jiang, K. Zhang, and S. Gong, "A high-gain circularly polarized Fabry-Pérot antenna with wideband Low-RCS property," *IEEE Antennas and Wireless Propagation Letters*, vol. 17, no. 5, pp. 853–856, 2018. DOI: 10.1109/LAWP.2018.2820015.

[61] Z. Liu and W. Lu, "Low-profile design of broadband high gain circularly polarized Fabry-Pérot resonator antenna and its array with linearly polarized feed," *IEEE Access*, vol. 5, pp. 7164–7172, 2017. DOI: 10.1109/ACCESS.2017.2675378.

[62] S. A. Muhammad, R. Sauleau, and H. Legay, "Purely metallic waveguide-fed Fabry-Pérot cavity antenna with a polarizing frequency selective surface for compact solutions in circular polarization," *IEEE Antennas and Wireless Propagation Letters*, vol. 11, pp. 881–884, 2012. DOI: 10.1109/LAWP.2012.2210693.

[63] Tianxia Zhao, D. R. Jackson, J. T. Williams, and A. A. Oliner, "General formulas for 2-D leaky-wave antennas," *IEEE Transactions on Antennas and Propagation*, vol. 53, no. 11, pp. 3525–3533, 2005. DOI: 10.1109/TAP.2005.856315.

[64] A. Oliner and T. Tamir, “Guided complex wave, part II: Relation to radiation pattern,” *Proc. IEE*, vol. 110, pp. 325–334, 1963.

[65] D. Sievenpiper, Lijun Zhang, R. F. J. Broas, N. G. Alexopolous, and E. Yablonovitch, “High-impedance electromagnetic surfaces with a forbidden frequency band,” *IEEE Transactions on Microwave Theory and Techniques*, vol. 47, no. 11, pp. 2059–2074, 1999. DOI: 10.1109/22.798001.

[66] N. Nguyen-Trong, H. H. Tran, T. K. Nguyen, and A. M. Abbosh, “Wideband Fabry-Pérot antennas employing multilayer of closely spaced thin dielectric slabs,” *IEEE Antennas and Wireless Propagation Letters*, vol. 17, no. 7, pp. 1354–1358, 2018. DOI: 10.1109/LAWP.2018.2846240.

[67] B. A. Zeb, M. U. Afzal, and K. P. Esselle, “Performance analysis of classical and phase-corrected electromagnetic band gap resonator antennas with all-dielectric superstructures,” *IET Microwaves, Antennas & Propagation*, vol. 10, no. 12, pp. 1276–1284, 2016. DOI: 10.1049/iet-map.2015.0426. eprint: https://ietresearch.onlinelibrary.wiley.com/doi/pdf/10.1049/iet-map.2015.0426.

[68] J. Kelly *et al.*, “Simulations and measurements of dual-band 2-D periodic leaky wave antenna,” in *2007 Loughborough Antennas and Propagation Conference*, 2007, pp. 293–296. DOI: 10.1109/LAPC.2007.367487.

[69] L. M. Araujo, R. H. C. Maniçoba, A. L. P. S. Campos, and A. G. dÁssunçao, “A simple dual-band frequency selective surface,” *Microwave and Optical Technology Letters*, vol. 51, no. 4, pp. 942–944, 2009. DOI: 10.1002/mop.24236. eprint: https://onlinelibrary.wiley.com/doi/pdf/10.1002/mop.24236.

[70] E. B. Lima, J. R. Costa, and C. A. Fernandes, “FSS design for dual-band and low profile Fabry-Pérot antenna at Ka-band,” in *The 8th European Conference on Antennas and Propagation (EuCAP 2014)*, 2014, pp. 542–544. DOI: 10.1109/EuCAP.2014.6901814.

[71] Young Ju Lee, Junho Yeo, R. Mittra, and Wee Sang Park, “Design of a frequency selective surface (FSS) type superstrate for dual-band directivity enhancement of microstrip patch antennas,” in *2005 IEEE Antennas and Propagation Society*

International Symposium, vol. 3A, 2005, 2–5 vol. 3A. DOI: 10.1109/APS.2005.1552158.

[72] H. Li, G. Wang, X. Gao, J. Liang, and H. Hou, "A novel metasurface for dual-mode and dual-band flat high-gain antenna application," *IEEE Transactions on Antennas and Propagation*, vol. 66, no. 7, pp. 3706–3711, 2018. DOI: 10.1109/TAP.2018.2835526.

[73] M. L. Abdelghani, T. A. Denidni, and H. Attia, "Dual band Fabry-Pérot antenna with broad radiation bandwidth," in *2016 17th International Symposium on Antenna Technology and Applied Electromagnetics (ANTEM)*, 2016, pp. 1–2. DOI: 10.1109/ANTEM.2016.7550156.

[74] Y. Liu and X. Zhao, "High-gain ultrathin resonant cavity antenna," *Microwave and Optical Technology Letters*, vol. 53, no. 9, pp. 1945–1949, 2011. DOI: 10.1002/mop.26213. eprint: https://onlinelibrary.wiley.com/doi/pdf/10.1002/mop.26213.

[75] J. Chen, Y. Zhao, Y. Ge, and L. Xing, "Dual-band high-gain Fabry-Pérot cavity antenna with a shared-aperture FSS layer," English, *IET Microwaves, Antennas & Propagation*, vol. 12, 2007–2011(4), 13 Oct. 2018. DOI: 10.1049/iet-map.2018.5183.

[76] T. Li and Z. N. Chen, "Shared-surface dual-band antenna for 5G applications," *IEEE Transactions on Antennas and Propagation*, vol. 68, no. 2, pp. 1128–1133, 2020. DOI: 10.1109/TAP.2019.2938584.

[77] A. D. Chuprin, E. A. Parker, and J. C. Batchelor, "Convoluted double square: Single layer FSS with close band spacings," *Electronics Letters*, vol. 36, no. 22, pp. 1830–1831, 2000.

[78] P. Xie and G.-M. Wang, "Design of a frequency reconfigurable Fabry-Pérot cavity antenna with single layer partially reflecting surface," *Progress in Electromagnetics Research*, vol. 70, pp. 115–121, 2017.

[79] R. Xu, H. Zhao, Z. Zong, and W. Wu, "Dual-band capacitive loaded frequency selective surfaces with close band spacing," *IEEE Microwave and Wireless Components Letters*, vol. 18, no. 12, pp. 782–784, 2008. DOI: 10.1109/LMWC.2008.2007697.

[80] D. Ferreira, I. Cuiñas, R. F. Caldeirinha, and T. R. Fernandes, "Dual-band single-layer quarter ring frequency selective surface for Wi-Fi applications," English, *IET Microwaves, Antennas & Propagation*, vol. 10, 435–441(6), 4 Mar. 2016. DOI: 10.1049/iet-map.2015.0641.

[81] A. Pirhadi, M. Hakkak, F. Keshmiri, and R. Karimzadeh Baee, "Design of compact dual band high directive electromagnetic bandgap (EBG) resonator antenna using artificial magnetic conductor," *IEEE Transactions on Antennas and Propagation*, vol. 55, no. 6, pp. 1682–1690, 2007. DOI: 10.1109/TAP.2007.898598.

[82] T. Li and Z. N. Chen, "A dual-band metasurface antenna using characteristic mode analysis," *IEEE Transactions on Antennas and Propagation*, vol. 66, no. 10, pp. 5620–5624, 2018. DOI: 10.1109/TAP.2018.2860121.

[83] N. Llombart, G. Chattopadhyay, A. Skalare, and I. Mehdi, "Novel terahertz antenna based on a silicon lens fed by a leaky wave enhanced waveguide," *IEEE Transactions on Antennas and Propagation*, vol. 59, no. 6, pp. 2160–2168, 2011. DOI: 10.1109/TAP.2011.2143663.

[84] F. Scattone, M. Ettorre, R. Sauleau, and N. J. G. Fonseca, "Leaky-wave-based dual-band phased array for satellite communications," in *2016 10th EuCAP*, Apr. 2016, pp. 1–4. DOI: 10.1109/EuCAP.2016.7481890.

[85] R. Mailloux, "Synthesis of spatial filters with Chebyshev characteristics," *IEEE Transactions on Antennas and Propagation*, vol. 24, no. 2, pp. 174–181, 1976. DOI: 10.1109/TAP.1976.1141323.

[86] R. Mailloux, L. Zahn, and A. Martinez, "Grating lobe control in limited scan arrays," *IEEE Transactions on Antennas and Propagation*, vol. 27, no. 1, pp. 79–85, 1979. DOI: 10.1109/TAP.1979.1142034.

[87] Youngju Lee, Sung Hun Jeong, Wee Sang Park, Jae Seung Yun, and Soon Ik Jeon, "Multi-layer spatial angular filter with air gap tuner to suppress the grating lobes of microstrip patch arrays," in *2002 IEEE MTT-S International Microwave Symposium Digest (Cat. No.02CH37278)*, vol. 2, 2002, 1329–1332 vol.2. DOI: 10.1109/MWSYM.2002.1011914.

[88] R. Gardelli, M. Albani, and F. Capolino, "Array thinning by using antennas in a Fabry-Pérot cavity for gain enhancement," *IEEE Transactions on Antennas and Propagation*, vol. 54, no. 7, pp. 1979–1990, 2006.

[89] D. Blanco, N. Llombart, and E. Rajo-Iglesias, "On the use of leaky wave phased arrays for the reduction of the grating lobe level," *IEEE Transactions on Antennas and Propagation*, vol. 62, no. 4, pp. 1789–1795, Apr. 2014. DOI: 10.1109/TAP.2013.2272573.

[90] C. A. Balanis, *Antenna theory: analysis and design*. John wiley & sons, 2016.

[91] N. Memeletzoglou, E. Rajo-Iglesias, and D. Blanco, "Single-layer dual-band leaky wave antennas design methodology with directivity control," in *2018 IEEE International Symposium on Antennas and Propagation USNC/URSI National Radio Science Meeting*, 2018, pp. 1875–1876. DOI: 10.1109/APUSNCURSINRSM.2018.8608717.

[92] N. Llombart, A. Neto, G. Gerini, M. Bonnedal, and P. De Maagt, "Impact of mutual coupling in leaky wave enhanced imaging arrays," *IEEE Transactions on Antennas and Propagation*, vol. 56, no. 4, pp. 1201–1206, 2008. DOI: 10.1109/TAP.2008.919223.

[93] F. Scattone, "Phased array antenna with significant reduction of active controls," Theses, Université Rennes 1, Dec. 2015. [Online]. Available: https://tel.archives-ouvertes.fr/tel-01417803.

[94] G. Krieger *et al.*, "Advanced concepts for ultra-wide-swath SAR imaging," in *7th European Conference on Synthetic Aperture Radar*, VDE, 2008, pp. 1–4.

[95] G. Krieger *et al.*, "Advanced L-band SAR system concepts for high-resolution ultra-wide-swath SAR imaging," 2017.

[96] S. Huber, M. Younis, and G. Krieger, "Tandem-L: SAR system design aspects," 2017.

[97] Y. P. Zhang, "Design and experiment on differentially-driven microstrip antennas," *IEEE Transactions on Antennas and Propagation*, vol. 55, no. 10, pp. 2701–2708, 2007. DOI: 10.1109/TAP.2007.905832.

[98] L. Han, W. Zhang, X. Chen, G. Han, and R. Ma, "Design of compact differential dual-frequency antenna with stacked patches," *IEEE Transactions on Antennas and Propagation*, vol. 58, no. 4, pp. 1387–1392, 2010. DOI: 10.1109/TAP.2010.2041146.

[99] W. Fan, A. Lu, L. Wai, and B. Lok, "Mixed-mode S-parameter characterization of differential structures," in *Proceedings of the 5th Electronics Packaging Technology Conference (EPTC 2003)*, 2003, pp. 533–537. DOI: 10.1109/EPTC.2003.1271579.

[100] A. Chlavin, "A new antenna feed having equal E-and H-plane patterns," *Transactions of the IRE Professional Group on Antennas and Propagation*, vol. 2, no. 3, pp. 113–119, 1954. DOI: 10.1109/T-AP.1954.27983.

[101] R. King and G. Owyang, "The slot antenna with coupled dipoles," *IRE Transactions on Antennas and Propagation*, vol. 8, no. 2, pp. 136–143, 1960. DOI: 10.1109/TAP.1960.1144818.

[102] P. Mayes, W. Warren, and F. Wiesenmeyer, "The monopole slot: A small broadband unidirectional antenna," *IEEE Transactions on Antennas and Propagation*, vol. 20, no. 4, pp. 489–493, 1972. DOI: 10.1109/TAP.1972.1140250.

[103] A. Clavin, D. Huebner, and F. Kilburg, "An improved element for use in array antennas," *IEEE Transactions on Antennas and Propagation*, vol. 22, no. 4, pp. 521–526, 1974. DOI: 10.1109/TAP.1974.1140845.

[104] K.-M. Luk and H. Wong, "A new wideband unidirectional antenna element," *Int. J. Microw. Opt. Technol.*, vol. 1, no. 1, pp. 35–44, 2006.

[105] L. Ge and K. M. Luk, "A wideband magneto-electric dipole antenna," *IEEE Transactions on Antennas and Propagation*, vol. 60, no. 11, pp. 4987–4991, 2012. DOI: 10.1109/TAP.2012.2207689.

[106] ——, "A low-profile magneto-electric dipole antenna," *IEEE Transactions on Antennas and Propagation*, vol. 60, no. 4, pp. 1684–1689, 2012. DOI: 10.1109/TAP.2012.2186260.

[107] M. Li and K.-M. Luk, "A differential-fed magneto-electric dipole antenna for UWB applications," *IEEE Transactions on Antennas and Propagation*, vol. 61, no. 1, pp. 92–99, 2013. DOI: 10.1109/TAP.2012.2220100.

[108] Q. Xue, S. W. Liao, and J. H. Xu, "A differentially-driven dual-polarized magneto-electric dipole antenna," *IEEE Transactions on Antennas and Propagation*, vol. 61, no. 1, pp. 425–430, 2013. DOI: 10.1109/TAP.2012.2214998.

[109] B. Q. Wu and K.-M. Luk, "A broadband dual-polarized magneto-electric dipole antenna with simple feeds," *IEEE Antennas and Wireless Propagation Letters*, vol. 8, pp. 60–63, 2009. DOI: 10.1109/LAWP.2008.2011656.

[110] P.-S. Kildal, "Artificially soft and hard surfaces in electromagnetics," *IEEE Transactions on Antennas and Propagation*, vol. 38, no. 10, pp. 1537–1544, 1990. DOI: 10.1109/8.59765.

[111] C. Granet and G. L. James, "Design of corrugated horns: A primer," *IEEE Antennas and Propagation Magazine*, vol. 47, no. 2, pp. 76–84, 2005. DOI: 10.1109/MAP.2005.1487785.

[112] J. Robinson, S. Sinton, and Y. Rahmat-Samii, "Particle swarm, genetic algorithm, and their hybrids: Optimization of a profiled corrugated horn antenna," in *IEEE Antennas and Propagation Society International Symposium (IEEE Cat. No.02CH37313)*, vol. 1, 2002, 314–317 vol.1. DOI: 10.1109/APS.2002.1016311.

[113] E. Lier and P. .-. Kildal, "Soft and hard horn antennas," *IEEE Transactions on Antennas and Propagation*, vol. 36, no. 8, pp. 1152–1157, 1988. DOI: 10.1109/8.7229.

[114] M. Aly and S. Mahmoud, "Propagation and radiation behaviour of a longitudinally slotted horn with dielectric-filled slots," in *IEE Proceedings H (Microwaves, Antennas and Propagation)*, IET, vol. 132, 1985, pp. 477–479.

[115] P.-S. Kildal, A. A. Kishk, and A. Tengs, "Reduction of forward scattering from cylindrical objects using hard surfaces," *IEEE Transactions on Antennas and Propagation*, vol. 44, no. 11, pp. 1509–1520, 1996. DOI: 10.1109/8.542076.

[116] P.-S. Kildal, E. Alfonso, A. Valero-Nogueira, and E. Rajo-Iglesias, "Local metamaterial-based waveguides in gaps between parallel metal plates," *IEEE Antennas and Wireless Propagation Letters*, vol. 8, pp. 84–87, 2009. DOI: 10.1109/LAWP.2008.2011147.

[117] P.-S. Kildal, "Three metamaterial-based gap waveguides between parallel metal plates for mm/submm waves," in *2009 3rd European Conference on Antennas and Propagation*, Mar. 2009, pp. 28–32.

[118] A. U. Zaman and P.-S. Kildal, "Gap waveguides," in *Handbook of Antenna Technologies*, Springer, Singapore, 2015, pp. 1–61.

[119] P.-S. Kildal and A. Kishk, "EM modeling of surfaces with STOP or GO characteristics-artificial magnetic conductors and soft and hard surfaces," *Applied Computational Electromagnetics Society Journal*, vol. 18, no. 1, pp. 32–40, 2003.

[120] M. G. Silveirinha, C. A. Fernandes, and J. R. Costa, "Electromagnetic characterization of textured surfaces formed by metallic pins," *IEEE Transactions on Antennas and Propagation*, vol. 56, no. 2, pp. 405–415, Feb. 2008. DOI: 10.1109/TAP.2007.915442.

[121] E. Rajo-Iglesias and P.-S. Kildal, "Numerical studies of bandwidth of parallel-plate cut-off realised by a bed of nails, corrugations and mushroom-type electromagnetic bandgap for use in gap waveguides," *IET Microwaves, Antennas & Propagation*, vol. 5, no. 3, pp. 282–289, Feb. 2011. DOI: 10.1049/iet-map.2010.0073.

[122] J. Zhang, X. Zhang, D. Shen, T. Liu, and K. Wu, "Gap waveguide-based PMC packaging for via holes-caused nonsmooth PEC surface," *IEEE Transactions on*

Components, Packaging and Manufacturing Technology, vol. 5, no. 12, pp. 1828–1838, 2015. DOI: 10.1109/TCPMT.2015.2489923.

[123] E. Rajo-Iglesias, P.-S. Kildal, A. U. Zaman, and A. Kishk, "Bed of springs for packaging of microstrip circuits in the microwave frequency range," *IEEE Transactions on Components, Packaging and Manufacturing Technology*, vol. 2, no. 10, pp. 1623–1628, Oct. 2012. DOI: 10.1109/TCPMT.2012.2207957.

[124] E. Rajo-Iglesias, E. Pucci, A. A. Kishk, and P.-S. Kildal, "Suppression of parallel plate modes in low frequency microstrip circuit packages using lid of printed zigzag wires," *IEEE Microwave and Wireless Components Letters*, vol. 23, no. 7, pp. 359–361, 2013. DOI: 10.1109/LMWC.2013.2265257.

[125] A. Uz Zaman, V. Vassilev, P.-S. Kildal, and A. Kishk, "Increasing parallel plate stop-band in gap waveguides using inverted pyramid-shaped nails for slot array application above 60 GHz," in *Proceedings of the 5th European Conference on Antennas and Propagation (EUCAP)*, 2011, pp. 2254–2257.

[126] S. I. Shams and A. A. Kishk, "Printed texture with triangle flat pins for bandwidth enhancement of the ridge gap waveguide," *IEEE Transactions on Microwave Theory and Techniques*, vol. 65, no. 6, pp. 2093–2100, 2017. DOI: 10.1109/TMTT.2017.2650230.

[127] M. Ebrahimpouri, E. Rajo-Iglesias, Z. Sipus, and O. Quevedo-Teruel, "Cost-effective gap waveguide technology based on glide-symmetric holey EBG structures," *IEEE Transactions on Microwave Theory and Techniques*, vol. 66, no. 2, pp. 927–934, 2018. DOI: 10.1109/TMTT.2017.2764091.

[128] M. Ebrahimpouri, O. Quevedo-Teruel, and E. Rajo-Iglesias, "Design guidelines for gap waveguide technology based on glide-symmetric holey structures," *IEEE Microwave and Wireless Components Letters*, vol. 27, no. 6, pp. 542–544, 2017. DOI: 10.1109/LMWC.2017.2701308.

[129] Z. Sipus, K. Cavar, M. Bosiljevac, and E. Rajo-Iglesias, "Glide-symmetric holey structures applied to waveguide technology: Design considerations," *Sensors*, vol. 20, no. 23, 2020. DOI: 10.3390/s20236871. [Online]. Available: https://www.mdpi.com/1424-8220/20/23/6871.

[130] P.-S. Kildal, A. U. Zaman, E. Rajo-Iglesias, E. Alfonso, and A. Valero-Nogueira, "Design and experimental verification of ridge gap waveguide in bed of nails for parallel-plate mode suppression," *IET Microwaves, Antennas & Propagation*, vol. 5, no. 3, pp. 262–270, Feb. 2011. DOI: 10.1049/iet-map.2010.0089.

[131] A. Polemi, S. Maci, and P.-S. Kildal, "Dispersion characteristics of a metamaterial-based parallel-plate ridge gap waveguide realized by bed of nails," *IEEE Transactions on Antennas and Propagation*, vol. 59, no. 3, pp. 904–913, Mar. 2011. DOI: 10.1109/TAP.2010.2103006.

[132] E. Rajo-Iglesias and P.-S. Kildal, "Groove gap waveguide: A rectangular waveguide between contactless metal plates enabled by parallel-plate cut-off," in *Proceedings of the Fourth European Conference on Antennas and Propagation*, Apr. 2010, pp. 1–4.

[133] A. Berenguer, D. Sánchez-Escuderos, B. Bernardo-Clemente, M. Baquero-Escudero, and V. Boria, "Groove gap waveguide as an alternative to rectangular waveguide for H-plane components," *Electronics Letters*, vol. 52, no. 11, pp. 939–941, 2016.

[134] H. Raza, J. Yang, P.-S. Kildal, and E. Alfonso Alós, "Microstrip-ridge gap waveguide–study of losses, bends, and transition to WR-15," *IEEE Transactions on Microwave Theory and Techniques*, vol. 62, no. 9, pp. 1943–1952, 2014. DOI: 10.1109/TMTT.2014.2327199.

[135] A. Valero-Nogueira *et al.*, "Gap waveguides using a suspended strip on a bed of nails," *IEEE Antennas and Wireless Propagation Letters*, vol. 10, pp. 1006–1009, 2011. DOI: 10.1109/LAWP.2011.2167591.

[136] A. A. Brazález, E. Rajo-Iglesias, J. L. Vázquez-Roy, A. Vosoogh, and P.-S. Kildal, "Design and validation of microstrip gap waveguides and their transitions to rectangular waveguide, for millimeter-wave applications," *IEEE Transactions on Microwave Theory and Techniques*, vol. 63, no. 12, pp. 4035–4050, 2015. DOI: 10.1109/TMTT.2015.2495141.

[137] E. Pucci, E. Rajo-Iglesias, and P.-S. Kildal, "New microstrip gap waveguide on mushroom-type EBG for packaging of microwave components," *IEEE Microwave*

and Wireless Components Letters, vol. 22, no. 3, pp. 129–131, Mar. 2012. DOI: 10.1109/LMWC.2011.2182638.

[138] D. Sánchez-Escuderos, M. Ferrando-Bataller, A. Berenguer, M. Baquero-Escudero, and A. Valero-Nogueira, "Dielectric bed of nails in gap-waveguide technology at millimeter-wave frequencies," *IEEE Microwave and Wireless Components Letters*, vol. 24, no. 8, pp. 515–517, 2014. DOI: 10.1109/LMWC.2014.2321496.

[139] Z. Pi and F. Khan, "An introduction to millimeter-wave mobile broadband systems," *IEEE Communications Magazine*, vol. 49, no. 6, pp. 101–107, 2011. DOI: 10.1109/MCOM.2011.5783993.

[140] O. Quevedo-Teruel *et al.*, "Roadmap on metasurfaces," *Journal of Optics*, vol. 21, no. 7, p. 073 002, 2019.

[141] E. Rajo-Iglesias, M. Ferrando-Rocher, and A. U. Zaman, "Gap waveguide technology for millimeter-wave antenna systems," *IEEE Communications Magazine*, vol. 56, no. 7, pp. 14–20, 2018. DOI: 10.1109/MCOM.2018.1700998.

[142] N. Memeletzoglou and E. Rajo-Iglesias, "Array of stacked leaky-wave antennas in groove gap waveguide technology," *Scientific Reports*, vol. 11, no. 1, pp. 1–10, 2021.

[143] A. Berenguer *et al.*, "Propagation characteristics of groove gap waveguide below and above cutoff," *IEEE Transactions on Microwave Theory and Techniques*, vol. 64, no. 1, pp. 27–36, Jan. 2016. DOI: 10.1109/TMTT.2015.2504501.

[144] A. U. Zaman, P.-S. Kildal, and A. A. Kishk, "Narrow-band microwave filter using high-Q groove gap waveguide resonators with manufacturing flexibility and no sidewalls," *IEEE Transactions on Components, Packaging and Manufacturing Technology*, vol. 2, no. 11, pp. 1882–1889, 2012.

[145] A. del Olmo-Olmeda, M. Baquero-Escudero, V. E. Boria-Esbert, A. Valero-Nogueira, and A. J. Berenguer-Verdú, "A novel band-pass filter topology for millimeter-wave applications based on the groove gap waveguide," in *2013 IEEE MTT-S International Microwave Symposium Digest (MTT)*, IEEE, 2013, pp. 1–4.

[146] Z. Liu, J. Deng, and D. Sun, "Slow-wave groove gap waveguide bandpass filter," *IEEE Access*, vol. 7, pp. 52 581–52 588, 2019. DOI: 10.1109/ACCESS.2019.2912496.

[147] E. A. Alós, A. U. Zaman, and P.-S. Kildal, "Ka-band gap waveguide coupled-resonator filter for radio link diplexer application," *IEEE Transactions on Components, Packaging and Manufacturing Technology*, vol. 3, no. 5, pp. 870–879, 2013. DOI: 10.1109/TCPMT.2012.2231140.

[148] M. Ferrando-Rocher, A. Valero-Nogueira, and J. I. Herranz-Herruzo, "New feeding network topologies for high-gain single-layer slot array antennas using gap waveguide concept," in *2017 11th European Conference on Antennas and Propagation (EUCAP)*, 2017, pp. 1654–1657. DOI: 10.23919/EuCAP.2017.7928169.

[149] M. Ferrando-Rocher, A. Valero-Nogueira, J. I. Herranz-Herruzo, and J. Teniente, "60 GHz single-layer slot-array antenna fed by groove gap waveguide," *IEEE Antennas and Wireless Propagation Letters*, vol. 18, no. 5, pp. 846–850, 2019. DOI: 10.1109/LAWP.2019.2903475.

[150] A. J. Sáez, A. Valero-Nogueira, J. I. Herranz, and B. Bernardo, "Single-layer cavity-backed slot array fed by groove gap waveguide," *IEEE Antennas and Wireless Propagation Letters*, vol. 15, pp. 1402–1405, 2015.

[151] A. Vosoogh and P.-S. Kildal, "Corporate-fed planar 60-GHz slot array made of three unconnected metal layers using amc pin surface for the gap waveguide," *IEEE Antennas and Wireless Propagation Letters*, vol. 15, pp. 1935–1938, 2016. DOI: 10.1109/LAWP.2015.2510296.

[152] D. Zarifi, A. Farahbakhsh, A. U. Zaman, and P.-S. Kildal, "Design and fabrication of a high-gain 60-GHz corrugated slot antenna array with ridge gap waveguide distribution layer," *IEEE Transactions on Antennas and Propagation*, vol. 64, no. 7, pp. 2905–2913, 2016. DOI: 10.1109/TAP.2016.2565682.

[153] A. Farahbakhsh, D. Zarifi, and A. U. Zaman, "60-GHz groove gap waveguide based wideband H -plane power dividers and transitions: For use in high-gain slot array antenna," *IEEE Transactions on Microwave Theory and Techniques*, vol. 65, no. 11, pp. 4111–4121, 2017. DOI: 10.1109/TMTT.2017.2699680.

[154] J. Liu, A. Vosoogh, A. U. Zaman, and J. Yang, "Design and fabrication of a high-gain 60-GHz cavity-backed slot antenna array fed by inverted microstrip gap waveguide," *IEEE Transactions on Antennas and Propagation*, vol. 65, no. 4, pp. 2117–2122, 2017. DOI: 10.1109/TAP.2017.2670509.

[155] D. Sun and J. Xu, "Rectangular waveguide coupler with adjustable coupling coefficient using gap waveguide technology," *Electronics Letters*, vol. 53, no. 3, pp. 167–169, 2016.

[156] D. Zarifi and A. Shater, "Design of a 3-dB directional coupler based on groove gap waveguide technology," *Microwave and Optical Technology Letters*, vol. 59, no. 7, pp. 1597–1600, 2017.

[157] D. Zarifi, A. Farahbakhsh, and A. U. Zaman, "Design and fabrication of wideband millimeter-wave directional couplers with different coupling factors based on gap waveguide technology," *IEEE Access*, vol. 7, pp. 88 822–88 829, 2019.

[158] X. Dong, H. Wang, F. Xue, and Y. Liu, "Design and measurement of a novel seamless scanning leaky wave antenna in ridge gap waveguide technology," *Progress In Electromagnetics Research*, vol. 58, pp. 147–157, 2017.

[159] M. Al Sharkawy, A. Foroozesh, A. A. Kishk, and R. Paknys, "A robust horn ridge gap waveguide launcher for metal strip grating leaky wave antenna," *IEEE Transactions on Antennas and Propagation*, vol. 62, no. 12, pp. 6019–6026, Dec. 2014. DOI: 10.1109/TAP.2014.2364050.

[160] M. R. Rahimi, N. Bayat-Makou, and A. A. Kishk, "Millimeter-wave substrate integrated gap waveguide leaky-wave antenna for WiGig applications," *IEEE Transactions on Antennas and Propagation*, vol. 67, no. 9, pp. 5790–5800, Sep. 2019. DOI: 10.1109/TAP.2019.2922446.

[161] N. Bayat-Makou and A. A. Kishk, "Millimeter-wave substrate integrated dual level gap waveguide horn antenna," *IEEE Transactions on Antennas and Propagation*, vol. 65, no. 12, pp. 6847–6855, 2017.

[162] M. Vukomanovic, J. Vazquez-Roy, O. Quevedo-Teruel, E. Rajo-Iglesias, and Z. Sipus, "Gap waveguide leaky-wave antenna," *IEEE Transactions on Antennas and Propagation*, vol. 64, no. 5, pp. 2055–2060, May 2016. DOI: 10.1109/TAP.2016.2539376.

[163] H. Raza, J. Yang, P.-S. Kildal, and E. Alfonso, "Resemblance between gap waveguides and hollow waveguides," *IET Microwaves, Antennas & Propagation*, vol. 7, no. 15, pp. 1221–1227, 2013.

[164] N. Marcuvitz, "On field representations in terms of leaky modes or eigenmodes," *IRE Transactions on Antennas and Propagation*, vol. 4, no. 3, pp. 192–194, 1956. DOI: 10.1109/TAP.1956.1144410.

[165] W. W. Hansen, *Radiating electromagnetic wave guide*, US Patent 2,402,622, Jun. 1946.

[166] V. Rumsey, "Traveling wave slot antennas," *Journal of Applied Physics*, vol. 24, no. 11, pp. 1358–1365, 1953.

[167] J. N. Hines, V. H. Rumsey, and C. H. Walter, "Traveling-wave slot antennas," *Proceedings of the IRE*, vol. 41, no. 11, pp. 1624–1631, 1953. DOI: 10.1109/JRPROC.1953.274190.

[168] A. Cullen, "XXXVII. Channel section waveguide radiator," *The London, Edinburgh, and Dublin Philosophical Magazine and Journal of Science*, vol. 40, no. 303, pp. 417–428, 1949.

[169] R. F. Harrington, "Propagation along a slotted cylinder," *Journal of Applied Physics*, vol. 24, no. 11, pp. 1366–1371, 1953.

[170] C. H. Walter, *Traveling wave antennas*. New York: Dover Publications, 1970.

[171] R. Honey, *Horizontally polarized long slot array*, 1954.

[172] W. Rotman, "The channel guide antenna," in *Proc. Natl. Electronics Conf*, vol. 5, 1949, p. 190.

[173] L. Goldstone and A. Oliner, "Leaky-wave antennas I: Rectangular waveguides," *IRE Transactions on Antennas and Propagation*, vol. 7, no. 4, pp. 307–319, Oct. 1959. DOI: 10.1109/TAP.1959.1144702.

[174] Y. T. Lo and S. Lee, *Antenna Handbook: theory, applications, and design*. Springer Science & Business Media, 2013.

[175] M. Pasian, M. Bozzi, and L. Perregrini, "Radiation losses in substrate integrated waveguides: A semi-analytical approach for a quantitative determination," in *2013 IEEE MTT-S International Microwave Symposium Digest (MTT)*, 2013, pp. 1–3. DOI: 10.1109/MWSYM.2013.6697593.

[176] N. Memeletzoglou and E. Rajo-Iglesias, "Holey metasurface prism for the reduction of the dispersion of gap waveguide leaky-wave antennas," *IEEE Antennas and Wireless Propagation Letters*, pp. 1–1, 2019. DOI: 10.1109/LAWP.2019.2943812.

[177] H. Wang, R. Gao, Y. Gu, J. Cao, and Z. Ye, "Low sidelobe leaky wave antenna based on gap waveguide technology," in *2017 International Applied Computational Electromagnetics Society Symposium (ACES)*, Aug. 2017, pp. 1–2.

[178] L. Wang, J. L. Gómez-Tornero, E. Rajo-Iglesias, and O. Quevedo-Teruel, "Low-dispersive leaky-wave antenna integrated in groove gap waveguide technology," *IEEE Transactions on Antennas and Propagation*, vol. 66, no. 11, pp. 5727–5736, Nov. 2018. DOI: 10.1109/TAP.2018.2863115.

[179] O. Dahlberg, E. Pucci, L. Wang, and O. Quevedo-Teruel, "Low-dispersive glide-symmetric leaky-wave antenna at 60 GHz," in *2019 13th European Conference on Antennas and Propagation (EuCAP)*, Mar. 2019.

[180] J. Cao, H. Wang, R. Gao, Y. Wang, and S. Mou, "2-Dimensional beam scanning gap waveguide leaky wave antenna array based on Butler matrix in metallic 3D printed technology," in *2019 13th European Conference on Antennas and Propagation (EuCAP)*, Mar. 2019, pp. 1–4.

[181] J. Cao, H. Wang, S. Tao, S. Mou, and Y. Guo, "Highly integrated beam scanning groove gap waveguide leaky wave antenna array," *IEEE Transactions on Antennas and Propagation*, pp. 1–1, 2020. DOI: 10.1109/TAP.2020.2995470.

[182] A. Oliner, "The impedance properties of narrow radiating slots in the broad face of rectangular waveguide: Part I–theory," *IRE Transactions on Antennas and Propagation*, vol. 5, no. 1, pp. 4–11, 1957. DOI: 10.1109/TAP.1957.1144488.

[183] L. Wang, Q. Cheng, W. Tang, X. Yin, and O. Quevedo-Teruel, "On the enhancement of scanning and gain flatness of leaky-wave gap-waveguide antennas with glide symmetry," in *2019 13th European Conference on Antennas and Propagation (EuCAP)*, Mar. 2019, pp. 1–4.

[184] J. Chen, C. Zhang, and Q. Cheng, "Continuous leaky-wave scanning using gap waveguide and gradient metasurface," in *2019 IEEE MTT-S International Wireless Symposium (IWS)*, May 2019, pp. 1–3. DOI: 10.1109/IEEE-IWS.2019.8803987.

[185] T. Ueda *et al.*, "Dispersion-free and tunable nonreciprocities in composite right-/left-handed metamaterials and their applications to beam squint reduction in leaky-wave antennas," *IEEE Transactions on Microwave Theory and Techniques*, vol. 67, no. 6, pp. 2227–2237, Jun. 2019. DOI: 10.1109/TMTT.2019.2909022.

[186] A. Mehdipour, J. W. Wong, and G. V. Eleftheriades, "Beam-squinting reduction of leaky-wave antennas using Huygens metasurfaces," *IEEE Transactions on Antennas and Propagation*, vol. 63, no. 3, pp. 978–992, Mar. 2015. DOI: 10.1109/TAP.2015.2389240.

[187] M. A. Antoniades and G. V. Eleftheriades, "A CPS leaky-wave antenna with reduced beam squinting using NRI-TL metamaterials," *IEEE Transactions on Antennas and Propagation*, vol. 56, no. 3, pp. 708–721, 2008. DOI: 10.1109/TAP.2008.916965.

[188] K. M. Kossifos and M. A. Antoniades, "A NRI-TL metamaterial leaky-wave antenna radiating at broadside with zero beam-squinting," *IEEE Antennas and Wireless Propagation Letters*, vol. 17, no. 12, pp. 2223–2227, 2018. DOI: 10.1109/LAWP.2018.2871722.

[189] C. Caloz, S. Abielmona, H. Van Nguyen, and A. Rennings, "Dual composite right/left-handed (D-CRLH) leaky-wave antenna with low beam squinting and tunable group velocity," *physica status solidi (b)*, vol. 244, no. 4, pp. 1219–1226, 2007. DOI: 10.1002/pssb.200674510. eprint: https://onlinelibrary.wiley.com/doi/pdf/10.1002/pssb.200674510.

[190] O. Zetterstrom, E. Pucci, P. Padilla, L. Wang, and O. Quevedo-Teruel, "Low-dispersive leaky-wave antennas for mmwave point-to-point high-throughput communications," *IEEE Transactions on Antennas and Propagation*, vol. 68, no. 3, pp. 1322–1331, 2020. DOI: 10.1109/TAP.2019.2943437.

[191] Q. Chen *et al.*, "Glide-symmetric holey leaky-wave antenna with low dispersion for 60-GHz point-to-point communications," *IEEE Transactions on Antennas and Propagation*, pp. 1–1, 2019. DOI: 10.1109/TAP.2019.2944535.

[192] L. Wang, J. L. Gómez-Tornero, and O. Quevedo-Teruel, "Substrate integrated waveguide leaky-wave antenna with wide bandwidth via prism coupling," *IEEE Transactions on Microwave Theory and Techniques*, vol. 66, no. 6, pp. 3110–3118, Jun. 2018. DOI: 10.1109/TMTT.2018.2818149.

[193] E. Rajo-Iglesias, M. Ebrahimpouri, and O. Quevedo-Teruel, "Wideband phase shifter in groove gap waveguide technology implemented with glide-symmetric holey EBG," *IEEE Microwave and Wireless Components Letters*, vol. 28, no. 6, pp. 476–478, 2018. DOI: 10.1109/LMWC.2018.2832013.

[194] Á. Palomares-Caballero, A. Alex-Amor, P. Padilla, and J. F. Valenzuela-Valdés, "Dispersion and filtering properties of rectangular waveguides loaded with holey structures," *IEEE Transactions on Microwave Theory and Techniques*, vol. 68, no. 12, pp. 5132–5144, 2020. DOI: 10.1109/TMTT.2020.3021087.

[195] O. Quevedo-Teruel, G. Valerio, Z. Sipus, and E. Rajo-Iglesias, "Periodic structures with higher symmetries: Their applications in electromagnetic devices," *IEEE Microwave Magazine*, vol. 21, no. 11, pp. 36–49, 2020. DOI: 10.1109/MMM.2020.3014987.

[196] Q. Chen, F. Mesa, X. Yin, and O. Quevedo-Teruel, "Accurate characterization and design guidelines of glide-symmetric holey EBG," *IEEE Transactions on Microwave Theory and Techniques*, vol. 68, no. 12, pp. 4984–4994, 2020. DOI: 10.1109/TMTT.2020.3023751.

[197] M. Ebrahimpouri, A. Algaba Brazalez, L. Manholm, and O. Quevedo-Teruel, "Using glide-symmetric holes to reduce leakage between waveguide flanges,"

IEEE Microwave and Wireless Components Letters, vol. 28, no. 6, pp. 473–475, 2018. DOI: 10.1109/LMWC.2018.2824563.

[198] J. Liu, D. R. Jackson, and Y. Long, "Modal analysis of dielectric-filled rectangular waveguide with transverse slots," *IEEE Transactions on Antennas and Propagation*, vol. 59, no. 9, pp. 3194–3203, 2011. DOI: 10.1109/TAP.2011.2161444.

[199] A. Ghasemi and J. Laurin, "A continuous beam steering slotted waveguide antenna using rotating dielectric slabs," *IEEE Transactions on Antennas and Propagation*, vol. 67, no. 10, pp. 6362–6370, 2019. DOI: 10.1109/TAP.2019.2925272.

[200] P. Lampariello, F. Frezza, H. Shigesawa, M. Tsuji, and A. A. Oliner, "A versatile leaky-wave antenna based on stub-loaded rectangular waveguide .I. theory," *IEEE Transactions on Antennas and Propagation*, vol. 46, no. 7, pp. 1032–1041, 1998. DOI: 10.1109/8.704806.

[201] J. L. Gomez-Tornero, G. Goussetis, A. P. Feresidis, and A. A. Melcon, "Control of leaky-mode propagation and radiation properties in hybrid dielectric-waveguide printed-circuit technology: Experimental results," *IEEE Transactions on Antennas and Propagation*, vol. 54, no. 11, pp. 3383–3390, 2006. DOI: 10.1109/TAP.2006.884298.

[202] E. Pucci, E. Rajo-Iglesias, J. Vázquez-Roy, and P.-S. Kildal, "Planar dual-mode horn array with corporate-feed network in inverted microstrip gap waveguide," *IEEE Transactions on Antennas and Propagation*, vol. 62, no. 7, pp. 3534–3542, 2014. DOI: 10.1109/TAP.2014.2317496.

[203] A. Vosoogh *et al.*, "W-band low-profile monopulse slot array antenna based on gap waveguide corporate-feed network," *IEEE Transactions on Antennas and Propagation*, vol. 66, no. 12, pp. 6997–7009, 2018. DOI: 10.1109/TAP.2018.2874427.

[204] Á. Palomares-Caballero, A. Alex-Amor, J. Valenzuela-Valdés, and P. Padilla, "Millimeter-wave 3-D-printed antenna array based on gap-waveguide technology and split E-plane waveguide," *IEEE Transactions on Antennas and Propagation*, vol. 69, no. 1, pp. 164–172, 2021. DOI: 10.1109/TAP.2020.3008620.

[205] M. Ng Mou Kehn, C.-K. Hsieh, and E. Rajo-Iglesias, "Array of horns fed by a transverse slotted groove gap waveguide at 28 GHz," *Sensors*, vol. 20, no. 18, 2020. DOI: 10.3390/s20185311. [Online]. Available: https://www.mdpi.com/1424-8220/20/18/5311.

[206] R. S. Elliott, "The design of waveguide-fed slot arrays," in *Antenna handbook*, Springer, 1988, pp. 805–842.

[207] L. Josefsson, "Analysis of longitudinal slots in rectangular waveguides," *IEEE Transactions on Antennas and Propagation*, vol. 35, no. 12, pp. 1351–1357, 1987. DOI: 10.1109/TAP.1987.1144042.

[208] S. R. Rengarajan, "Analysis of a centered-inclined waveguide slot coupler," *IEEE Transactions on Microwave Theory and Techniques*, vol. 37, no. 5, pp. 884–889, 1989. DOI: 10.1109/22.17455.

[209] ——, "Compound radiating slots in a broad wall of a rectangular waveguide," *IEEE Transactions on Antennas and Propagation*, vol. 37, no. 9, pp. 1116–1123, 1989. DOI: 10.1109/8.35791.

[210] K. Tekkouk *et al.*, "Corporate-feed slotted waveguide array antenna in the 350-GHz band by silicon process," *IEEE Transactions on Antennas and Propagation*, vol. 65, no. 1, pp. 217–225, 2017. DOI: 10.1109/TAP.2016.2631132.

[211] J. C. Coetzee and S. Sheel, "Improved model for inclined coupling slots in the feed of a planar slot array," *IEEE Transactions on Antennas and Propagation*, vol. 68, no. 2, pp. 1166–1169, 2020. DOI: 10.1109/TAP.2019.2938676.

[212] G. Stern and R. Elliott, "Resonant length of longitudinal slots and validity of circuit representation: Theory and experiment," *IEEE Transactions on Antennas and Propagation*, vol. 33, no. 11, pp. 1264–1271, 1985. DOI: 10.1109/TAP.1985.1143509.

[213] R. Elliott and L. Kurtz, "The design of small slot arrays," *IEEE Transactions on Antennas and Propagation*, vol. 26, no. 2, pp. 214–219, 1978. DOI: 10.1109/TAP.1978.1141814.

[214] A. K. Tiwari, D. Poddar, and B. Das, "Centered inclined slot coupling between waveguides with coplanar axes," *International Journal of RF and Microwave Computer-Aided Engineering*, vol. 21, no. 1, pp. 52–58, 2011. DOI: 10.1002/mmce.20486. eprint: https://onlinelibrary.wiley.com/doi/pdf/10.1002/mmce.20486.

[215] S. Sekretarov and D. M. Vavriv, "A wideband slotted waveguide antenna array for SAR systems," *Progress in Electromagnetics Research*, vol. 11, pp. 165–176, 2010.

[216] J. C. Coetzee, J. Joubert, and W. L. Tan, "Frequency performance enhancement of resonant slotted waveguide arrays through the use of wideband radiators or subarraying," *Microwave and Optical Technology Letters*, vol. 22, no. 1, pp. 35–39, 1999. DOI: https://doi.org/10.1002/(SICI)1098-2760(19990705)22:1<35::AID-MOP9>3.0.CO;2-M. eprint: https://onlinelibrary.wiley.com/doi/pdf/10.1002/\%28SICI\%291098-2760\%2819990705\%2922\%3A1\%3C35\%3A\%3AAID-MOP9\%3E3.0.CO\%3B2-M. [Online]. Available: https://onlinelibrary.wiley.com/doi/abs/10.1002/%5C%28SICI%5C%291098-2760%5C%2819990705%5C%2922%5C%3A1%5C%3C35%5C%3A%5C%3AAID-MOP9%5C%3E3.0.CO%5C%3B2-M.

[217] M. Hamadallah, "Frequency limitations on broad-band performance of shunt slot arrays," *IEEE Transactions on Antennas and Propagation*, vol. 37, no. 7, pp. 817–823, 1989. DOI: 10.1109/8.29375.